AN EXPERIMENTAL STUDY OF ENTRAINMENT AT A DENSITY INTERFACE BY MEAN VELOCITY SHEAR

A thesis

submitted for the degree of

Doctor of Philosophy

at the

University of Canterbury

by

Seeto Chun Ming

Department of Mechanical Engineering

University of Canterbury

New Zealand

1987

To Shirley

ABSTRACT

An experimental study of turbulent entrainment at a density interface due to mean velocity shear is reported in this thesis. The model which is comprised of a layer of initially quiescent salt water contained in a finite size cavity of length 290 mm under a flowing layer of freshwater, represents ambient windflow over a cloud of dense gas lying in a recess in the terrain. The density ratio in the fullscale situation is retained in the model and the density profile is a step function.

The mean component $\overline{U}(z)$ and the fluctuating components $\sqrt{\overline{u'^2}}$ and $\sqrt{\overline{w'^2}}$ of velocity are recorded at the channel centreline and at two positions away from the centreline. Although the flow structure across the channel is not uniform due to local variation near the sides, the effect on the overall flow structure is small and the flow regime can be represented by laterally-averaged values of mean velocity and mean shear stress.

The entrainment of dense saline solution by the upper layer is due to the interface becoming unstable, forming interfacial waves which break and eject saline solution upwards. The three length scales which are associated with the wake behind the backward-facing step, the change in surface roughness and the depth of the new turbulent boundary layer over the cavity are suitable to describe the interfacial region during entrainment and are all of similar order. The depth of the new turbulent boundary layer was chosen as it is an exact length scale for very high Richardson number when the interface is smooth and flat.

The non-dimensional entrainment velocity of the saline solution was found to vary as the Richardson number to the (-3/2) power. This behaviour is in general agreement with the results of Lofquist (1960) except that the effect of the cavity ends in these experiments caused the

entrainment velocity to nearly double those measured by Lofquist.

Estimates of the length and phase velocity of the interfacial waves are compared with the Kelvin-Helmholtz instability and the hypothesis that the phase velocity of the interfacial waves was equal to the mean velocity of the upper layer. The experimental results were located between these two theoretical results.

TABLE OF CONTENTS

Page

Page

Page

LIST OF FIGURES

LIST OF TABLES

LIST OF SYMBOLS

Note :

Symbols which have limited use and are defined in the text or appendices are not listed here.

a	-	Amplitude of wave or instability at the interface
c	-	Phase velocity of wave or instability at the interface
d'	-	Viscous lengthscale = $[\nu_1 x/\overline{U}_o]^{1/2}$
E	-	Non-dimensional entrainment velocity = $u_e/\overline{U}$
$\overline{E}$	-	Non-dimensional entrainment velocity = $u_e(F)/\overline{U}_o$
E_*	-	Non-dimensional entrainment velocity = $u_e(F)/u_*$
g	-	Gravitational acceleration
h_o	-	Depth of upper or mixed layer
h_1	-	Depth of lower or dense layer
H	-	Combined depth of upper and lower layers = $h_o + h_1$
k	-	Von Karman coefficient
K	-	Keulegan number = $\overline{U}_o^3/g'\nu_1$
L	-	Length scale
L_1	-	Length of cavity
Pe	-	Peclet number based on thermal diffusivity = UL/κ
	-	Peclet number based on molecular mass diffusivity = UL/α
Re	-	Reynolds number = UL/ν
Re_δ	-	Reynolds number based on the boundary layer depth = $\overline{U}_\infty\delta/\nu$
Ri	-	Richardson number = $g\Delta\rho L/\rho_o U^2$
Ri_h	-	Richardson number based on the mixed layer depth = $g\Delta\rho h_o/\rho_o u_*^2$
Ri_o	-	Richardson number based on the overall flow situation = $g\Delta\rho L/\rho_o U^2$

Ri_δ - Richardson number based on the depth of the new turbulent boundary layer over the cavity = $g\Delta\rho\delta_t/\rho_o\overline{U}_o^2$

Ri_* - Richardson number based on the roughness parameter and the friction velocity = $g\Delta\rho z_o/\rho_o u_*^2$

Ro - Rossby number = $U/L\Omega_r$

t - Time

T - Time required to recycle the volume of water in the recirculating system

u,v,w - Velocities in the longitudinal, lateral and vertical directions respectively

u_e - Entrainment velocity

$u_e(b)$ - Boundary entrainment velocity

$u_e(f)$ - Flow entrainment velocity

$u_e(F)$ - Flux entrainment velocity

u_* - Friction velocity = $[\tau_o/\rho_o]^{1/2}$

U - Velocity scale

$\overline{U}$ - Mean velocity or mean velocity difference

$\overline{U}_b$ - Local bulk velocity at each of the measuring stations

$\overline{U}_o$ - Overall bulk mean velocity of the upper layer

$\overline{U}_\infty$ - Maximum mean velocity in the upper layer

$\overline{U}(z)$ - Mean velocity at height z above ground or floor level

$\sqrt{\overline{u'^2}}/\overline{U}(z)$ - Longitudinal component of turbulence intensity at height z.

$\sqrt{\overline{w'^2}}/\overline{U}(z)$ - Vertical component of turbulence intensity at height z.

x,y,z - Longitudinal, lateral and vertical distance coordinates respectively

z_o - Roughness parameter

α - Molecular diffusivity

δ - Boundary layer depth

δ_ℓ - Depth of laminar boundary layer

δ_t - Depth of turbulent boundary layer

θ	-	Intersection angle of the two laser beams
κ	-	Thermal diffusivity
λ	-	Wavelength
λ_c	-	Critical or unstable wavelength at interface
υ	-	Kinematic viscosity
υ_1	-	Kinematic viscosity of lower or saline layer
ρ	-	Density
ρ_0	-	Density of upper or mixed layer fluid
ρ_1	-	Density of lower or saline layer of fluid
$\Delta\rho$	-	Density difference = $\rho_1-\rho_0$
τ	-	Shear stress
τ_0	-	Shear stress at the ground or floor

CHAPTER ONE

INTRODUCTION

1.1 The Case for Dense Gas Dispersion

The widespread use of toxic and/or flammable substances has brought about large amounts of these substances being transported and stored near areas which may be high density work or residential regions. Many of these substances become gaseous or gaseous with liquid droplets when first released into the atmosphere. The fact that some of the released substances become heavier-than-air means that interaction with people or other forms of life is inevitable. Some unfortunate incidents which have already proven to be disastrous include the release of methyl isocyanate at Bhopal and the liquefied petroleum Gas fires in Mexico City in 1984 and more recently the fatal poisoning of many villagers near Lake Nyos in north-west Cameroun in August 1986.

By obtaining a better understanding of the behaviour of dense gases in the atmosphere, the people involved in the design, planning and construction of facilities associated with dense gases can have not only a qualitative knowledge but also a quantitative knowledge of the possible hazards. This information will also be of help to the emergency services such as the fire service in the event of a release of dense toxic and/or flammable gas.

In a favourable situation, the dense gas is quickly dispersed and concentration reduced below flammable or toxic level so that no hazard prevails. However, in some adverse situations such as slightly stable atmospheric conditions with low wind speed, the gas concentration may remain high enough for concern. It is under these adverse conditions that some aspects of dense gas behaviour are studied.

1.2 The Heavier-than-Air Gas Cloud

The study of the dispersion of dense gases contains many facets with one of the most important being the negatively buoyant character. The other interesting factors which contribute to the problems include the method of release, whether the terrain is flat or sloping, the roughness of the terrain, the atmospheric conditions, the presence of large structures or obstacles and whether there is a heat source such as a fire. Other factors can be important but those mentioned above appear to be discussed more often in the literature.

The negatively buoyant character of dense gases arises in a number of ways :

(i) The substance has a higher molecular weight than air.

(ii) The substance is heavier-than-air at low temperatures. For example, methane evolved from refrigerated Liquefied Natural Gas at its boiling point.

(iii) The substance may be lighter than air but due to the presence of liquid droplets within the gas cloud or plume, the density exceeds that of air.

(iv) The substance may have a lower molecular weight than air but which may form dense mixtures due to molecular association, for example, hydrogen fluoride.

1.3 The General Problem

The behaviour of a dense gas cloud released at ground level in uniform flat terrain can be described well by the box model which is briefly discussed in Chapter 2. There are situations however to which

this box model cannot directly apply but which have elements common to the box model. One of these situations is where the cloud of dense gas is trapped in a low-lying area and the ambient wind, though turbulent, cannot transport the cloud in its entirety. An example is the ponding dike built around a refrigerated storage tank holding Liquefied Natural Gas (LNG) (Meroney and Neff 1977). The situation may also arise if the terrain includes low-lying regions such as a riverbed or drains into which a dense gas can accumulate.

The action of wind shear and turbulence on the cloud surface will encourage mixing of gas out of the cloud as well as dilution of the cloud concentration. Any gas which enters the ambient airstream is a result of the wind action rather than from any initial vertical momentum. The rate at which the dense gas enters the ambient airstream will assist in the determination of the gas concentration at a downstream region. The measurement of this entrainment rate is the aim of this work.

The windspeeds of interest are about 2 m/s at ten metres in height over uniform terrain. This can correspond to slightly stable atmospheric conditions at night-time with thin low cloud cover. Such low windspeeds also occur in slightly unstable atmospheric conditions during the day with slight incident solar radiation (Panofsky and Dutton 1984). In the case of slightly stable atmospheric conditions, the windflow may not be aerodynamically rough.

It was decided to study a two-dimensional configuration as it was considered to be the most simple, and the observed behaviour will be representative of most of the dense gas cloud-air interfacial region. Figure 1.1 is a sketch of the field or prototype situation. It shows a pool of dense gas lying in a recess in the terrain and an ambient wind flowing over the dense gas. The wind structure and gas cloud are assumed not to vary significantly in the lateral direction.

This particular problem was chosen for study as it was considered to be a fundamental one. If the physics of the dense gas-air interfacial

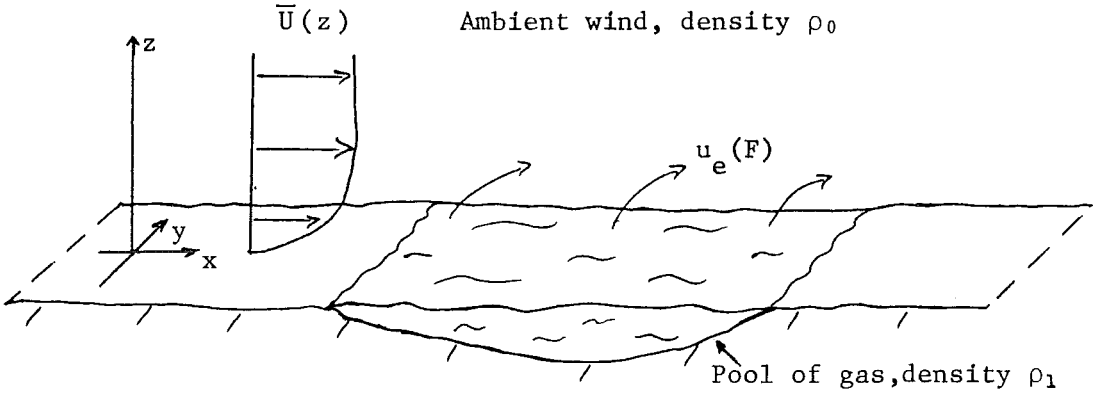

Figure 1.1 : Sketch of the Two-dimensional Prototype Situation of a Cloud of Dense Gas in a Recess in the Terrain.

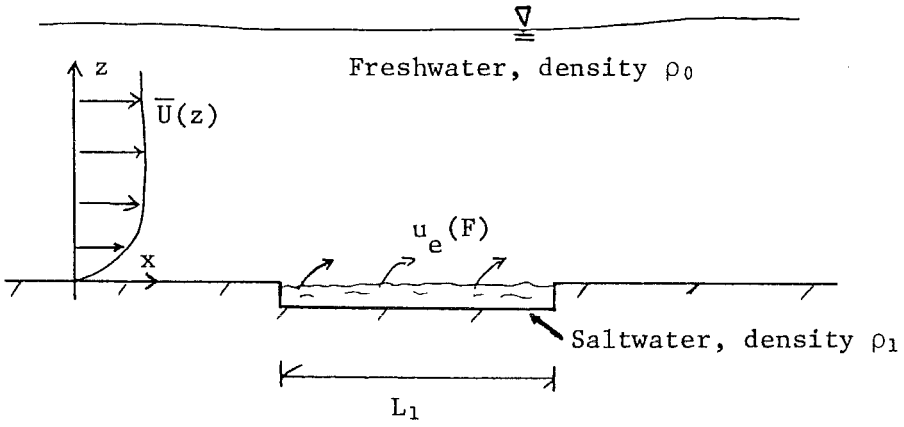

Figure 1.2 : Sketch of the Laboratory Model of a Dense Gas Cloud in a Cavity.

region can be understood in this configuration, then this understanding can be applied to the more complex situations in which some elements of the fundamentals will be present.

1.4 The Scope and Objectives of this Study

This study involves the physical modelling of the entrainment of a dense gas cloud by the ambient wind and turbulence. The dense gas cloud is retained in the cavity and the windshear is insufficient to move the whole cloud downstream. The resulting model is a combination of the laboratory experiments where mean velocity shear is present (Keulegan 1949, Ellison and Turner 1959 and others) and where deliberate end effects are introduced by way of a finite size cavity. The model is sketched in Figure 1.2.

The density of a heavier-than-air gas such as propane, butane or Liquefied Petroleum Gas (LPG) may be up to 1.5 times that of ambient air. To obtain this density ratio it was decided to use freshwater to model ambient air and saline solutions to represent the dense gas. Sodium chloride and calcium chloride were dissolved in distilled water to represent the dense gas. A fully recirculating system which included an open channel was used to contain the water and salt solutions.

The objectives of this study are :

(i) To obtain a flow regime upstream of the cavity which is representative of the atmospheric boundary layer at low windspeed.

(ii) To study the behaviour of the density interface and how it is related to the entrainment process at relatively large Richardson numbers.

(iii) To obtain measurements of entrainment of the dense fluid by the ambient fluid and to compare these results with those already published in the literature.

1.5 The Layout of this Thesis

A brief review of the box model dense gas dispersion is presented in Chapter 2. Of particlar interest are the various definitions of entrainment velocity, and the application of the laboratory results to field models.

Similarity criteria for the study of atmospheric pollution problems are presented in Chapter 3. The non-dimensional parameters are identified as well as the boundary condtions. The physical model is also discussed.

The equipment which is required for this study is described in Chapter 4. The experimental procedures and programme are also outlined.

The measurements of the background flow are presented in Chapter 5. The observations of the experiments and the entrainment results are presented and discussed in Chapter 6.

The conclusions of this work are summarised in Chapter 7, and some suggestions on possible areas for future research are indicated.

CHAPTER TWO

SURVEY OF LITERATURE

2.1 Introduction

The study of the dispersion of dense gases in the atmosphere is relatively recent when compared to work on neutrally or positively buoyant gases. The bulk of the literature on dense gas dispersion has only appeared in the last 15 years. Although this survey is concerned with the release of discrete dense gas clouds, there are many elements which are also common to the continuous release of dense gases.

The general problem discussed in Section 1.3 has some elements in common with the integral box model which was originally developed by Van Ulden (1974). For this reason, it is considered appropriate to briefly review the dense gas dispersion models and in particular, the box model.

The development of models for dense gas dispersion has proceeded along two lines :

(ii) The box models are based on the solution of integral equations. The mean velocity and concentration profiles are represented by similarity profiles and integral variables. These models are limited to mean values but do have a small number of adjustable constants which have a physical interpretation.

(ii) The numerical approach is based on the solution of the relevant differential equations which have been simplified by the introduction of eddy diffusivity coefficients. These models are much more flexible than the box model even though some uncertainty exists in the choice of eddy diffusivities. For example, not all models stress that the Reynolds analogy (the equivalence of eddy diffusivities of heat, mass, and momentum) is not valid when the

flow has a stable density stratification (Turner 1973, Chapter 5).

As this work is concerned with the particular entrainment aspect of the box models, no more discussion on the eddy diffusion models will be raised. The two recent collective works edited by Britter and Griffiths (1982), and by Ooms and Tennekes (1984), contain a number of articles concerning the numerical approach.

This survey of the literature will cover briefly the isothermal box model of dense gas dispersion. This model concerns the behaviour of a dense gas cloud which has been released into a turbulent wind at ground level. The survey will concentrate on the entrainment phase of the box model as this is one aspect which has involved much discussion and is the topic of this work. The box model is discussed in the next section.

The entrainment hypothesis is discussed in Section 2.3 and this covers the different definitions of entrainment velocity and entrainment mechanisms. The laboratory experiments which involve mean velocity shear and no external buoyancy sources are reviewed.

The final section discusses the practice of using laboratory entrainment data for field models of dense gas dispersion.

2.2 The Box Model

The box model was initially proposed by Van Ulden (1974) who, based on data obtained from one field experiment, found agreement with the model. Van Ulden also found that the Gaussian approach was no longer suitable when the gas density was significantly greater than the air density.

There have been modifications to the box model by Eidsvik (1980), Fay (1980, 1984), Meroney (1983), Chatwin (1984), Webber (1984) and others who accounted for variations in ambient temperature, gas release conditions, phase transformation and wind shear. Some of the work on particular aspects of dense gas dispersion up to 1980 has been surveyed by

Seeto (1982) in an unpublished report. The two collective works edited by Britter and Griffiths (1982) and by Ooms and Tennekes (1984) cover the current problems and advances which have been made in the area of dense gas dispersion in the atmosphere.

2.2.1 Summary of the Isothermal Model

The box model is an idealisation which assumes that the dense gas cloud behaves in a number of phases which may not be distinct. These phases are :

(i) The cloud formation,

(ii) the spreading of the cloud due to excess buoyancy,

(iii) the entrainment of air into the gas cloud, and

(iv) the dispersion of a neutrally buoyant gas cloud.

The assumptions which accompany the box model are :

(i) The homogeneous cloud is a circular cylinder of height h, and radius r, and is formed immediately after the release,

(ii) the dense gas cloud does not undergo any chemical or physical reaction except dilution by the ambient air,

(iii) the fluctuations in gas concentrations are not predicted,

(iv) the terrain is flat and of constant roughness with no large structures or obstacles,

(v) the terrain has constant thermal properties, and

(vi) the air flow over the cloud is turbulent.

The volume of the dense gas cloud is given by :

$$V = \pi r^2 h \qquad (2.1a)$$

and conservation of negative buoyancy requires :

$$Vg' = \pi r^2 hg' \qquad (2.1b)$$

The spreading velocity of the front of the dense gas cloud is :

$$U_r = \alpha_1 (g'h)^{1/2} \tag{2.2a}$$

and the cloud radius is given by :

$$r^2 = r_0^2 (1 + \frac{t}{t_0}) \tag{2.2b}$$

where α_1 is a constant of order unity, t_0 is a characteristic time scale, and $g' = g\frac{\Delta\rho}{\rho_0}$. ρ_0 is the ambient air density, ρ_1 the gas density such that $\Delta\rho = \rho_1 - \rho_0$ and g is gravitational acceleration. The dominant nondimensional parameter in flows in which buoyancy forces are appreciable is the Richardson number (Chapter 3). This is defined as $Ri_c = g'h/u_*^2$ for a dense gas cloud of height h, where $u_* = (\tau_0/\rho_0)^{1/2}$ is the friction velocity, and τ_0 the shear stress at the ground. The entrainment of air into the gas cloud is :

$$\frac{dV}{dt} = \pi\, r^2 u_z + 2\pi\, rhu_p \tag{2.3}$$

where u_z is an entrainment velocity for the cloud upper surface, and u_p is an entrainment velocity for the cloud periphery. A sketch of the model is shown in Figure 2.1a. The expressions for u_z and u_p are assumed to vary, depending on the cloud Richardson number. Chatwin (1984) has included the effect of wind shear in the model, and by assuming that the gas cloud becomes a tilting cylinder of circular cross-section with an angle ϕ to the vertical, has found that (see Figure 2.1b) :

$$u_z = \frac{\beta\beta_1\, u_*}{\{\beta^2 + \beta_1^2 Ri_c^2\}^{1/2}} \tag{2.4}$$

and

$$u_p = \frac{(g'h)^{1/2}\{\gamma Ri_c + \gamma_1\gamma_*\}}{Ri_c \cos\phi + \gamma_* Ri_c^{1/2}} \tag{2.5}$$

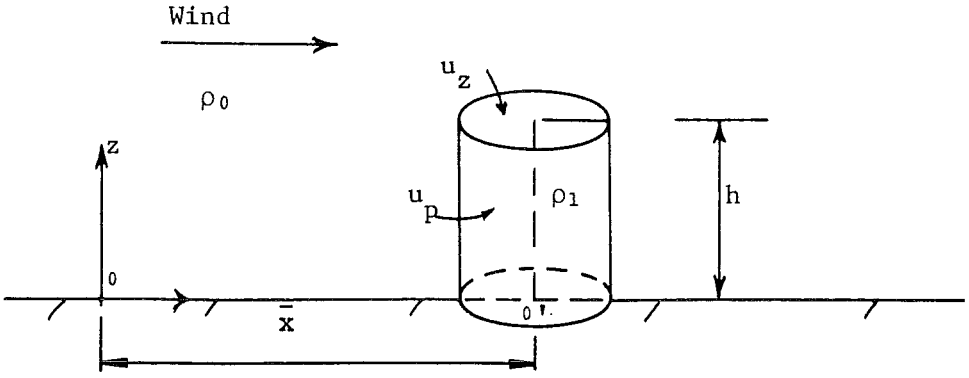

Figure 2.1a : Model of a Dense Cylindrical Gas Cloud in Assumed Upright Position.

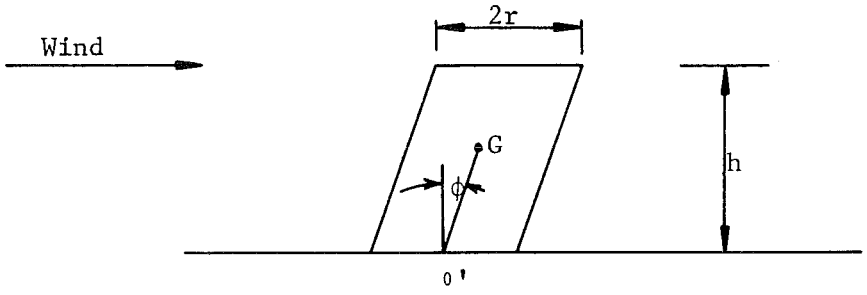

Figure 2.1b : The Tilted Cylinder of Chatwin's (1984) Model.

The tilting of the cylinder does not affect u_z and Chatwin has argued that the tilting is only important for $Ri_c >> 1$.

The relation between the angle ϕ and other parameters is, according to Chatwin (1984) :

$$\tan \phi = \delta \left(\frac{u_* t}{h}\right) \ell n \left(\frac{h}{e z_0}\right) \qquad (2.6)$$

where t is time after cloud formation, z_0 is the roughness parameter, and e is the base of the natural logarithm. The constants $\beta, \beta_1, \gamma, \gamma_1, \gamma_*$ and δ are to be determined empirically and δ is of order 5. The constants $\beta, \beta_1, \delta, \gamma_1$ and γ_* are all associated with the entrainment of air into the dense gas cloud and atmosperhic conditions. By selecting values of these constants, the box model can be 'tuned' to particular sets of experiments (Eidsvik 1980, Fay and Ranck 1983 and others).

The expressions for u_z and u_p are valid for large Ri_c when buoyancy is the dominant force and for small Ri_c when turbulence and mean velocity shear are dominant. The transition from large Ri_c to small Ri_c is achieved gradually.

The dense gas cloud can also be carried downwind by the mean wind and the cloud travel speed is suggested by Fay (1980) to be related to the undisturbed wind field by :

$$\overline{U}_c = 2.5\, u_* \ell n \left[\frac{\alpha_2 h}{z_0} + 1\right] \qquad (2.7)$$

where α_2 is a constant of order unity. This constant causes the cloud travel speed to be viewed as a weighted average over the cloud height.

The expressions (2.2b) to (2.7) constitute a system of equations which are used to determine the cloud volume as a function of time after

release and cloud formation. The average gas concentration can be easily evaluated after the cloud volume is known.

After considerable dilution, that is, when $\rho_1 \sim \rho_0$, the gas cloud behaves as a passive cloud, and the subsequent dispersion can be treated by the Gaussian method (Gifford 1961, Pasquill 1961, 1974 and others).

2.2.2 The Box Model with Nonisothermal Conditions

In the case where significant temperature differences exist between the dense gas cloud and the surroundings, modifications to the box model are required. Eidsvik (1980), Fay (1980), Meroney (1983) and others have included modifications to the box model. As this work is concerned with a simple isothermal model, no further discussion on the nonisothermal effects will be held and the above references should be consulted for further details.

2.2.3 The Concentration Intensity

The simplified approach of the box model only provides information about mean values such as mean velocities and mean gas concentration $\overline{C}(x_i, t)$ where x_i are coordinates in three directions and t is time since gas release. Chatwin (1982) however has argued that the root mean square of the concentration fluctuation $[\overline{c'^2}(x_i, t)]^{1/2}$ or c' of gas concentration should not be ignored, especially when these fluctuations are at least of the same order as $\overline{C}$. Although there has not been any reported measurements for negatively buoyant gases, Chatwin (1982) quotes Csanady (1973) who in turn has reported values of concentration intensity :

$$I(x_i, t) = c'/\overline{C}$$

between 5 and 10 in plumes of positively buoyant material released from a

continuous source. The measurements were taken at distances from the centreline of the order of the plume width. However, $\overline{C}$ is assumed to have a Gaussian distribution and at the centreline, the values of $I(x_i,t)$ lie in the range $0<I(x_i,t)<1$ (Figure 7.11 Csanady 1973). Theoretical work by Chatwin and Sullivan (1979) has suggested large values of $I(x_i,t)$, and according to Chatwin (1982), there is no theoretical or experimental support for the hypothesis that $I(x_i,t)$ is much less than 1. Chatwin (1982) then dismisses the models which ignore the concentration fluctuations as being inadequate in principle and practice. However, it is stressed that the Gaussian approach has been shown to be unsuitable for the dispersion of dense gases (Van Ulden 1974, Britter 1980 and others) except for very small concentrations. In practical terms, this means that only dense gases which are toxic or flammable at very small concentrations will require consideration of the concentration intensity.

2.3 Entrainment at a Density Interface

2.3.1 The Entrainment Hypothesis

The idea of entrainment was first introduced by Sir Geoffrey Taylor in 1949, but it did not receive much exposure until the 1950's when Batchelor (1954) presented a review and a subsequent paper by Morton, Taylor and Turner (1956) appeared. The background to the entrainment hypothesis has been presented by Turner (1986) who also discussed various applications to geological studies.

2.3.2 Definitions of Entrainment

The term entrainment is a very useful concept in box models of dense gas dispersion, even though it has been used to refer to different mixing mechanisms. Hunt, Rottman and Britter (1984) have clarified this concept and the uses of the term which in general correspond to transfer

of mass in regions of inhomogeneous turbulence. The following definitions are from Hunt, Rottman and Britter (1984) :

(i) In regions of shear flow and inhomogeneous turbulence, the gradients of Reynolds stresses which not only act on any mean flow to reduce the mean velocity gradients (like molecular viscosity) and thereby induce a mean flow in towards the turbulent region (as in a laminar or turbulent jet), but also induce additional mean recirculating flows in planes perpendicular to the primary shear flow, such as in flow over surfaces with different roughness. These secondary flows are primarily caused by differences in the normal stresses and are unlike any effect caused by viscosity. The inwards velocity in either of these two flows is called an entrainment velocity $u_e(f)$. The shear in a jet or at the head of a gravity current induce flows in towards the region of high turbulence with characteristic velocity $u_e(f)$ proportional to the difference between the mean velocity inside and outside the turbulent region (Figure 2.2a). This entrainment velocity of the fluid transfers the external uncontaminated fluid into gravity current. This was the definition of entrainment velocity which was first introduced by Morton, Taylor and Turner (1956) in their study of a rising plume.

(ii) The volume occupied by regions of locally intense turbulence tend to increase as the eddies induce each other to spread outwards (Figure 2.2b). This tends to disperse outward any contaminant together with the region of high turbulence. This outward velocity of the boundary of a region of high turbulence or of a region of significant concentration of a contaminant is also called an entrainment velocity $u_e(b)$ or is defined by means of an entrainment parameter (Turner 1973, Chapter 6). It is usually defined in some fixed coordinate system (so that $u_e(b) = -2u_e(f)$

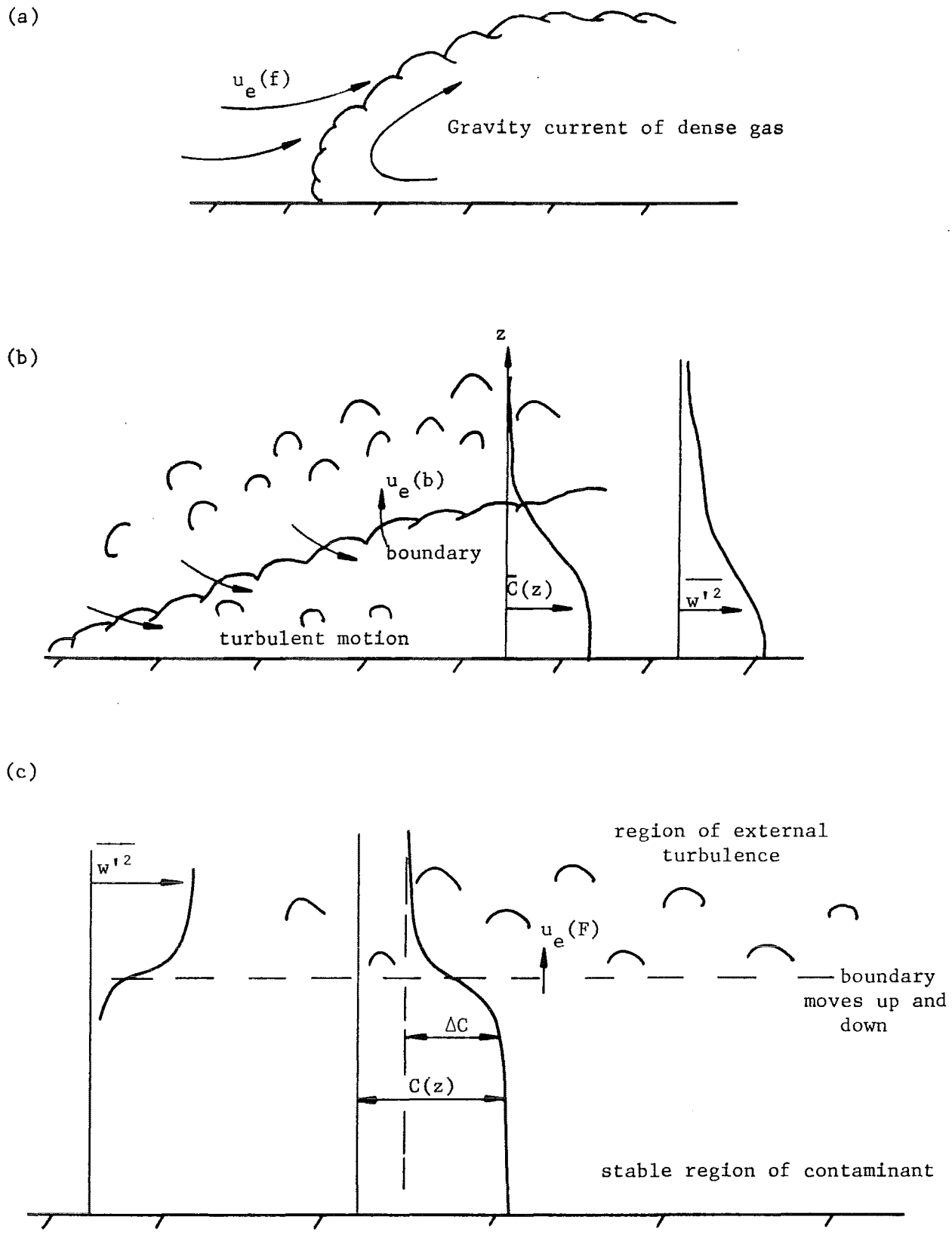

Figure 2.2 : Definitions of the Entrainment Velocity

for a round jet). Alternatively, the entrainment velolcity $u_e^*(b)$ can be defined relative to the local mean flow so that :

$$u_e^*(b) = u_e(b) - u_e(f)$$
$$= -3u_e(f) \quad .$$

Note that $u_e(b)$ and $u_e(f)$ are usually in opposite directions. This definition can be generalised to include the rate of growth of a boundary of a region of marked fluid (for example, by a contaminant) when the region of marked fluid does not contain turbulence of any greater intensity than the surroundings (Turner 1973 Section 6.2, and Webber 1984). In such cases $u_e(b)$ may be non-zero while $u_e(f)$ is zero as in the case of a neutrally buoyant gas diffusing upwards in the atmosphere boundary layer where $u_e(b) \propto u_*$, and $u_e(f)=0$ because there is no local turbulence associated with the cloud.

(iii) The third way for marked fluid or a contaminant to be transferred out of a particular region is by turbulence outside the region as shown in Figure 2.2c when the region is stably stratified (Turner 1973, Chapter 9). If this external turbulence is relatively vigorous, any contaminant diffusing out of the region is quickly dispersed so that the concentration outside the region is small. Then the effective boundary of the turbulent region remains at the interface between the contaminated region and the external region. The external turbulence does not penetrate the interface because of the stable stratification. In such cases the fluxes F(c), $F(\rho)$ of concentration and density outwards across a fixed surface

can be characterised by a flux entrainment velocity :

$$u_e(F) = \frac{F(\rho)}{\Delta\rho} \quad .$$

The flux entrainment velocity $u_e(F)$ is independent of the difference in concentration across the interface.. Note that the $u_e(F)$ may be in the opposite direction to $u_e(b)$; when $u_e(b)<0$, the process is usually referred to as 'erosion'. It is possible to have $u_e(F)$ to be non-zero while both $u_e(b)$ and $u_e(f)$ are zero.

These definitions have also been discussed by Turner (1986) in a review article on turbulent entrainment.

2.3.3 **Mechanisms of Entrainment**

The external flow interacts with the stratified layer of dense gas as it flows over the cloud. This interaction of a region of turbulent motion with a region of stably stratified fluid occurs in many natural flows such as the mixing layer in the upper ocean. As the available ideas for this interaction are not in agreement, Hunt, Rottman and Britter (1984) have suggested four mechanisms of entrainment which have been reported in the literature. The discussion by Hunt *et al* deals initially with the absence of mean velocity gradients at the interface and their descriptions are given below :

(i) Turbulent eddies impinge on the interface and generate sufficiently large fluctuating velocity gradients that the local Richardson number :

$$\frac{-g\partial\rho/\partial z}{\rho(\partial u/\partial z)^2}$$

is small enough for the interface to become unstable and form the Kelvin-Helmholtz billows (Thorpe 1973 and others) which grow and eventually break inducing molecular mixing (Figure 2.3a). One expects this process to be relevant when the stratification is strong enough to damp the vertical turbulence component at the interface. Long (1978) has remarked that in this limit fluctuations near the interface are expected to be similar to those in a turbulent flow near a rigid surface moving at the same velocity as the mean flow. An example is a moving belt in a wind tunnel or a free surface of a liquid in turbulent flow (Hunt and Graham, 1978).

(ii) With strong stratification at the interface, impinging energetic turbulent eddies distort it sufficiently for fine filaments of the stratified fluid layer to be drawn into the turbulent region where molecular diffusion completes the process (Linden 1973). Linden hypothesised that such eddies are similar to vortex rings and by experiment and analysis was able to estimate entrainment rates across a density discontinuity (see Figure 2.3b).

(iii) Turbulent eddies distort the interface and set up internal waves in the stratified layer whose energy and form depend on stratification. In a uniformly stratitied layer shown in Figure 2.3c, the waves propagate energy away from the interface but their amplitude at the interface may be large enough to cause mixing. If the stratified layer is strong near the interface and weak or non-existent far above the interface, then trapped and resonant waves of large amnplitude can be induced by relatively weak turbulence.

(i) Impinging of interface by eddies induce K-H billows

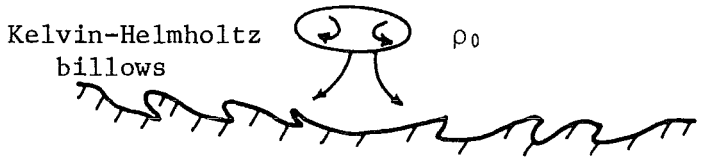

(ii) Turbulent eddies distort interface and cause filaments of stratified fluid to be drawn upwards

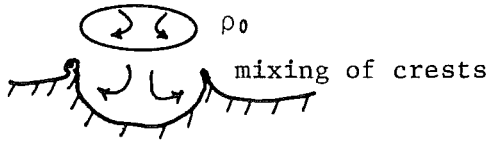

(iii) Turbulent eddies distort interface and set up internal waves

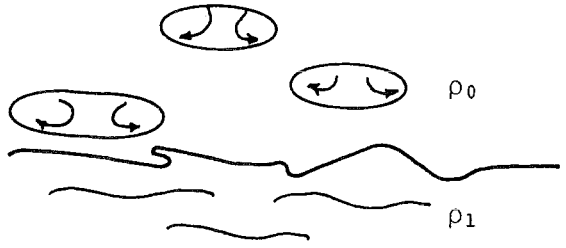

Internal waves

(iv) Engulfing process

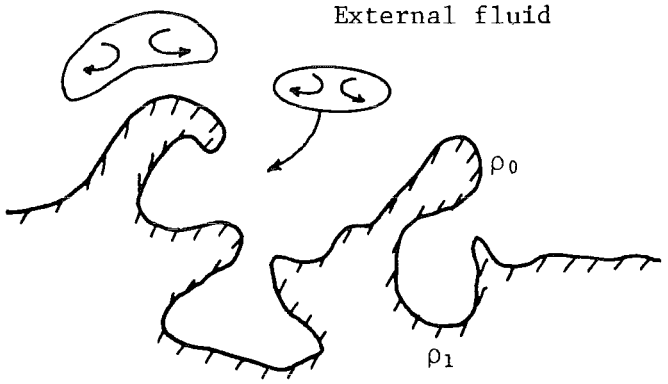

Figure 2.3 : Four Mechanisms for Producing a Flux of Contaminant across a Stable Density Interface

(iv) With weak stratification, the turbulent layer can also grow and entrain by the same processes as occurring at the edge of a turbulent boundary layer or wake in neutral stratification. The large eddies in the turbulent layer induce large random motions in the upper layer leading to the engulfing of external fluid as depicted in Figure 2.3d (Townsend 1976, Chapter 6).

In the presence of mean velocity along the interface, billowing motions are generated and are similar to Kelvin-Helmholtz billows and these largely control the mixing : (i) is the dominant mechanism under these circumstances. For mechanisms (i), (ii), (iii), there is a net flux of contaminant outwards across the interface which is quantified by the flux entrainment velocity $u_e(F)$. When either of these mechanisms control the upward flux, the interface is sharp and the upward boundary entrainment velocity $u_e(b)$ is small. Most experiments and theoretical models show that in these situations $u_e(F)/u_* = \text{function } (Ri_*)$ where Ri_* is a local Richardson number. If there is a step of $\Delta\rho$ between the density in the upper layer of the cloud and that of the ambient flow, Ri_* is defined as :

$$Ri_* = g \frac{\Delta\rho}{\rho_0} \frac{L}{u_*^2}$$

where L is a lengthscale for external vertical turbulence. An overall form of the Richardson number has also been used :

$$Ri_0 = g \frac{\Delta\rho}{\rho_0} \frac{L}{\overline{U}^2}$$

where $\overline{U}$ is the mean velocity difference between layers.

There have been models advanced for $u_e(F)/u_* = \text{function } (Ri_*)$ and these have been of the form $u_e(F)/u_* = Ri_0^{-m}$ where $\frac{5}{6} \quad m \quad \frac{3}{2}$. However, there has not been sufficient detailed testing of these models.

2.3.4 Entrainment due to Mean Velocity Shear

The windflow over a dense gas cloud is hydrodynamically the same as the flow of a fluid layer over a more dense fluid. Many laboratory studies have been carried out and some ideas and results may be useful in understanding the mixing between air and a dense gas.

The structure of the density interface across which exists a mean velocity difference has been extensively studied with various applications in mind (Keulegan 1949, Ellison and Turner 1959, Lofquist 1960, Kato and Phillips 1969, Kantha, Phillips and Azad 1977, Deardorff and Willis 1982, Scranton and Lindberg 1983, Kranenburg 1984, and others).

Keulegan (1949) studied interfacial instability and mixing and obtained measurements of entrainment $u_e(F)$. By keeping the level of the higher density layer constant, Keulegan measured $u_e(F)$ by relating the concentration of colouring particles in the upper (lower density) water layer to the rate of mixing. Keulegan's (1949) results shown in Figure 2.4 are in the range $Ri_0 \approx 1$–10. The corresponding values of $u_e(F)/\overline{U}$ lie in the range 10^{-5}–10^{-4}.

As Figure 2.4 will contain results from different sources, the nondimensional entrainment $E = \frac{u_e}{\overline{U}}$, where u_e can represent any of the definitions of entrainment velocity (Section 2.3.2), which are the flux entrainment velocity $u_e(F)$, the boundary entrainment velocity $u_e(b)$ or the flow entrainment velocity $u_e(f)$.

The classical work of Ellison and Turner (1959) involved the study of a surface jet overrunning a more dense layer of salt water. Measurements of entrainment were made and have been shown in Figure 2.4. The boundary entrainment velocity $u_e(b)$ was nondimensionalised by a velocity scale $\overline{U}$ to obtain E and plotted against the Richardson number. The data was extracted from Figure 2 of the Ellison–Turner paper and the values of E were of order 10^{-1} for $Ri_0 \sim 0.1$–1.0.

Figure 2.4 : Nondimensional Entrainment versus Overall Richardson Number for Experiments with Mean Velocity Shear at a Density Interface

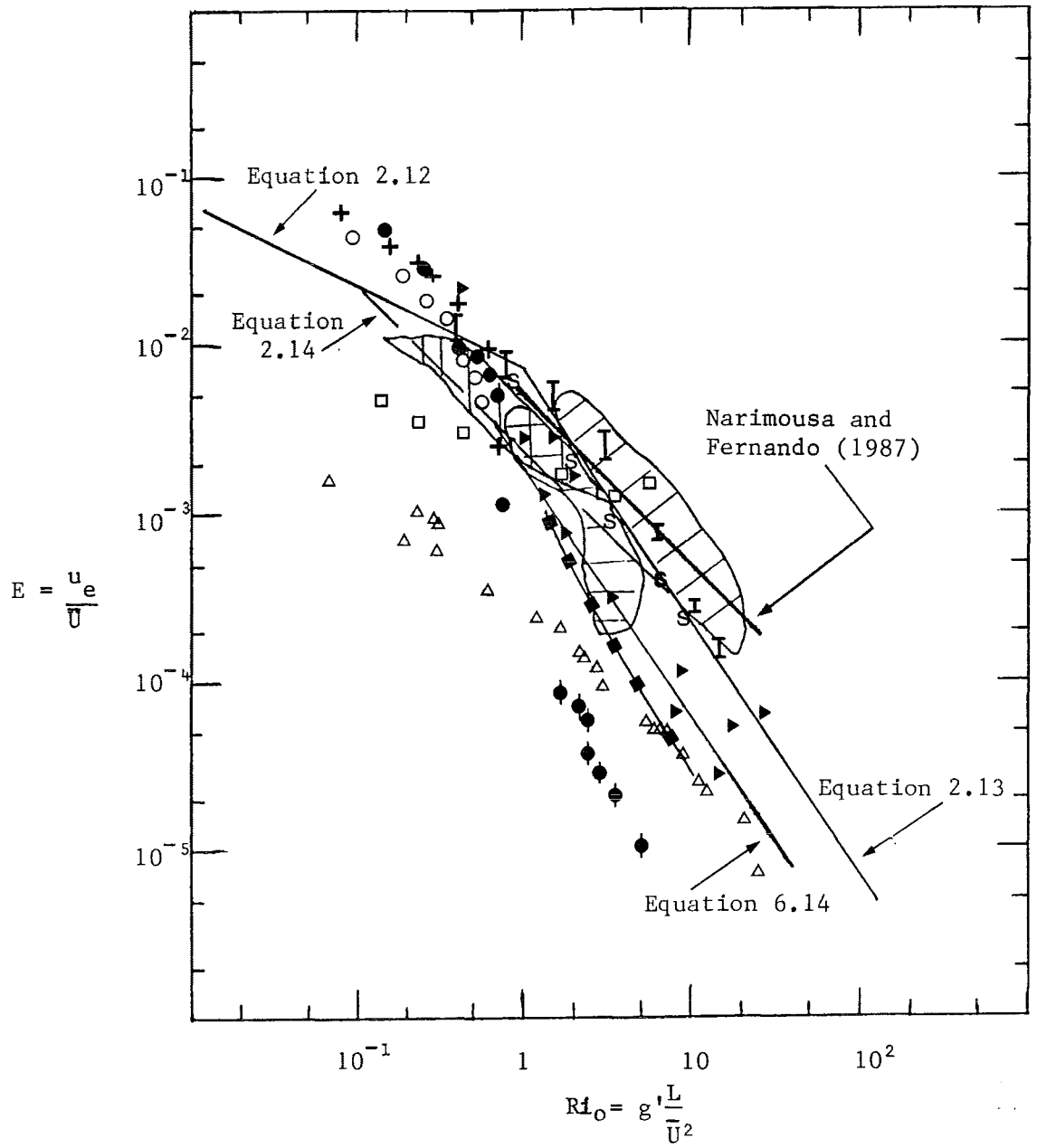

Keulegan (1949)

Ellison and Turner (1959)

Lofquist (1960)

Kato and Phillips (1969)

Moore and Long (1971)

Kantha, Phillips and Azad (1977)

Anwar and Weller (1981)

Deardorff and Willis (1982)

Kranenburg (1984)

Narimousa, Long and Kitaigorodskii (1986)

Lofquist (1960) studied the entrainment between a stagnant upper layer and a turbulent underflow of dense saline solution. The appropriate definition of u_e was the boundary entrainment velocity $u_e(b)$. The data plotted on Figure 2.4 shows $10^{-5} \lesssim E \lesssim 10^{-4}$, a range which is similar to Keulegan's (1949) results, but at a larger value of Richardson number.

Kato and Phillips (1969) (or KP) and Kantha, Phillips and Azad (1977) (or KPA) used the same annular tank to avoid endwalls. KP used a stable linear gradient or a stratified outer layer (SOL) in their experiments while KPA used a two-layer system (2LS) with fresh water as the upper layer and saline solution as the dense lower layer. The fluid was driven by a shear stress which was applied by a rotating wheel just below the free surface. The data of KP was initially presented in the form $u_e(b)/u_*$ versus $g(\frac{\partial \rho}{\partial z})D^2/2\rho u_*^2$, and following Denton (1978) and Christodoulou (1986) the conversion to the form of Ri_0 and $u_e(b)/\overline{U}$ was achieved by assuming that :

$$u_* \sim 0.1\ \overline{U} \tag{2.8}$$

and

$$g(\frac{\partial \rho}{\partial z})\ D^2/2\rho u_*^2 \sim 100\ Ri_0 \tag{2.9}$$

The KPA data has also been organised with similar conversions and both sets of data are shown in Figure 2.4. The KP data show a considerable amount of scatter even though the authors have proposed a relation $\frac{u_e(b)}{u_*} \propto \left\{g(\frac{\partial \rho}{\partial z})D^2/2\rho u_*^2\right\}^{-1}$. The KPA data fall above the KP data and display a relation $u_e(b)/\overline{U} \propto Ri_0^{-m}$ where $1/2 \lesssim m \lesssim 2$ for $10^{-1} \lesssim Ri_0 \lesssim 10$.

Price (1979) has re-analysed the KP and KPA data and proposed that the rate of entrainment should be scaled with the mean velocity $\overline{U}$ of the upper layer (or generally with the mean velocity differnce $\Delta\overline{U}$ across the interface). Price (1979) found that sidewall friction played a major

role in the mixing process and suggested that the entrainment relation should be of the form :

$$E_* = u_e(b)/u_* = nRi_0^{\frac{1}{2}} Ri_*^{-\frac{1}{2}}(1-2CRi_0^{-1}Ri_* \frac{h_0}{W}) \qquad (2.10)$$

where

$$n = \begin{cases} 1/2 & (SOL) \\ 1 & (2LS) \end{cases}$$

and h_0/W is the depth to width ratio. The drag coefficient C is of order 10^{-3}. At small h_0/W, or vanishing sidewall friction, the entrainment relation reduces to :

$$E_* = n\ Ri_0^{1/2}\ Ri_*^{-1/2}. \qquad (2.11)$$

Further experiments by Deardorff and Willis (1982) and Scranton and Lindberg (1983) and others were conducted in an annular tank without endwalls. Deardorff and Willis (1982) applied the shear at the bottom of the tank and also investigated the entrainment in a smaller tank to observe the effects of smaller curvature. The data of Willis and Deardorff (1982) for 2LS experiments is shown in Figure 2.4. The data for the smaller annular-tank is plotted at higher E for the same Ri_0 than for the larger tank. The data shows as much scatter as the KP experiments but at the larger values of Ri_0, the entrainment E shows an approximate $Ri_0^{-3/2}$ relation with much scatter.

The data from Scranton and Lindberg (1983) has not been included because it falls in the same region as the results of Deardorff and Willis (1982) with the same amount of scatter. However, Scranton and Lindberg did conclude that significant secondary motions were generated in the annular tank due to the curvature of the tank and the radial component of stress. The resulting three-dimensional complex flow was not homogeneous and radial stratifications of density, momentum and turbulent kinetic energy were present.

The work of Moore and Long (1971) involved annular shearing flow but the fluid was driven by a combination of fluid jets and compensating suction. The entrainment data is shown in Figure 2.4 after the component due to molecular diffusion has been deducted. The data tends to the relation $E \propto Ri_0^{-1}$. There have been suggestions that a second velocity scale associated with the jets should have been included in the scaling (Deardorff and Willis 1982).

Anwar and Weller (1981) studied the entrainment by a fresh water layer overrunning a quiscent body of salt water. The data from Anwar and Weller (1981) is within a small Ri_0 range and behave as $E \sim Ri_0^{-3/2}$ (see Figure 2.4).

By using a long (27 metre) wind tunnel and open channel configuration, Kranenburg (1984) studied the rate of entrainment of a layer of saline solution by the upper layer of water. The shear stress at the water surface was applied by the wind. Conversion of Kranenburg's (1984) data was achieved with $\frac{\overline{U}}{u_*} \sim 17$ from his experiment 10. The entrainment data also shown in Figure 2.4 give lower E values than Ellison and Turner (1959) and larger values than Moore and Long (1971).

Narimousa, Long and Kitaigorodskii (1986) who studied the turbulent entrainment in a race-track type tank with flow driven by a disc pump, obtained measurements which when plotted against Ri_0 looked like the KPA data except for $Ri_0 \gtrsim 10$. There was a large amount of scatter as shown in Figure 2.4.

Recent measurements by Narimousa and Fernando (1987) who used a disc pump to drive a shear flow in a continuous race-track type tank display a relation $E \propto Ri_0^{-1}$. This is displayed in Figure 2.4 and lie near the KP and KPA data.

Christodoulou (1986) has proposed a set of scaling relationships in which the entrainment E and Richardson numbers are defined with a

consistent set of scaling factors. The scaling velocity is chosen to be the mean velocity or the difference in mean velocities and the lengthscale is chosen to be the depth of the mixed layer. This produces an overall Richardson number, and as shown in Figure 5 of Christodoulou (1986), the agreement is good. At small values of Ri_0, that is $Ri_0 \ll 1$, Christodoulou (1986) proposed that :

$$u_e/\overline{U} = 0.007\ Ri_0^{-1/2} \tag{2.12}$$

and for $Ri_0 \gg 1$,

$$u_e/\overline{U} = 0.007\ Ri_0^{-3/2} \tag{2.13}$$

An intermediate relation can also be chosen :

$$u_e/\overline{U} = 0.002\ Ri_0^{-1} \tag{2.14}$$

to be valid for $10^{-1} < Ri_0 < 10$. Curves represented by equations (2.12), (2.13), and (2.14) are all shown in Figure 2.4. The entrainment relationships proposed by Christodoulou (1986) show good agreement with the data (Figure 2.4). The large amount of scatter has been caused by a number of different factors including different experimental equipment and influence of sidewall friction. The overall behaviour can be reasonably modelled with the scaling laws of Christodoulou (1986) where for supercritical flow ($Ri_0 < 1$) the entrainment is given by equation (2.12) and for subcritical flow ($Ri_0 > 1$) the entrainment given by equation (2.13) is valid. However, the transition from subcritical to supercritical flow is not abrupt as shown by the results of individual studies when $E \propto Ri_0^{-1}$. This relationship appears attractive because it has been taken to imply that the rate of change of potential energy in the mixed layer is proportional to the rate of working of the surface stress

(Kato and Phillips 1969,Turner 1973 p. 294). As shown earlier, there are sets of laboratory data which fit the relation.

The data of Figure 2.4 show that despite the different scaling factors and effects of sidewall friction, that the entrainment by a flow with mean velocity shear is a composite function of the Richardson number and that the function is not a constant.

2.4 Use of Data from Laboratory Entrainment Experiments for the Box Model

The discussion in Section 2.3.4 has shown that large differences exist in the values of E from laboratory studies in which mean flow is present. The data from the annular experiments is also questionable and its use is cautioned. If the annular experimental data is disregarded, then for $Ri_0 = 0.1$, differences of an order of magnitude exist for values of E (see Figure 2.4).

The selection of scaling factors for the Richardson number is not a simple process. In field experiments and box models the friction velocity u_* and the cloud height h are chosen as scales, but when the cloud height becomes the order of the roughness, then z_0 becomes the lengthscale (Chatwin 1984). The data in Figure 2.4 are based on length, and velocity scales of the flow regime and as these scales may be different from those in the box model and field experiment in the entrainment phase, it is suggested that the data from Figure 2.4 be used cautiously.

In the first box model Van Ulden (1974), based on one field experiment proposed that during the gravity spreading stage that u_z and u_p were of order zero because the cloud volume was not observed to have changed. Under the controlled conditions of the wind tunnel, Meroney (1982) has suggested that $u_z \sim 0.1(g'h)^{1/2}$. The data in Figure 8 of

Meroney (1982) indicates that the cummulative value of the constants lie in the range 0.05 — 0.2. Fay (1980) has suggested that $u_z \sim c_z(g'h)^{1/2}$ where $10^{-4} \lesssim c_z \lesssim 10^{-2}$ by extrapolating laboratory data from gravity currents. This large variation in estimates of c_z suggests that the models are not universally applicable to all situations. Hence sufficient caution must be exercised when using laboratory data for large scale modelling purposes.

In respect of using current models, and the laboratory data to model dispersion of dense gases, the concluding remarks by Hunt, Rottman and Britter (1984) would be the most useful guide :

> "...the dispersion of a dense gas is a complicated and sensitive function of the particular atmospheric and release conditions. Therefore it seems unlikely that a single simplified model, such as are in common use at the present could accurately model the many different types of release conditions or indeed the different phases of a particlar release. Models should be developed with particular release conditions in mind, and attempt only to model particular phases of the evolution of a dense gas cloud."

2.5 Summary

The brief description of the box model for dense gas dispersion has shown that it has a similarity with the general problem of Section 1.3. This similarity is the entrainment of air into the gas cloud at the upper surface of the cloud.

The box model is simple in that it does not account for large roughness or obstacles, phase transformation of the contaminant nor does it account for temperature differences between the cloud and surroundings.

The term "entrainment velocity" has been shown to have three

meanings in the literature even though these meanings can be related to one another. Four different possible mechanisms of entrainment have been discussed and these mechanisms can also be dependent on the Richardson number.

The use of laboratory entrainment data in the box model is cautioned as the respective length and velocity scales have to be carefully chosen. It is also advised that separate models be developed for different phenomena rather than rely on the box model to give reasonable results for the behaviour of the cloud during all the phases.

CHAPTER THREE

SIMILARITY CRITERIA FOR THE STUDY OF ATMOSPHERIC POLLUTION PROBLEMS

3.1 Introduction

The similarity criteria for modelling atmospheric pollution problems are stated briefly. These criteria are applied to the general problem described in Section 1.3 to obtain a working physical model.

3.2 Similarity Criteria for the Simulation of the Atmospheric Boundary Layer

The problem outlined in Section 1.3 consists of two parts, the structure of the ambient wind near the ground, and the interaction of the wind with the dense gas cloud. For a rigorous model of the wind behaviour, it is essential that the model and field situation possess geometric, kinematic, dynamic, and thermodynamic similarities for the boundary and initial conditions.

The five nondimensional parameters are obtained from nondimensionalising the equations of motion and the molecular diffusion equation (Snyder 1972 and others). These nondimensional parameters are :

the Rossby number, $Ro = [U/L\ \Omega_r]$ (3.1)

the Richardson number, $Ri = [g\delta T_r L/T_o U^2]$ (3.2)

which is also the square of the inverse of the densimetric Froude number, F_r^{-2},

the Reynolds number, $Re = [LU/\nu]$ (3.3)

and the two forms of the Peclet number

$$Pe = [LU/\kappa] \quad (3.4)$$

and $$Pe = [LU/\alpha] \qquad (3.5)$$

Equation (3.5) is also the Reynolds-Schmidt number.

The symbols have the following meanings :

υ = kinematic viscosity

κ = thermal molecular diffusivity

α = mass molecular diffusivity

T_o = air temperature

P_o = air pressure.

The following are assumed from the boundary conditions :

L = length scale

U = velocity scale

δT_r = temperature deviation

Ω_r = angular velocity of earth.

The full scale atmospheric or prototype flow and model flow which are governed by identical equations of motion will be similar if they are described by identical solutions. The solutions will be identical if and only if the parameters Ro, Ri, Re and Pe plus the nondimensional boundary conditions are identical (Batchelor 1953, Birkhoff 1960 and others). The presence of a contaminant in the prototype and model flows require both forms of Pe to be satisfied in addition to the above requirements.

3.3 A Physical Model

The similarity criteria are applied to a boundary layer flow. A physical model is developed after a discussion of the nondimensional parameters, the flow regime and the boundary conditions.

3.3.1 The Non-dimensional Parameters

3.3.1.1 *The Rossby Number, Ro*

The Rossby number describes the relative importance of the Coriolis acceleration when compared with local acceleration. If the Rossby number is large, then the Coriolis accelerations are small, so that the increased dispersion due to directional wind shear can be ignored. Snyder (1972) has discussed the importance of the Rossby number, and suggests from the available literature and data that this criterion can be neglected if the lengthscale in the prototype is less than 5 kilometres under neutral or stable atmospheric conditions for relatively flat terrain. The prototype and model flows have lengthscales which are less than the 5 kilometres in question and therefore the Rossby number is assumed not to play a signficiant role.

3.3.1.2 *The Reynolds Number, Re*

The Reynolds number criterion is the most difficult to obtain between the model and prototype. In the study of atmospheric boundary layers, the prototype Reynolds number is very large, and it would be impossible to reproduce the same Reynolds number for a reduced model scale of say 1:2000. However, a hypothesis put forward by Townsend (1956), called the Reynolds number similarity stated that "geometrically similar flows are similar at all sufficiently high Reynolds numbers". The basis of this hypothesis is that for sufficiently high Reynolds numbers, the turbulent energy-containing eddies are low wavenumber while the viscous dissipation eddies are high wavenumber. The effect of a change in

Reynolds number is to change the high wavenumber end of the spectral distribution so that the total dissipation remains unchanged, even though there is a change in the non-dimensional viscosity. Consequently, at large Reynolds numbers, the ratio of sizes of the dissipation eddies to the sizes of the energy-containing eddies becomes very small, but changes to the eddies not contributing to dissipation are not significnt.

The Reynolds number based on the boundary layer depth δ, for the model are of order 10^3 to 10^4, while the prototype Reynolds number may be in excess of 10^7. This mismatch is common in atmospheric models and is an accepted consequence of the modelling procedure provided that the dominant parameter is matched (Snyder 1972, Plate 1982 and others).

Another form of a Reynolds number but applied as a boundary condition is that formed by the roughness parameter z_o, and the friction velocity u_*. Almost all atmospheric boundary layers are aerodynamically rough with the exception of ice, very smooth sea and snow. Low windspeed at night results in a slightly stably stratified flow which can also be aerodynamically smooth.

The critical roughness Reynolds number for which flow is aerodynamically rough is well established and given by (Deacon 1949 and others) :

$$\frac{u_* z_o}{\upsilon} \gtrsim 2.5 \qquad (3.6)$$

The corresponding value for a hydrodynamically smooth flow is (Brutsaert 1982) :

$$\frac{u_* z_o}{\upsilon} < 0.13 \qquad (3.7)$$

In the range $0.13 < \frac{u_* z_o}{\upsilon} < 2.5$, the flow is in the transition regime from smooth to rough. A third application of the Reynolds number criterion by

Jensen (1958) enables a model scale to be deduced from a comparison of model and prototype roughness lengths when the flow is aerodynamically rough, that is :

$$\frac{(z_o)_m}{(z_o)_p} = \frac{L_m}{L_p} \tag{3.8}$$

where the subscripts m and p refer to model and prototype respectively. This criterion is commonly used in modelling of atmospheric boundary layers when the roughness z_o is a critical factor.

3.3.1.3 *The Peclet Number, Pe*

It has been assumed that there are no variations in thermal properties in this work but there are large differences in density which can drive molecular diffusion. Denton and Wood (1981) have shown that molecular diffusion is only significant at low Peclet numbers. Also Crapper and Linden (1974) have shown that the molecular diffusion is only important for Peclet numbers less than 10^3. Peclet numbers in this work are of order 10^5 and as entrainment due to molecular diffusion is proportional to Pe^{-1} (Denton and Wood 1981), it can be assumed that molecular diffusion does not play a significant role in the entrainment process.

3.3.1.4 *The Richardson Number, Ri*

The final parameter to be discussed is the Richardson number. Batchelor (1953) has established that the Richardson number is the sole governing parameter for a class of flow systems which consist of low-speed motions of a frictionless perfect-gas atmosphere. The restrictions include that the pressure and density everywhere depart by small fractional amounts from the values for an equivalent atmosphere in

adiabatic equilibrium. The vertical length scale of the velocity distribution is small compared with the scale height of the atmosphere.

Hence the Richardson number is the single most important parameter to be matched between the model and prototype flows involving atmospheric dispersion (Snyder 1972 and others). This work involved layers of water and saline solution with different densities and the appropriate form of the Richardson number is :

$$Ri = g' \frac{L}{U^2} \qquad (3.9)$$

where $g' = g' \frac{\Delta\rho}{\rho_o}$. Various scales are used for L and U depending on the particular application. The choices of scales for this work are discussed in Chapter 6.

3.3.2 Compatibility of the Richardson and Reynolds Numbers

To match simultaneously the Richardson and Reynolds numbers in model and prototype is a difficult, if not impossible, task. The matching of Richardson number requires the velocity to be decreased as the square root of the ratio of length scales, while matching of the Reynolds number requires the velocity scale to be increased for a typical scale reduction of 1:200 to 1:2000. To match the Reynolds number in a wind tunnel at this scale would require near supersonic wind speeds. Water has been substituted as the working fluid (Britter 1980, Plate 1982 and others), and even with the ratio $\upsilon_{air}/\upsilon_{water}$ equal to about 10, it is not possible to achieve the above scale reductions with matching of Re and Ri. This conflict can be resolved if the flow is independent of Reynolds number, and the Richardson number is satisfied. The above discussion required that the ratio $\frac{\rho_i}{\rho_o}$ was the same in prototype and model. There have been wind tunnel studies in which the ratio $\frac{\rho_i}{\rho_o}$ was increased so as to reduce the model velocity scale (Hall, Barrett and Ralph 1976) but

Meroney (1982) has suggested against this practice because it modified time scale ratios and volume dilution rates. By matching the density ratio in model and prototype, the Richardson number criterion is reduced to :

$$\left(\frac{L}{U^2}\right)_m = \left(\frac{L}{U^2}\right)_p \quad . \tag{3.10}$$

For large reductions in scale, the model velocity scale becomes very small, and in some cases the turbulent flow criterion will not be satisfied (Neff and Meroney 1982). As the Richardson number is the dominant parameter, the Reynolds criterion will be waived.

3.3.3 **The Flow Regime**

The available atmospheric wind data which has been recorded and analysed, emphasised strong wind behaviour (ESDU 1972) and more recently stable and unstable conditions. Strong winds is the term applied to behaviour when the mean wind speed at a ten metre height exceeds 5 metres per second. This situation is indicative of a neutral atmosphere where the heating or cooling of air is minimal hence convective motions are eliminated (ESDU 1972). In strong winds the dense gas cloud would be easily transported downwind and dispersed. The interesting and complex situation arises when the winds are not strong but unfortunately it also means that heating or cooling of the atmosphere can cause significant convective motions. The low mean wind speeds of interest are of order 2 m/s at a ten metre height (Dirkmaat, 1981 and others). The terrain is of constant roughness and flat, except for a low-lying area or ditch which will contain the dense gas cloud.

A complete physical model for an atmospheric boundary layer requires that the nondimensional parameters in Section 3.3.1 be identical in prototype and model, and that the initial and boundary conditions must be to scale. These requirements can only be satisfied if the prototype

and model are identical, removing the need for a model. Hence a model would be useless were it not for the possibility of relaxing some of the conditions subject to the particular application (Plate 1982 and others).

To be able to study the more interesting case of low wind speed, it was necessary to relax the boundary conditions for the prototype and model, and not consider heating or cooling of the working fluid. It was realised that a low mean wind speed of 2 m/s coincided with slightly unstable atmospheric conditions during daytime and slightly stable nighttime conditions such that the atmosphere was heated and cooled (Pasquill 1961, Gifford 1961 and others). In spite of these conditions it was considered useful to study a model in which heating or cooling effects were ignored and the efforts were concentrated on an isothermal model. A study of the effects of heating or cooling of the air and dense gas are beyond the scope of this work.

3.3.4 The Flow Boundary Conditions

The boundary conditions for the prototype flow are turbulent air flow over level terrain of grass and with no difference in temperature between the dense gas and surroundings. For a mean wind of 2 m/s at 10 metres height and a roughness z_o = 0.01 m, ESDU (1972) gives $u_* = 0.12$ m/s so that $\frac{u_* z_o}{\upsilon} = 76$ which exceeds the criterion of 2.5 for fully aerodynamically rough flow. However, as reported in Chapter 5, the model flow does not satisfy the aerodynamically rough criterion but is in the transition from aerodynamically smooth to aerodynamically rough regime (Table 5.1).

3.3.5 The Model and Assumptions

The assumptions for the model are that :

(i) The dense gas cloud is homogeneous and remains in the recess or cavity.

(ii) The air flow over the gas is not of sufficient strength to shift the cloud totally but it causes mixing at the air–dense gas interface.

(iii) The air–dense gas interface is assumed to remain at the same level.

(iv) The differences in density between the air and dense gas cloud are due solely to concentration differences. All other sources of density difference are assumed to be insignificant.

(v) The density of the dense gas remains constant during the mixing process.

Most of the assumptions have either been discussed earlier in reference to the prototype or do not need any comment with the exception of the third and fifth assumptions. In the prototype cloud, the effect of the wind is to reduce the gas concentration in the cloud, and the level of the gas–air interface. So that measurements could be made at known values of parameters, it was decided to run the experiments at a steady–state. This included maintaining the density of the gas cloud at a constant value, and the air–dense gas interface in the model at a constant level. By keeping the initial density ratio constant, the behaviour of the interface can be assumed not to change significantly during the course of

the experiment. This is an important aspect as the value of the Richardson number will otherwise alter.

A sketch of the model situation is shown in Figure 3.1. The dense gas represented by saline solution lies in a recessed cavity of rectangular cross-section, and the ambient air flow is represented by fresh water running over the cavity. The flow structure of the fresh water (also referred to as the upper layer, and the saline solution as the lower layer) changes as the water flows over the perspex model onto the saline solution. The upper layer applies a shear stress at the interface, and this stress subsequently drives the saline solution in a circulatory pattern (Chapter 6). The densities of the upper and lower layers are assumed to be nearly constant for the duration of an experiment. These layers are separated by a thin interfacial region which may have large gradients of velocity and density (Spigel, Imberger and Rayner 1986). The applied stress at the interface also causes mixing at the interface. An exchange of fluid between layers will result in the upper layer becoming more dense, and the lower layer becoming less dense. As the aim of this work was to measure mixing of the saline solution out of the cavity, the interface was kept at a near constant level by an influx of saline solution through the bottom of the cavity. Care is needed so that the saline solution is not forced over the downstream wall. The results of experiments are discussed in Chapter 6.

3.4 Summary

Similarity criteria required that five nondimensional parameters be satisfied in the model and prototype situations. The boundary conditions also had to be satisfied in order to obtain complete similarity. However, the conflicting requirements of the Richardson and Reynolds numbers meant that the dominant parameter was satisfied. In this work the dominant parameter was the Richardson number and the Reynolds number criterion was waived.

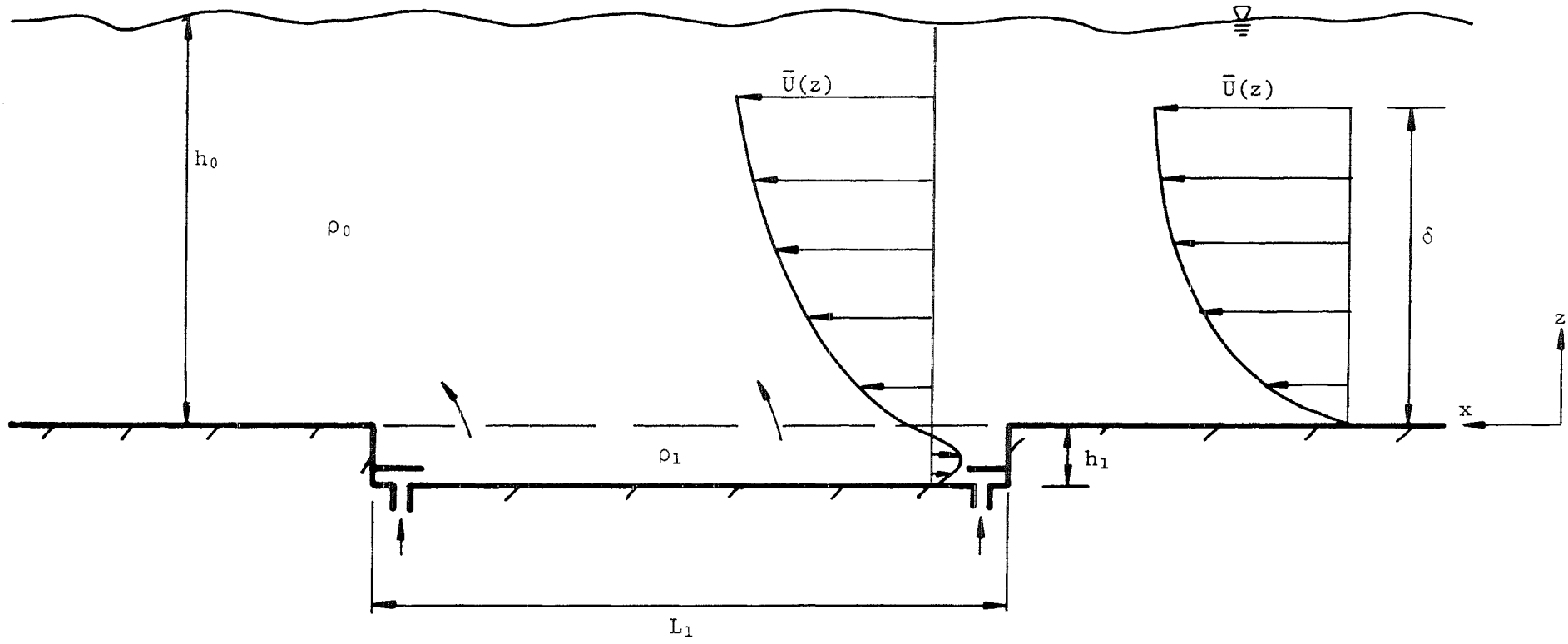

Figure 3.1 : The Laboratory Model Comprising the Cavity with the Saline Solution and the Upper Turbulent Layer in Mean Motion

CHAPTER FOUR

LABORATORY EQUIPMENT AND EXPERIMENTAL PROCEDURES

4.1 Introduction

The equipment which was used in the project is described in this chapter as well as the experimental procedures and programme. The main item of equipment is the recirculating system which contained the water and included an open channel. The recirculating system is described in Section 4.2. The mean and fluctuating components of velocity were recorded with a Laser Doppler Anemometer (LDA) which was mounted on a lifting table. These two items of equipment are described in Section 4.3. Section 4.4 describes the saline solutions which were used to model the dense gas, the control of saline solution flow to the cavity, and the conductivity meter and probes which were used to measure the conductivity changes in the water. Section 4.4 also describes the light source and the perspex model which includes the cavity. The experimental procedures for conducting the velocity and entrainment experiments are described in Section 4.5. The experimental programme is outlined in Section 4.6.

4.2 The Recirculating Water System

4.2.1 The Open Channel, Piping and Pump

The freshwater and saltwater solutions were contained in a fully recirculating system which included, as the major component, an open channel with a working section of 610 mm wide, 300 mm high and over 7.3 metres long. The open channel was originally constructed of mild steel sections but was modified to suit the needs of the experiments. The modifications involved the replacement of part of the channel sides with

framed perspex windows to allow access for photography, video recording, observation and laser beams. The open channel was made available by, and located in, the laboratory of the Civil Engineering department. The floor of the open channel was adjusted to be horizontal to within ±0.5 mm. Over a distance of 7.3 metres the corresponding error in slope is 0.00007. The general assembly of the recirculating system is shown in Figure 4.1. The flow of freshwater through the system was driven by a 4"x4" centrifugal pump which in turn was driven by a 7.5 kilowatt electric motor. The electric motor speed was 1450 rpm but with a suitable choice of pulley ratio and vee-belts, the pump was operated at about 760 rpm.

The piping was 150 mm diameter aluminium and steel sections with lengths of flexible hosing installed between the open channel and pump to reduce the transmission of pump vibration.

4.2.2 The Measurement of Volume Flowrate

An orifice plate was installed downstream of the pump and the head loss across the plate was monitored by a water manometer. A comparison of the head loss with an earlier calibration enabled the volume flowrate to be evaluated.

4.2.3 The Water Supply

The freshwater required for experiment was drawn from the local high pressure system. The maximum capacity of the recirculating system was about 2900 litres and the filling time was 15-20 minutes. After an experiment, the contaminated water was released into the sewerage drain.

The quantity of water in the system was calculated from the expression :

$$V_s = 6.62\ (h-138) + 1945 \qquad (a-1)$$

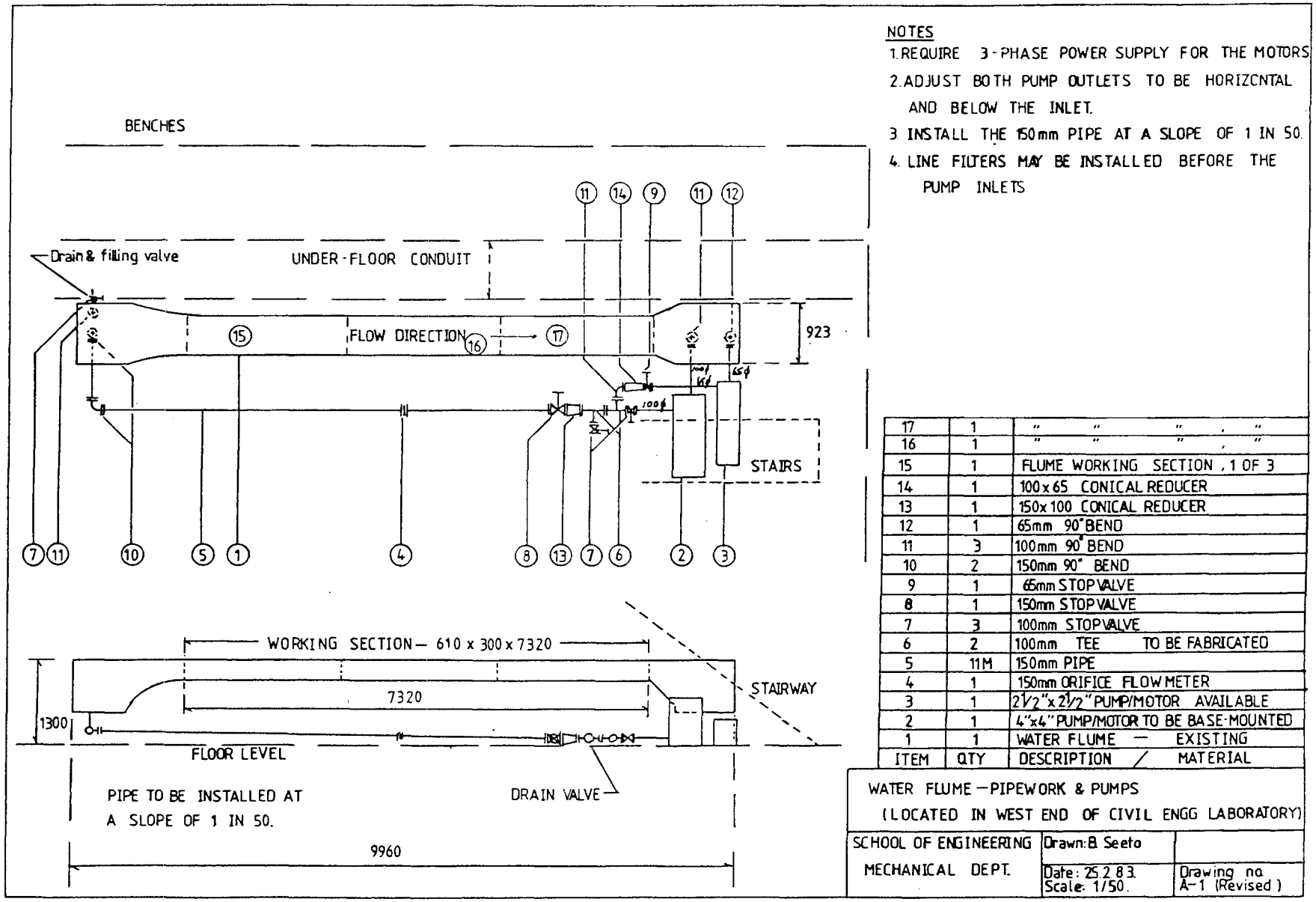

Figure 4.1 : General Assembly Diagram of the Fully Recirculating System

where h (mm) is the water depth in the working section of the open channel, and V_s is the volume of water in the system in litres. The error in equation (a-1) is about 3%. The background to equation (a-1) is given in Appendix A.

4.2.4 The Fine Wire Gauze and Wire Grid

A fine wire gauze was placed at the entrance to the working section of the open channel to make the flow uniform and as it was later observed, the gauze also filtered the larger particles from the flow.

A wire grid was installed in the working section just upstream of the leading edge of the perspex model. This served to increase the background level of turbulence intensity. The wire mesh size was M = 15.75 mm and the wire diameter was 2.1 mm, thereby giving a mesh to diameter ratio of M/d = 7.5.

Figure 4.2a shows part of the channel working section looking downstream with the installed wire grid and many of the other items of equipment. Figure 4.2b shows another view of the channel, looking upstream.

4.3 Velocity Measurements

The lifting table and the Laser Doppler Anemometer (LDA) are described in this section.

4.3.1 The Lifting Table

The lifting table was specially designed and built so that the LDA could be mounted and traversed across the working section of the open channel. The lifting table was designed with two degrees of freedom which were movements in the vertical and longitudinal directions (see Figure 4.3). This enabled vertical profiles of velocities to be recorded

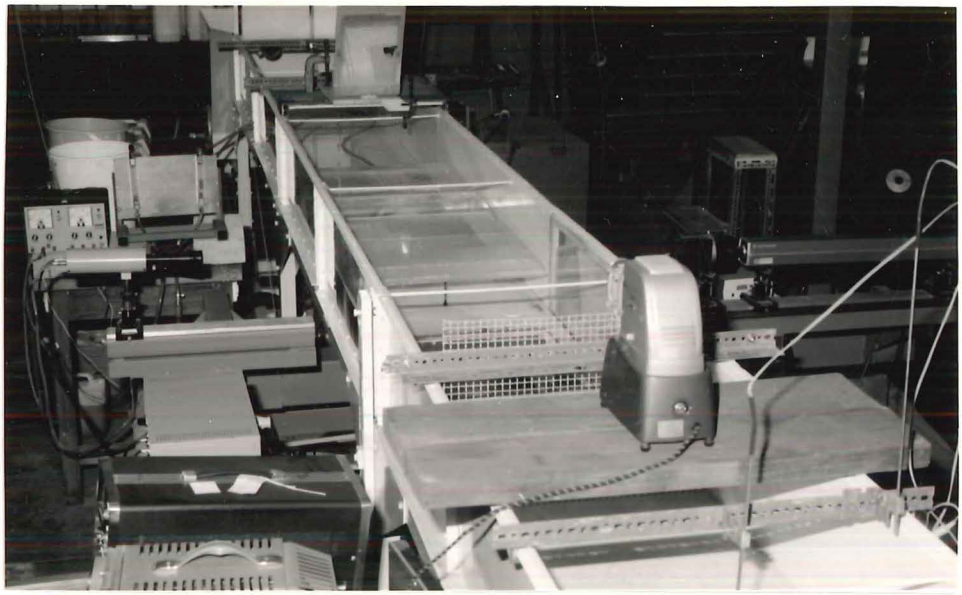

Figure 4.2a : A View of the Channel looking downstream

Figure 4.2b : A View of the Channel looking upstream

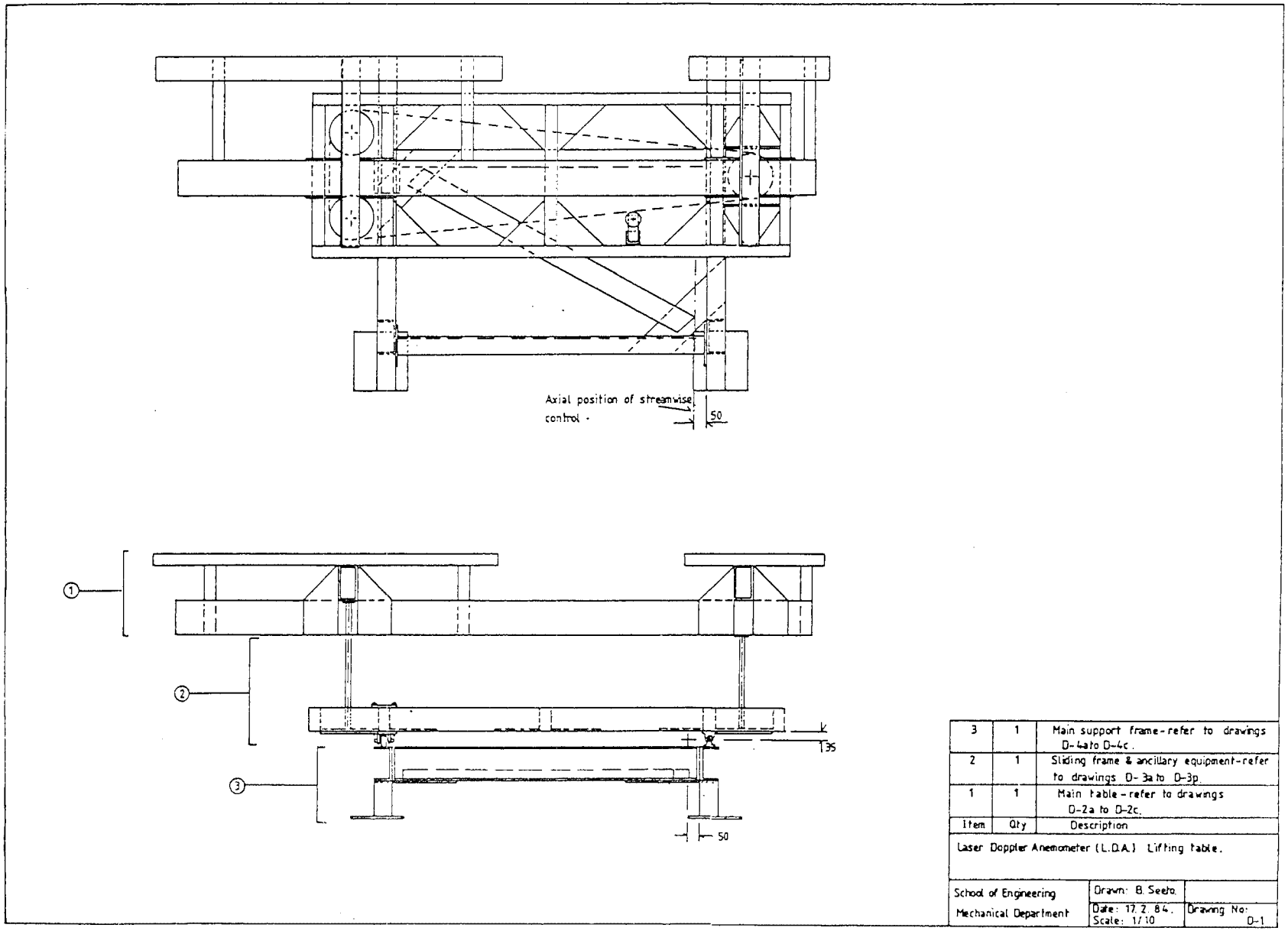

Figure 4.3 : General Assembly Diagram of the Lifting Table

at various downstream stations. Measurements of velocities at a station which was towards either side of the open channel required the LDA to be moved relative to the lifting table. Two views of the lifting table are shown in Figures 4.4 and 4.5. The details of the design requirements and operation have been presented in Appendix C.

4.3.2 The Laser Doppler Anemometer

The mean and fluctuating velocity components at stations upstream of the cavity were measured with a LDA. The available LDA system was a Disa type 55L with a Spectra-Physics model 124A, 15 milliwatt helium-neon laser providing the light source. The laser wavelength is $\lambda = 632.8 \times 10^{-9}$ metres. The LDA system was made available by the Civil Engineering department.

The LDA was operated in the forward scattering differential-Doppler mode (Figure 4.6a) which required the test section to be located between the laser and a detector. In differential-Doppler mode, the laser beam is optically split into two beams which are then re-focused to intersect within the test section (Figures 4.6b and 4.7). The common space formed by the two intersecting beams is the intersecting volume (Figure 4.6b). Any particles in the fluid which pass through this volume scatter the light. The photoelectronic detector is focused on the measuring volume and picks up from the original direction, the scattered light signals from each of the scattering beams. The photoelectronic detector or photomultiplier emits an alternating current with a Doppler frequency which is proportional to the scattering particle velocity. (There is an implied assumption that the particle has the same local velocity as the fluid particle.) The measured velocity is in the plane of the two intersecting beams. The tracker unit of the Disa system analyses the signal from the photomultiplier and produces a voltage which is linearly related to the particle velocity. The mean component of this

Figure 4.4 : A View of the Lifting Table

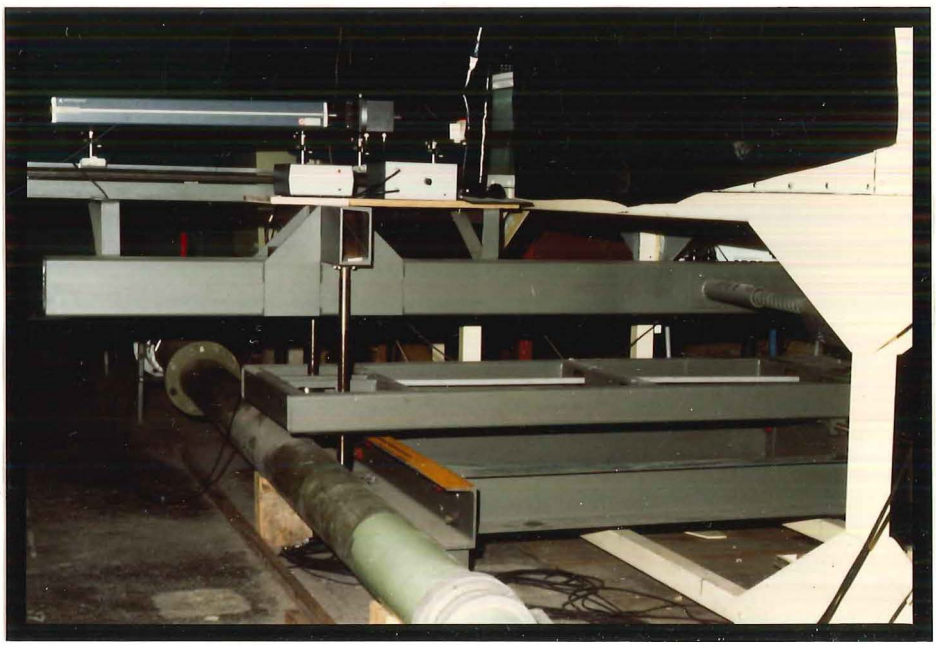

Figure 4.5 : A View of the Lifting Table with LDA mounted

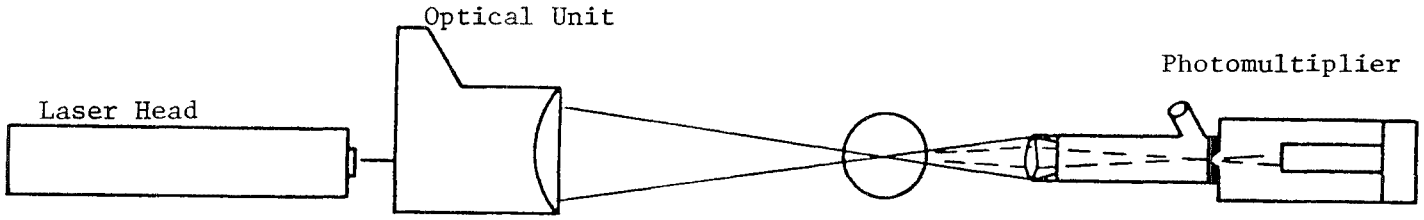

Figure 4.6a : The Forward Scattering Differential Doppler Mode of the LDA

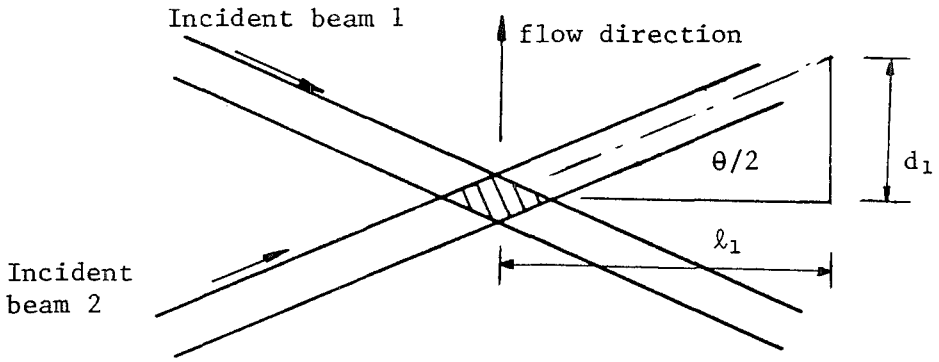

Figure 4.6b : The Intersecting Volume

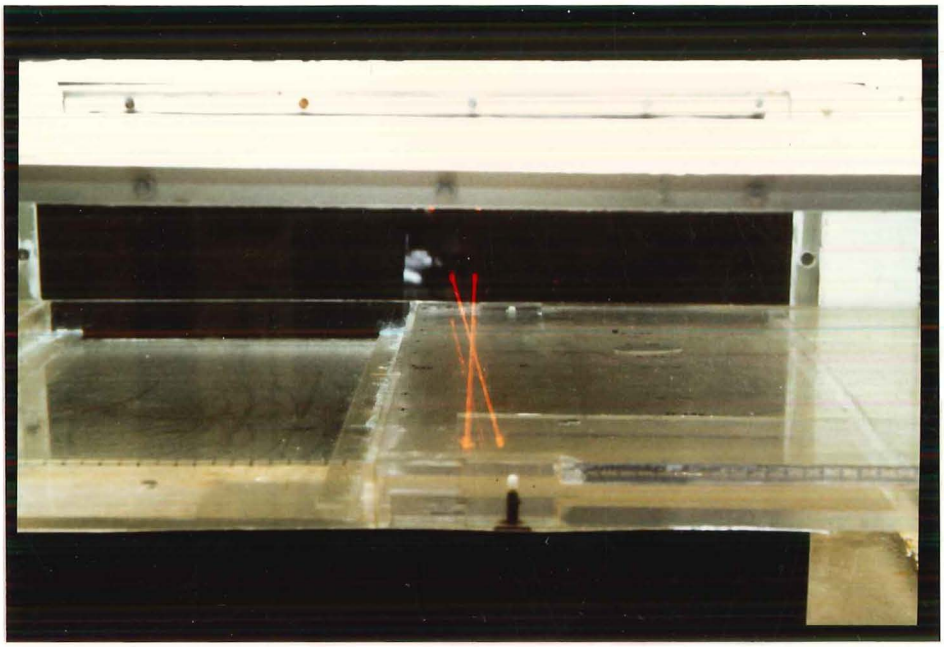

Figure 4.7 : A View of the Two Intersecting Beams

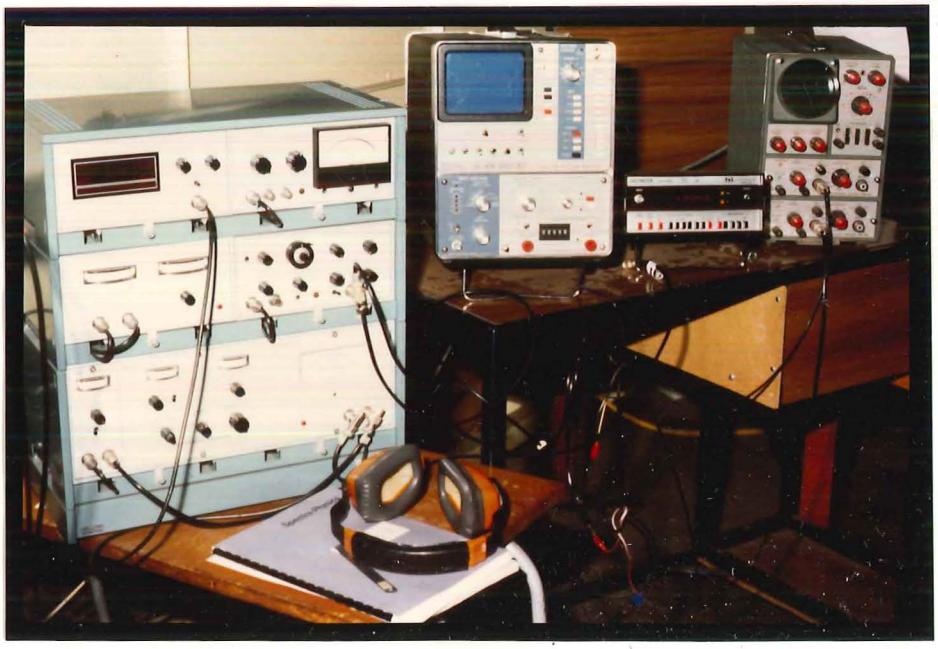

Figure 4.8 : A View of the Signal Processing Equipment

voltage represents the mean velocity and the fluctuating component of voltage represents the fluctuating velocity. A calibration (Figure B-3) relates the tracker output voltage to the frequency.

The other items which form part of the Disa LDA system are shown in Figure 4.8 and these are the DC voltmeter, rms meter, power source for the photomultiplier, and the signal conditioner. Also shown in Figure 4.8 are the FFT computing spectrum analyser, a multi-purpose meter and a two-channel oscilloscope.

A Bragg cell unit and power source was also available to resolve directional ambiguity and to measure highly turbulent flows. Figure 4.5 also shows the laser head and the integral optical/Bragg cell unit mounted on the lifting table with the respective power sources.

A brief description of LDA principles relating to the differential Doppler mode is given in Appendix D. The text by Durst, Melling and Whitelaw (1976) discusses the LDA principles and practice in detail.

4.3.3 Sources of Error in Velocity Measurement

The main sources of error in velocity measurement are derived from the determination of the intersection angle θ and the changes of refractive index of the water due to changes in temperature. These amount to less than 5% while the error due to positioning of the intersection volume is 0.33 mm or half a beam diameter. These errors are discussed in Appendix E.

4.4 The Saline Solutions and Conductivity Measurement

4.4.1 The Saline Solutions

The more dense fluid was obtained by dissolving either sodium chloride or calcium chloride in distilled water. The highest density ratio obtained by dissolving sodium chloride is $\frac{\rho_1}{\rho_0} \sim 1.18$. A higher

density ratio $\frac{\rho_1}{\rho_0} \sim 1.39$ was obtained by dissovling calcium chloride. The density of the saline solutions was checked in two ways. Firstly, the conductivity was measured with a Radiometer CDM83 conductivity meter and compared with standard data from the handbook of chemistry and physics (Weast, 1975). The second method was to weigh a known volume of saline solution, usually 100 mls, and compare this with the weight of 100 mls of tap water at the same temperature. Both of these methods produced results which differed from standard data (Weast, 1975) by less than 1%.

Fluorescein was added to the saline solutions to highlight the interfacial region. This did not greatly affect the density of the saline solution as only about 20 grams was added to a container of 26 litres. A check on the conductivity showed that the addition of fluorescein changed the value by less than 0.5% in a solution of density $\rho_1 \sim 1.03\ \rho_0$.

4.4.2 The Saline Solution Supply System

The supply system of the saline solution is shown in Figure 4.9. The solution is stored in two holding buckets which supply two small centrifugal pumps. These pumps are powered by a DC source. The output of these pumps are connected to flowmeters which have an in-built fine control valve. The output of the flowmeters is connected to the bottom of the cavity. Each pump had a maximum output of 0.5 litres per second. The flowrate was controlled by altering the output of the DC power source and the flowmeter control valve provided the fine control. Figure 4.10 shows the centrifugal pumps, the DC power source, and the flowmeters.

4.4.3 The Probes

All the conductivity measurements were made with the same three probes. One of the probes is shown in Figure 4.11 and these were the same ones used by McNulty (1983). The probes had two 0.5 mm diameter

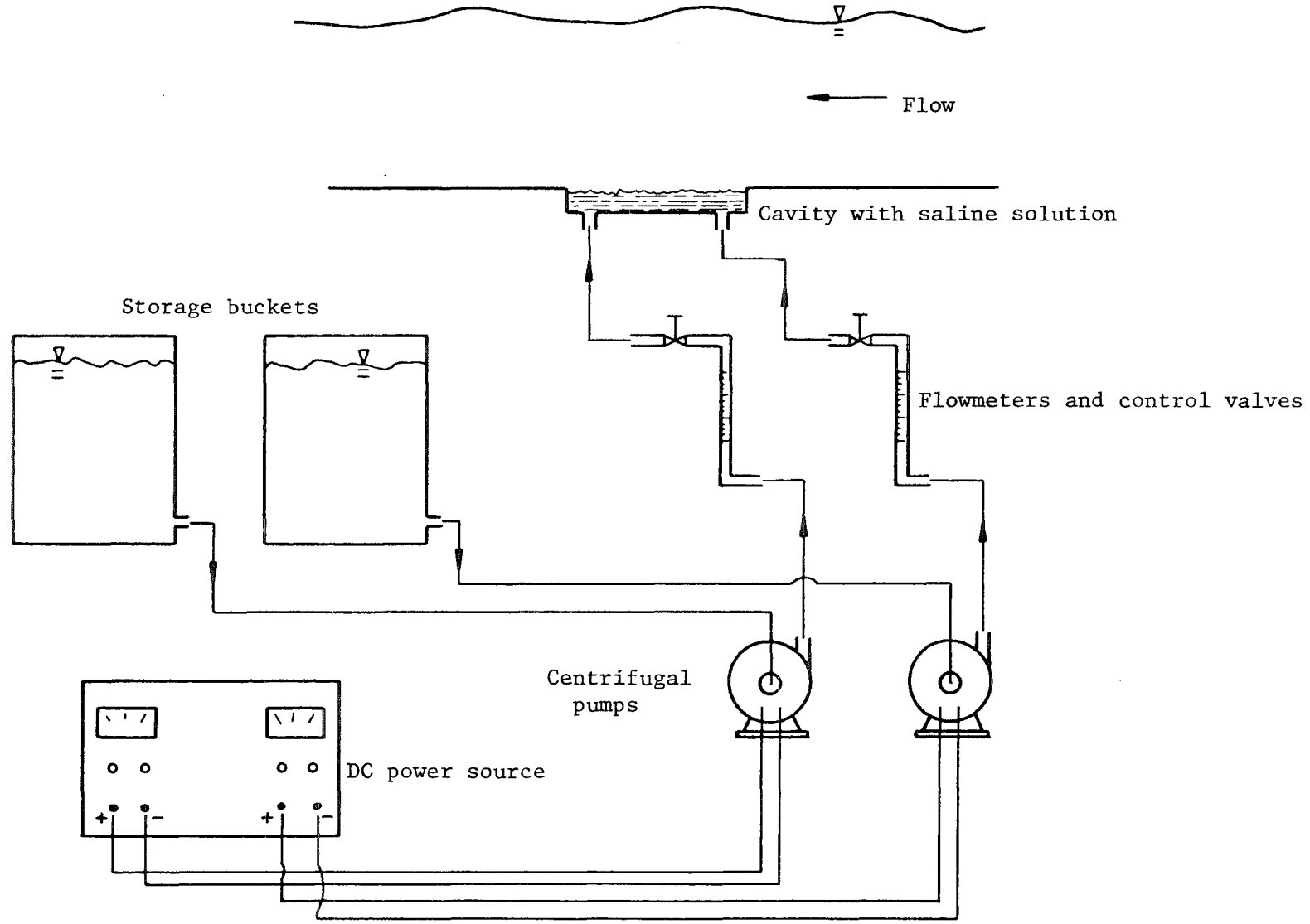

Figure 4.9 : Flow Diagram of Saline Solution supply to Cavity

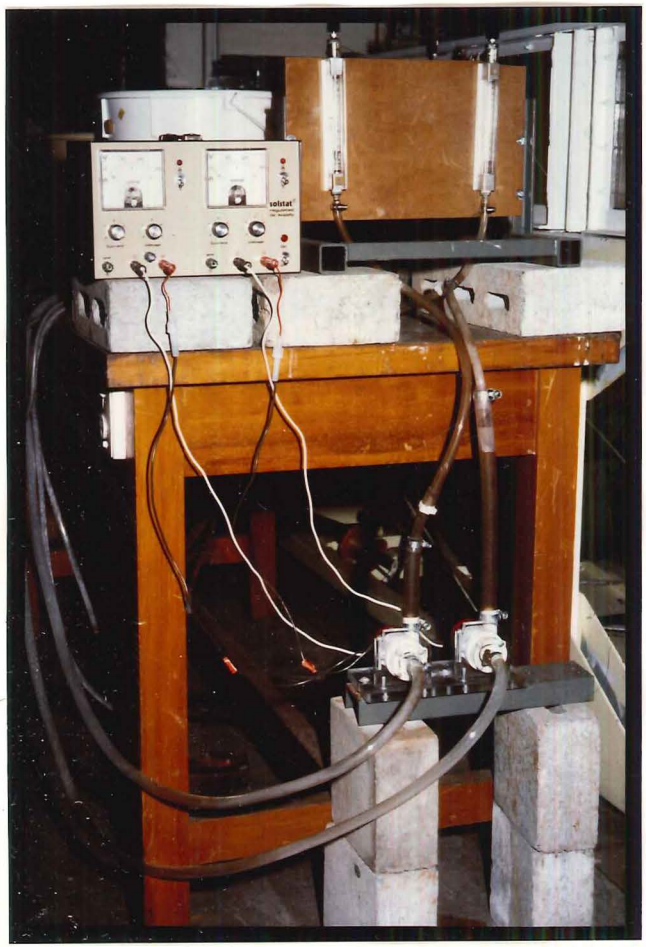

Figure 4.10 : A View of the Saline Pump, Flowmeters and DC Power Source

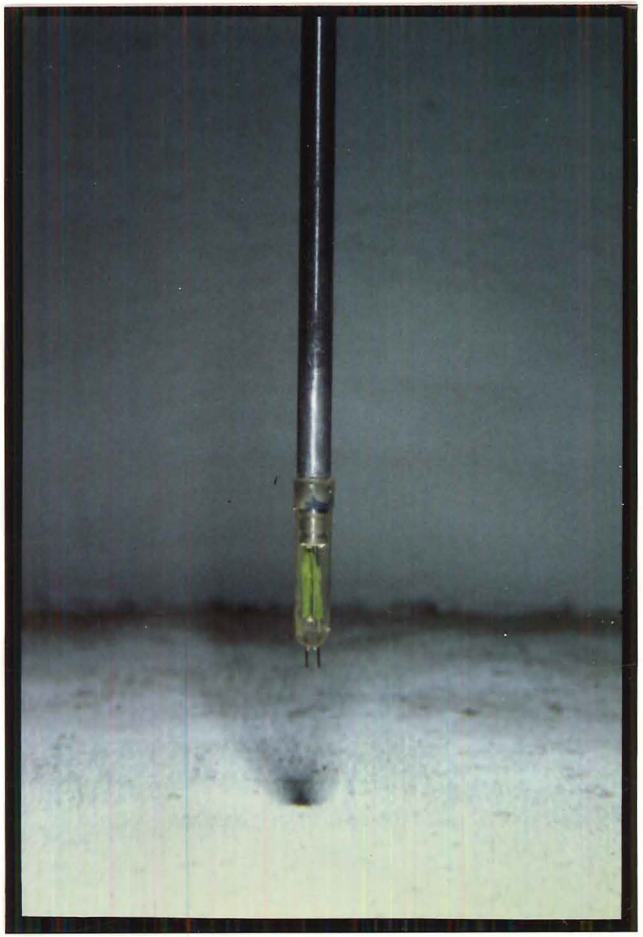

Figure 4.11 : The Conductivity Probe

platinum electrodes which were cast into an araldite tip which in turn was cast into the end of a stainless steel tube.

The probes were calibrated prior to and after an experiment with standard solutions. The probe was found to operate within a linear range (Figure B–4). The standard solutions were placed in the water channel to minimise any temperature differences.

The probes were placed in the positions shown in Figure 4.12. Two of the probes were placed downstream of the model and the third probe was placed upstream of the model. The measurement of the upstream probe was of most interest as it recorded the conductivity after the main pump had thoroughly mixed the saline solution and water.

4.4.4 The Conductivity Meter

The conductivity meter used in conjunction with the probes was built to a design developed by the Iowa Institute of Hydraulic Research (Glover, 1970). This instrument had previously been used by Valentine (1978) and McNulty (1983). The meter was designed to minimise the channel–to–channel interference and up to six channels could be operated at one time. Each channel had seven gain settings although it was found that a gain setting of 4 was suitable for all the probes in all of the experiments. A check on possible probe–to–probe interference was made but there were no discernible changes. The meter was left on permanently to eliminate any warm–up period and to maintain it under a 'constant' condition.

The probe–conductivity meter output DC voltage was directly related to the water conductivity which, in the range of operation, was in turn related to the salt concentration level by a calibration curved similar to that shown in Figure B–4. A calibration curve was produced for each experiment. The output of the probe–conductivity meter was also

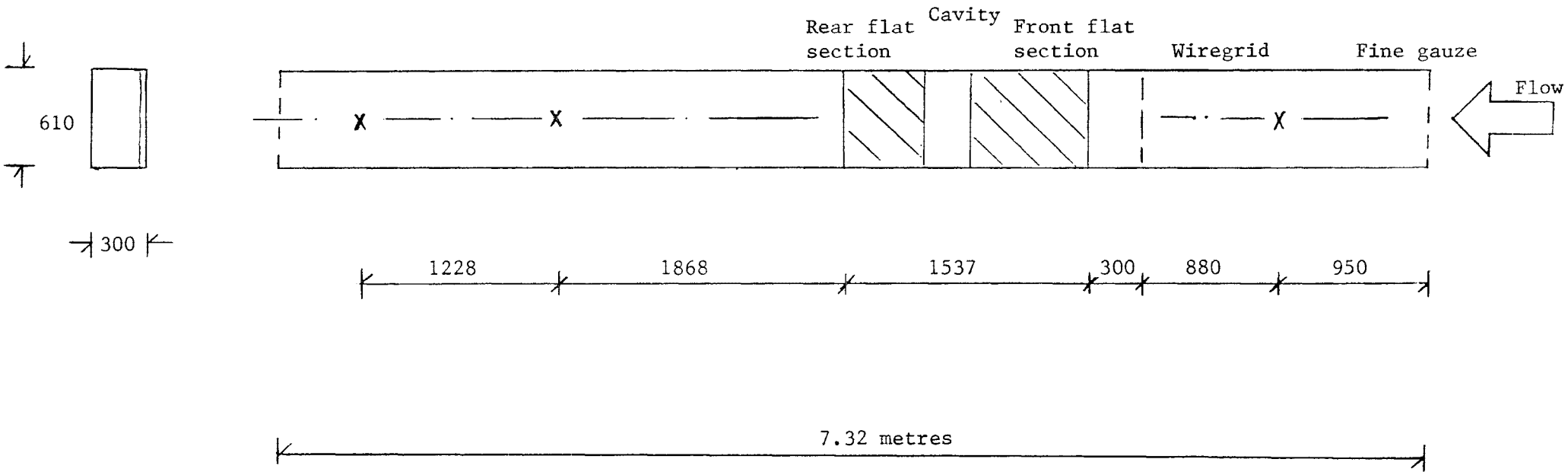

Figure 4.12 : Positions of Model and Conductivity Probes in Open Channel.
Notes : (i) Dimensions in millimtres unless stated.
(ii) X - position of conductivity probes.

connected to a continuous chart recorder and a DC voltmeter. The continuous voltage plot was later used to evaluate the average flux entrainment velocity.

4.4.5 The Perspex Model

The free-standing model was fabricated from perspex and consisted of three separate units (Figure 4.13), a front 600 mm long flat section with a profiled leading edge and taper section, a cavity and a rear 400 mm long flat section with a tapered section and profiled trailing edge. The overall dimensions of the model were nominally 1537 mm long, 600 mm wide, and 38 mm deep. Each flat section was mounted on threaded rods to allow height adjustment and levelling of the sections. The model was placed within the water channel so that the flat sections were about 135 mm above the channel floor. The incident flow was parted by the leading edge so that a fraction of the flow passed under the model and the remaining flow became the ambient flow over the cavity. The boundary layer on the channel floor which had developed from the entrance was effectively destroyed by the upstream wire grid. This was evidenced by preliminary measurements at 300 mm downstream of the wire grid. The front flat section was inserted to allow the boundary layer to grow in equilibrium from the leading edge. The cavity was 290 mm long, 587 mm wide, and 32.5 mm deep. The cavity contained the saline solution during the experiments and the replacement solution was pumped in through openings in the cavity floor. Covers were installed over the inlets to divert the vertical momentum.

After the model was fabricated, it was found to be 590 mm wide instead of the required 600 mm. As the open channel was 610 mm wide, this meant that gaps of 10 mm were present on either side of the model.

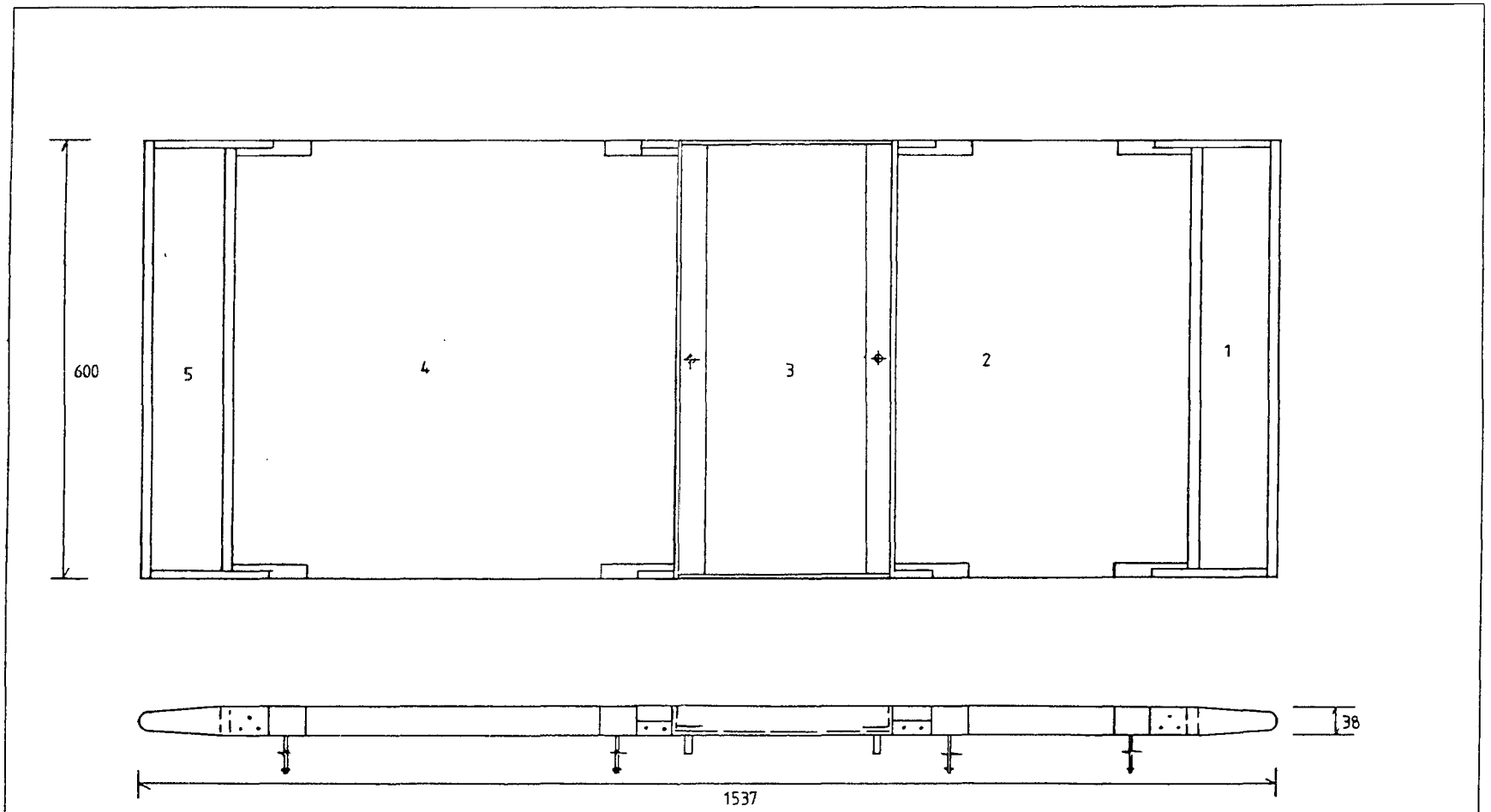

No	Description	Reference Drawing
5	Leading edge	E-2a, E-2b, E-2c.
4	600 mm flat section	E-2c, E-2d, E-2e
3	Saline well	E-2g
2	400 mm flat section	E-2e, E-2f
1	Trailing edge	E-2a, E-2b, E-2c

WATER FLUME – Saline well & ancillary structure

School of Engineering Mechanical Department.	Drawn: B Seeto Date 10.7.85. Scale: 1/5	Drawing No. E-1

Figure 4.13 : Drawing of Perspex Model

This was found to cause quite a significant effect on the mean velocity upstream of the cavity (Chapter 5).

4.4.6 The Light Source

A light source was required to illuminate the interfacial region for observations, photography and video-tape recording. A combination of a slide projector and a plane mirror provided the necessary light. A piece of cardboard with a thin slit cut out enabled the projector beam to be reduced to a narrow slit of light. The slide projector and plane mirror are shown in Figures 4.2a and 4.2b.

4.5 Experimental Procedures

4.5.1 Procedure for Velocity Measurements

The Disa electronic equipment was usually left on to avoid any warm-up periods although due to obvious danger, the laser was never left on whenever no experiment was in progress. The procedure prior to any experiment being carried out consisted of a number of items in the following order :

(i) The laser was switched on to allow warm-up and the system was filled with tap water to the required level.

(ii) The flat section of the model was checked to be level (the floor of the channel was levelled earlier).

(iii) The Bragg cells were adjusted for maximum diffraction and the geometry of the two laser beams were adjusted to ensure proper intersection. This was a critical aspect in the LDA system because poor tracking always resulted from improper beam adjustment.

(iv) To check that the geometry of the beams were correct, measurements of the beam heights across the water channel were taken. It was found that after the initial adjustment of the beam geometry, only fine tuning was necessary due to the slight movement of the model.

(v) The angle of beam intersection θ was measured. The measurements were taken *in situ* and this practice avoided possible difficulties with changes in refractive indices and different or uneven thickness of the perspex windows. The angle θ could be measured to an accuracy of 2%.

(vi) The photomultiplier was mounted on a second optical bench which was bolted to the lifting table but on the opposite side of the channel. The photomultiplier was pointed in the general direction of the measuring volume but precise alignment was unnecessary because the photomultiplier will collect scattered light from any general direction. The image of the measuring volume was observed through the viewfinder and the photomultiplier was moved along the bench until the image was focused on the pinhole aperture. The pinhole centre was adjusted by two screws until it coincided with the measuring volume. A high voltage source powered the photomultiplier, and with fresh water a power source output of 900 volts across the photomultiplier terminals was sufficient to produce the prerequisite anode current of 50 μA. No seeding of the water was required as the fresh water contained sufficient particles.

(vii) The Bragg cells were set at a frequency differential of 75 kHz and the tracker operated in the 150 kHz range. This range was sufficient for all the velocity measurements and a calibration in Figure B-3 related the output voltage to the frequency.

(viii) The Doppler signal due to the scattered light from the intersecting beams with pre-shifted frequencies was tracked and the output voltage corresponding to zero velocity was recorded. This zero velocity voltage was checked before and after each experiment. This completed the preparations for the running of an experiment to measure the flow properites. All velocity measurements were taken upstream of the cavity and without any saline solution present.

(ix) After checking the water level, the main centrifugal pump was started and the recirculating flow was allowed to become steady. As the Doppler signal was already being tracked, the data was immediately recorded manually. An intermediate frequency bandwidth setting of 2% was found to be adequate for the frequency tracker to follow the Doppler signal.

4.5.2 Procedure for Entrainment Experiments

The entrainment experiments were conducted during the period October 1985 to February 1986 when the water temperature ranged from 14^0C to 18^0C. The water conductivity was less than 100 micro-Siemens/cm.

The procedure for conducting entrainment experiments was as follows:

(i) The recirculating system was filled from the local mains to the required level and the container of saline solution was placed into the water to reduce the temperature difference.

(ii) The calibration of the conductivity probes was carried out.

(iii) When the temperature difference between the water and the saline solution was less than $0.2^{0}C$, the solution was poured into the holding buckets.

(iv) Two methods of filling the cavity with saline solution were tried :

(a) With a large fraction of the cavity covered with a lid, saline solution was gradually pumped into the cavity until full. The lid was placed over the whole cavity and the main flow was started and upon reaching steady state, the lid was removed downstream. When the lid was removed, some solution was swept out of the cavity. This was quickly replaced and the saline solution pumps were adjusted for steady-state entrainment at the density interface.

(b) The second method involved leaving the cavity uncovered, starting the main flow and allowing it to become steady. The saline solution pumps were then turned on to force the solution into the cavity. Some saline solution was again swept out but the outputs of the two solution pumps were sufficient to fill the cavity under the unsteady conditions. When the interface reached the prerequisite level, the solution pumps were adjusted so that the outputs were equal to the entrainment rate.

Either of the two methods were suitable, and the second one was chosen as it took less time.

(v) The control of the interface height was made difficult due to the presence of progressive waves at the interface. At low Richardson number, the wave height was about 10 mm and the outputs of the solution pumps were adjusted so that saline solution was not forced over the downstream edge of the cavity. In this manner, the interface was kept as near as possible to the level of the downstream edge of the cavity.

The changes in the background conductivity were continuously monitored by the probes and conductivity meter. At the end of the experiment, the small pumps were switched off and the probes were calibrated again. The contaminated water was subsequently released into the sewer drain and fresh water was used to wash the channel and piping.

The rise in the water temperature during the course of an experiment was usually less than 1^0C. The effect of this rise on the density was considered negligible when compared to the larger differences in water conductivity and density which were caused by mixing with saline solution.

4.6 The Experimental Programme

There are two parts to the experimental programme.

(i) The first part consisted of making measurements of the upstream flow field. These measurements included the mean velocity $\overline{U}(z)$ (where the z-direction is positive upwards and x is in the downstream direction) and the fluctuating components in the downstream $\overline{u'^2}$ and the vertical $\overline{w'^2}$ directions. These measurements were made on the channel centreline and at three positions away from the centreline to check on the effect of the walls.

The main flow pump was operated at constant speed and by varying the water level in the working section, different mean velocities were attained. Three different water depths were used in the experiments, and the flow measurements are presented in Chapter 5.

(ii) The second part of the programme involved the mixing experiments where the saline solution in the cavity was overrun by the layer of fresh water. The density ratio of the sodium chloride solutions used in experiments was in the range $1.02 \lesssim \frac{\rho_1}{\rho_0} \lesssim 1.18$ and the corresponding range for calcium chloride was $1.10 \lesssim \frac{\rho_1}{\rho_0} \lesssim 1.39$. The observations and results are presentd in Chapter 6.

A small number of experiments were also carried out in cavities of reduced length to investigate the effect of the cavity ends. These are presented in Appendix K.

CHAPTER FIVE

THE FLOW STRUCTURE UPSTREAM OF THE CAVITY

5.1 Summary

The measurements of the mean and fluctuating components of velocity in the downstream direction and the vertical component of the fluctuating velocity are presented in this chapter. Measurements were recorded at the centreline, at two positions 150 mm either side of the centreline and at a position 260 mm south of the channel centreline. As the measurements from the two positions at 150 mm either side of the centreline were similar, only data recorded from the 150 mm south has been presented. All the measurements were recorded in a plane 16 mm upstream of the cavity normal to the direction of mean flow (see Figures 3.1 and 5.1).

The values of the roughness z_o, friction velocity u_*, and boundary layer depth were evaluated from the measurements. The upward flow at the sides of the model resulted in a complex three-dimensional flow structure near the sides. Although differences of 25% in $\overline{U}(z)$ were recorded between the channel centreline and the 260 mm station, variations of this magnitude were confined to $z/\delta \lesssim 0.2$. Subsequent analyses have shown that by representing the vertical profiles of $\overline{U}(z)$ with a uniform or local bulk velocity $\overline{U}_b$, the variations between $(\overline{U}_b)_c$ and $(\overline{U}_b)_{260}$ were about 10%. A laterally-averaged bulk velocity $(\overline{U}_b)_{av}$ was found to be about 4% larger than $(\overline{U}_b)_c$ and 6-12% larger than $\overline{U}_o$, the overall bulk mean velocity (see Figure 5.1).

The complex three-dimensional flow structure near the sides also resulted in the friction velocity at the 260 station $(u_*)_{260}$ being nearly twice the centreline value $(u_*)_c$. A laterally-averaged friction velocity $(u_*)_{av}$ was used to represent the region y = - 260 mm to y = + 260 mm.

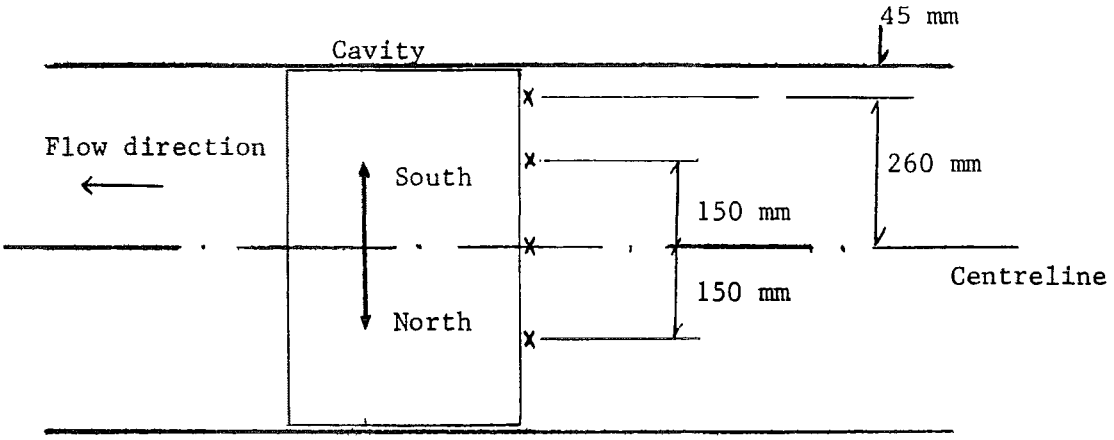

Figure 5.1 a : Positions at which Flow Measurements were recorded

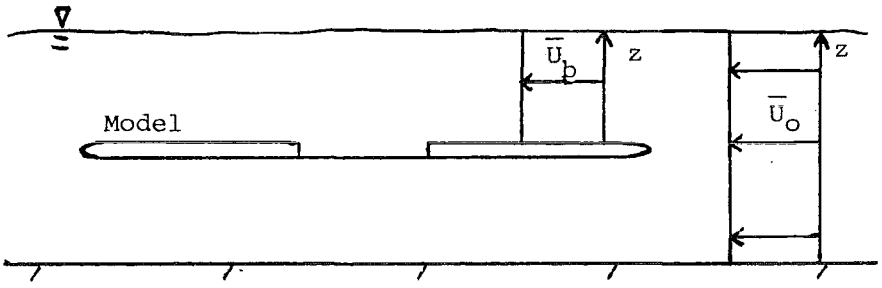

Figure 5.1 b: Relationship between $\bar{U}_b$ and $\bar{U}_o$

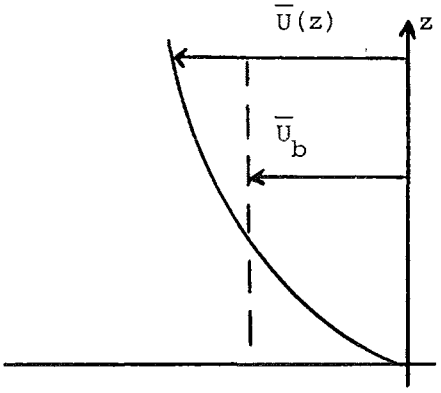

Figure 5.1 c: Relationship between $\bar{U}_b$ and $\bar{U}(z)$ at each measuring station

Comparisons of calculated interfacial slope at y = ± 260 mm with the observed slope at the cavity side (y = ± 295 mm) have suggested an effective shear stress at the latter position to be 4 to 5 times that calculated at the 260 station. This gives an effective friction velocity at the side which is 2 to 3 times $(u_*)_{av}$. This indicates that the large variations of u_* are confined to a region near the cavity sides. The effects of the side leakage are large only within a region 35 mm wide at the sides of the cavity. The remaining width of the cavity can be represented by laterally-averaged values of $(\overline{U}_b)_{av}$ and $(u_*)_{av}$. Finally, a model scale is evaluated.

5.2 The Mean Flow Characteristics

The mean velocity distributions for the constant stress layer over aerodynamically rough and aerodynamically smooth surfaces are briefly stated. The measurements of mean velocity are presented in this section. These include measurements made at the centre of the open channel and at two of the positions south of the channel centreline as shown in Figure 5.1a.

5.2.1 The Constant Stress Layer

The lower 10 to 15% of a turbulent boundary layer with zero pressure gradient and of the neutrally stable atmospheric boundary layer can be approximated by a constant stress layer (Cebeci and Smith 1974, Arya 1982 and others). The resulting mean velocity distributions over an aerodynamically rough surface is (Arya 1982 and others) :

$$\overline{U}(z) = \frac{u_*}{k} \ell n \frac{z}{z_o} \qquad (5.1)$$

and over a smooth surface is (Cebeci and Smith 1974 and others) :

$$\overline{U}(z) = \frac{u_*}{k} \ell n \frac{u_* z}{\nu} + c_1 \qquad (5.2)$$

where k is the von Karman coefficient, z is height, c_1 is a constant and $\overline{U}(z)$ is the mean velocity at height z. The coefficient k for atmospheric boundary layers is about 0.4 (Panofsky and Dutton 1984, Cebeci and Smith 1974 and others). The friction velocity u_* can be evaluated from measurements using :

$$u_* = k\left[\frac{\overline{U}(z2) - \overline{U}(z1)}{\ell n\ z2 - \ell n\ z1}\right] \qquad (5.3)$$

where z1 and z2 are heights at which Equation (5.1) is applicable. The roughness parameter z_o can be evaluated by plotting $\overline{U}(z)$ in semilogarithmic form and extrapolating to zero mean velocity.

5.2.2 The Mean Velocity Profile at the Centre of the Channel

The mean velocity profiles at the centre of the channel for three flows are shown in Figure 5.2. The logarithmic form of Equation (5.1) is valid for $0.03 \lll \frac{z}{\delta} \lll 0.15$. Some of the data points are within the viscous sublayer. Table 5.1 lists the data of all three flows.

Table 5.1 Data for Flow at Centre of Channel

δ, mm	$\overline{U}_o$, m/s	$\overline{U}_\infty$, m/s	$Re_\delta = \frac{\overline{U}_\infty \delta}{\nu}$	u_* centre, m/s	z_o, mm	$\frac{u_* z_o}{\nu}$
δ_1=115	0.0732	0.088	8398	0.0051	0.054	0.23
δ_2= 85	0.0813	0.098	6913	0.0057	0.040	0.19
δ_3= 55	0.0909	0.116	5295	0.0069	0.046	0.26

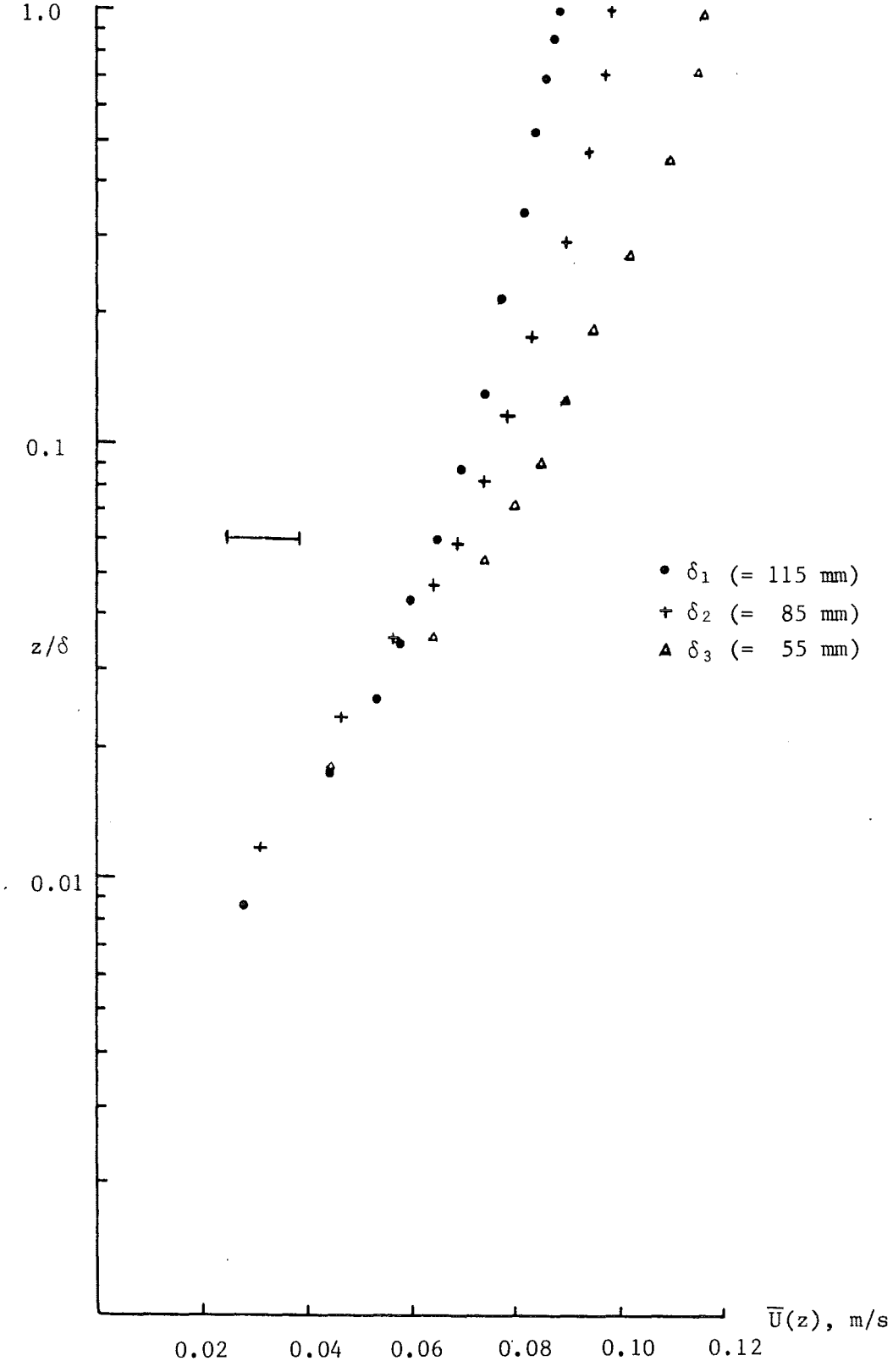

Figure 5.2 : Mean Velocity Profiles at the Centre of the Channel for the Three Flows

The overall bulk mean velocity is $\overline{U}_o = Q_o/A$ where Q_o is the volume flowrate and A is the wetted cross-sectional area upstream of the model. Q_o was evaluated by measurement of the pressure drop across the orifice plate and consulting a calibration chart. $\overline{U}_o$ was chosen as the velocity scale as it was convenient to measure and control. The accuracy of Q_o and $\overline{U}_o$ is of order ± 8%. The maximum mean velocity at the centre $\overline{U}_\infty$ was measured with the LDA. The Reynolds numbers based on the boundary layer depth all exceed the critical value of $Re_\delta \sim 2800$ (Schlichting 1979). The roughness parameter z_o of the flows are of order 0.05 mm, and the roughness Reynolds numbers are greater than 0.13 and less than 2.5. The model flows are in the transition from smooth to aerodynamically rough regime.

5.2.3 The Spatial Distribution of Mean Velocity

Measurements of mean velocity were also recorded at three stations away from the channel centreline. One station was at 150 mm away from the centreline on the north side, and two stations on the south of the centreline at 150 mm and 260 mm respectively. Figures 5.3 a,b,c, show the profiles for the three flows. Only one half of the mean channel flow is shown as the measurements at 150 mm north of the centreline were similar to those recorded at the 150 mm south station. Figures 5.3 a,b, both show a decrease at the top of the boundary layer in mean velocity while Figure 5.3c shows that at the 260 mm station, the maximum velocity is the same. In the region $\frac{z}{\delta} \lesssim 0.2$, all three flow regimes exhibited larger values of $\overline{U}(z)$ at the 150 mm and 260 mm than at the channel centreline by about 25%.

The increase in flow mean velocity near the channel walls (Figures 5.3a,b,c) does not conform to normal boundary layer flows in a channel (Henderson 1966, Townsend 1976). This increase may have been caused by an upward flow from under the model through two gaps of order 10 mm wide between the sides of the model and the channel walls. No measurements of the mean velocity vectors were made in these regions but a possible

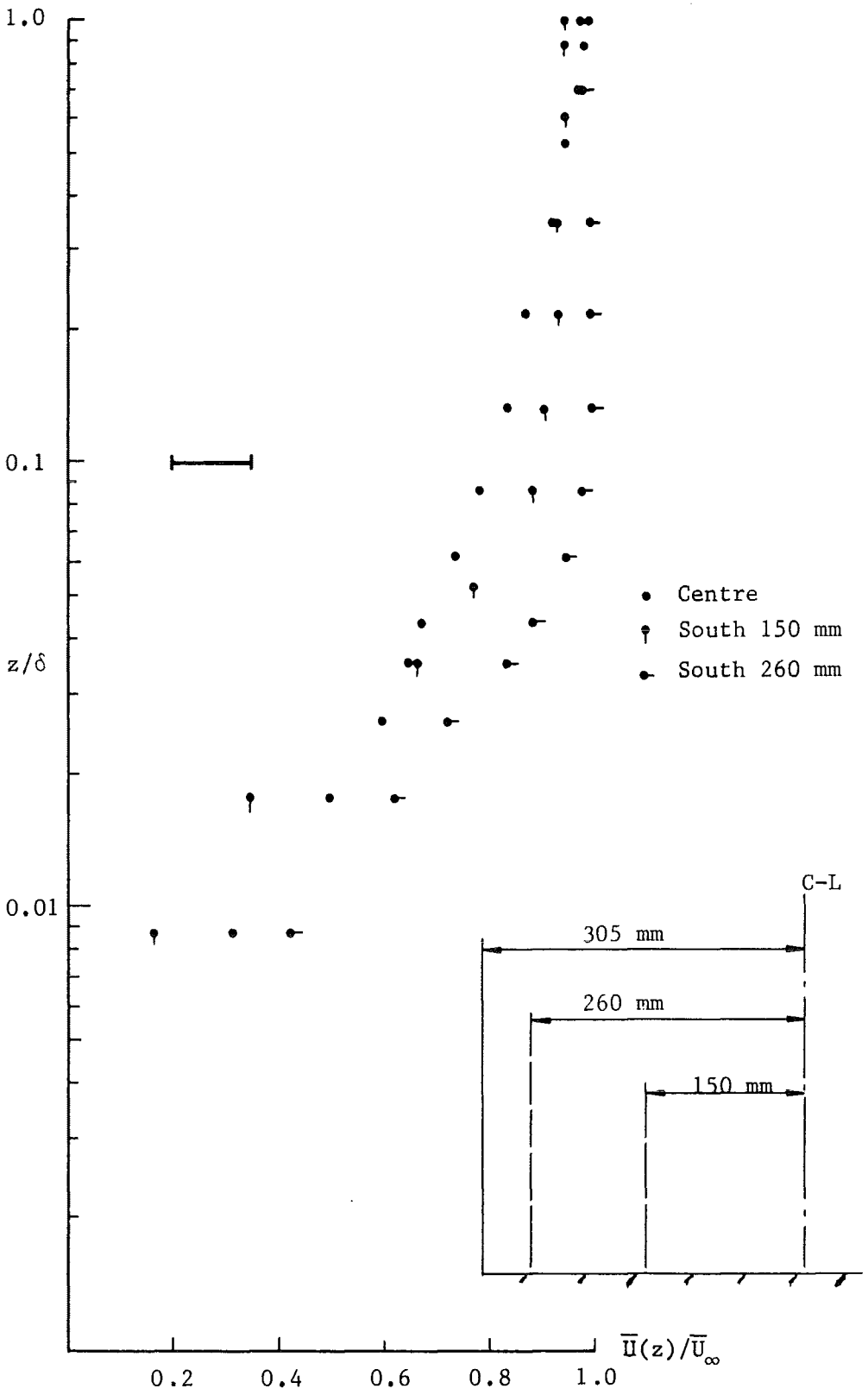

Figure 5.3a : Mean Velocity Distribution across Channel, δ = 115 mm

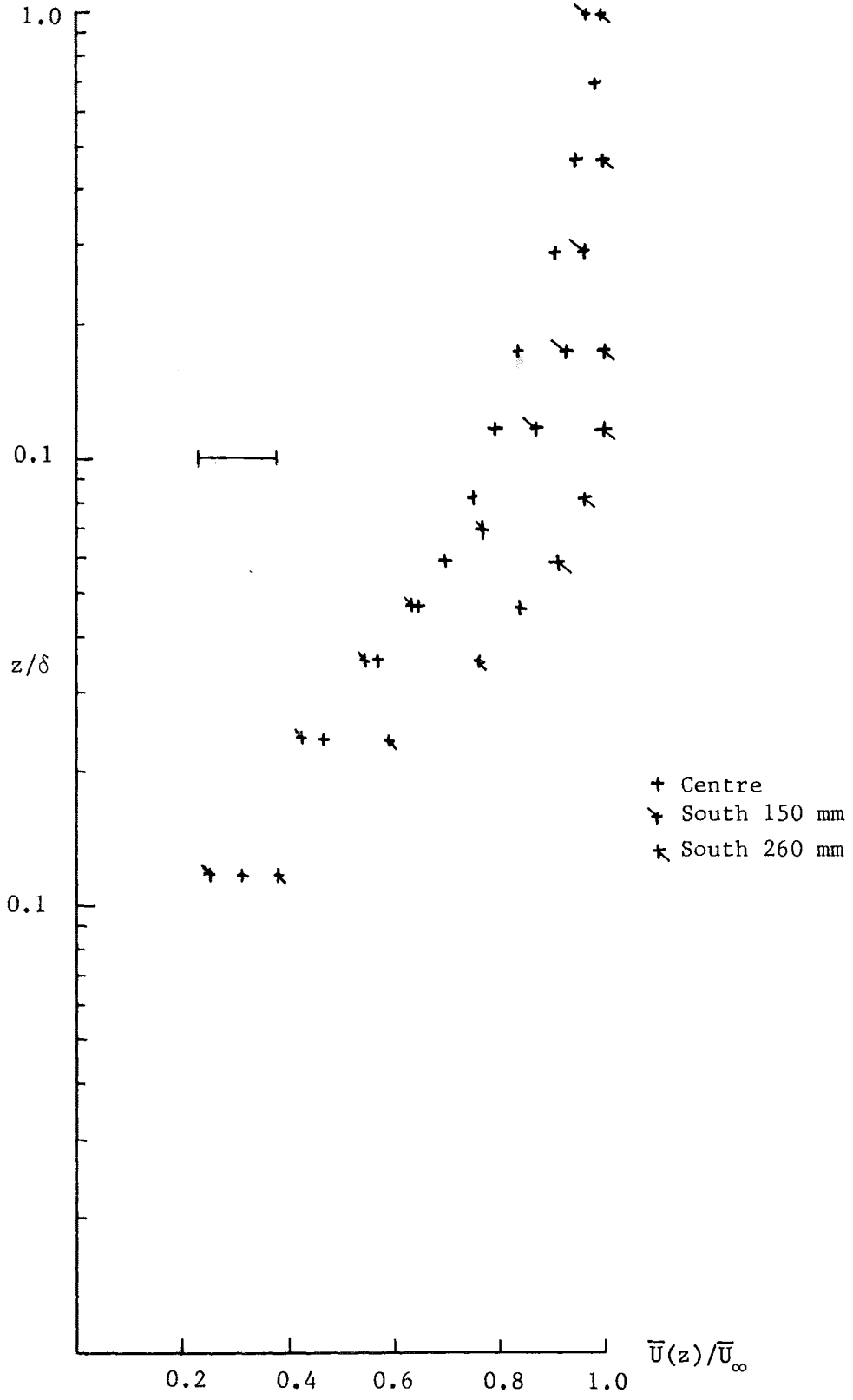

Figure 5.3b : Mean Velocity Distribution across Channel, δ = 85 mm

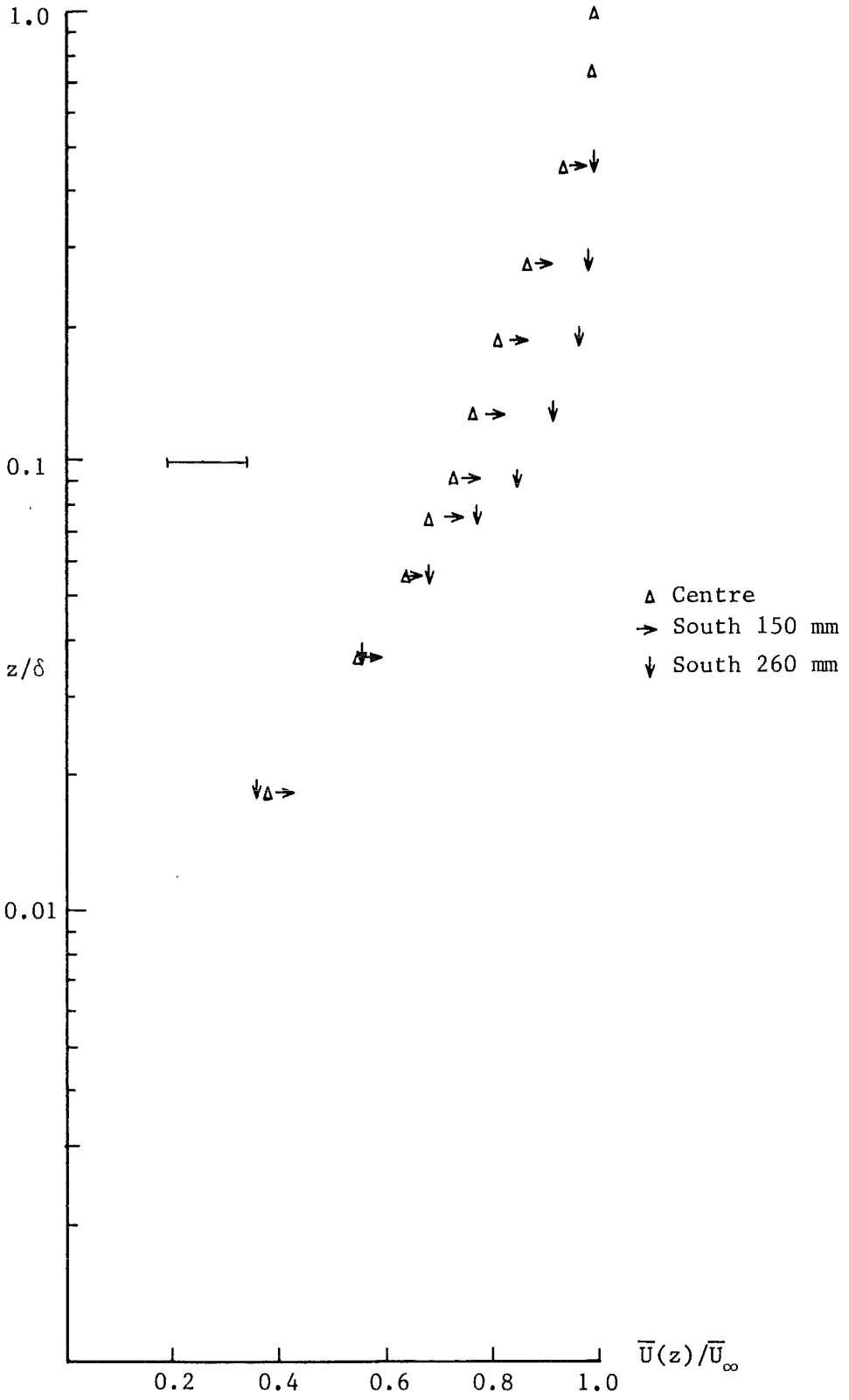

Figure 5.3c : Mean Velocity Distribution across Channel, δ = 55 mm

mechanism for upward flow is now discussed.

The incoming flow is divided by the twin-tapered leading edge of the model (Figure 4.13) such that appoximately equal volumes of water pass over as pass under the model. The almost totally enclosed flow region beneath the model experiences, in comparison to the open channel flow above the model, a greater resistance to flow due to the larger wetted surface area. The consequential pressure difference between the flows under and over the model will result in a 'leakage' of water upwards through the gaps at the edges of the model. The horizontal component of this leakage will add to the mean velocity vector near the channel sides as was observed in Figures 5.3 a,b,c.

The local bulk velocity $\overline{U}_b$ represents a uniform mean velocity over the model at each measuring station such that :

$$\overline{U}_b = \frac{1}{\delta} \int_0^{\delta} \overline{U}(z)\, dz \ .$$

The relationship between $\overline{U}_o$, the overall bulk mean velocity and $\overline{U}_b$ the local bulk velocity is shown in Figures 5.1b,c. The values of $\overline{U}_b$ at the 150 mm and 260 mm stations have been compared with the centreline value $(\overline{U}_b)_c$ for the three flows in Table 5.2. The data show an increase in $\overline{U}_b$ as the channel side is approached. The $(\overline{U}_b)_{260}$ values are up to 10% larger than $(\overline{U}_b)_c$. A laterally-averaged value $(\overline{U}_b)_{av}$ can be evaluated to represent the mean velocity in the region y = - 260 mm to y = + 260 mm. This value, also shown in Table 5.2, is evaluated by assuming a linear variation across the channel. The values of $(\overline{U}_b)_{av}$ are very close to $(\overline{U}_b)_{150}$ for all flows and represent the mean flow over 88% of the model width.

Table 5.2 Variation of $\overline{U}_b$ Across the Channel

Boundary layer depth mm	$(\overline{U}_b)_{150}/(\overline{U}_b)_c$	$(\overline{U}_b)_{260}/(\overline{U}_b)_c$	$(\overline{U}_b)_{av}/(\overline{U}_b)_c$
δ_1 = 115	1.029	1.103	1.036
δ_2 = 85	1.035	1.094	1.037
δ_3 = 55	1.031	1.081	1.033

Table 5.3 Variation of $\overline{U}_b/\overline{U}_o$ Across the Channel

Boundary layer depth mm	$(\overline{U}_b)_c/(\overline{U}_o)$	$(\overline{U}_b)_{150}/(\overline{U}_o)$	$(\overline{U}_b)_{260}/(\overline{U}_o)$	$(\overline{U}_b)_{av}/\overline{U}_o$
δ_1 = 115	1.058	1.089	1.167	1.096
δ_2 = 85	1.07	1.108	1.17	1.109
δ_3 = 55	1.099	1.144	1.199	1.146

The values of $\overline{U}_b$ at all the measuring stations have also been compared with $\overline{U}_o$ for all flows and shown in Table 5.3. The largest differences of 17-20% were found at the 260 mm measuring positions while the centreline differences were 6-11 %. Comparisons of $(\overline{U}_b)_{av}$ with $\overline{U}_o$ showed differences of 10-15%. The assumption of linear variation of $\overline{U}_b$ across the model can produce errors of about 3% which have been included in the above-mentioned differences (see Figure 5.3d). The differences between $(\overline{U}_b)_{av}$ and $\overline{U}_o$ should then be in the order of 12%. The mean value of the three $(\overline{U}_b)_{av}$ has also been plotted in Figure 5.3d. The flow structure across the model can be reasonably approximated by $(\overline{U}_b)_{av}$ and hence $\overline{U}_o$ as these two parameters are related by a constant of proportionality. The value $\overline{U}_o$ was chosen as the mean velocity scale as it was convenient to control and measure.

5.2.4 The Spatial Variation of Friction Velocity and Shear Stress

Another consequence of the upward flow at the sides of the model is the increase in shear stress and subsequently the friction velocity. The values of u_* were evaluated from Figures 5.3a,b,c and shown in Table 5.4 in the form $(u_*/\overline{U}_b)$. The values of u_* increased as the side walls were approached such that the values of $(u_*/\overline{U}_b)_{260}$ were nearly twice the values of $(u_*/\overline{U}_b)$.

So that the effects of the side "leakage" on the interfacial mixing can be quantified, it is appropriate to discuss the variations in terms of the surface shear stress τ_o rather than u_*. The lateral variation of τ_o is shown in Figure 5.3e. Comparisons of $(\tau_o)_{150}$ and $(\tau_o)_{260}$ with $(\tau_o)_c$ show variations of up to $(\tau_o)_{260}/(\tau_o)_c \sim 4$. No measurements were made in the region between the 260 mm station and the channel side but information from Table G-1 and Figures G-3 a,b,c has been found to be of use. Table G-1 compares the calculated interfacial slope

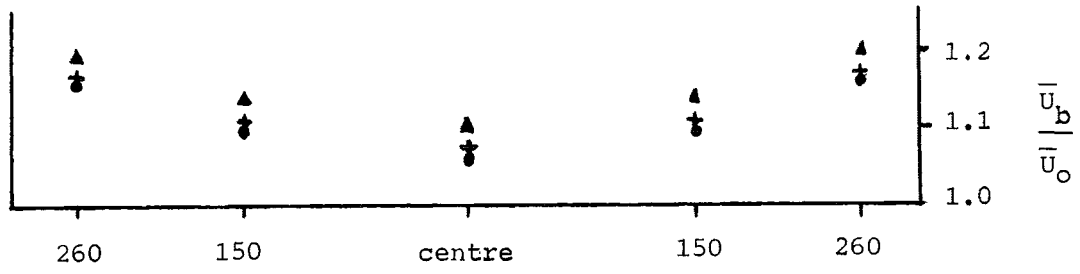

Figure 5.3d : Variation of $\bar{U}_b/\bar{U}_o$ Across the Channel

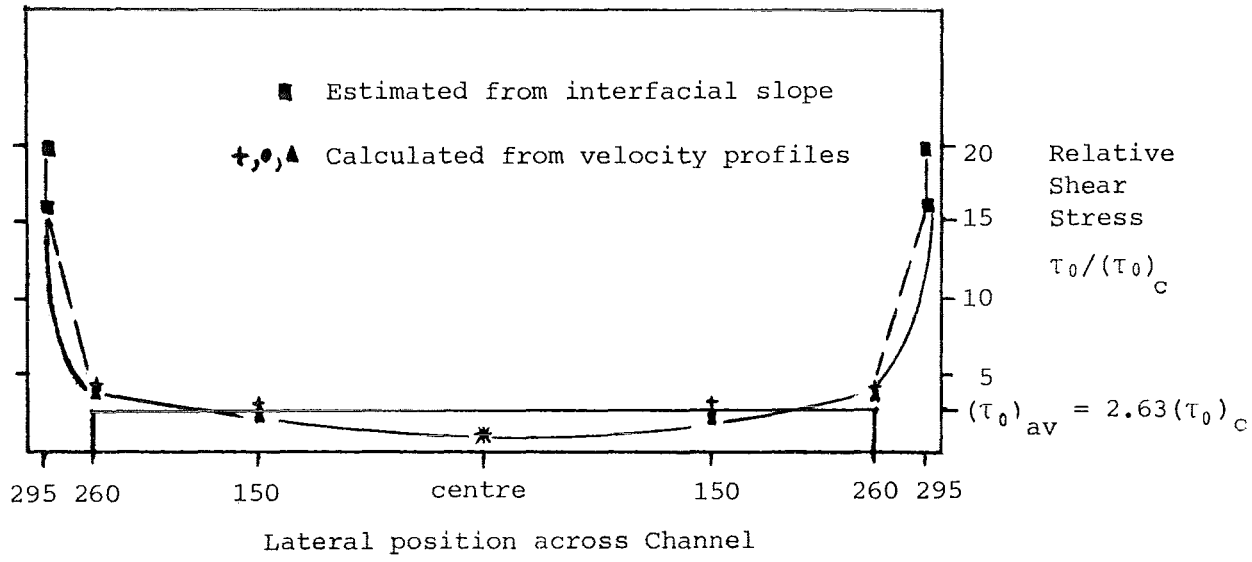

Figure 5.3e : Variation of Relative Shear Stress Across the Channel

Table 5.4 Variation of $u_*/\overline{U}_b$ Across the Channel

Boundary layer depth mm	$\left(\frac{u_*}{\overline{U}_b}\right)_c$	$\left(\frac{u_*}{\overline{U}_b}\right)_{150}$	$\left(\frac{u_*}{\overline{U}_b}\right)_{260}$	$\left(\frac{u_*}{\overline{U}_b}\right)_{av}$	$(z_o)_{150}$
δ_1 = 115	0.066	0.109	0.117	0.102	0.26
δ_2 = 85	0.066	0.110	0.124	0.104	0.31
δ_3 = 55	0.068	0.101	0.119	0.098	0.13

at the 260 mm station with the measured slope at the side of the cavity which is at a distance of 35 mm towards the side. In this discussion it has been assumed that the flow structure over most of the model width did not vary greatly when the lower boundary changed from perspex to saline solution. The flow structure over the cavity can then be assumed to be similar to the flow over the perspex. These assumptions are discussed in Chapter 6 and also in Appendix G.

The results of this comparison show that the measured slopes at the cavity side were 4 to 5 times the calculated slopes at the 260 mm station. As the interfacial slope is proportional to the applied shear stress (Appendix G) it can then be inferred that the effective shear stress at the cavity side $(\tau_{oe})_{295}$ is 4 to 5 times the value of $(\tau_o)_{260}$. This $(\tau_{oe})_{295}$ was not measured in contrast to the values of $(\tau_o)_c$, $(\tau_o)_{150}$ and $(\tau_o)_{260}$ which were all evaluated from measured vertical profiles of mean velocity. The range of $(\tau_{oe})_{295}$ is also shown in Figure 5.3e at y = ± 295 mm and is significantly higher than τ_o over the rest of

the cavity width. The lateral variation in shear stress is thus in keeping with the observed difference in interfacial slope between most of the cavity width and that near the side walls. By ignoring the edge effects, an average value of τ_o can be estimated for the region y = - 260 mm to y = + 260 mm by assuming a linear lateral variation. This assumption is not unreasonable when compared to the curve in Figure 5.3e. The average applied shear force between y = - 260 mm to y = + 260 mm is :

$$(s.f.)_{av} = (\tau_o)_c \left\{ \left(\frac{1+3}{2}\right) \times 0.3 + \left(\frac{3+4}{2}\right) \times 0.22 \right\} \text{ per unit length of cavity.}$$

This shear force can be expressed as the product of the cavity area and $(\tau_o)_{av}$ which provides an average value of τ_o over the affected area :

$$(s.f)_{av} = (\tau_o)_{av} \times 0.52 \text{ per unit length of cavity.}$$

Then $$(\tau_o)_{av} = 2.63\ (\tau_o)_c$$

and $$(\tau_o)_{av} \sim 0.66\ (\tau_o)_{260} \ .$$

Note also that :

$$(\tau_o)_{av} \sim (\tau_o)_{150} \text{ (Figure 5.3e)} \ .$$

Assume that :

$$(\tau_{oe})_{295} \sim 4(\tau_o)_{260} \ ,$$

then :

$$(\tau_{oe})_{295} \sim 6(\tau_o)_{av} \ .$$

The stress $(\tau_o)_{av}$ is assumed to be effective over the region y = - 260 mm to y = + 260 mm, that is 88% of the cavity surface area. The edge

regions between y = - 260 mm to y = - 295 mm and y = + 260 mm to y = + 295mm represent the remaining 12% of the cavity surface area. Denote the average shear stress in these edge regions as τ_{os}. To evaluate τ_{os}, an assumption about τ_{oe} and the variation of shear stress in this area to y = ± 295 mm is required. From the above assumption :

$$\text{if} \qquad (\tau_{oe})_{295} \sim 6(\tau_o)_{av}$$

and the variation from $(\tau_o)_{260}$ to $(\tau_{oe})_{295}$ is assumed to be linear, then the fraction of the total shear force due to τ_{os} is 32%. If however the variation of shear stress is not linear as shown by the full curve in Figure 5.3e, then τ_{os} contributes 24% of the total shear force. This latter non-linear assumption results in $\tau_{os} \sim 2.4\ (\tau_o)_{av}$.

The magnitude of $(\tau_{oe})_{295}$ and subsequently τ_{os} is determined not only by the interaction of the side "leakage" with the mean flow but also by the inherent effects of the edge. These three-dimensional complexities may exist around bluff bodies, corners, appreciable changes in surface roughness and gross changes in geometry.

The above evaluation of u_* from Figures 5.3 a,b,c, depended on an appropriate choice of slope of the straight line representing the constant stress layer in the vertical velocity profiles. This can involve errors of 15-20% in u_* which can in turn result in errors of 30-40% in τ_o. Hence the accuracy of $(\tau_o)_{av}$ is of order 30-40%. The values of $(u_*)_{av} = [(\tau_o)_{av}/\rho_o]^{1/2}$ have been compared with the evaluated u_* at the different measuring stations. The values of $(u_*/\bar{U}_b)_{av}$ are very close to $(u_*/\bar{U}_b)_{150}$ (Tables 5.2 and 5.4) and considering the accuracies of both the evaluation of $(u_*/\bar{U}_b)_{150}$ and the linear representation of τ_o across the cavity, these values can be assumed to be the same without introducing any further error. Furthermore, the values of $(u_*/\bar{U}_b)_{150}$ were evaluated from measurements and therefore are appropriate for later use and comparison.

A difference of 14% was found when the vaue of $(\tau_o)_{av}$ was assumed for the full cavity width as compared to the case where $(\tau_o)_{av}$ represented 88% of the area and τ_{os} represented the remaining 12%. This difference of 14% was less than the accuracy of the u_* and τ_o values. As the values of $(\tau_{oe})_{295}$ and subsequently τ_{os} were not obtained from measurements, it was decided to use the measured $(u_*)_{150}$ and resulting $(\tau_o)_{150}$ in later applications. These parameters are considered to be representative of the flow structure over most of the model width.

The ratio of $\overline{U}_o/(u_*)_{150}$ for all flows has been shown in Table 5.5 and these ratios can be represented by $\overline{U}_o/(u_*)_{150} = 8.43 \pm 3\%$. The fact that this value may be taken as a constant for all flow conditions used in the experiments is an important result. The ratio of the turbulence energy which scales with $\overline{U}_o$ to the turbulence energy which scales with $(u_*)_{150}$ may therefore be considered constant for all experiments.

Table 5.5 Values of $\overline{U}_o/(u_*)_{150}$ for Different Flows

Boundary layer depth mm	$\frac{\overline{U}_o}{(u_*)_{150}}$
$\delta_1 = 115$	8.41
$\delta_2 = 85$	8.21
$\delta_3 = 55$	8.65

This flow structure was not fully appreciated until the experimental equipment had been dismantled, but as shown above the large variations are confined to a region very close to the sides of the model and channel. Over the major part of the model, the flow structure can be suitably represented by average values of $\overline{U}_o$, u_* and τ_o .

5.3 The Longitudinal Turbulence Intensity

5.3.1 The Turbulence Intensity at the Channel Centreline

The measurements of longitudinal turbulence intensity at the centre of the channel for all three flows are shown in Figure 5.4. The profiles of the flows are all very similar with the background level of approximately 7% to 8%, and this increases to over 20% very close to the floor. Atmospheric data (ESDU 1974) has also been included for z_o = 0.01 m. The small increase in turbulence intensity at the top of the boundary layer was due to the presence of a small amplitude wave travelling on the water surface.

5.3.2 The Spatial Structure of Turbulence Intensity

The structure of turbulence intensity across the channel for each of the three flows has been shown in Figures 5.5 a,b,c. Each flow regime showed a gradual decrease in the turbulence intensity as the side is approached although the background level was about 6% at the 260 mm position.

5.4 The Vertical Turbulence Intensity

5.4.1 The Turbulence Intensity at the Channel Centreline

The distributions with height of the vertical components of turbulence intensity at the channel centre for all flows are shown in Figure 5.6. The atmospheric data (ESDU 1974) for the identical component for z_o = 0.01 m has also been included. For $\frac{z}{\delta} \lesssim 0.4$, there is good agreement among the flows and the atmospheric data with the turbulence intensity at about 5%. There are no measurements very close to the floor as a finite height is required for the laser beams to cross. For $\frac{z}{\delta} >$

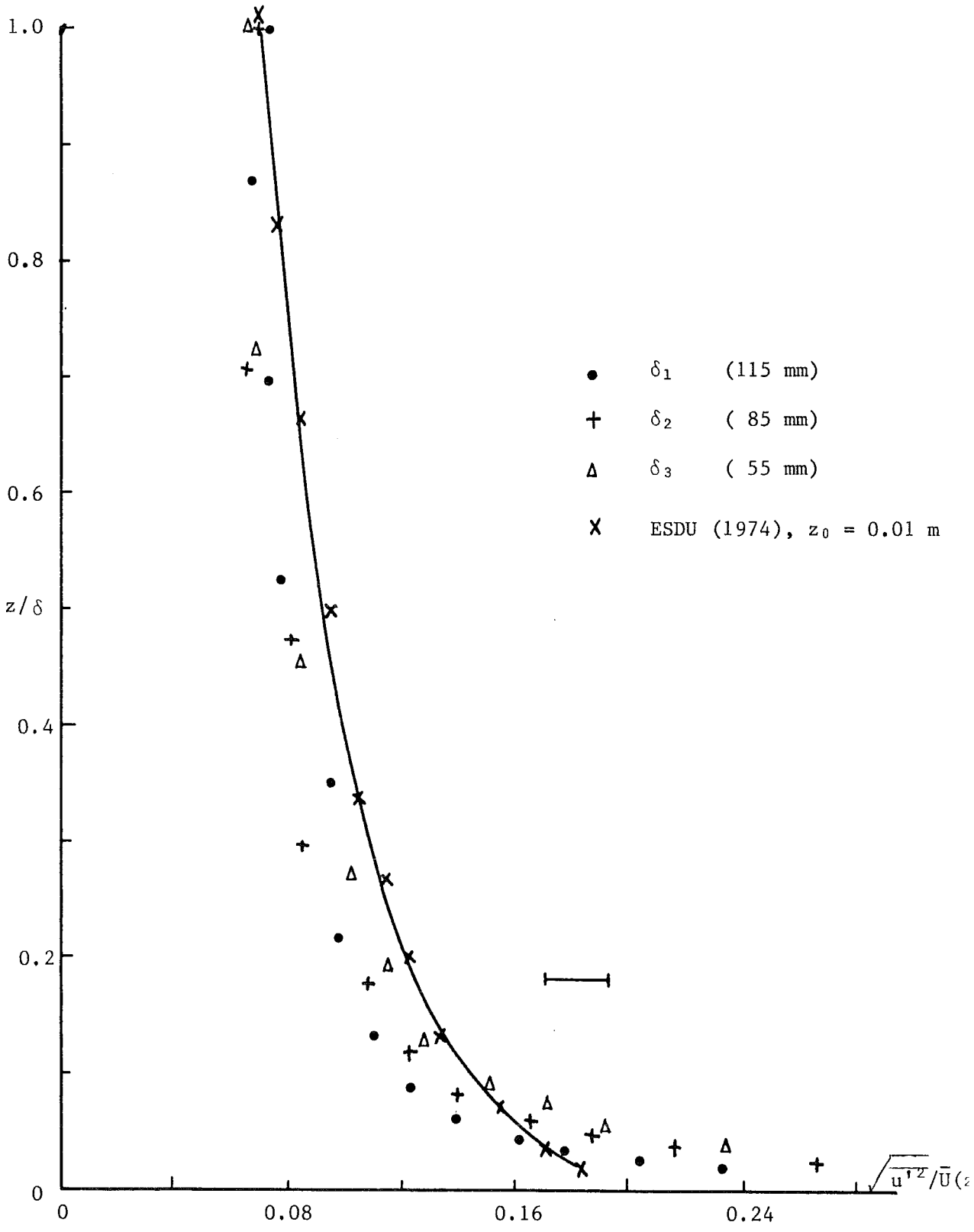

Figure 5.4 : Longitudinal Component of Turbulence Intensity at the Centre of the Channel for Three Flows

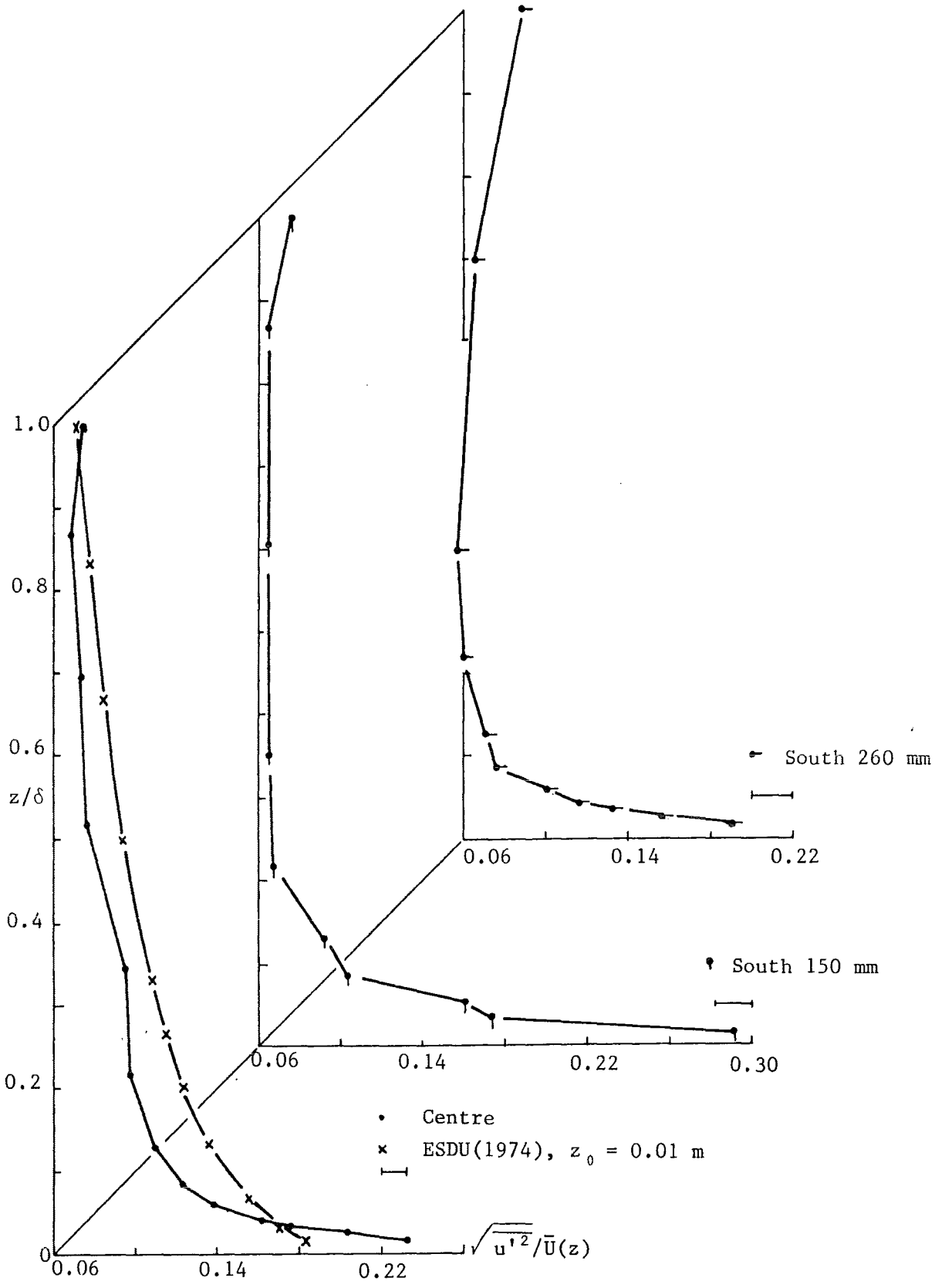

Figure 5.5a : Distribution of Longitudinal Component of Turbulence Intensity, δ = 115 mm

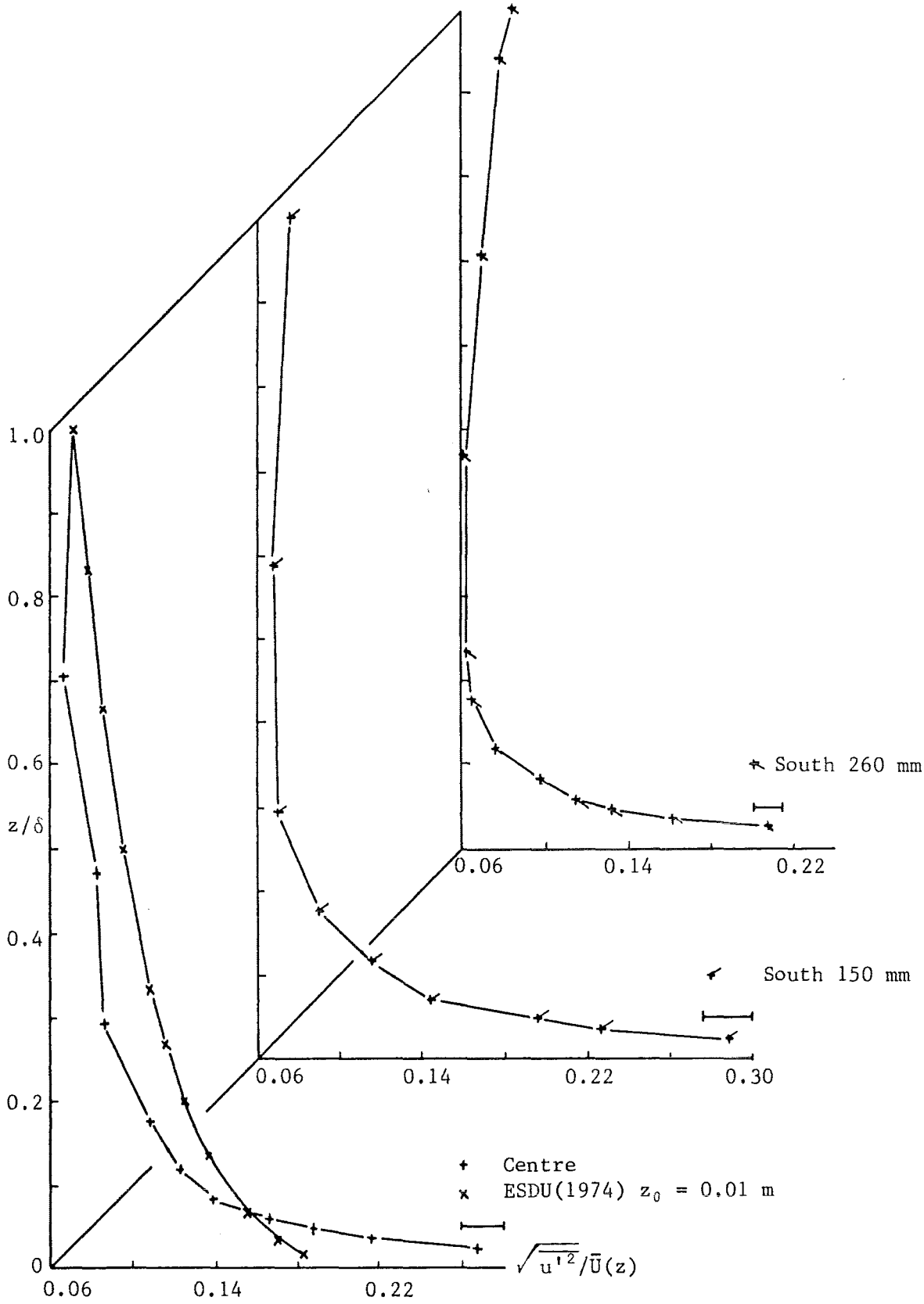

Figure 5.5b : Distribution of Longitudinal Component of Turbulence Intensity, δ = 85 mm

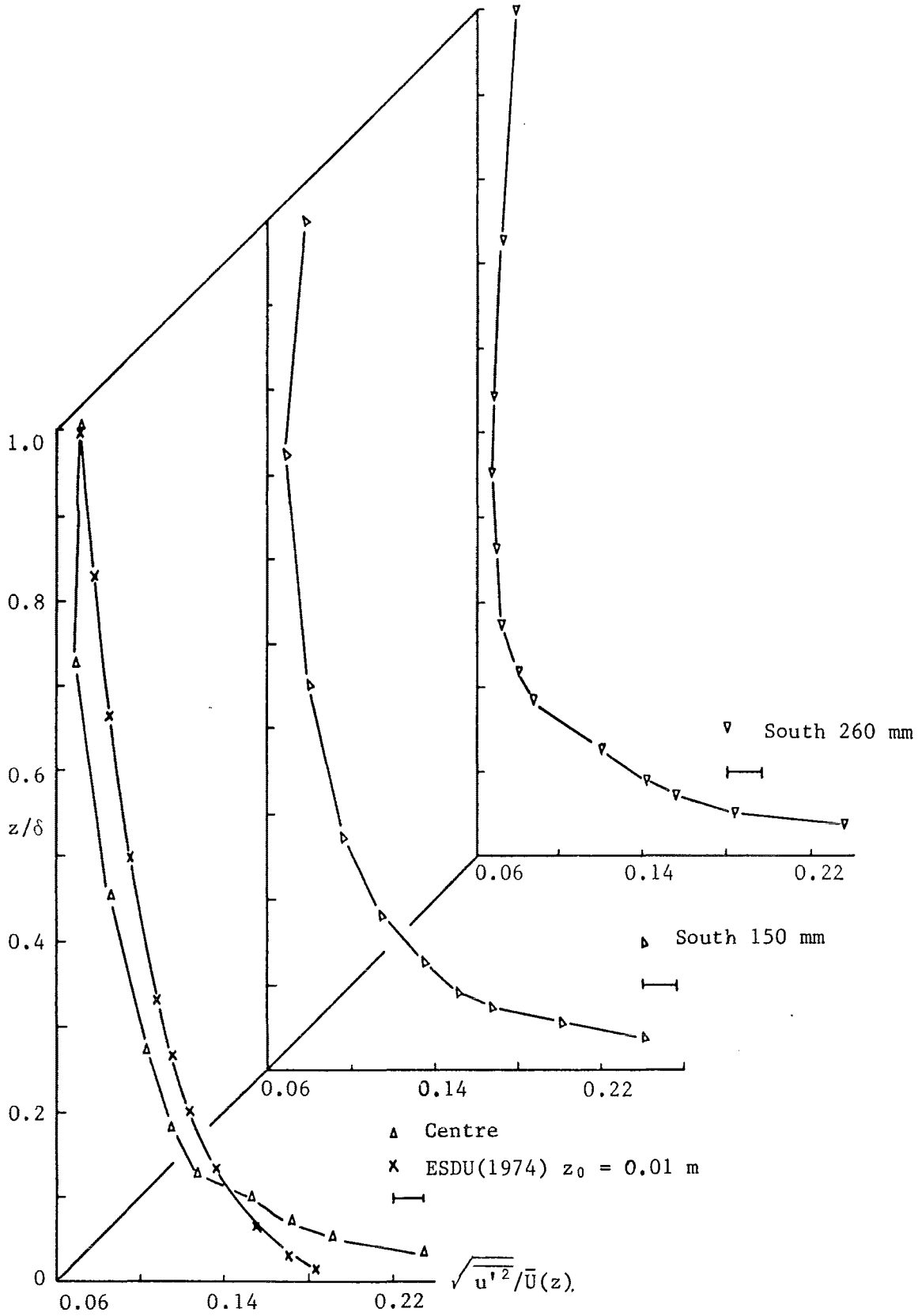

Figure 5.5c : Distribution of Longitudinal Component of Turbulence Intensity, δ = 55 mm

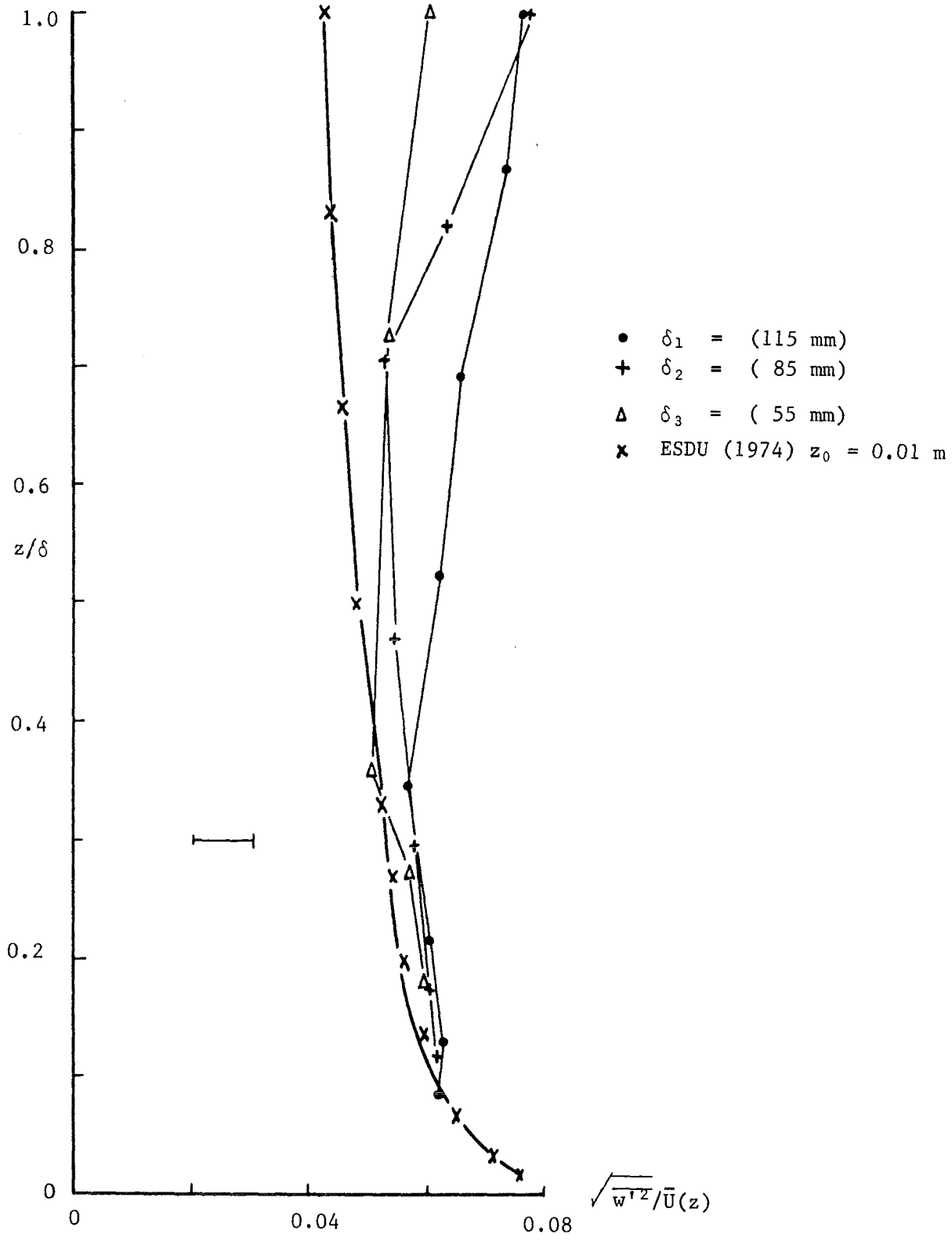

Figure 5.6 : Vertical Component of Turbulence Intensity at the Centre of the Channel for Three Flows

0.4, the atmospheric (ESDU 1974) data continues to decrease, while the measured data increases to a maximum at the top of the boundary layer. This maximum at $\frac{z}{\delta} = 1.0$ was due to a wave travelling on the water surface which was nominally at $z = \delta + 20$ mm.

5.4.2 The Spatial Structure of Turbulence Intensity

The distribution of the vertical component of turbulence intensity for the three flows are shown in Figures 5.7 a,b,c. The flows all show an increase in turbulence intensity as the channel wall is approached. The trend in all the distributions is for $\sqrt{\overline{w'^2}}/\overline{U}(z)$ to increase as z increases. At the top of the boundary layer, the turbulence intensity is about 8%. At positions away from the channel centre, the turbulence intensity near the floor is of order 4%.

5.5 Scaling the Model Flow

The important scaling criterion for this work is the Richardson number:

$$Ri_o = g \frac{\Delta\rho}{\rho_o} \frac{L}{\overline{U}^2} \quad .$$

The prototype mean velocity is of order 2 m/s, and by retaining the reduced buoyancy ratio $\frac{\Delta\rho}{\rho_o}$ in the model and prototype, the Richardson number reduces to :

$$\left[\frac{L}{\overline{U}^2}\right]_m = \left[\frac{L}{\overline{U}^2}\right]_p \quad .$$

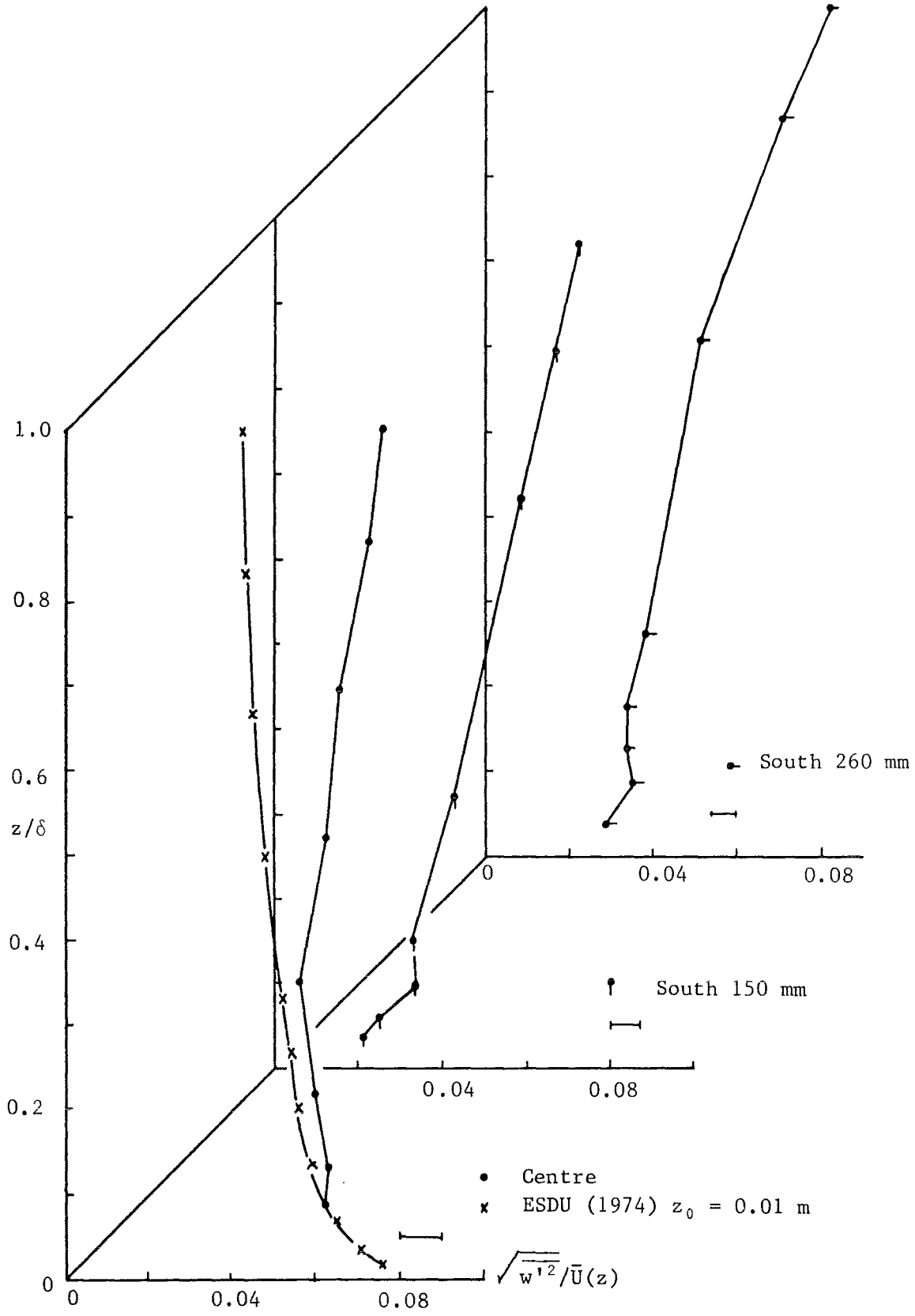

Figure 5.7a : Distribution of Vertical Component of Turbulence Intensity, δ = 115 mm

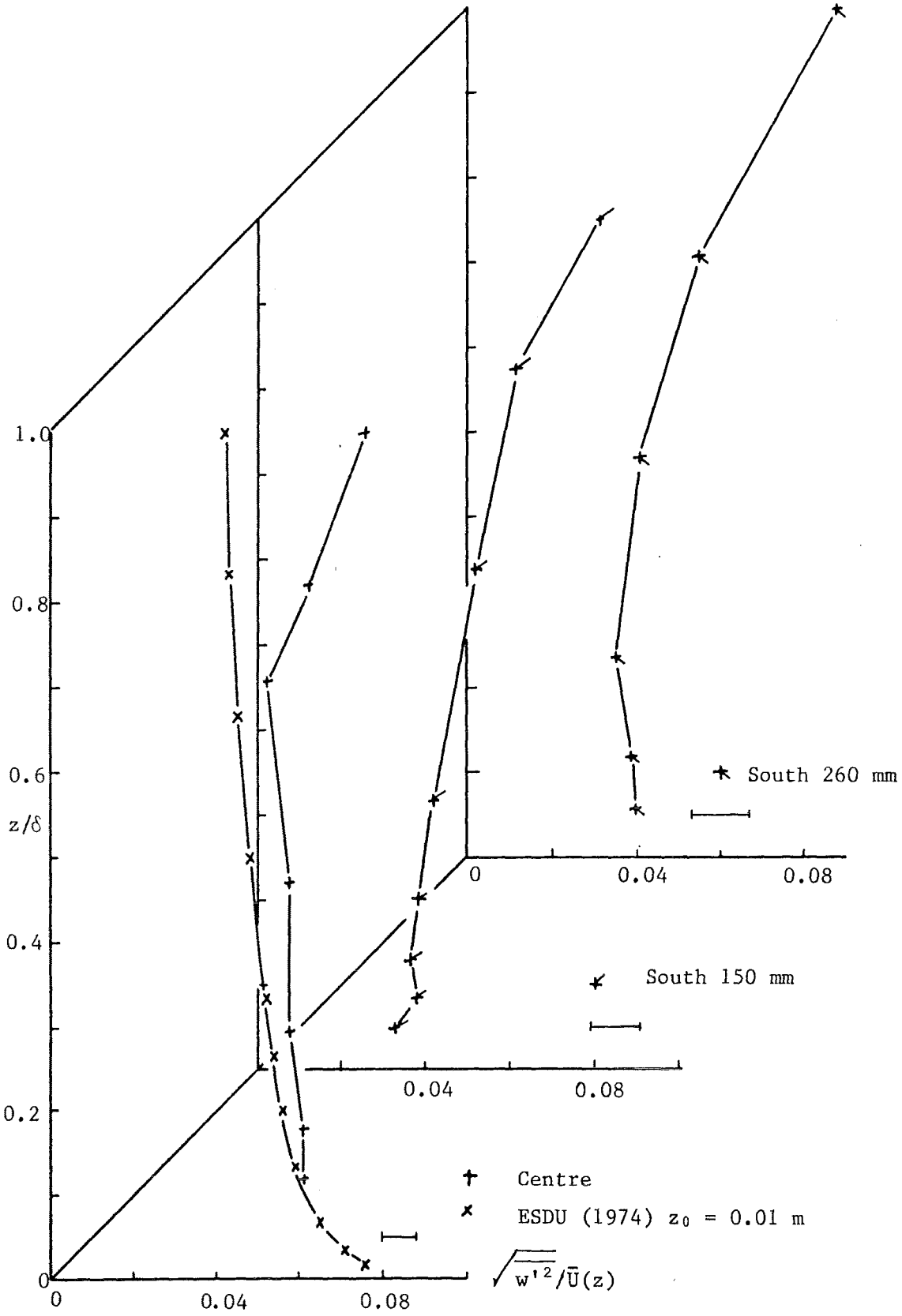

Figure 5.7b : Distribution of Vertical Component of Turbulence Intensity, δ = 85 mm

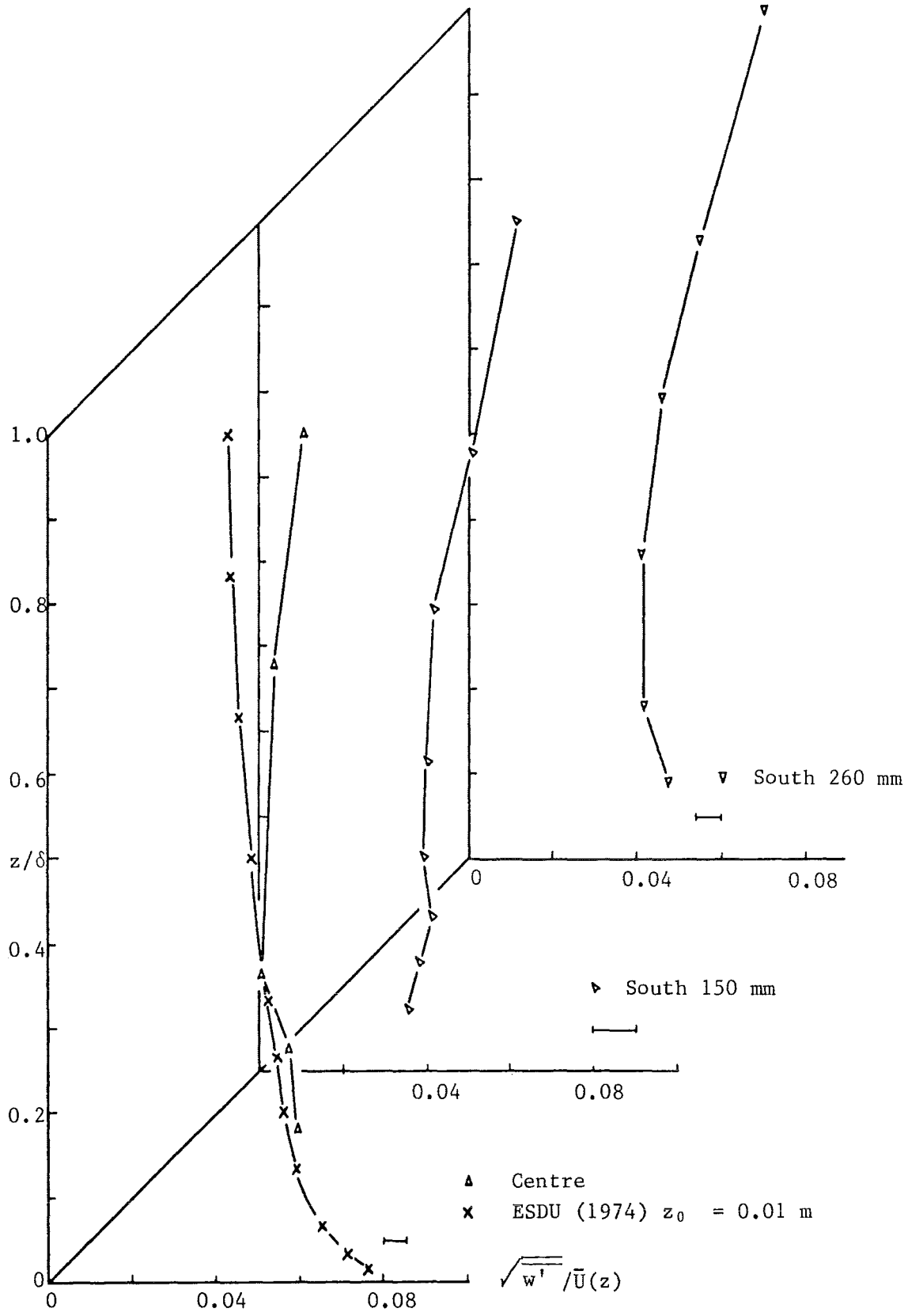

Figure 5.7c : Distribution of Vertical Component of Turbulence Intensity, δ = 55 mm

The ratio of lengthscales becomes :

$$\left[\frac{L_m}{L_p}\right] = \left[\frac{\overline{U}_m}{\overline{U}_p}\right]^2$$

The range of mean velocities in the model was 0.073 to 0.091 m/s and the ratio of lengthscales become :

$$\frac{1}{750} < \frac{L_m}{L_p} < \frac{1}{480} \quad .$$

Jensen's (1958) criterion is not valid for comparison because the model flow is not aerodynamically rough.

CHAPTER SIX

OBSERVATIONS AND RESULTS OF ENTRAINMENT EXPERIMENTS

6.1 Summary

The observations and results of the entrainment experiments are presented in this chapter. A total of 53 runs were carried out in the 290 mm cavity for three mean velocities during 1985 and 1986. Prior to presentation of the results, the length and velocity scales for the Richardson number are selected. The observations of the interface are compared with two theoretical results. Measurements of entrainment are reported for the full-size cavity and two shorter cavities. The comparison of the results from this full-size cavity with the data of Lofquist (1960) shows that the end-effects cause a doubling of the entrainment rate. An empirical model is proposed for turbulent entrainment from this cavity.

6.2 Choice of Length and Velocity Scales for the Richardson Number

6.2.1 Introduction

The Richardson number is the most important parameter in this study and as it forms an integral part of this chapter, it is necessary to select the relevant length and velocity scales before any observations and results are presented. However, the confirmation of the choice of length and velocity scales relies on the results of the entrainment experiments and as these results are to be presented later, it is necessary to refer to them in advance.

The appropriate form of the Richardson number for two-layer experiments is:

$$Ri = \frac{g'L}{U^2} \qquad (6.1)$$

where L and U are length and velocity scales. There are a number of combinations of L and U which may be suitable for these experiments. These are:

(i) The roughness parameter z_o and the friction velocity u_*. These parameters are characteristic of the atmospheric surface layer.

(ii) The mixed or upper layer depth h_o and the friction velocity u_*. These parameters are commonly used in the study of mixed layers in the atmosphere and ocean.

(iii) The depth of the new turbulent boundary layer δ_t over the cavity and the overall bulk mean velocity of the upper layer $\overline{U}_o$. The lengthscale δ_t is suitable for very large Richardson number flows where the interface can be assumed to be a rigid surface (Turner, 1986).

(iv) The lengthscale associated with the wake behind a backward facing step (Bradshaw and Wong 1972) and $\overline{U}_o$.

(v) The different surface roughness appropriate to the dense fluid-ambient fluid interface as the lengthscale and $\overline{U}_o$.

These combinations of length and velocity scales are used to form Richardson numbers using Equation (6.1) and are presented later in this

section. The entrainment data are then plotted against these forms of Richardson number and discussed in Section 6.4. The suitability of each combination of length and velocity scaling parameters is also discussed.

The ratio of $\overline{U}_o/(u_*)_{150}$ for the three flow regimes is effectively constant (Table 5.5). This means that the turbulent energy generated by the mean flow and the turbulent energy generated by the lower boundary are in the same ratio for all flows. Also the selection of one velocity as a scaling parameter can be related to the other velocity by a constant of proportionality. However, the three lengthscales z_o, h_o and δ_t cited above are independent of one another to a much greater degree than the two possible velocity scales $\overline{U}_o$ and u_*. Both z_o and h_o are properties of the model surface and the channel flow and are set experimentally, independent of the conditions at the interface or in the cavity. Hence, the experimental configuration here differs fundamentally from mixed layer experiments in which one is interested in predicting the growth of an entraining mixed layer. In this experiment the upper layer depth h_o and the level of turbulence are fixed *a priori*, and what is of interest is the entrainment flux out of the cavity. As will be convincingly shown later, the entrainment depends crucially on the local conditions at the interface itself, and cannot be explained in terms of the lengthscales z_o and h_o which are representative of the turbulence only in the upper flowing layer. Hence, it is argued that the proper choice of lengthscale is that which is directly associated with the mass and momentum transfer at the interface itself, that is, the new turbulent boundary layer thickness over the cavity.

It has been repeatedly shown in mixed layer experiments that an entraining mixed layer has a depth which remains in approximately constant proportion to the thickness of the shear layer (Long 1973 and others). Hence, choosing the cavity boundary layer thickness as the appropriate lengthscale does not contradict the results of previous mixed layer experiments. In this experiment the mixed layer depth is set by

hydraulic considerations (of flowrate, surface roughness) independently of the entrainment and cannot be expected to provide a reliable index of entrainment conditions at the interface.

The length and velocity scales were expected to change as the upper layer flowed from the solid perspex surface to the dense fluid, thereby forming the density interface. However, scaling of the possible models on the upstream flow structure was considered to be justified when the experimental results were to be interpreted to a full scale prototype and to follow precedents in the published literature. This model can only represent the prototype reliably if the transition regions are similar.

6.2.2 The Roughness Parameter and the Friction Velocity

Fully aerodynamically rough flow in the atmosphere is characterised by z_o and u_*. These parameters are important when a dense gas cloud is moving with the mean wind near the ground. The form of the Richardson number with these scaling parameters is:

$$Ri_* = g' \frac{z_o}{u_*^2} \qquad (6.2)$$

The entrainment results are plotted in the form $E_* = \frac{u_e(F)}{u_*}$ versus Ri_* in Figure 6.7. Although there is some scatter, the results follow a $E_* \propto Ri_*^{-3/2}$ relation.

6.2.3 The Mixed Layer Depth and the Friction Velocity

The mixed or upper layer depth h_o and the friction velocity u_* are also a reliable set of scaling parameters which have been applied in atmospheric and oceanic studies (Phillips 1977 and others) and also in experiments (Kranenburg 1984 and others). The form of the Richardson number for mixed layer experiments is:

$$Ri_h = g' \frac{h_o}{u_*^2} \tag{6.3}$$

The plot of E_* versus Ri_h is shown in Figure 6.8. The distribution shows scatter as in Figure 6.7 and the results follow a $E_* \alpha Ri_h^{-3/2}$ relation.

The mixed layer model of Sherman, Imberger and Corcos (1978), and utilized by Spigel, Imberger and Rayner (1986) and others has been applied to these experiments and the results are also shown in Figure 6.8. This model indicates a (-1) dependence on the Richardson number in contrast to the strong (- 3/2) dependence of the experimental data in this project. Although there appears to be some agreement at high Richardson numbers, the model is not representative of the range of experimental conditions encountered. Hence this model is not considered suitable for predicting the range of these experimental results.

6.2.4 The Depth of the New Cavity Boundary Layer and the Mean Velocity

The two previous combinations of length and velocity scales have been shown (in Section 6.4) not to be very suitable for presenting the measurements of entrainment in this set of laboratory experiments. Both Figures 6.7 and 6.8 showed considerable scatter, more than the bounds of experimental error. Both Figures 6.7 and 6.8 also show a dependence on the Reynolds number, as each set of experiments which were conducted at a particular value of $\overline{U}_o$ could be plotted on a single curve with a slope proportional to Richardson number to (- 3/2) power.

In a discussion of viscous effects at a density interface with particular reference to Keulegan's (1949) work, Turner (1973) found that the parameter:

$$K^{-1} = g' \nu_1 / \overline{U}_o^3 \tag{6.4}$$

could be interpreted as a type of Richardson number with a weak dependence on the Reynolds number if re-written as:

$$K^{-1} = \frac{g'd'}{\bar{U}_o^2} \left[\frac{\upsilon_1}{\bar{U}_o x}\right]^{1/2} \tag{6.5}$$

The viscous lengthscale $d' = \left[\frac{\upsilon_1 x}{\bar{U}_o}\right]^{1/2}$ scaled as the thickness of the boundary layer which formed in time $\frac{x}{\bar{U}_o}$ as the flow travelled a distance x from the entrance of the channel. The term υ_1 represents the kinematic viscosity of the heavier fluid. In Keulegan's experiments, the cavity was nearly the same length as the channel.

The comparable viscous lengthscale in this work would be the depth of the new boundary layer which formed over the cavity. For a laminar boundary layer, the viscous lengthscale is of the form:

$$\delta_\ell \; \alpha \left[\frac{\upsilon_1 L_1}{\bar{U}_o}\right]^{1/2} \tag{6.6a}$$

where L_1 is the length of the cavity and the constant of proportionality is of order 5 (Schlichting 1979). For a turbulent boundary layer on a smooth surface, the depth is given by (Schlichting 1979 and others):

$$\delta_t = 0.37 \; L_1 \left[\frac{\upsilon_1}{\bar{U}_o L_1}\right]^{1/5} \tag{6.6b}$$

No velocity measurements were made of the flow over the cavity to ascertain whether the flow was laminar or turbulent. Any attempts with the LDA may have proven to be difficult due mainly to the large local fluctuations of density and, subsequent changes in the refractive index of the water. However, earlier work by Plate and Hidy (1967) who studied turbulent air flow over a roughness change from a smooth aluminium plate

to water surface, found that the flow remained turbulent and recorded increases in u_* and z_o.

In a review of full-scale measurements in the marine surface layer, Tieleman (1987) has found that under strong winds, the ocean surface which would inevitably involve significant wave action is aerodynamically smooth. The surface roughness is reported to be within the range $0.1 < z_o < 1$ mm. The turbulence intensity $\sqrt{\overline{u'^2}}/\overline{U}(z)$ was found to increase with windspeed and the turbulence ratio $\sqrt{\overline{u'^2}}/u_*$ did not vary with windspeed but was about 12.5% larger than those observed over land. Finally, the longitudinal integral scale of turbulence was found to be larger over the ocean while the lateral scales were less than those over land. Although the review by Tieleman (1987) has opposite conclusions to the laboratory study reported by Plate and Hidy (1967), it must be stressed that Tieleman's work was concerned with strong winds which means $\overline{U} > 10$ m/s at a 10 metre height. It is uncertain as to whether a strong wind will have the same effect on surface waves on the ocean as it does on blades of long grass (Deacon 1949) where a smaller z_o was recorded due to grass bending more in the wind direction. This difference in reported behaviour of windflow over grassland and water does not indicate qualitatively whether in the present experiments, z_o should increase or decrease when the upper layer flows from the perspex floor onto the dense saline solution. Observations of the interface have shown that the detached filaments of saline solution in these experiments were moved around by the flow and did not remain in one plane. This indicated that the flow over the cavity was turbulent.

At very high Richardson number, the interface of a turbulent layer and a very stable layer will be almost flat and devoid of waves (Figures 6.2c and G-3c). The effect of this very stable layer on the turbulent upper layer would be very similar to that of a smooth rigid surface (Turner 1986). For mean turbulent motion over a rigid surface, an

appropriate lengthscale is the depth of the turbulent boundary layer over the surface. Assuming that the boundary layer begins at the upstream edge of the cavity in a fully turbulent regime, then the lengthscale is given by δ_t as defined in equation (6.6b).

It is stressed that the choice of δ_t as the lengthscale and $\overline{U}_o$ as the velocity scale is based on the behaviour of the density interface at high Richardson number. This choice is relevant for high values of Richardson number and it was decided to see if the model could be extrapolated to include all the experimental data which also represented lower Richardson numbers. If successful, as is indicated in Figure 6.9, the experimental data over the wide range of Richardson numbers could be conveniently displayed together.

The lengthscale δ_t is dependent on the Reynolds number to the (-1/5) power. More interestingly, δ_t has a (1/5) dependence on the kinematic viscosity ν_1 of the more dense fluid. At large density differences the ratio of kinematic viscosities may be up to 6 and this raised to the (1/5) power can eventually alter the Richardson number by over 40%. So the value of δ_t is dependent not only on L_1 and $\overline{U}_o$, but also on the kinematic viscosity (which varies as the density). This set of experiments was designed to study the large density-difference, high Richardson number regime and it is to be expected that the range of Richardson numbers would be effected by changes in density, viscosity and to a lesser degree, L_1 and $\overline{U}_o$.

The appropriate form of the Richardson number is :

$$Ri(\delta_t) = \frac{g'\delta_t}{\overline{U}_o^2}$$

or

$$Ri_\delta = \frac{g'\delta_t}{\overline{U}_o^2} \qquad (6.7)$$

The non-dimensional entrainment, $u_e(F)/u_*$ versus Ri_δ is shown in Figure 6.9. The result is a marked improvement on the presentations of Figures 6.7 and 6.8. The data in Figure 6.9 fall very close to the curve of slope (-3/2) and suggest that $u_e(F)/u_* \propto Ri_\delta^{-3/2}$.

The earlier dependence on the Reynolds number displayed in Figures 6.7 and 6.8 has disappeared and there is excellent agreement between the experimental data and the high Richardson number model for $Ri_\delta > 5$.

The data has also been plotted in the form $u_e(F)/\overline{U}_0$ versus Ri_δ in Figure 6.10. The result is very similar to Figure 6.9 and this was expected as the ratio $\overline{U}_0/(u_*)_{150}$ is constant for all three flows (Table 5.5). This behaviour support the choice of δ_t and $\overline{U}_0$ as scaling factors for the Richardson number.

6.2.5 The Lengthscale of the Wake Structure behind a Backward Facing Step

The flow over the leading edge of the cavity may be considered to be dominated by the presence of a backward facing step caused by the drop in the interface. Work by Bradshaw and Wong (1972), Nakagawa and Nezu (1987) and others have shown that a complex wake structure exists downstream of the step under most flow conditions. The definitions of perturbation strength by Bradshaw and Wong for a shear layer of depth δ and step height h' suggest that in these experiments the flow over the cavity leading edge constituted a weak perturbation as $h'/\delta \ll 1$. The shear layer depth $\delta \approx h_0$ where h_0 is the depth of the upper layer.

The mean upper layer flow was not uniform across the channel and cavity (Chapter 5) and this caused corresponding variations in the step height across the cavity width (Section 6.3). The largest step height was recorded at the side of the cavity where h' ~ 5-7 mm. At these positions, $h'/\delta \lesssim 0.1$ whereas at the centre of the cavity $h'/\delta \sim 0.02$. As discussed in Chapter 5, the region where h' ~ 5-7 mm is that part of the cavity where a large effective shear stress is present. This

occupies a region of approximately 12% of the cavity area.

A flow over a change in surface roughness is also defined as a weak perturbation (Bradshaw and Wong 1972). The resulting growth of an "internal boundary layer" into the existing original shear layer show that the properties on a given streamline outside the new shear layer remain unaffected. This means that the region of change is the new shear layer down to the rigid surface or in this case, the interface. The lengthscale for the new shear layer should be of the same order as the step height, h'.

The measurements reported by Bradshaw and Wong (1972) are concerned with a strong perturbation. Bradshaw and Wong also reported a new sub-boundary layer which started to grow from the reattachment point. This layer is in local equilibrium and spreads at about the same rate as after a weak perturbation caused by a change of surface roughness. As a comparison, it is assumed that the integral turbulence lengthscale of Bradshaw and Wong can provide a limiting lengthscale L_{max}. That is :

$$L_{max}/\delta = 0.095\ (1-0.3\exp\{-(x-x_r)/40h'\}) \quad ,$$

where x is the downstream distance from the step and x_r is the reattachment length. Substitution of the experimental data into the above expression gives values of L_{max} in the range 5-12 mm.

Another estimate for an integral scale for a wake has been given by Townsend (1976, Table 6.2, p208). Townsend gives the integral scale $L_u \sim \ell_o$ where ℓ_o is a lateral lengthscale. An appropriate ℓ_o in these experiments is the depth of the new shear layer which scales as the step height. Then $\ell_o \sim h'$ and $L_u \sim h'$. Near the side of the cavity $h' \sim 5$-7 mm, so $L_u \sim 5$-7 mm. The values of L_u and L_{max} are of a similar order and are about half the values of δ_t.

The velocity scale for the flow over a backward facing step is the mean velocity scale for the upper layer, that is, $\overline{U}_o$. The turbulence

structure is described using $\bar{U}_o$ as the velocity scale (Bradshaw and Wong).

Re-defining the Richardson number with the scales L_u and L_{max} in place of δ_t will not greatly affect the presentations of data in Figures 6.9 and 6.10. The Richardson number will be approximately halved but the relative positions of the data points will remain the same.

It has been remarked earlier in this discussion that the step height h' ~ 5-7 mm is limited to a region near the sides of the cavity. In the case of a strong perturbation, the influence of the wake structure is felt for a distance up to 50 h' (Bradshaw and Wong). In this case, 50 h' will consume the length of the cavity. However, it has been established that these experimental flows are not strong perturbations but are instead weak perturbations. The scales L_{max} and L_u are associated with a limiting situation and as such are not generally applicable to these experiments.

Over the major part of the cavity width the value of h' ~ 1-3 mm (Section 6.3) and the flow over this region is a weaker perturbation than that occurring at the sides. The lengthscales L_{max} and L_u are not relevant here and a more appropriate scaling factor would be that associated with a weak perturbation. As the major fraction of the shear force is applied in the region of the weak perturbation (Chapter 5), the bulk of the entrainment should also occur there. The scaling parameters should also be relevant to this region.

The other limiting situation would be the case of no change in surface roughness or gross geometrical conditions. The interface would be a continuation of the perspex floor. No new scales would be introduced and the flow over the cavity would be identical to the upstream conditions.

6.2.6 The Lengthscale due to a Change in Surface Roughness

The weak perturbation which occurs for $h'/\delta \ll 1$ when there is flow over a backward facing step is similar, in behaviour, to that which

results from a step change in surface roughness. A new internal boundary layer grows from the step change and the rate of growth of this new layer depends on the relative magnitudes of the two surface roughnesses. If z_{o2}/z_{o1}, where z_{o1}, and z_{o2} are the surface roughness associated with the upstream and downstream conditions of the step change, is much greater than unity, then the growth rate of the new internal layer would be much greater than the upstream boundary layer (for neutral atmospheric conditions considered herein). The resulting lengthscale would also become larger (see Figure 7.4b of Hunt and Simpson 1982). Conversely when z_{o2}/z_{o1} is much less than unity, the new internal boundary layer growth rate is less than the upstream boundary layer growth rate and the lengthscale of the surface roughness would be less. It was noted in 6.2.4 that it was not possible to take measurements over the cavity to determine the (interfacial) roughness and hence it is not known whether this exceeded or was less than the upstream roughness.

Some qualitative comparisons can be obtained by considering the works of Antonia and Luxton (1971, 1972) who studied the response of a turbulent boundary layer to a step change in surface roughness. In a smooth to rough transition Antonia and Luxton (1971) found that the growth of the internal layer δ_{ir} was proportional to $x^{0.79}$ where x is downstream distance. In a rough to smooth transition, Antonia and Luxton (1972) found that $\delta_{is} \propto x^{0.43}$. Note that the growth of δ_{ir} has nearly the same dependence on length as δ_t given in Equation (6.6b), that is, $\delta_t \propto L_1^{0.8}$. The similarity however ends there as the assumptions in arriving at Equation (6.6b) were that the flow was originally a free turbulent shear flow which was incident on a flat plate (at zero incidence angle) and a boundary layer developed over the plate. In that sense, the 'roughness' increased from zero to finite. There is one further consideration with δ_t in that $\delta_t \propto \nu_1^{0.2}$. This dependence is very important as one considers that (ν_1/ν_0), the ratio of kinematic viscosities of dense solution and fresh water can be about 6 at large density difference.

Without this dependence, the data in Figures 6.9 and 6.10 will plot at values of Ri_δ which are approximately 40% smaller. This will shift the entrainment data for $Ri_\delta < 5$ to the left and this data will not correlate as well with the (-3/2) dependence on Richardson number.

This dependence on ν_i is important as the results have shown in Figures 6.9 and 6.10. It may be possible to describe the results for $Ri_\delta < 5$ by some of the other lengthscales already discussed in 6.2. However, as already noted, the scales of L_{max} and L_u are of similar order to δ_t such that using these scales will not greatly alter the presentation of the data. As the kinematic viscosity of the dense solution is significantly higher than the fresh water value, it cannot be ignored and must be included in the entrainment mechanism (Keulegan 1949).

The velocity scale for the change of roughness remains the overall bulk mean velocity $\overline{U}_o$, as for $z > \delta_{ir}$ and $z > \delta_{is}$, the outer layer remains unaffected by the boundary (Hunt and Simpson 1982 and others). Hence the velocity scale does not alter the Richardson number and presentation of data.

6.2.7 The Wave Height as a Lengthscale

For a smooth interface with small amplitude waves, the vertical lengthscale of turbulence is the depth of the new boundary layer over the cavity. In the case of larger amplitude waves at the interface as described in Section 6.3 for small Richardson number, the wave amplitude 2a may be nearly equal to δ_t. Hence either 2a or δ_t may be used as the relevant lengthscale.

A number of experiments were carried out in shorter cavities and the corresponding value of δ_t was also smaller. However, as discussed in Appendix K, the wave height 2a exceeded the value of δ_t and hence 2a should be used as the lengthscale. This difference in choices of lengthscale is consistent with boundary layer theory. For flow over a smooth surface, turbulence scales with the boundary layer depth δ_t and for

flow over a rough surface, the turbulence also scales with the boundary layer depth but, in this case, a direct measure of roughness is available as the wave height. Hence 2a is the vertical lengthscale of turbulence.

6.3 Observations of the Density Interface

The application of a shear stress at the density interface resulted in a train of progressive waves at the interface, the tilting of the interface and regions of recirculating flow at the upstream and downstream ends of the cavity. This section describes these observations and the variation of behaviour with Richardson number.

6.3.1 The Behaviour of the Density Interface

6.3.1.1 *Observations of Interfacial Waves*

At very small Richardson number, the entrainment of the saline solution by the upper layer appeared like a scouring process. The interfacial region was very chaotic with intense mixing and saline solution being thrown upwards and forwards from the crests of wave-like structures. At $Ri_\delta \sim 0.6$ where $\frac{\Delta\rho}{\rho_o} = 0.0282$ and $\overline{U}_o = 0.0813$ m/s, the interface appeared like the sketch in Figure 6.1. The interface would become unstable due to the velocity shear and waves would form and move downstream with the upper mean flow. These waves appeared like the Kelvin-Helmholtz (K-H) instability (Thorpe 1971, Thorpe 1973, Turner 1973 and others) but did not roll up as expected. Rather, as the crest started to roll, the velocity shear of the upper layer dragged the crest forward until thin wisps or filaments of fluid were broken off. The turbulence and the velocity shear in the upper layer eroded this instability and prevented the roll up process from continuing to the K-H billows. The appearance of the wave-like structures could also be interpreted as rotating eddies or vortices scouring the interface. The interfacial region appeared similar to that shown in Figure 9.2 of

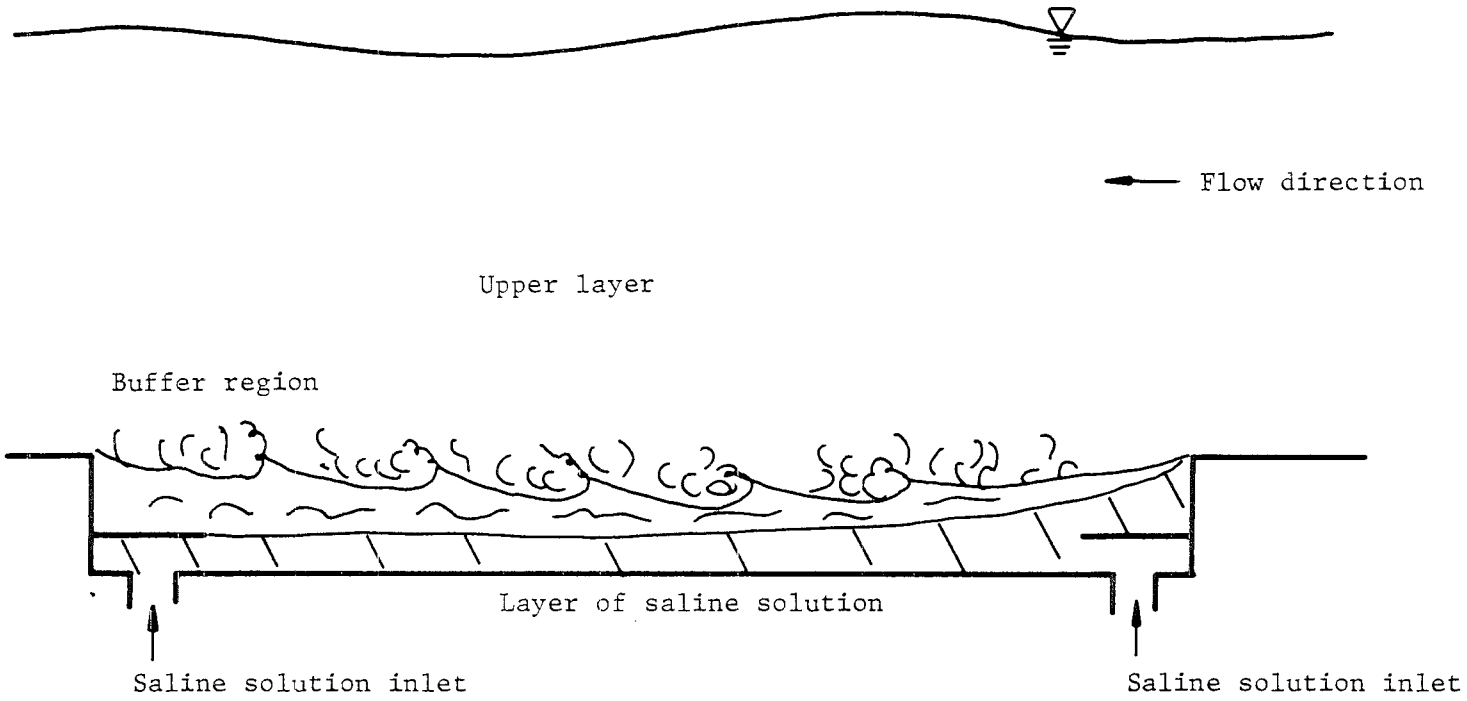

Figure 6.1 : Sketch of Interfacial Region : $Ri_\delta = 0.6$, $\frac{\Delta\rho}{\rho_0} = 0.0282$, $\bar{U}_o = 0.0813$ m/s

Turner's (1973) monograph except that a mean velocity transported the ejected filaments of saline solution away.

The saline solution on the bottom of the cavity and the upper layer were separated by a buffer layer of intermediate density. This buffer layer was very thin at the upstream end of the cavity, of order 1 mm. However, the buffer layer became thicker with distance downstream and was about 25 mm thick at the opposite end of the cavity. Correspondingly the layer of saline solution was about 25 mm deep at the upstream wall but this was reduced to about 5 mm deep at the downstream end.

For $\frac{\rho_i}{\rho_o} = 1.0486$, $\overline{U}_o = 0.0813$ m/s and $Ri_\delta = 1.05$, the mixing was less intense than the previous experiment. The interface remained sharp and supported a train of progressive waves as shown in Figure 6.2a. Wisps of saline solution were ejected from the wave crests and carried downstream in a manner similar to that which has also been observed by Keulegan (1949), Ellison and Turner (1959), Lofquist (1960) and others. The ejection of the wisps of saline solution was the result of the breaking interfacial waves (Thorpe 1968). The observed waves had narrow sharp crests and broad troughs and have also been observed in the ocean (Turner 1973, Figure 3.1). The shape of the interfacial waves depended on the ratio of layer depths (Thorpe 1968). The narrow part of the wave always pointed into the deeper layer (Turner 1973).

The wavetrain in Figure 6.2a also shows a disturbance at the downstream (left-hand) end. This is a result of the reflected wave interacting with the incident wave. The height difference between the trough and the crest is of order 10 mm. Figure 6.2a shows the wave structure at 50 mm from the side of the cavity and near the region of high effective shear stress. The periodic step height h' from the interface to the leading edge of the cavity in Figure 6.2a is about 5 mm. However, towards the centre of the cavity this value of h' reduces to about 1 mm where the shear stress is much less.

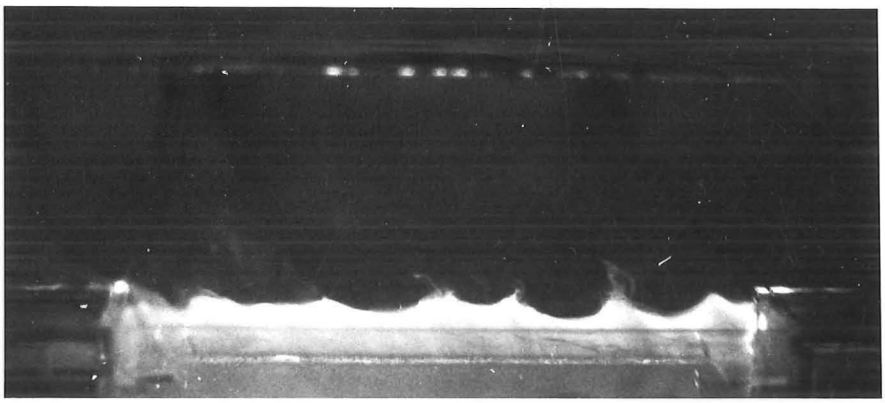

Figure 6.2a : View of Interfacial Wave Region at 50 mm from Cavity Side : Ri_δ = 1.05, $\Delta\rho/\rho_0$ = 0.0486, $\bar{U}_o$ = 0.0813 m/s

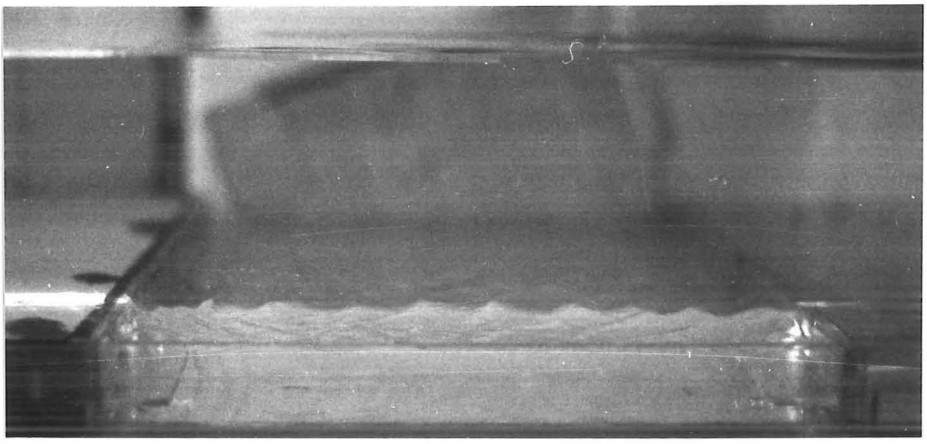

Figure 6.2b : View of Interfacial Wave Region at 100 mm from Cavity Side : Ri_δ = 2.76, $\Delta\rho/\rho_0$ = 0.124, $\bar{U}_o$ = 0.0813 m/s

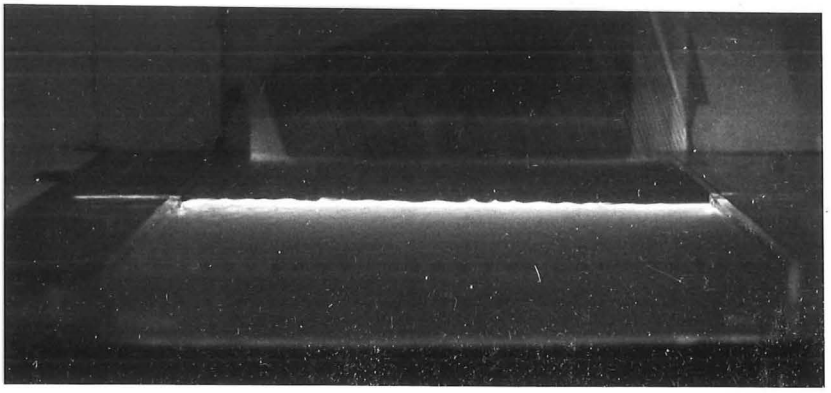

Figure 6.2c : View of Interfacial Wave Region at the Centre of the Cavity Region : Ri_δ = 7.95, $\Delta\rho/\rho_0$ = 0.2516, $\bar{U}_o$ = 0.0732 m/s

A similar wave pattern (Figure 6.2b) resulted from a higher density ratio of $\frac{\rho_1}{\rho_o}$ = 1.124 and Ri_δ = 2.76. The wave amplitude and length were reduced but the sharp crests and broad troughs remained. Although not shown, wisps of saline solution were ejected from the wave crests and transported by the upper layer flow. The reflected wave distorted the wave at the downstream end as in the case of Ri_δ = 1.05 (Figure 6.2a). The wave structure was observed at a distance of 100 mm from the side of the cavity.

Figure 6.2c shows the wavetrain at the centre of the channel for Ri_δ = 7.95. The density ratio was $\frac{\rho_1}{\rho_o}$ = 1.2516 and $\overline{U}_o$ = 0.0732 m/s. The wave dimensions are much reduced from the experiments at smaller Richardson numbers with some sharp crests and some rounded crests. Wisps of saline solution were being thrown upwards occasionally.

A Ri_δ = 15.39 experiment was carried out with $\frac{\rho_1}{\rho_o}$ = 1.39 and $\overline{U}_o$ = 0.0732 m/s. The interface was almost smooth except for a wavetrain with rounded troughs and crests. The wave height was about 1-2 mm. The viscosity of saline solution was over six times that of fresh water (Weast 1975). Review of video-tape recordings showed that the cavity downstream wall did not affect the wave behaviour in a significant manner.

6.3.1.2 *Comparison of Observations with Theory*

The observed interfacial wavelength and phase velocity are compared with:

(i) The Kelvin-Helmholtz instability which gives the unstable wavelength as:

$$\lambda_c(1) = \frac{2\pi\ \overline{U}_o^2}{g} \quad \frac{1}{\frac{\Delta\rho}{\rho_1}\left[1 + \frac{\rho_1}{\rho_o}\right]} \qquad (6.8)$$

and the phase speed:

$$c(1) = \overline{U}_o \Big/ \left[1 + \frac{\rho_1}{\rho_o}\right] \quad . \tag{6.9}$$

(ii) The results of the hypothesis that the phase speed of the interfacial waves is equal to the velocity of the upper layer, that is:

$$c(2) = \overline{U}_o \tag{6.10}$$

and the unstable wavelength is:

$$\lambda_c(2) = \frac{2\pi\ \overline{U}_o^{\,2}}{g\ \frac{\Delta\rho}{\rho_1}} \tag{6.11}$$

The derivations of Equations (6.8) to (6.11) are given in Appendix F.

The observed range of values of λ_c are shown in Figure 6.3 which also includes the curves corresponding to Equations (6.8) and (6.11). These curves are derived from three different values of $\overline{U}_o$ hence a standard deviation of 3% about these curves will represent all the possible values of $\lambda_c(1)$ and $\lambda_c(2)$ over the range of Ri_δ. At small Richardson number, the values of λ_c are close to the solution of $\lambda_c(1)$. This is consistent with the Kelvin-Helmholtz criterion which is valid for small $\frac{\Delta\rho}{\rho_o}$ and small Ri_δ. At larger Ri_δ, the observed λ_c approach $\lambda_c(2)$ although some observations of small values of λ_c have been recorded. These two theoretical results may be considered to provide upper and lower bounds for the interfacial wavelength.

Some estimates of the phase speed were also made during experiments and from video-tape recordings. These estimates have been

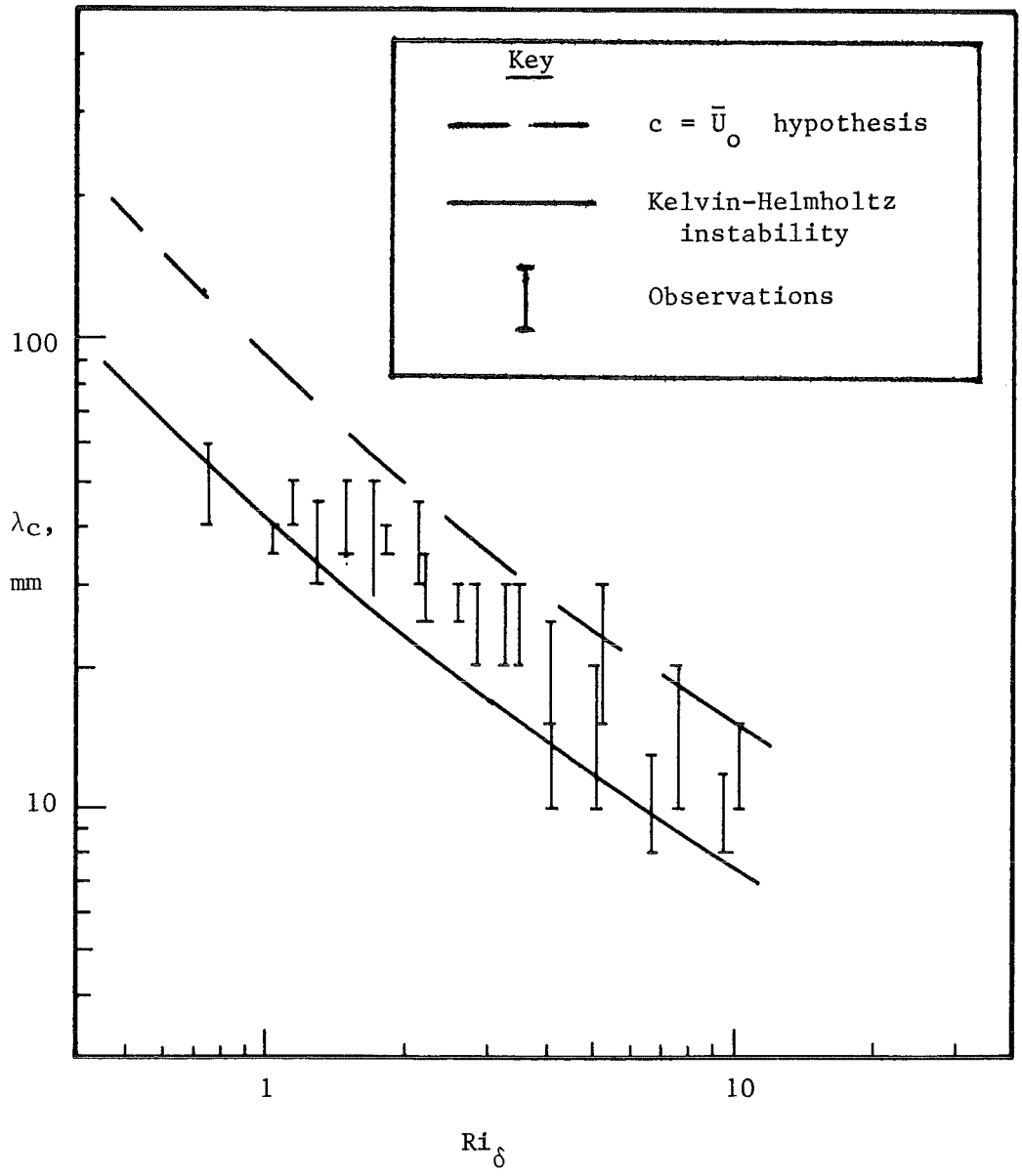

Figure 6.3 : Observed Interfacial Wavelengths
(Same as Figure F-3)

plotted in Figures 6.4 and 6.5 which also include the curves from Equations (6.9) and (6.10). Figure 6.4 shows the data from flows with $\overline{U}_o$ = 0.0732 m/s and $\overline{U}_o$ = 0.0813 m/s while Figure 6.5 shows data from the flow with $\overline{U}_o$ = 0.0909 m/s. There were only a small number of results and most of them fall between the two inviscid results. However, the above suggestions can be extended to also provide upper and lower bounds for the phase velocity of the interfacial waves.

The bottom of the cavity was found not to affect the interfacial waves so these were similar to deep water waves. The details of this discussion are also presented in Appendix F.

6.3.2 **The Influence of the Cavity Endwalls**

The walls of the cavity not only contained the saline solution but also balanced the shear stress applied by the upper layer. An immediate observation was the tilt or slope of the interface. The tilting of the interface created the periodic backward facing step at the upstream end of the cavity discussed earlier. This backward facing step enabled regions of recirculating flow to form at the upstream end of the cavity. A smaller recirculating flow region formed periodically at the downstream end. These effects are now discussed.

6.3.2.1 *The Slope of the Density Interface*

The observed slope of the interface was compared with an ideal estimate of the slope in Appendix G. The ideal estimate ignored the interfacial waves, sidewall stresses, secondary velocities, and the entrainment of the heavier fluid. The observed slope was estimated from photographs of the interface at the side of the cavity and compared with the calculated slope at the 260 mm station. The results of the experiments of Figures G-3a,b,c have been listed in Table G-1. Also listed are the calculated slopes at the 260 mm station. The observed slopes were 4 to 5 times the calculated slopes and this difference has

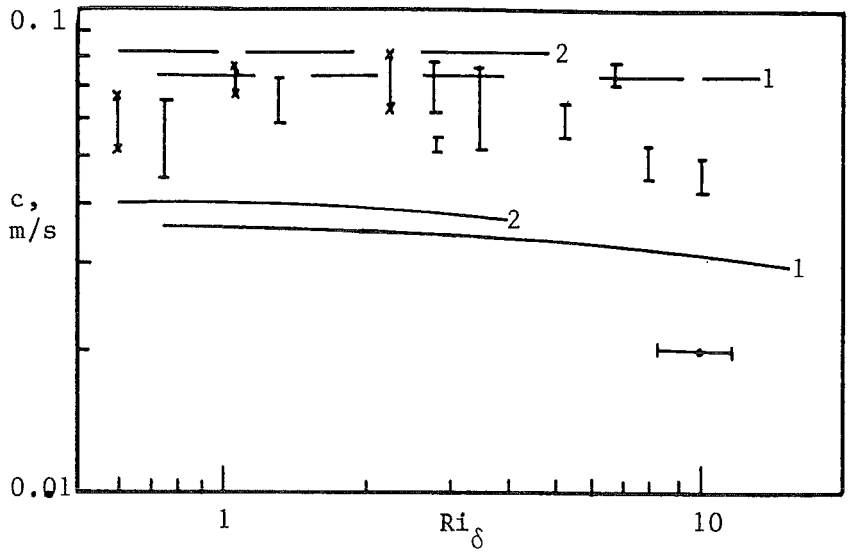

Figure 6.4 : Observed Values of Phase Velocity of Interfacial Waves, $\bar{U}_o$ = 0.0732 m/s and $\bar{U}_o$ = 0.0813 m/s. (Same as F-4).

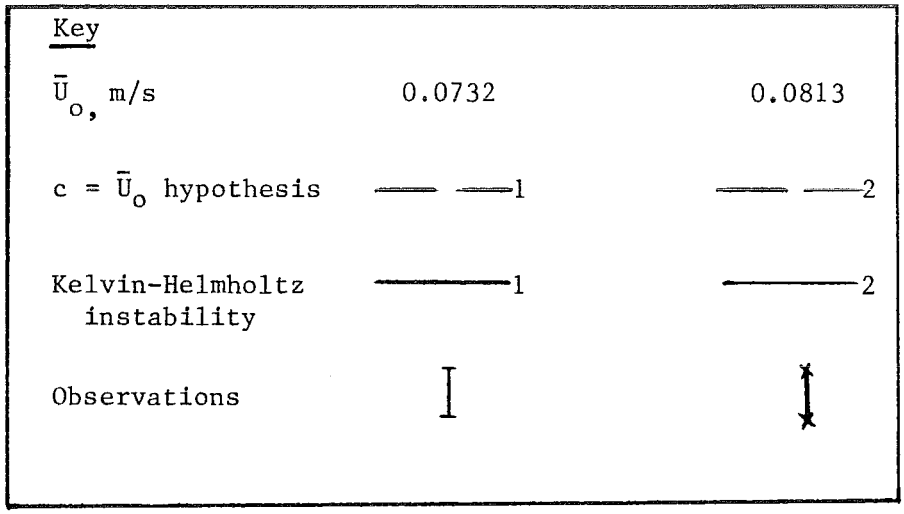

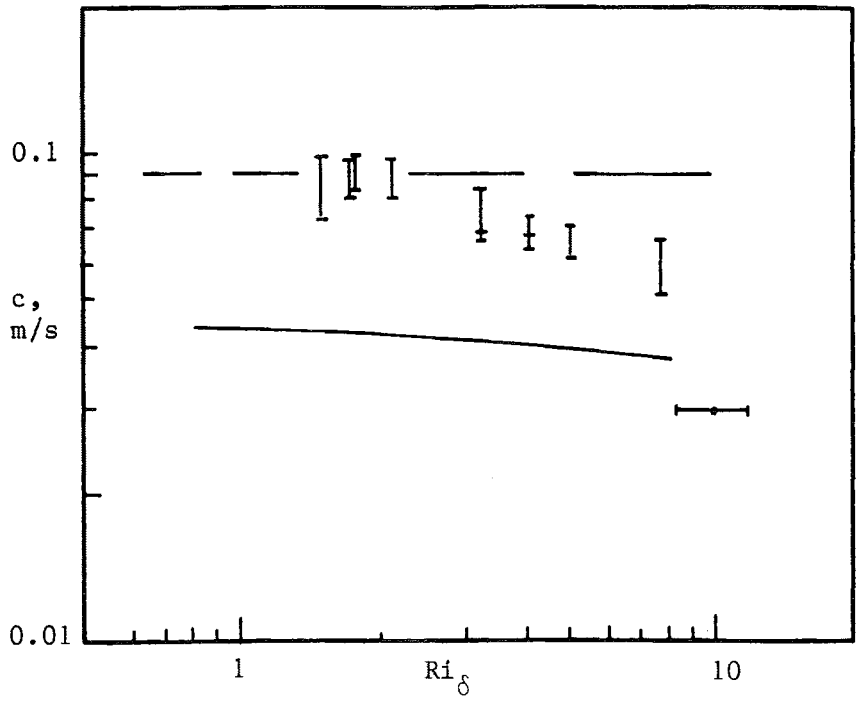

Figure 6.5 : Observed Values of Phase Velocity of Interfacial Waves, $\bar{U}_o$ = 0.0909 m/s. (Same as Figure F-5).

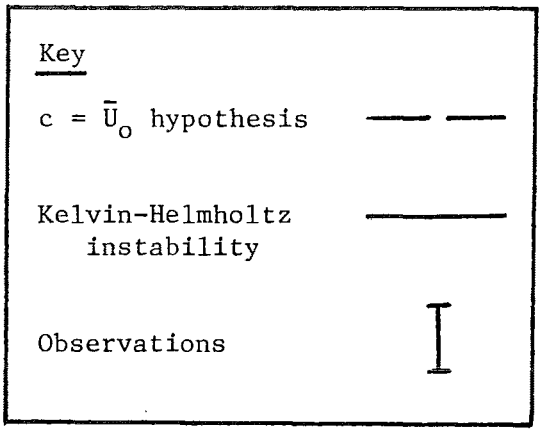

been attributed to the relatively large effective surface shear stress at the sides of the cavity and channel. The side of the cavity is 35 mm from the 260 mm station in the direction of the channel side. The background to this flow situation has been discussed in detail in Chapter 5.

6.3.2.2 *The backward facing step*

The tilting of the interface created a backward facing step of height h' at the upstream end of the cavity. There were three important observations in regard to the step. These were :

(i) the periodic nature of the step,

(ii) the magnitude of the mean step height, and

(iii) the variation of h' across the cavity.

The periodic nature of the step was a direct result of the wavetrain at the interface. At small values of Ri_δ, it was difficult to distinguish the wave amplitude from the actual step as in Figure 6.2a. The wavetrain on the interface is also shown at larger Ri_δ in Figures G-3a,b. These photographs were taken at the side of the cavity and show that h' ~ 5-7 mm. The wave amplitude was approximately 1-2 mm. Figure G-3c was also taken at the side of the cavity. The step height was of order 5 mm. From Figures 6-2a,b,c and G-3a,b,c and observations, the value of h' did not vary greatly with Ri_δ even though Equation (g-21) suggests that the interfacial slope and hence h' should be inversely proportional to the Richardson number. The small variation of h' with Richardson number can be attributed to the presence of interfacial waves.

The flow structure across the channel and cavity had a differential effect on the step height at various lateral positions. The high effective shear stress near the side of the cavity caused a step height h' ~ 5-7 mm as discussed earlier. At the 150 mm station, the

applied shear stress was reduced and correspondingly h' ~ 2-3 mm. At the centre of the cavity, the step height was approximately 1-2 mm. The step height h' is directly proportional to the value of τ_o and under ideal conditions of no interfacial waves, the variation of h' across the cavity should be similar to the variation of τ_o. This variation was observed and as discussed above, the large values of h' were confined to regions near the cavity sides.

The flow over the backward facing step of height h' has some similarities with the work of Bradshaw and Wong (1972), Nakagawa and Nezu (1987) and others. However, the above-mentioned publications were concerned with the wake region of a homogeneous fluid flowing over a rigid stepped boundary whereas in this work, the upper layer of fluid, though homogeneous, flowed over a rigid leading edge onto a more dense fluid in a cavity. The interface of the two fluids acted as a flexible, porous and sloping boundary with a step height which varied with time.

The regions of flow separation and recirculation at the leading edge reported by Bradshaw and Wong (1972) and others were also present in these experiments. However by applying the definition of the perturbation strength of Bradshaw and Wong, the flow over the step in these experiments would be classified as a 'weak perturbation' due to $h'/h_o \ll 1$ where h_o is the depth of the upper layer. Note that in these experiments the boundary layer depth $\delta \sim h_o$. Under these conditions, the length and velocity scales are altered without significant change in the dimensionless properties of the turbulence structure.

6.3.2.3 *Local Regions of Recirculating Flow*

The regions of recirculating flow were continually present although these were unsteady at the upstream end of the cavity and periodic at the downstream end of the cavity. The unsteady region at the upstream end was due to the presence of an interfacial wavetrain. The length of the recirculating region was 2-5 cm at the upstream end and 1-2

cm at the downstream end. These lengths are relevant to the flow at the side regions of the cavity where there is a high effective shear stress. Towards the centre of the cavity where τ_o was much less, the step height was small (6.3.2.2) and the corresponding length of the recirculating region would be reduced. The large recirculating regions at the side of the cavity affect about 12% of the area and are not considered to be a major influence on the entrainment of dense solution from the cavity. Further discussion is presented in Appendix H.

6.3.3 The Lateral Structure of the Interfacial Waves

The unusual mean velocity structure across the channel described in Section 5.2.3, whereby the mean velocity was higher at the sides of the channel than at the centre of the channel, caused a similarly unusual wave pattern across the interface. The wave crests near the sides of the channel travelled faster than the wave crests in the middle of the channel. This behaviour was in agreement with the mean velocity structure across the channel (Figures 5.3 a,b,c). Figure 6.6a shows the interfacial wave structure across the channel for $Ri_\delta = 1.77$. The central part of the wave crest is observed to be behind the wave crest at the sides of the channel. The mean flow direction is from right to left and the thin slit of light is illuminating the centre of the channel. Figure 6.6b is a sketch of the lateral structure of the interfacial waves showing a higher phase speed near the channel sides than at the centre. This general pattern was observed in all the experiments.

6.4 The Measurements of Flux Entrainment Velocity

The average flux entrainment velocity is given by:

$$u_e(F) = \frac{V_o}{A_i} \times \frac{1}{\Delta\rho}\overline{\left[\frac{\rho_o(t+T) - \rho_o(t)}{T}\right]} \qquad (6.12)$$

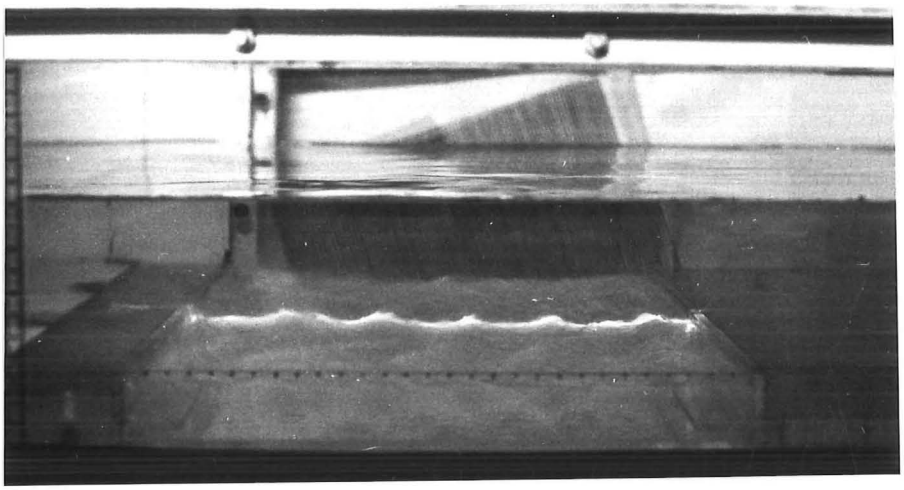

Figure 6.6a : View of Wave Structure across Channel :
$Ri_\delta = 1.77$, $\Delta\rho/\rho_0 = 0.1014$, $\bar{U}_o = 0.0909$ m/s

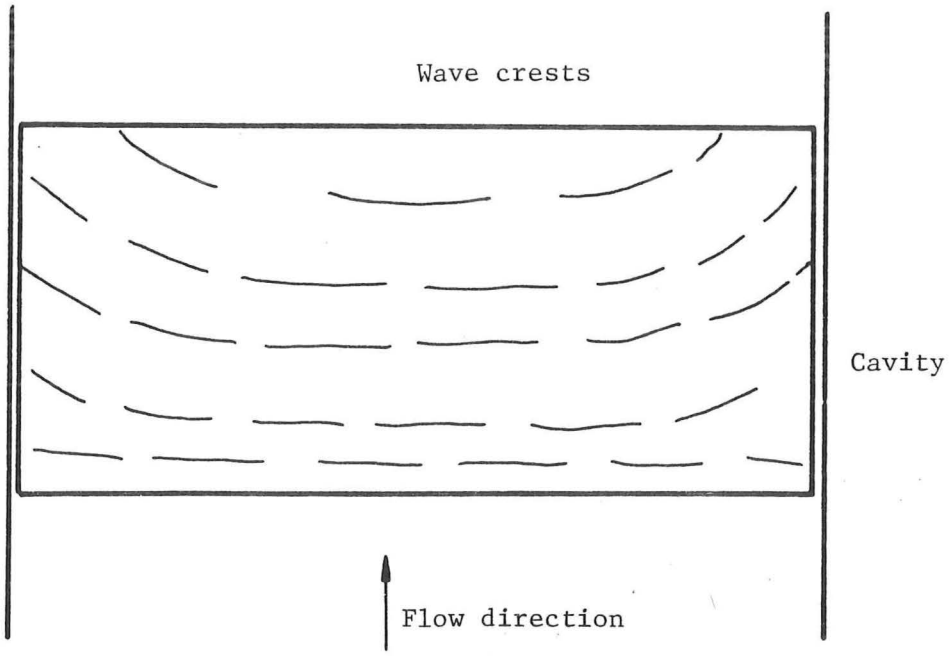

Figure 6.6b : Sketch of Interfacial Wave Pattern across Channel

where V_o is the volume of water in the recirculating system at the beginning of the experiment, A_1 is the area of the cavity opening, $\rho_o(t)$ is the density of the upper layer water at time t, and $\rho_o(t+T)$ is the density at time (t+T). The time T is that required to recycle V_o and $\Delta\rho = \rho_1 - \rho_o$ before the experiment. The derivation of Equation (6.12) is given in Appendix I. The overbar in Equation (6.12) indicates that $u_e(F)$ is a time as well as a space average.

The experiments have been analysed and the entrainment velocity $u_e(F)$ has been evaluated with Equation (6.12). The results have been non-dimensionalised with u_* and plotted in three ways against Ri_*, Ri_h and Ri_δ. These results are presented in the rest of this section. Appendix J tabulates all the entrainment data of this section.

6.4.1 Scaling with Ri_*

The entrainment data have been plotted in the form $E_* = \frac{u_e(F)}{u_*}$ versus Ri_* in Figure 6.7. The range of Richardson numbers is $0.6 \lesssim Ri_* \lesssim 14$. There is a considerable amount of scatter in the data although each set of data points follows a $E_* \propto Ri_*^{-3/2}$ relation. The data obtained from the calcium chloride experiments require a smaller coefficient of proportionality than the data from the sodium chloride experiments. The data also shows that the experiments which were conducted with u_* = 0.0105 m/s were located below the data obtained with lower values of u_*. Figure 6.7 shows that although each data set which is a function of u_* and the type of salt used follow $E_* \propto Ri_*^{-3/2}$, the scaling factors are insufficient to collapse all the data onto a single curve. Hence the combination of z_o and u_* is not considered to be a suitable set of scaling factors.

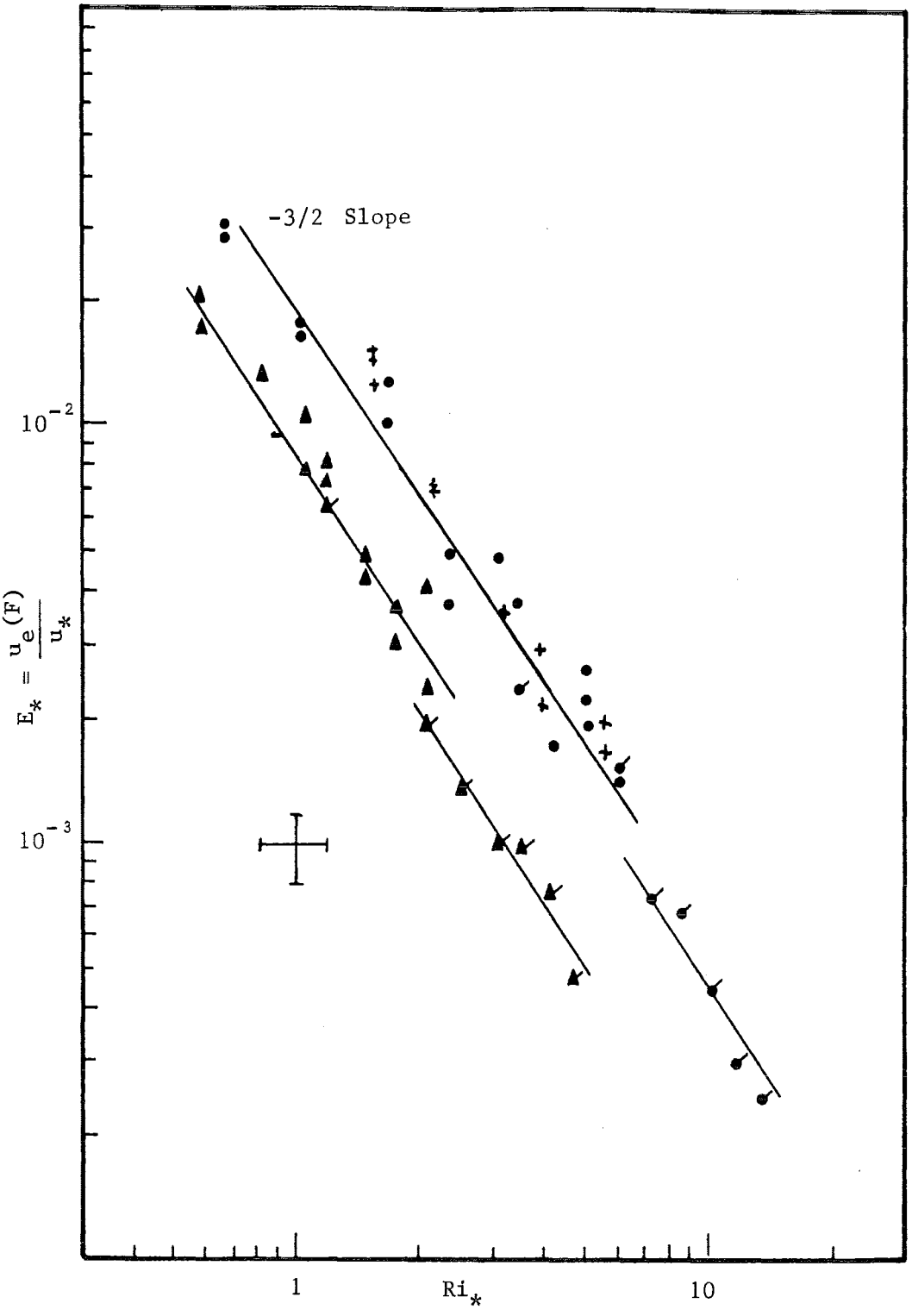

Figure 6.7 : Entrainment Data : E_* vs. Ri_*

Key

	Solute	
$\bar{U}_o$, m/s	NaCℓ	$CaCℓ_2$
0.0732	●	◖
0.0813	+	
0.0909	▲	◣

6.4.2 Scaling with Ri_h

The entrainment data has been plotted in Figure 6.8 in the form E_* versus Ri_h. While there is considerable scatter in the data, Figure 6.8 is not an improvement on the distribution of Figure 6.7. The data follows a $E_* \propto Ri_h^{-3/2}$ relation rather than the $E_* \propto Ri_h^{-1}$ relation which is predicted by the mixed layer models (Sherman, Imberger and Corcos 1978, Spigel Imberger and Rayner 1986 and others). Figure 6.8 shows that the combination of h_o and u_* is not a suitable set of scaling factors even though this is also an entrainment experiment.

6.4.3 Scaling with Ri_δ

The entrainment data has been plotted in the form E_* versus Ri_δ in Figure 6.9. The scatter which was present in Figures 6.7 and 6.8 has now been reduced, and the data points lie within the bounds of experimental error. The data can be represented by the relation:

$$E_* = 0.016\ Ri_\delta^{-3/2} \pm 25\% \qquad (6.13)$$

for $0.6 \lesssim Ri_\delta \lesssim 16$. Figure 6.9 shows that δ_t and $\overline{U}_o$ are suitable scaling factors for the Richardson number. Note that for $Ri_\delta > 8$, the correlation of Equation 6.13 is excellent. This high Richardson number model agrees well with the data. However for $Ri_\delta < 4$, there is variation between the data and Equation (6.13). Also note that the dependence on Reynolds number which was exhibited in Figures 6.7 and 6.8 has been removed. At $Ri_\delta \sim 0.5$ there is a large deviation of the model from the data and this is to be expected as δ_t will not be a suitable scaling parameter.

The data can be rearranged in the form $\overline{E} = \dfrac{u_e(F)}{\overline{U}_o}$ versus Ri_δ as shown in Figure 6.10. In this form the data can be compared with the scaling laws, Equations (2.13) and 2.14) as suggested by Christodoulou

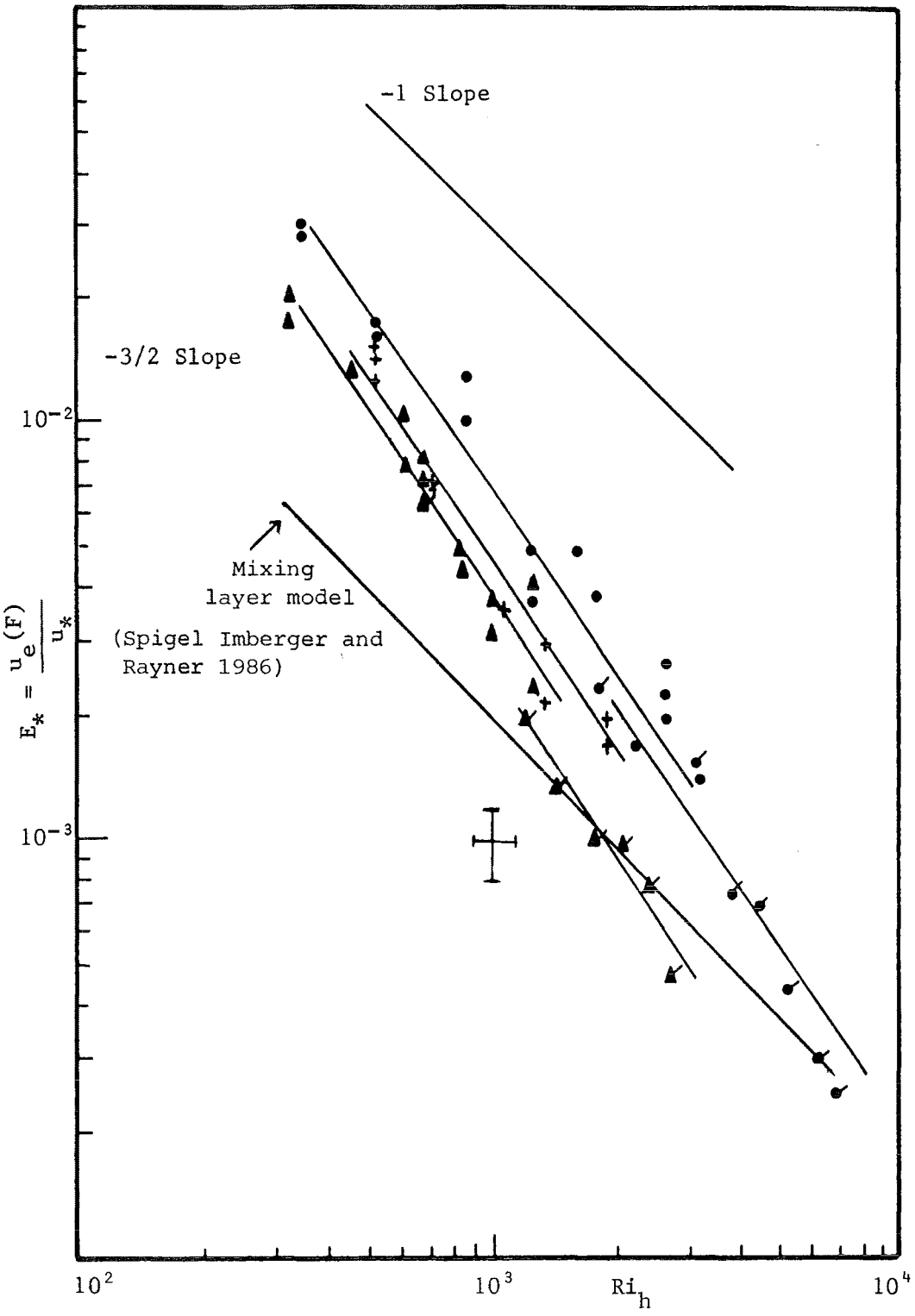

Figure 6.8 : Entrainment Data : E_* vs. Ri_h

Key

	Solute	
$\bar{U}_o$, m/s	NaCℓ	$CaCℓ_2$
0.0732	●	●
0.0813	+	
0.0909	▲	▲

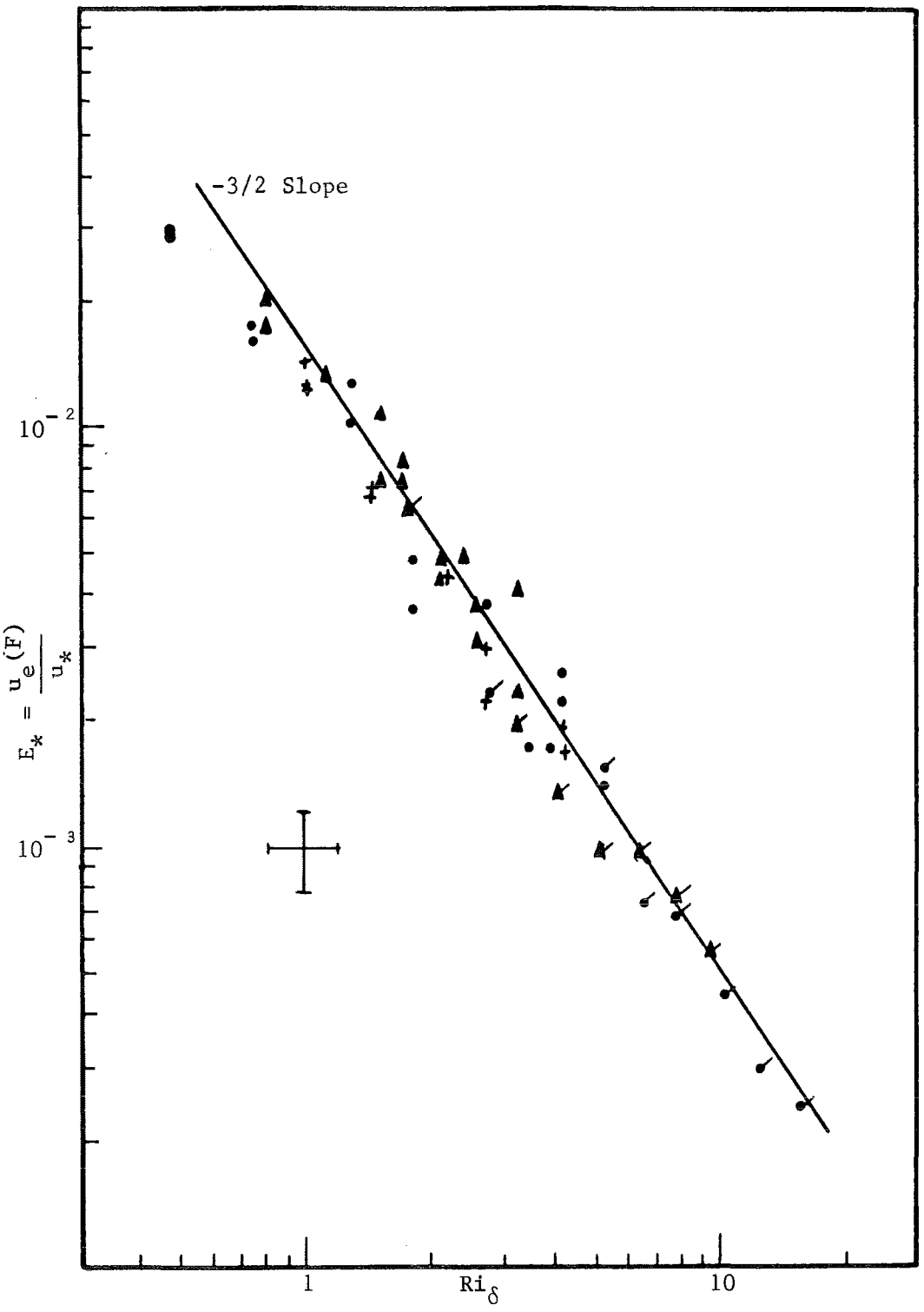

Figure 6.9 : Entrainment Data : E_* vs. Ri_δ

Key	Solute	
$\bar{U}_o$, m/s	NaCℓ	$CaCℓ_2$
0.0732	●	●
0.0813	+	
0.0909	▲	▲

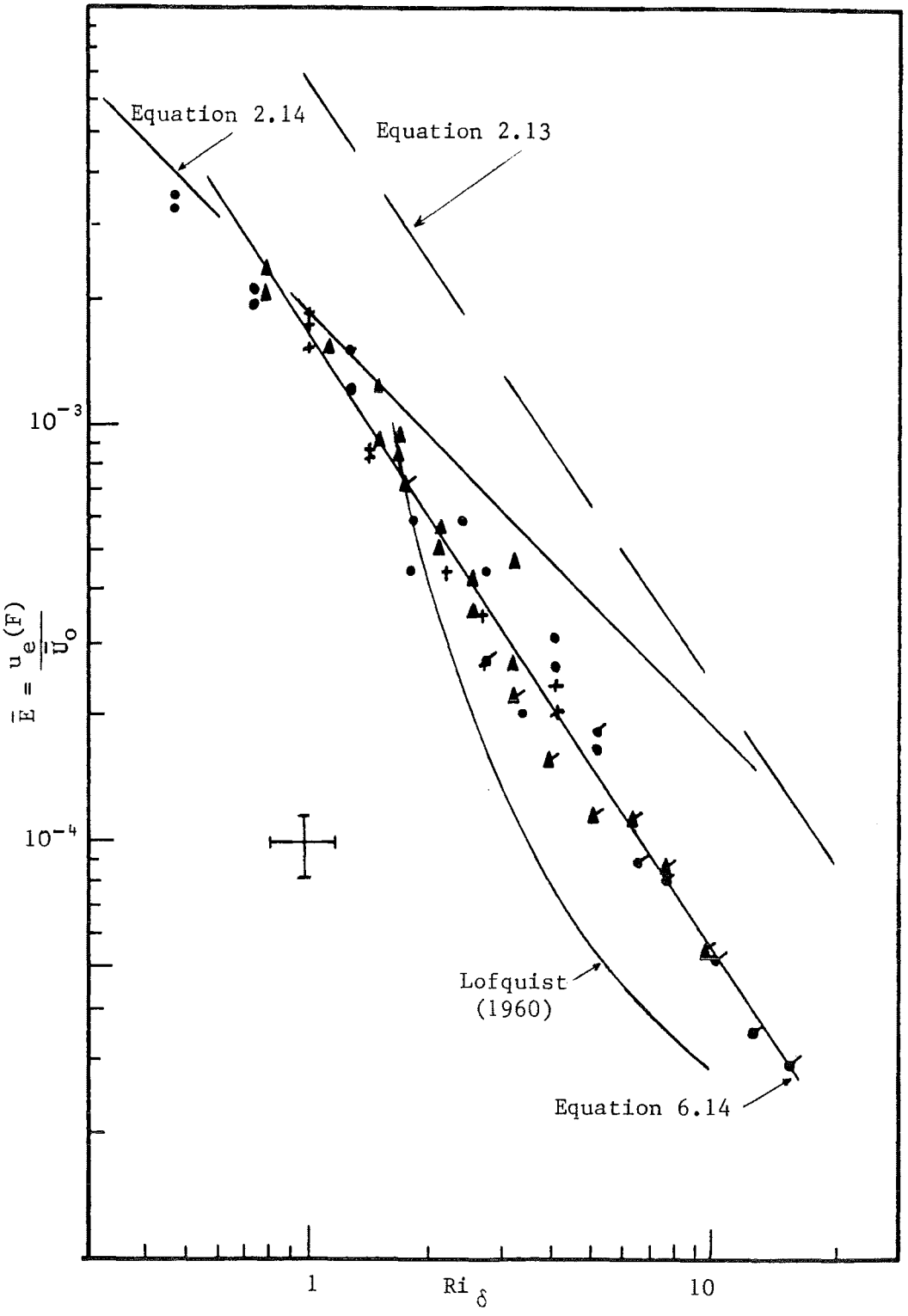

Figure 6.10 : Entrainment Data : $\bar{E}$ vs. Ri_δ

Key	Solute	
$\bar{U}_o$,m/s	NaCℓ	$CaCℓ_2$
0.0732	●	●
0.0813	+	
0.0909	▲	▲

(1986). The curves representing these equations have also been included in Figure 6.10. The experimental data of Figure 6.10 is similar to Figure 6.9 in that all the data points lie within the bounds of experimental error. The data in Figure 6.10 can be represented by the relation:

$$\overline{E} = 0.0018\ Ri_{\delta}^{-3/2} \quad \pm 25\% \qquad (6.14)$$

for

$$0.6 \lesssim Ri_{\delta} \lesssim 16 \quad .$$

6.4.4 **Comparison of Experimental Data with Other Data and Models**

The variation of the non-dimensional flux entrainment velocities E_* and $\overline{E}$ with Richardson number has been observed to follow a (-3/2) relation (Figures 6.9 and 6.10). This behaviour was observed by Turner (1968) in early grid stirring experiments with no mean velocity. This behaviour has also been observed by others for high Peclet number mixing across a density interface and is supported by Linden's (1973) mechanistic model. In a tank containing a layer of brine below a layer of freshwater, Linden propelled a vortex ring of lengthscale ℓ and velocity u at the density interface and observed the depth of indentation of the interface, the change of vortex lengthscale, and estimated the timescale for the recoil of the interface. Linden assumed that the turbulent kinetic energy was stored temporarily as potential energy in the distorted interface. Upon recoil of the interface, the rate of release of potential energy is equated to the rate of increase of potential energy of the upper layer and the non-dimensional entrainment rate $\frac{u_e}{u}$ was found to be proportional to the Richardson number to the (-3/2) power. Linden (1973) in a footnote, pointed out that a vortex ring can excite waves of length $\lambda \sim \ell$, and if the ejection of fluid into the upper layer is caused

by breaking of by breaking of these waves, then the interface has the same timescale as these waves. The kinetic energy available for mixing is the same as the vortex ring model.

Later grid stirring experiments reported by E and Hopfinger (1986) and others support Turner's (1968) observations and Linden's (1973) model but others, including Long (1978), have produced a model which led to $E_* \propto Ri^{-7/4}$. Turner (1986) notes that the controversy over the different views will continue for sometime. Reviews of grid stirring experiments have been given by E and Hopfinger (1986) and Turner (1986).

The observations of these experiments show that for $Ri_\delta \gg 1.0$ the breaking of the interfacial waves with the resultant ejection of fluid from the crests is the entrainment mechanism. Christodoulou (1986) describes the turbulent entrainment for $Ri_o \gg 1$ as due to a combination of the cusp and massive convolutions, the latter of which is interpreted by Hunt, Rottman and Britter (1984) as the engulfing mechanism. The cusp entrainment mechanism is that observed by Crapper and Linden (1974, Figure 3b,c) at large Peclet numbers. These experiments were of the grid stirring type with both layers being stirred and turbulent. The wave breaking mechanism which has been observed in the current experiments look like the cusps of Crapper and Linden (1974) except that the waves were moving with the flow. The measurements of entrainment shown in Figure 6.10 and represented by Equation (6.14) lie below the curve given by Equation (2.13). The coefficient of Equation (2.13) is nearly four times larger than the coefficient of Equation (6.14). This apparent large difference can be explained by consulting Figure 2.4 of this work or Figure 5 of Christodoulou (1986). Most of the referenced data lie below the curve given by Equation (2.13). The coefficient in that equation could have been chosen to be in the range 0.002-0.007 without any large inaccuracies being introduced for $1 < Ri_o < 100$. This is a result of the deviations in the data caused in part by the use of different experimental equipment.

The study by Lofquist (1960) of a saline current flowing under a quiescent freshwater layer in a long (30 metres) channel is similar to the current experiments except that there were no cavity ends and the lower layer was in motion. The data of Lofquist (1960) has been represented by a single curve on Figure 6.10 and is located near the current data for $Ri_\delta = 2$. For $Ri_\delta > 2$, the curve falls below the current data. The values of $\overline{E}$ from Lofquist (1960) are approximately half of those obtained in this work. These results show that for the finite length cavity of these experiments and the associated endwalls, the entrainment rate is approximately double the rates obtained by Lofquist (1960) for a full length cavity for $2 < Ri_\delta < 16$.

6.4.5 Entrainment Results from a Shorter Cavity

A small number of experiments were conducted in two shorter cavities, one of 30 mm and the other of 90 mm. Both of these cavities were the same width as the large cavity, that is, 587 mm. The results for both cavities are shown in Figure 6.11 for E_* versus Ri_a and in Figure 6.12 for $\overline{E}$ versus Ri_a, where $Ri_a = g' \frac{2a}{\overline{U}_o^2}$ and 2a is twice the wave amplitude. The data from the 90 mm cavity shown in Figure 6.12 fall close to the curve given by Equation (6.14) and can also be represented by Equation (2.14). The $\overline{E}$ data from the 30 mm cavity display a Ri_a^{-1} trend and are not well represented by Equation (6.14). The data of the 30 mm cavity corresponding to $\overline{U}_o = 0.0909$ m/s are located near the data from the 90 mm cavity but the data corresponding to $\overline{U}_o = 0.0732$ m/s are nearly an order of magnitude less.

The results of experiments on shorter cavities have shown that the reduction of the length from 290 mm to 90 mm has not greatly affected the entrainment of the dense saline solution. However, a further reduction in length to 30 mm has shown that Equation (6.14) is no longer suitable for estimating the entrainment. Further observations of the experiments

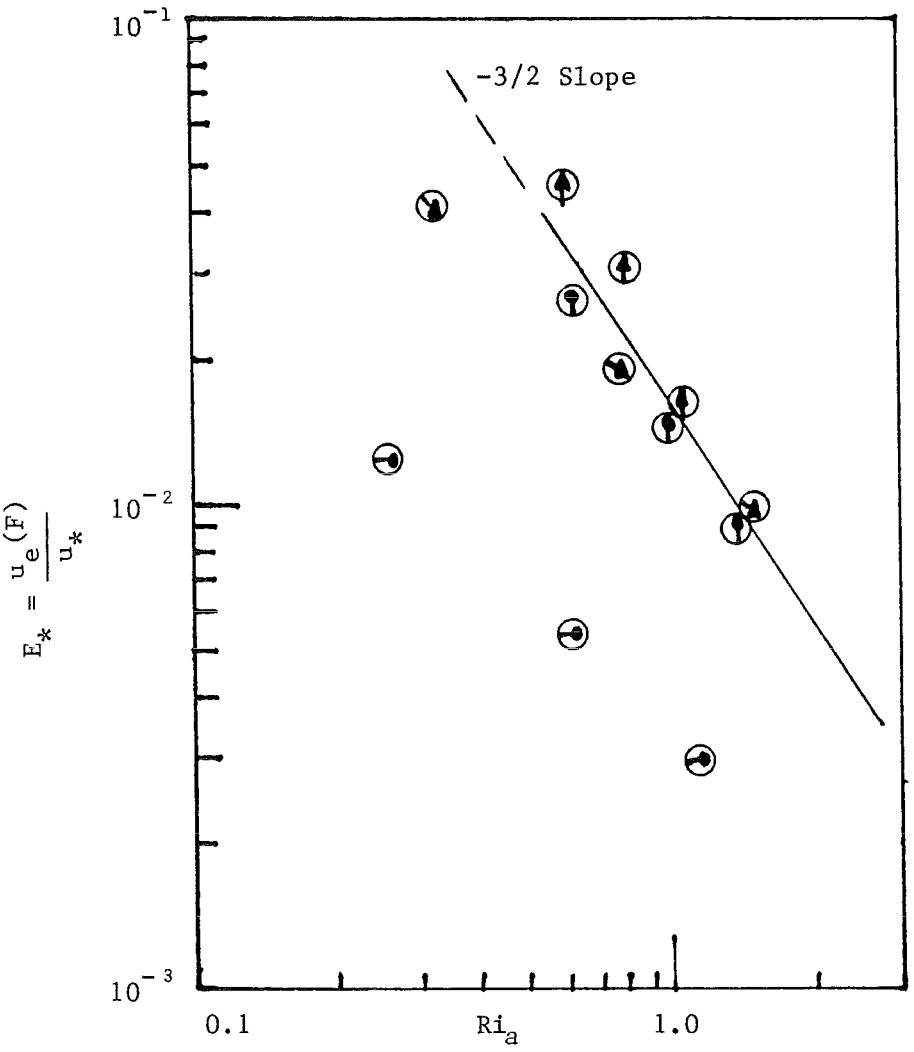

Figure 6.11 : Entrainment Data - 90 mm and 30 mm Cavities : E_* vs. Ri_a

(same as Figure K-3)

Key		
$\bar{U}_o$, m/s	30 mm Cavity	90 mm Cavity
0.0732	⊙	⊙
0.0909	⊙	⊙

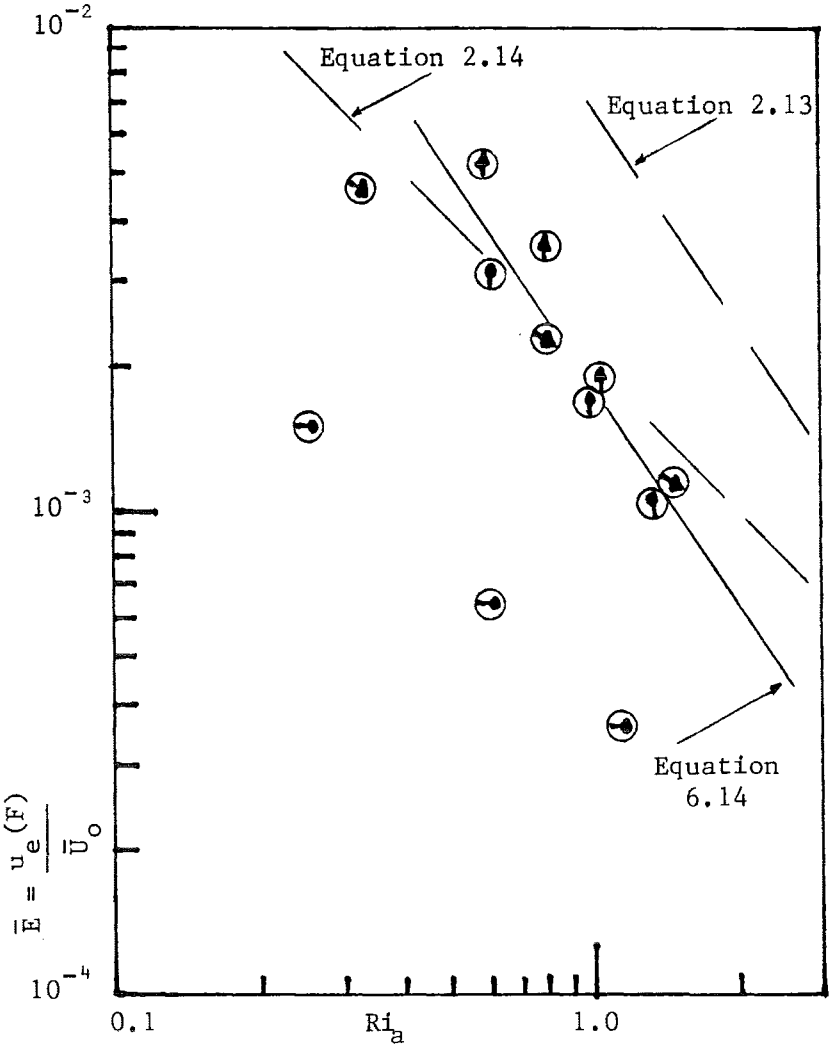

Figure 6.12 : Entrainment Data - 90 mm and 30 mm Cavities : $\bar{E}$ vs. Ri_a (same as Figure K-4)

Key		
$\bar{U}_o$, m/s	30 mm Cavity	90 mm Cavity
0.0732	◉	◉
0.0909	◉	◉

carried out in the shorter cavities are presented in Appendix K.

6.5 A Model for Entrainment from a Cavity

The entrainment from this finite size cavity can be represented by an empirical model which is accurate for very large Richardson numbers. This model is based on the viscous lengthscale of the turbulent boundary layer over a rigid flat smooth surface. Other possible lengthscales for the model have been discussed in Section 6.3 and include scales representative of the wake structure behind a backward facing step and of a step change in surface roughness. It was concluded in Section 6.2.6 that the scales L_{max} (Bradshaw and Wong 1972) and L_u (Townsend 1976) associated with a wake structure would not result in a significantly different presentation from Figures 6.9 and 6.10. It was decided to propose an empirical model based on the average entrainment over the whole interfacial region rather than that based on a number of different mechanisms and lengthscales. Although L_{max} and L_u were scales of similar order to δ_t, it was decided not to use L_{max} or L_u because these were representative of the flow structure in a small region at the side of the cavity and not of the major cavity area. Furthermore L_{max} and L_u result from flow behaviour which, by the definitions of Bradshaw and Wong (1972) is a limiting form of the observed behaviour in these experiments.

The roughness length of the interface z_{o2} can form another possible scaling length although values of z_o in the literature are at least an order of magnitude less than the boundary layer depth δ (Schlichting 1979, Panofsky and Dutton 1984 and others) in neutrally stratified flows. Also note that δ and z_o are not independent parameters in fully rough turbulent flow and the value of δ will be determined in part by z_{o2}.

It was decided to choose δ_t as the lengthscale for the model because of its appropriateness for very large Richardson numbers and that

it helps to provide a reasonable correlation at low Richardson numbers (Figures 6.9 and 6.10) for engineering purposes.

6.5.1 An Empirical Model

The non-dimensional flux entrainment velocity can be represented by the equation:

$$\overline{E} = 0.0018\ Ri_{\delta}^{-3/2} \quad \pm \quad 25\% \tag{6.14}$$

The lengthscale δ_t is the depth of the new turbulent boundary layer which forms over the cavity of length L_1. The value of δ_t is given by (Schlichting 1979):

$$\delta_t = 0.37\ L_1 \left[\frac{\nu_1}{\overline{U}_{\infty} L_1}\right]^{1/5} \tag{6.15}$$

where $\overline{U}_{\infty}$ is the maximum mean velocity at the top of the boundary layer. This velocity can be scaled with the bulk mean velocity $\overline{U}_0$ if δ_t is less than the upper layer depth and Equation (6.15) becomes Equation (6.6b). Equation (6.15) is valid in the range $0.6 \lesssim Ri_{\delta} \lesssim 16$.

6.5.2 The Limitations of the Model

The empirical model has a few associated limitations. These are concerned with the lengthscale δ_t, the cavity dimensions, and sufficiently large Reynolds and Peclet numbers.

The lengthscale, δ_t, is suitable for very high Richardson numbers and, as shown in Figure 6.9, also for lower values of Richardson number. The correlation at the lower values of Ri_{δ} is not as good as for high Ri_{δ}. At these lower Ri_{δ} values, the more appropriate scaling length would be that associated with the effective roughness z_{02} of the interfacial waves. Values of surface roughness z_0 recorded in experiments have usually been

at least an order of magnitude less than δ_t or, more generally, for a neutrally stratified boundary layer. Hence to compare data for low and high values of Ri_δ, it is necessary to select a scale $\delta(z_{02})$ comparable to δ_t. It is then natural to specify the depth of a boundary layer δ which grows over surface roughness of scale z_{02} as the relevant lengthscale.

The full-size cavity had a length to depth ($\frac{L_1}{D}$) ratio of about 9 and comparison with data from Lofquist (1960) showed that for $Ri_\delta > 2$, the experimental $\overline{E}$ values were about twice the values obtained by Lofquist. The effect of the cavity ends is to double the entrainment velocity for this experimental model. By reducing the cavity length to 90 mm or a $\frac{L_1}{D}$ ratio of about 3, the empirical model gave good predictions down to $Ri_a \sim 0.5$. In this case the wave height was the appropriate lengthscale.

The cavity depth h_1 had to be large enough so that $h_1/\lambda_c \gtrsim \frac{1}{2}$, where λ_c is the unstable wavelength at the interface. A conservative choice of λ_c was given by Equation (6.11), although for small Ri_δ Figure 6.3 showed that Equation (6.8) was suitable. This constraint was necessary so that the bottom of the cavity did not affect the interfacial behaviour.

The ratio of depths was $h_0/h_1 \gtrsim 2$ in the experiments. For application to atmospheric dispersion, the prototype value of h_0/h_1 is well in excess of 2.

The Reynolds number has to be large enough to allow turbulent flow in the upper layer. The Reynolds number of the flow based on the boundary layer depth just upstream of the cavity was $Re_\delta > 5x10^3$ in all three flow regimes. The critical Reynolds number is about 2800.

So that molecular diffusion is not significant, the Peclet number also has to be large enough. In these experiments the Peclet number was larger than 10^5 and at these values the molecular diffusion is negligible.

CHAPTER SEVEN

CONCLUSIONS AND RECOMMENDATIONS FOR FUTURE RESEARCH

7.1 Summary of the Important Results of this Work

A series of experiments have been carried out to investigate the behaviour of the density interface which was subjected to mean velocity shear. The main results are summarised below.

7.1.1 The Entrainment Mechanism

The observations have shown that the entrainment mechanism is the breaking of the interfacial waves and the subsequent ejection of denser fluid upwards. This mechanism was observed for low Richardson number of $Ri_\delta \sim 1$ and at $Ri_\delta \sim 15$, although there was less solution being ejected.

This wave breaking mechanism is in agreement with other studies which have also referred to it as the cusped waves or impinging vortices at the interface.

7.1.2 The Lengthscale for the Richardson Number

(i) The lengthscale was chosen to be the depth of the new turbulent boundary layer δ_t over the cavity. This scale is exact for a smooth rigid surface which can be used to model the interface at very large Richardson numbers and is consistent with the relevant lengthscale that scales the turbulence near the interface.

(ii) At the lower Richardson numbers when the interface is not flat but is disrupted by the wavetrain, a relevant scaling length is the new internal boundary layer depth associated with the effective roughness z_{o2} of the interfacial waves.

7.1.3 The Flux Entrainment Velocity

(i) Measurements of the flux entrainment velocity have shown that the non-dimensional entrainment velocity of these experiments can be represented by :

$$\overline{E} = 0.0018\ Ri_{\delta}^{-3/2} \qquad (7.1)$$

This Richardson number to the (-3/2) power relation is in agreement with grid-stirring experiments of Turner (1968) and Linden's (1973) model, as well as high Richardson number behaviour proposed by Christodoulou (1986).

(ii) The effect of the cavity ends on the entrainment is to increase the entrainment velocity. A comparison with the study by Lofquist (1960) has shown that the end-effects of these experiments amounted to an entrainment velocity which was about twice that measured by Lofquist.

7.1.4 The Interfacial Waves

At $Ri_{\delta} \sim 1$ the interfacial wave length λ_c and phase velocity c were predicted by the Kelvin-Helmholtz criterion. At larger values of Ri_{δ}, the value of λ_c was approximated by a hypothesis which assumed $c = \overline{U}_o$. The Kelvin-Helmholtz criterion and the latter hypothesis provided lower and upper bounds for the experimental values of λ_c and c.

The endwalls of the cavity caused reflection of the interfacial waves which in turn interacted with the advancing waves. The observed waves displayed an undisturbed wave profile only away from the endwalls.

7.2 Scaling for Full Size Prototype

A choice of length and velocity scales is required for full-size prototype situations. A possible velocity scale is the mean velocity at a ten (10) metre height (Panofsky and Dutton 1984 and others). However, the ratio $\overline{U}_o/\overline{U}$ (z=10 metres) needs to be close to 1.0 before any model data can be used for full-scale situations. For a neutral boundary layer over uniform grass terrain, the gradient height (Panofsky and Dutton 1984) is about 200 m. At z = 10 metres, $\frac{z}{\delta} = 0.05$. In the model flows for $\frac{z}{\delta} = 0.05$, $\overline{U}_o/\overline{U}$ (z = 10 metres) varies between 1.43 to 1.67. This is not significantly larger than unity hence the ten metre mean velocity is a suitable scale for full-size prototype work. This ten metre scale is also convenient because in current practice, atmospheric data which is recorded at different heights is usually scaled to the ten metre value.

The choice of lengthscale is less obvious except that it should be a function of the upstream turbulence conditions. Turbulence in the field can be generated in a number of ways. These include the surface roughness, the large obstacles such as vehicles, storage facilities or even buildings such as sheds or houses. The boundary layer depth over a dense gas cloud near the ground will not be easily evaluated, especially when the Richardson number is small. The effects of density and viscosity at small Richardson number will be small when compared to their effects at high Richardson number flow. The model presented in Section 6.5 is an idealised one where very large density differences are present. For small Richardson number entrainment, the lengthscale associated with one of the above roughnesses will possibly be more suitable.

7.3 Recommendations for future Research

The work which has been described in this thesis can be continued in a number of areas in the laboratory and in the field. Some of these areas are now described :

(i) There is a need for further study of entrainment at the density interface. Further measurements should include the flow structure of the upper layer just above the interface and flow within the cavity. The mean density profiles of the upper layer and of the cavity fluid should also be recorded.

The measurements of the flow structure in the upper layer above the interface can be used to estimate δ_t rather than rely on Equation (6.6b). These measurements can also verify the regions of recirculating flow at the upstream and downstream ends of the cavity. Measurements of the flow structure within the cavity will enable the shear stresses at the bottom and sides to be estimated. This will assist in the prediction of the slope of the density interface.

Due to the difficulties of measuring flows with continual changes in refractive indices with the LDA, another measurement technique or instrument will be required. The hot-film anemometer may be a suitable alternative although the accumulation of particles on the hot-film has been known to cause problems (Professor I.R. Wood, personal communciation). Other measurement techniques include the hydrogen bubble method, the release of polystyrene particles, and the release of dye.

(ii) A particular aspect which was not investigated in this work is the effect of the turbulence intensity on the interfacial behaviour. In all of these reported experiments, the upstream values of the background level of $\sqrt{\overline{u'^2}}/\bar{U}(z)$ was the same for the three flows and similarly the background level of $\sqrt{\overline{w'^2}}/\bar{U}(z)$ was also the same for the three flows. It would be interesting to

observe the effect of a highly turbulent upstream flow on the value of δ_t.

This may be accomplished by artificially roughening the perspex surface with sand or small strips of perspex to form a two-dimensional roughness pattern. In the limit of large roughness, obstacles may be placed upstream of the cavity to investigate the effects of the wake of a building or other structure such as a storage vessel.

(iii) The wave-breaking mechanism which caused the ejection of saline solution into the upper layer is in need of further study. Some work on this mechanism has been carried out but a full understanding is not yet available. Of particular interest is the wave-breaking mechanism at larger Richardson numbers and larger density differences of order $\Delta\rho \sim 0.2\ \rho_o$.

The wave-breaking mechanism is also of interest to other areas of study such as the atmosphere and oceans. However, the density differences in these case may be much less than $0.2\ \rho_o$.

(iv) There is a lack of data below 10 metres height for slightly stable atmospheric conditions. Field work is necessary so that the data can be collected for windspeeds up to 2 m/s at the 10 metre height. Although in slightly stable conditions with low windspeed the thermal effects may be significant, there does not appear to be any data presently available for comparison with laboratory studies. Heating and cooling effects greatly influence the behaviour of dense gases and the field data will provide a basis for laboratory model flows. Measurements should include the mean velocity, the spatial distribution of the fluctuating velocities, the temperature profile and fluxes of thermal energy from the ground or sun. A more detailed study may

include correlations of fluctuations of temperature and velocity components as well as correlations of fluctuating velocities.

ACKNOWLEDGEMENTS

I acknowledge the assistance given to me during the course of this project and extend my thanks to :

Dr A.J. Bowen, the supervisor of studies, for his advice;

Professor I.R. Wood, my associate supervisor, for his useful advice and criticisms. The laboratory equipment and space was also made available through the good office of Professor Wood, and this is gratefully acknowledged. The project would not have been completed without these facilities;

Dr R.H. Spigel, for providing advice and criticisms on the draft of this thesis;

My friends Chris Ure and Murray Aitken for providing a forum for the discussion of a range of topics, and their useful advice;

Jan McKenzie for her friendship, advice and boundless energy to help whenever requested;

Neil Stewart and Dave Healy for their technical skill and advice;

Ms. J. Shelton for doing some of the photographic and tracing work;

Mrs B. Bristowe for her typing and assistance in editing the manuscript.

Partial funding for the project was provided by the New Zealand Meteorological Service, and this is gratefully acknowledged.

I wish to thank my family, and my wife's family, for their moral and financial support. Their assistance is gratefully acknowledged.

Finally, I owe most to my wife, Shirley, and extend to her my deepest gratitude. She made many sacrifices so that this project would not be left incomplete, and made our place a home.

REFERENCES

Antonia, R.A., Luxton, R.E. (1971) The response of a turbulent boundary layer to a step change in surface roughness. Part 1. Smooth to rough. J. Fluid Mech., 48, 721-761.

Antonia, R.A., Luxton, R.E. (1972) The response of a turbulent boundary layer to a step change in surface roughness. Part 2. Rough to smooth. J. Fluid Mech., 53, 737-757.

Anwar, H.O., Weller, J.A. (1981) An experimental study of the structure of a freshwater-saltwater interfacial mixing. La Houille Blanche, 6, 405-412.

Arya, S.P. (1982) Atmospheric boundary layers over homogeneous terrain. In Engineering Meteorology edited by E.J. Plate, Elsevier, 233-267.

Baines, W.D., Knapp, D.J. (1965) Wind driven water currents. J. Hyd. Div., Proc. ASCE, HY2, 205-221.

Batchelor, G.K. (1953) The conditions for dynamical similarity of motions of a frictionless perfect-gas atmosphere. Quart. J. Roy. Met. Soc. 79, 224-235.

Batchelor, G.K. (1954) Heat convection and buoyancy effects in fluids. Quart. J. Roy. Met. Soc. 80, 339-358.

Birkhoff, G. (1960) Hydrodynamics. Princeton University Press, 184p.

Bradshaw, P., Wong, F.Y.F. (1972) The reattachment and relaxation of a turbulent shear layer. J. Fluid Mech., 52, 113-135.

Britter, R.E. (1980) The ground level extent of a negatively buoyant plume in a turbulent boundary layer. Atmospheric Environment, 14, 779-785.

Britter, R.E., Griffiths, R.F. (1982) (Editors). Dense gas dispersion. Elsevier, 247p.

Browand, F.K., Winant, C.D. (1973) Laboratory observations of shear-layer instability in a stratified fluid. Boundary-layer Met. 5, 67-77.

Brutsaert, W.H. (1982) Exchange processes at the earth-atmosphere interface. In Engineering Meterology edited by E.J. Plate, Elsevier, 319-369.

Caughey, S.J., Wyngaard, J.C., Kaimal, J.C. (1979) Turbulence in the evolving stable boundary layer. J. Atmos. Sci. 6, 1041-1052.

Cebeci, T., Smith, A.M.O. (1974) Analysis of turbulent boundary layers. Academic Press, 404p.

Chatwin, P.C. (1982) The use of statistics in describing and predicting the effects of dispersing gas clouds. In Dense Gas Dispersion edited by R.E. Britter and R.F. Griffiths, Elsevier, 213-230.

Chatwin, P.C. (1984) The incorporation of wind shear effects into box models of heavy gas dispersion. Proc. IUTAM Sym. Atmospheric Dispersion of Heavy Gases and Small Particles edited by G. Ooms and H. Tennekes, Springer-Verlag, 63-72.

Chatwin, P.C., Sullivan, P.J. (1979) Measurements of concentration fluctuations in relative turbulent diffusion. J. Fluid Mech. 94, 83-101.

Christodoulou, G.C. (1986) Interfacial mixing in stratified flows. J. Hydraulic Res. 24, 77-92.

Crapper, P.F., Linden, P.F. (1974) The structure of turbulent density interfaces. J. Fluid Mech. 65, 45-63.

Csanady, G.T. (1973) Turbulent diffusion in the environment. Reidel Publishing Co. 248p.

Csanady, G.T. (1982) Circulation in the coastal ocean. Reidel Publishing Co. 279p.

Deacon, E.L. (1949) Vertical diffusion in the lowest layers of the atmosphere. Quart. J. Roy. Met. Soc. 75, 89-103.

Deardorff, J.W., Willis, G.E. (1982) Dependence of mixed-layer entrainment on shear stress and velocity jump. J. Fluid Mech. 115, 123-149.

Debye, P., Sears, F.W. (1932) On the scattering of light by supersonic waves. Proc. National Academy of Science. 18, 409-414.

Denton, R.A. (1978) Entrainment by penetrative convection at low Peclet number. Ph.D. Thesis, University of Canterbury, N.Z., 202p plus Appendices.

Denton, R.A., Wood, I.R. (1981) Penetrative convection at low Peclet number. J. Fluid Mech. 113, 1-21.

Dirkmaat, J.J. (1981) Experimental studies on the dispersion of heavy gases in the vicinity of structures and buildings. Proc. Sym. Designing with the Wind. Nantes, 1, III-3-1 to III-3-13.

Disa, (1), Instruction manual for type 55L Laser-Doppler Anemometer, 45p.

Drazin, P.G., Reid, W.H. (1981) Hydrodynamic Stablility. Cambridge University Press, 525p.

Durst, F., Melling, A., Whitelaw, J.H. (1976) Principles and practice of Laser-Doppler Anemometry. Academic Press, 405p.

E, Xuequan, Hopfinger, E.J. (1986) On mixing across an interface in stably stratified fluid. J. Fluid Mech. 166, 227-244.

Eidsvik, K.J. (1980) A model for heavy gas dispersion in the atmosphere. Atmospheric Environment. 14, 769-777.

Ellison, T.H., Turner, J.S. (1959) Turbulent entrainment in stratified flows. J. Fluid Mech. 6, 423-448.

ESDU (1972) Characteristics of wind speed in the lower layers of the atmosphere near the ground: Strong winds (neutral atmosphere). Engineering Sciences Data Unit, Item 72026.

ESDU (1974) Characteristics of atmospheric turbulence near the ground, part II: single point data for strong winds (neutral atmosphere). Engineering Sciences Data Unit, Item 74031.

Fay, J.A. (1980) Gravitational spread and dilution of heavy vapor clouds. Proc. second Int. Sym. on Stratified Flows, Trondheim, 1, 471-494.

Fay, J.A. (1984) Experimental observations of entrainment tests in dense gas dispersion tests. Proc. IUTAM Sym. on Atmospheric Dispersion of Heavy Gases and Small Particles, edited by G. Ooms and H. Tennekes. Springer-Verlag, 39-51.

Fay, J.A., Ranck, D.A. (1983) Comparison of experiments on dense gas cloud dispersion. Atmospheric Environment, 17, 239-248.

Gifford, F.A. (1961) Use of routine meteorological observations for estimating atmospheric dispersion. Nuclear Safety, 2, 47-51.

Glover, J.R. (1970) Multiple-channel conductometer for measuring salinity concentrations in laboratory flows. Iowa Institute for Hydraulic Research Report No. 128, The University of Iowa, 17p.

Goldstein, S. (1931) On the stability of superposed streams of fluids of different densities. Proc. Roy. Soc. A132, 524-548.

Hall, D.J., Barrett, C.F., Ralph, M.O. (1976) Experiments on a model of an escape of a heavy gas. Report ISBN 0856240 65 6. Warren Spring Laboratory, Department of Industry, Hertfordshire, England, 24p.

Henderson, F.M. (1966) Open channel flow. McMillan Publishing Co. 522p.

Holmboe, J. (1962) On the behaviour of symmetric waves in stratified shear layers. Geofysiske Publikasjoner, Norway, 24, 67-113.

Hopfinger, E.J., Toly, J.-A. (1976) Spatially decaying turbulence and its relation to mixing across density interfaces. J. Fluid Mech. 78, 155-175.

Hunt, J.C.R., Graham, J.M.R. (1978) Free-stream turbulence near plane boundaries. J. Fluid Mech. 84, 209-235.

Hunt, J.C.R., Simpson, J.E. (1982) Atmospheric boundary layers over non-homogeneous terrain. In Engineering Meteorology edited by E.J. Plate, Elsevier, 269-318.

Hunt, J.C.R., Rottman, J.W., Britter, R.E. (1984) Some physical processes involved in the dispersion of dense gases. Proc. IUTAM Sym. on Atmospheric Dispersion of Heavy Gases and Small Particles, edited by G. Ooms and H. Tennekes, Springer-Verlag, 361-395.

Jensen, M. (1958) The model law for phenomena in a Natural Wind. Ingenioren, Denmark, 2, 121-128.

Kantha, L.H., Phillips, O.M., Azad, R.S. (1977) On turbulent entrainment at a stable density interface. J. Fluid Mech. 79, 753-768.

Kato, H., Phillips, O.M., (1969) On the penetration of turbulent layer into stratified flow. J. Fluid Mech. 37, 643-655.

Keulegan, G.H. (1949) Interfacial instability and mixing in stratified flows. J. of Research of the National Bureau of Standards, 43, RP2040, p487-500.

Kranenburg, C. (1984) Wind induced entrainment in a stably stratified fluid. J. Fluid Mech. 145, 253-273.

Krauss, W. (1973) Methods and results of theoretical oceanography. Vol. 1. Dynamics of the homogeneous and quasi-homogeneous ocean, Gebrüder, 302p.

Lamb, Sir Horace. (1932) Hydrodynamics, 6th edition. Cambridge University Press, 738p.

Linden, P.F. (1973) The interaction of a vortex ring with a sharp density interface: a model for turbulent entrainment. J. Fluid Mech. 60, 467-480.

Lofquist, K. (1960) Flow and stress near an interface between stratified fluids. Physics of Fluids, 3, 158-175.

Long, R.R. (1973) Some properties of horizontally homogeneous, statistically steady turbulence in a stratified fluid. Boundary-Layer Met. 5, 139-157.

Long, R.R. (1978) A theory of mixing in a stratified fluid. J. Fluid Mech. 84, 113-124.

McNulty, A.J. (1983) Dispersion of a continuous pollutant source in open channel flow. Ph.D. Thesis, University of Canterbury, N.Z., 210p plus Appendices.

Meroney, R.N. (1982) Wind tunnel experiments on dense gas dispersion. In Dense Gas Dispersion, edited by R.E. Britter and R.F. Griffiths, Elsevier, 85-106.

Meroney, R.N. (1983) Unsteady behaviour of a simulated LNG vapor cloud suddenly released into a wind-tunnel boundary layer. American Gas Association Transmission Conference, Seattle.

Meroney, R.N., Lohmeyer, A. (1982) Gravity spreading and dispersion of dense gas clouds released suddenly into a turbulent boundary layer. Gas Research Institute Report -81/0025.

Meroney, R.N., Neff, D.E. (1977) Behaviour of negatively buoyant gas plumes resulting from a LNG spill. Proc. 6th Australasian Hydraulics and Fluid Mechanics Conference, Adelaide, 472-475.

Moore, M.J., Long, R.R. (1971) An experimental investigation of turbulent stratified shearing flow. J. Fluid Mech. 49, 635-655.

Morton, B.R., Taylor, Sir Geoffrey I., Turner, J.S. (1956) Turbulent gravitational convection from maintained and instantaneous sources. Proc. Roy. Soc. London, A234, 1-23.

Nakagawa, H., Nezu, I. (1987) Experimental investigation on turbulent structure of backward-facing step flow in an open channel. J. Hydraulic Res., 25, 67-88.

Narimousa, S., Fernando, H.J.S. (1987) On the sheared density interface of an entraining stratified fluid. J. Fluid Mech. 174, 1-22.

Narimousa, S., Long, R.R., Kitaigorodskii, S.A. (1986) Entrainment due to turbulent shear flow at the interface of a stably stratified fluid. Tellus, 38A, 76-87.

Neff, D.E., Meroney, R.N. (1982) The behaviour of LNG vapor clouds: Wind tunnel tests on the modelling of heavy plume dispersion. Gas Research Instituted Report 80/0145.

Ooms, G., Tennekes, H. (1984) (Editors). Atmospheric Dispersion of Heavy Gases and Small Particles. Proc. IUTAM Symposium, Delft, 440p.

Panofsky, H.A., Dutton, J.A. (1984) Atmospheric Turbulence. John Wiley and Sons, 397p.

Pasquill, F. (1949) Eddy diffusion of water vapour and heat near the ground. Proc. Roy. Soc. A198, 116-140.

Pasquill, F. (1961) The estimation of the dispersion of windborne material. The Meteorological Magazine, 90, 33-49.

Pasquill, F. (1974) Atmospheric Diffusion. 2nd edition. Ellis Horwood, 429p.

Phillips, O.M. (1977) Dynamics of the upper ocean. 2nd edition. Cambridge University Press. 336p.

Plate, E.J. (1982) Wind tunnel modelling of wind effects in engineering. In Engineering Meteorology edited by E.J. Plate, Elsevier, 573-639.

Plate, E.J., Hidy, G.M. (1967) Laboratory study of air flowing over a smooth surface onto small water waves. J. Geophy. Res. 72, 4627-4641.

Price, J.R. (1979) On the scaling of stress driven experiments. J. Fluid Mech. 90, 509-529.

Radiometer Operating Instructions for CDM83 Conductivity Meter, Copenhagen, Denmark, 45p.

Raman, C.V., Nath, N.S.N. (1933) The diffraction of light by high frequency sound waves: Part 1. Proc. Indian Acad. of Sciences, A2, 406-412.

Robinson, R.A., Stokes, R.H. (1959) Electrolyte Solutions. 2nd edition, Butterworths, 571p.

Schlichting, H. (1979) Boundary Layer Theory. 7th edition, McGraw-Hill, 817p.

Scranton, D.R., Lindberg, W.R. (1983) An experimental study of entraining stress-driven stratified flow in an annulus. Physics of Fluids, 26, 1198-1205.

Seeto, B.C.M. (1982) Dispersal of Liquefied Petroleum Gas in the Atmosphere. Unpublished M.E. Thesis, University of Canterbury, N.Z., 181p.

Sherman, F.S., Imberger, J., Corcos, G.M. (1978) Turbulence and mixing in stably stratified waters. Ann. Rev. Fluid Mech. 10, 267-288.

Snyder, W.H. (1972) Similarity criteria for the application of fluid models to the study of air pollution meteorology. Boundary-Layer Met. 3, 113-134.

Spigel, R.H., Imberger, J. (1980) The classification of mixed-layer dynamics in lakes of small to medium size. J. Phys. Oceanogr. 10, 1104-1121.

Spigel, R.H., Imberger, J., Rayner, K.N. (1986) Modelling the diurnal mixed-layer. Limnol. Oceanogr. 31, 553-556.

Taylor, Sir Geoffrey I. (1931) Effect of variation of density on the stability of superposed streams of fluid. Proc. Roy. Soc. A132, 499-523.

Tieleman, H.W. (1987) A survey of the turbulence in the marine surface layer. Preprints of 7th Int. Conf. on Wind Engineering, Aachen, W. Germany, July 6-10 1987, Session 1, p.51-60. To be published in J. Wind Engineering and Indus. Aerodynamics.

Thompson, S.M., Turner, J.S. (1975) Mixing across an interface due to turbulence generated by an oscillating grid. J. Fluid Mech. 67, 349-368.

Thorpe, S.A. (1968) On the shape of progressive internal waves. Phil. Trans. London Roy. Soc. A263, 563-614.

Thorpe, S.A. (1971) Experiments on the stability of stratified shear flows: miscible fluids. J. Fluid Mech. 46, 299-319.

Thorpe, S.A. (1973) Turbulence in stably stratified fluids: A review of laboratory experiments. Boundary-Layer Meterollogy. 5, 95-119.

Thorpe, S.A. (1978) On the shape and breaking of finite amplitude internal gravity waves in a shear flow. J. Fluid Mech. 85, 7-31.

Townsend, A.A. (1956) The structure of turbulent shear flow. Cambridge University Press. 315p.

Townsend, A.A. (1976) The structure of turbulent shear flow, 2nd edition. Cambridge University Press, 429p.

Turner, J.S. (1968) The influence of molecular diffusivity on turbulent entrainment across a density interface. J.Fluid Mech. 33, 639-656.

Turner, J.S. (1973) Buoyancy effects in fluids. Cambridge University Press, 367p.

Turner, J.S. (1986) Turbulent entrainment: the development of the entrainment assumption and its application to geophysical flows. IUTAM Sym. Fluid Mechanics in the Spirit of G.I. Taylor. J. Fluid Mech. 173, 431-471.

Valentine, E.M. (1978) The effect of channel boundary roughness on longitudinal dispersion. Ph.D. Thesis, University of Canterbury, N.Z.

Van Ulden, A.P. (1974) On the spreading of a heavy gas released near the ground. Proc. 1st Int. Sym. Loss Prevention and Safety Promotion in the Process Industries, Delft. 221-226.

Weast, R.C. (1975) (Editor). Handbook of Chemistry and Physics, 56th edition, 1975-1976, CRC.

Webber, D.M. (1984) Gravity spreading in dense gas dispersion models. Proc. IUTAM Sym. Atmospheric Dispersion of Heavy Gases and Small Particles edited by G. Ooms and H. Tennekes. Springer-Verlag, 397-406.

Willard, G.W. (1949) Criteria for normal and abnormal ultrasonic light diffraction effects. J. Acous. Soc. Amer. 21, 101-108.

Yoshida, S. (1977) On a mechanism for breaking of interfacial waves. Coastal Eng. in Japan, 20, 7-15.

APPENDIX A

THE VOLUME OF WATER IN THE RECIRCULATING SYSTEM

The quantity of water in the channel and recirculating system was required so that the background level of conductivity could be evaluated. This was achieved by conducting a simple calibration test during which a known quantity of sodium chloride solution was added to the recirculating system. The water level, temperature and conductivity were all recorded and it was found that the depth h of water in the working section could be related to the volume V_s of water in the system by :

$$V_s = 6.62\ (h-138) + 1945 \quad [\text{litres}] \qquad (a-1)$$

and $300\ \text{mm} \geq h \geq 138\ \text{mm}$.

The volume occupied by the model is about 22 litres and has been deducted from Equation (a-1). The sodium chloride which was added to the water system produced a concentration that was less than 1 gm per litre. Separate measurements have shown that for constant temperature, the relationship between conductivity and concentration of sodium chloride is linear up to at least 2 gm of sodium chloride per litre (Figures B-1, B-2).

The sources of error in deriving expression (a-1) included the measurement of the water in the working section, the mass of sodium chloride added to the water system, and the measurement of the conductivity. The depth h of water in the working section can easily be estimated to 1 mm and for a minimum depth of 220 mm, this represents less than 0.5%. The measurement of the mass of salt is accurate to 0.2 gm and four separate masses were measured to a total of 1901.8 gms of sodium chloride. This represents an error much less than 0.5%. A Radiometer

CDM83 conductivity meter was used to measure the conductivity of the water. This meter has an accuracy of 0.75% of reading ±3 of the least significant digit (Radiometer p.42). This results in an error of less than 2% in the conductivity measurement. The CDM83 meter also compensates for temperature and all readings can be referred to a standard value, usually 20°C. The change in temperature during this calibration was of order 0.5°C and this was easily compensated. The sum of the above errors is less than 3% when expression (a-1) is used.

APPENDIX B

CALIBRATION CURVES

This Appendix contains calibrations for

(i) conductivity versus concentration of NaCℓ solution in figures B-1 and B-2.

(ii) The output voltage versus Doppler frequency for the 150 kHz range in Figure B-3, and

(iii) the concentration of saline solution versus probe output voltage for sodium chloride in Figure B-4. The calibration for calcium chloride solutions is very similar.

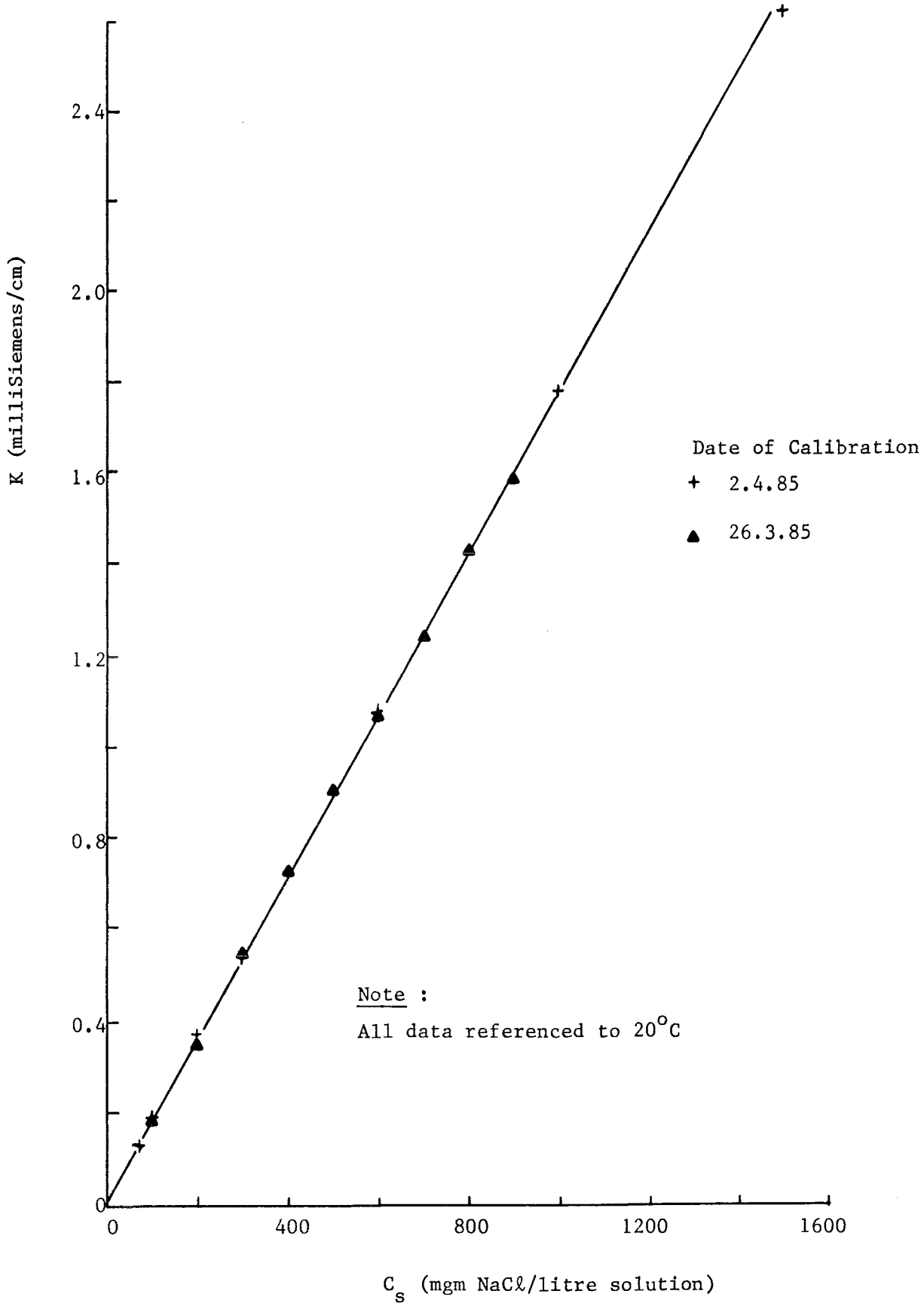

Figure B-1 : Calibration for NaCℓ solution (1500 mgm NaCℓ/litre)

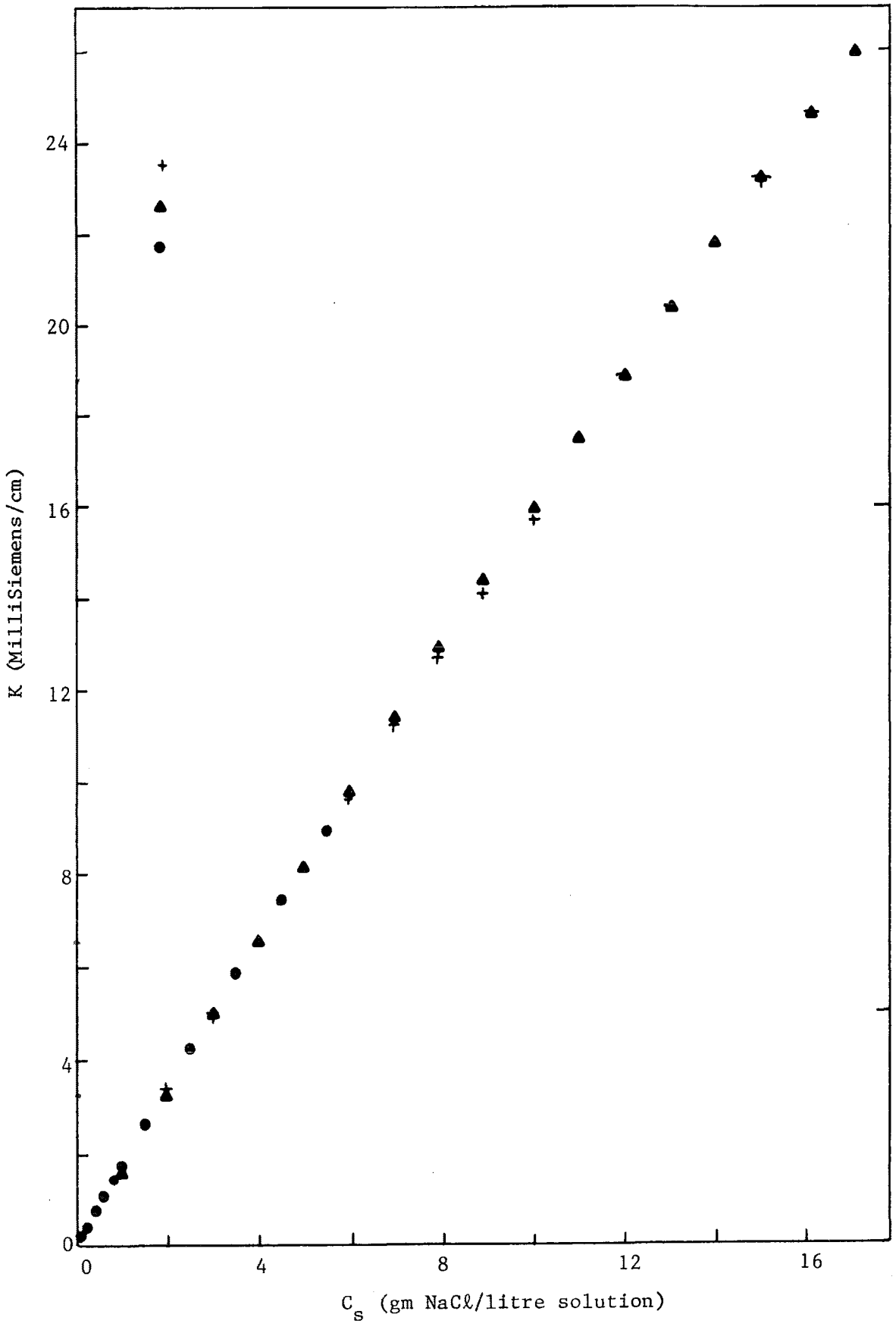

Figure B-2 : Calibration for NaCℓ solution (19 gm NaCℓ/litre)

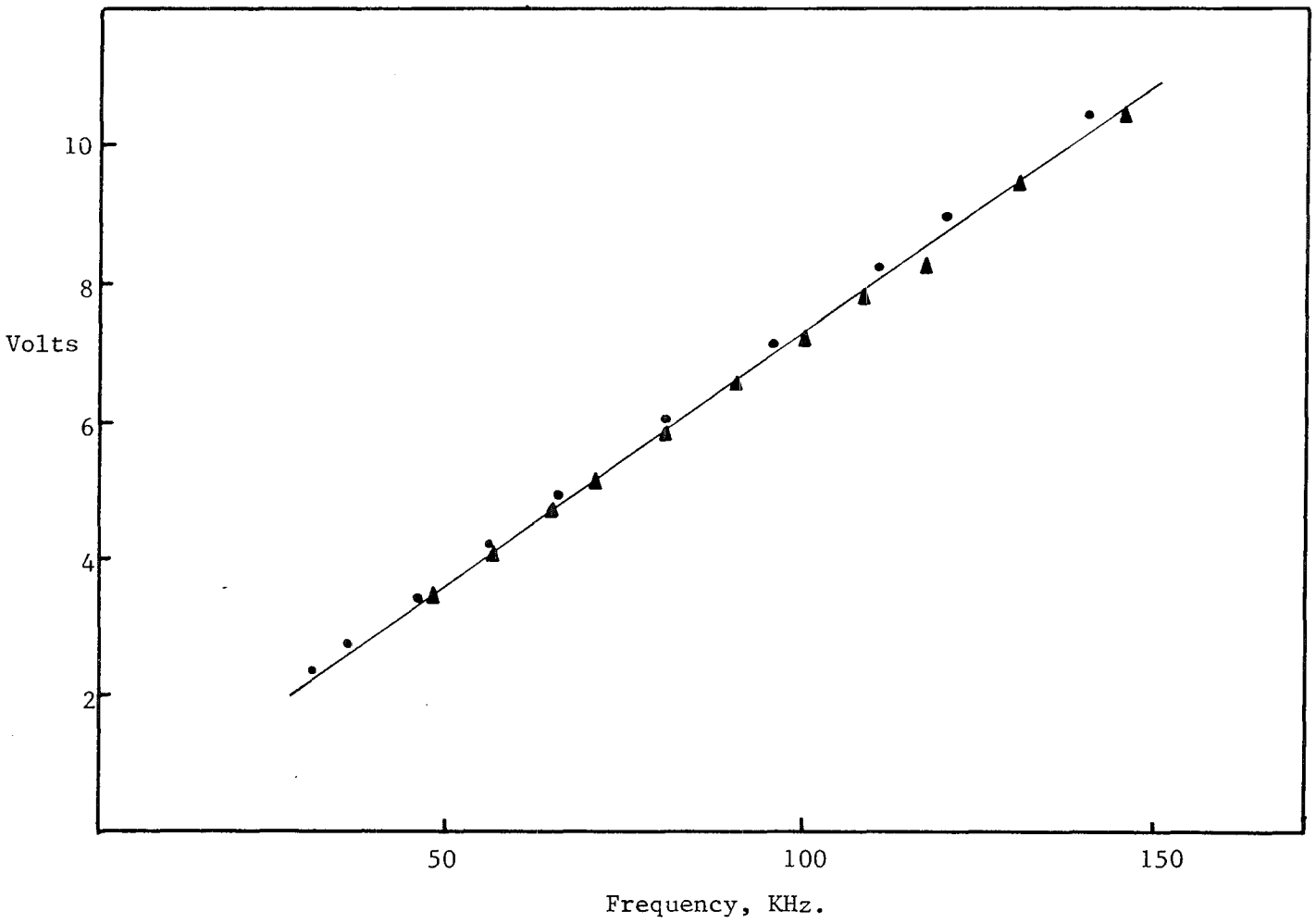

Figure B-3 : Calibration for the Frequency Tracker - 150 KHz range

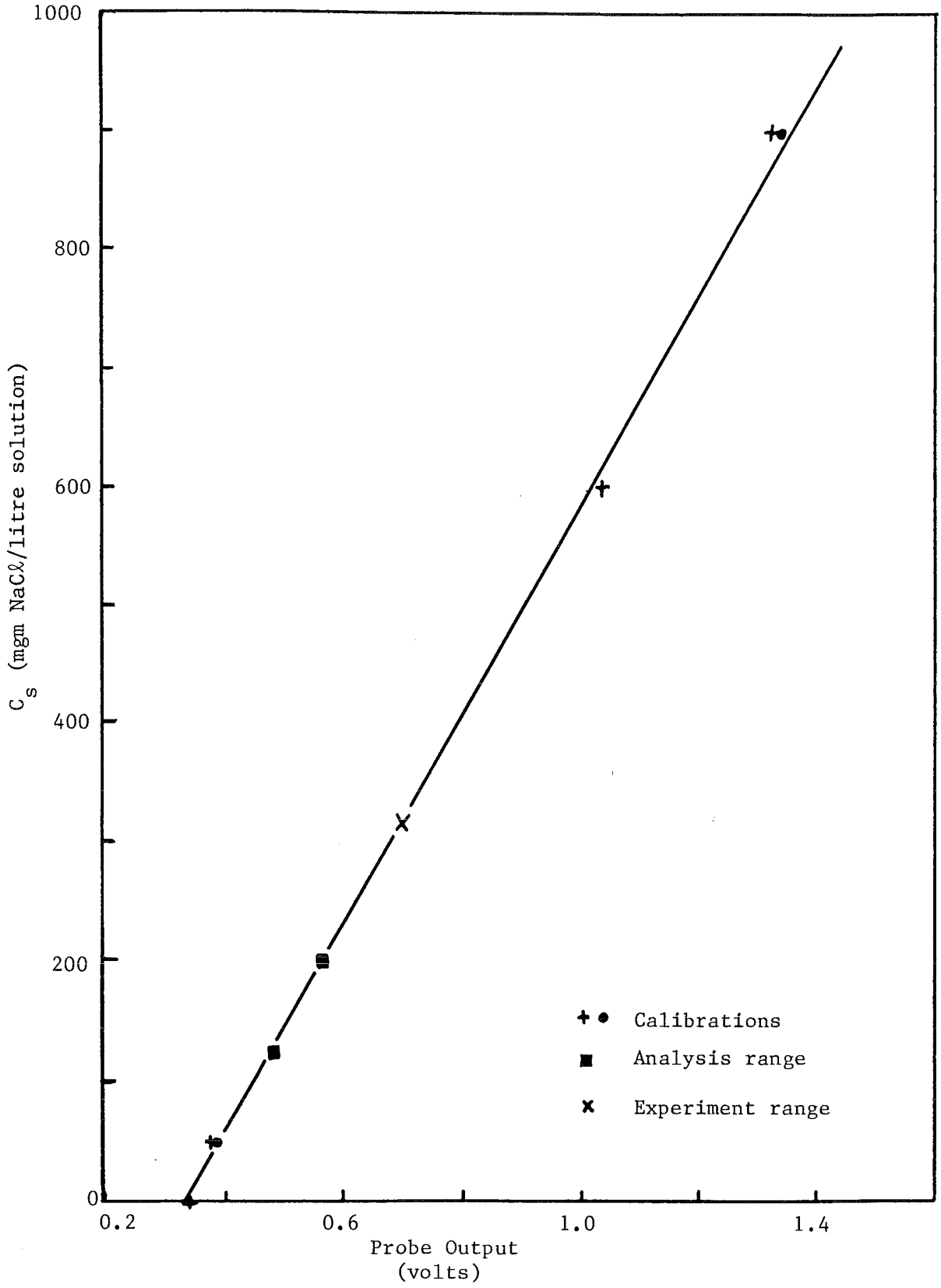

Figure B-4 : Sample Calibration for Conductivity Probe

APPENDIX C

THE LIFTING TABLE

A structure was required for supporting and moving the laser Doppler Anemometer. There was no suitable piece of equipment available so the table was designed and the construction was carried out in the Mechanical Engineering workshop. The requirements for the table were that

(i) There had to be sufficient vertical travel to obtain velocity profiles.

(ii) There had to be sufficient longitudinal travel to obtain measurements of the flow at downstream positions.

(iii) The structure had to be such that the deflection under load was negligible.

(iv) By virtue of being located in a laboratory where there were other large pieces of equipment, the table had to be of sufficient mass and strength so as to resist deformation.

(v) The table had to fit in the available space under the water channel.

Figure 4.3 is the general assembly drawing of the lifting table. The requirements (i, ii) dictated that the table had to have two degrees of freedom, hence it was built in three sections (items 1, 2,3 in Figure

4.3). Item 3 is the main support frame being fabricated of channel sections, and item 2 is the sliding frame which provided the longitudinal degree of freedom. This sliding frame was supported by a cam roller on one side and two linear bearings on the other side. The linear bearings moved on a hardened steel shaft as shown in Figure 4.4. A threaded rod and nut arrangement controlled the sliding movement. The main table shown in Figure 4.3 as item 1 comprised a central beam (150mm x 150mm RHS) and two cross members which supported the LDA (Figures 4.4 and 4.5). This main table was supported by three threaded rods which were located within brass bushes. The brass bushes were in turn mounted into the hub of identical sprocket and separately into a ball bearing. A continuous chain was used to synchronise the sprockets. The control of the main table height was accomplished with two more sprockets, a bevel gear box and a handle (Figure 4.4). A full turn of the handle resulted in a height difference of about 1 mm. The two grey tubes were installed as chain guides. A counterweight was located on the main table to balance the LDA equipment placed on the other side of the table. Figure 4.5 also shows the lifting table and the LDA components.

The overall dimensions of the lifting table are 2.8 metres long, 1.5 metres wide, and 1.4 metres high. The structure was designed as modules so that each section could be built independent of the other two sections and, by specifying bolted joints, it was relatively easy to assemble or dismantle. The critical aspect of the assembly process was to make sure that the main table was level in any position. A scale was installed so that the differential height can be recorded. The accuracy of the system will be discussed in Appendix E in conjunction with the errors in the LDA system.

APPENDIX D

LASER DOPPLER ANEMOMETER, BRAGG CELLS AND ELECTRONIC PROCESSING EQUIPMENT

The Laser Doppler Anemometer (LDA) was introduced in 1964 by Yeh and Cummins as a tool for measuring fluid velocity. The concept of the LDA is straightforward in that a region in space would be designated as the measuring volume by the intersection of at least two polarised coherent light beams. Particles which traverse this measuring volume will reflect light and the information would be collected by a photo-electronic device. (It is assumed that the particles are small enough to follow the fluid behaviour). See Figures D-1a,b. The following description will consider the two-beam single channel LDA, but can be easily extended to more than one channel.

D-1 The Single Channel LDA

The coherent light source is supplied by a laser, which is split into two beams within the optical unit. The two beams are re-focused at the point of measurement by the optical unit, and particles which traverse this intersection (or measuring) volume, reflect the light. The photo-electronic device referred to as the photmultiplier is also focused on the measuring volume. The photomultiplier receives the scattered light signals and emits an alternating current with a Doppler frequency proportional to the scattering particle velocity.

For a single incident, light beam of frequency f_i and wavelength λ, the scattered light frequency f_s is given by the expression :

$$f_s = f_i + \frac{1}{\lambda} \underline{u} \cdot (\underline{e}_s - \underline{e}_i) \qquad (d\text{-}1)$$

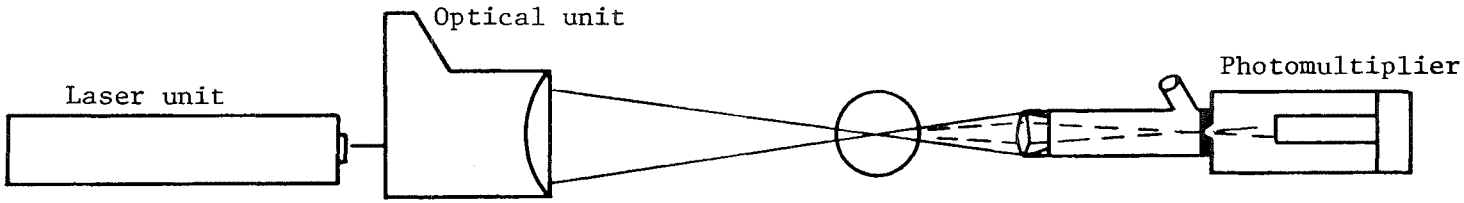

Figure D-1a : LDA in Forward Scattering Differential Doppler Mode

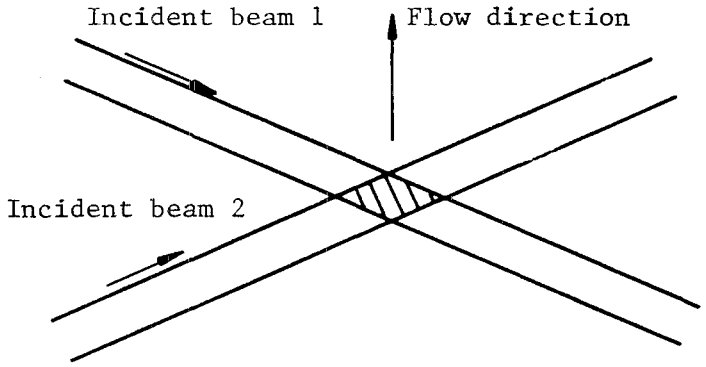

Figure D-1b : The Intersecting Volume

where $\underline{e}_i$, $\underline{e}_s$ = unit vectors in the incident and scattered directions respectively,

$\underline{u}$ = velocity vector of the particle crossing the measuring volume

For two incident beams, the corresponding expressions for beams (denoted with subscripts 1 and 2) are :

$$\left.\begin{aligned} f_{s1} &= f_{i1} + \frac{\underline{u}}{\lambda} \cdot (\underline{e}_{s1} - \underline{e}_{i1}) \\ \text{and} \qquad & \\ f_{s2} &= f_{i2} + \frac{\underline{u}}{\lambda} \cdot (\underline{e}_{s2} - \underline{e}_{i2}) \end{aligned}\right\} \qquad \text{(d-2)}$$

Correspondingly the photomultiplier emits an alternating current with a Doppler frequency :

$$f_D = f_{s2} - f_{s1} \qquad \text{(d-3)}$$

When operating in the forward scattering differential Doppler mode, Equation (d-3) becomes :

$$f_D = \frac{\underline{u}}{\lambda} \cdot (\underline{e}_{i1} - \underline{e}_{i2}) \qquad \text{(d-4)}$$

due to the following :

$$f_{i1} = f_{i2}$$

and

$$\underline{e}_{s1} = \underline{e}_{s2}$$

The above Equation (d-4) indicates that the Doppler frequency is a function of the incident unit vectors, the light wavelength and the particle velocity. Rearrangement of Equation (d-4) leads to :

$$u = \frac{f_D \times \lambda}{(\underline{e}_{i1} - \underline{e}_{i2})} \qquad \text{(d-5)}$$

$$= (f_D \times \lambda)/(2 \sin \frac{\theta}{2}) \qquad \text{(d-5a)}$$

where θ is the angle between $\underline{e}_{i1}$ and $\underline{e}_{i2}$.

In the measurement of turbulent flows and flows over obstacles, it may be necessary to discriminate between flow reversals. The LDA system described thus far is direction insensitive, i.e., it will not resolve the directional ambiguity, $\pm \underline{e}$

where $$\underline{e} = \frac{\underline{u}}{|\underline{u}|}$$

D-2 Frequency Shifting

Consider Equation (d-5) together with Figure D-1b. In order to alter the value of $\underline{u}$ the Doppler frequency has to be changed because λ is fixed by the light source and the term $(\underline{e}_{i1} - \underline{e}_{i2})$ is fixed by the optical system. One possible method is to add another component of frequency to Equation (d-4) so that when $\underline{u} \leq 0$, there is still a positive f_D. This is similar to converting to a moving coordinate system. Equation (d-4) becomes :

$$f_D + \Delta f = \frac{\underline{u}}{\lambda} \cdot (\underline{e}_{i1} - \underline{e}_{i2}) \qquad \text{(d-4a)}$$

To obtain this situation physically, each of the two split laser beams are superimposed with an acoustic wave at ultrasonic frequency such that the Bragg condition is satisfied. [See Debye and Sears (1932), Raman and Nath (1935), and Willard (1949)]. When an acoustic wave is imposed on a travelling light wave, a diffraction pattern results. A single sharp diffraction maximum occurs when the following condition is

satisfied :

$$\sin \theta_b = \frac{1}{2} \left(\frac{\lambda}{\lambda_a}\right) \tag{d-6}$$

λ_a = acoustic wavelength, and

θ_b = Bragg angle

as shown in Figure D-2. Equation (d-6) is known as the Bragg condition. In practice, for a two-beam anemometer, the extra frequency component is effected by a downwards shift on one beam and an upwards shift on the other beam. Equations (d-2) become :

$$\left.\begin{aligned} f_{s1} &= f_{i1} + \frac{\underline{u}}{\lambda} \cdot (\underline{e}_{s1} - \underline{e}_{i1}) + \frac{\Delta f}{2} \\ f_{s2} &= f_{i2} + \frac{\underline{u}}{\lambda} \cdot (\underline{e}_{s2} - \underline{e}_{i2}) - \frac{\Delta f}{2} \end{aligned}\right\} \tag{d-2a}$$

and Equation (d-4) becomes :

$$f_D = \frac{\underline{u}}{\lambda} (\underline{e}_{i1} - \underline{e}_{i2}) - \Delta f$$

or

$$f_D + \Delta f = \frac{\underline{u}}{\lambda} (\underline{e}_{i1} - \underline{e}_{i2}) \tag{d-4a}$$

The acousto-optic device is called a Bragg cell.

Figure D-2 shows the basic elements that constitute a Bragg cell. These are a quartz crystal or some other type for generating ultrasonic waves, a signal generator to excite the crystal, an acoustic absorber to eliminate reflection of waves, and the liquid cell through which the ultrasonic waves propagate to meet the light beam.

Ultrasonic waves are excited by the quartz crystal and these waves travel across the liquid cell with frequency Δf_u. The incident laser

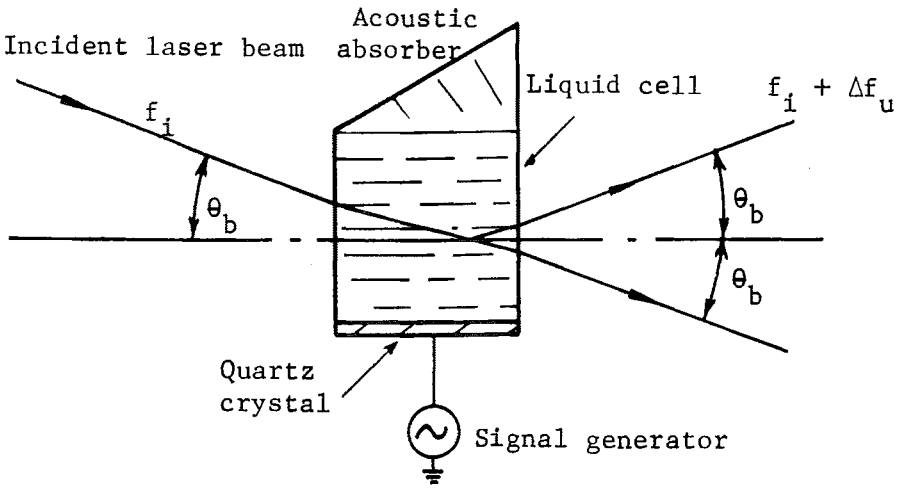

Figure D-2 : A Bragg Cell

beam at frequency f_i traversing the liquid cell at an angle θ_b to the ultrasonic wave is deflected through an angle $2\theta_b$ from its original path. The light frequency is also changed to $f_i + \Delta f_u$. The deflected wave (2) now follows a direction $2\theta_b$ from the original.

In order to cause a large enough frequency shift in the lasers to be of any useful purpose, two such Bragg cells are combined. In this manner, one laser beam can be pre-shifted up and the other beam pre-shifted downwards. Hence the Δf is obtained as equal to $2\Delta f_u$.

D-3 Signal Processing

The signal emitted by the photomultiplier may vary in amplitude, frequency and phase, as well as being random in nature. The method of signal analysis to be used will then depend on the flow properites required and the flow configuration. There are a number of methods which can be used for signal analysis and three of the more common methods are:

(i) frequency analysis,

(ii) frequency tracking, and

(iii) counting techniques.

These three methods are well documented by Durst, Melling and Whitelaw (1976). A brief description of the frequency tracking technique is presented as this was the method employed for this project. Figure D-3 is a block diagram of the frequency tracker.

The input Doppler signal of the form $A \cos(2\pi f_D + \phi)$ is mixed with the output signal from the voltage controlled oscillator (vco), $\cos 2\pi f_{vco} t$. The output signal at the difference frequency

$$\frac{A}{2} \cos[(f_{vco} - f_D)\ t - \phi]$$

is passed through af narrow band filter (IF/A) at the intermediate

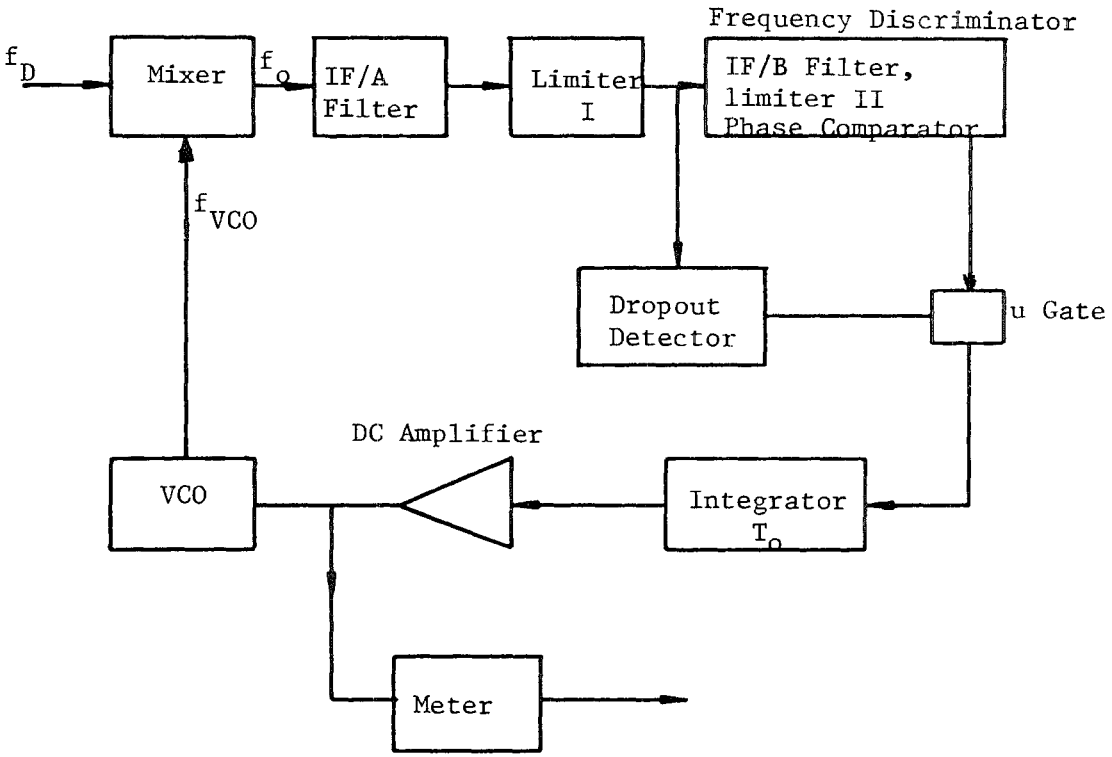

Figure D-3 : Block Diagram of the Frequency Tracker

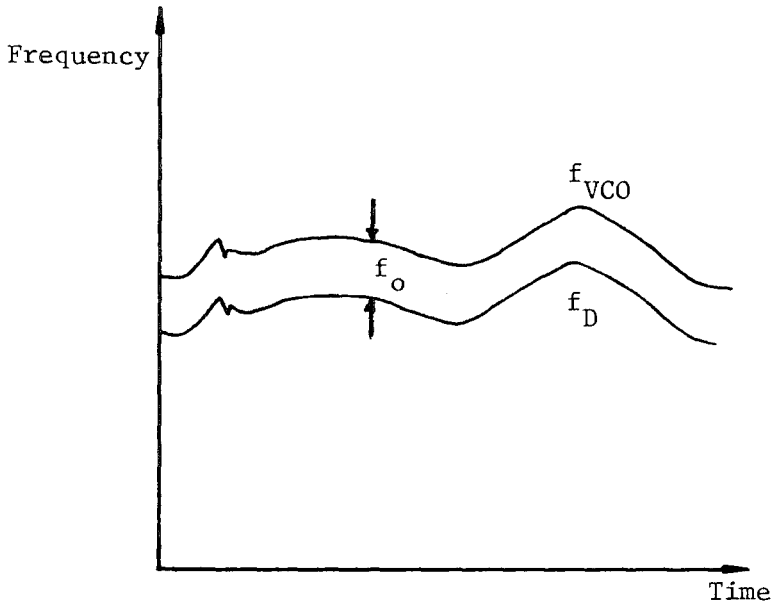

Figure D-4 : Frequency of VCO Tracking the Doppler Signal

frequency (IF), fo = $f_{vco} - f_D$ to remove as much noise as possible. The output is then fed into a limiter I which removes fluctuations in amplitude and the resultant signal is nearly a square waveform. This is then fed into a frequency discriminator. The frequency discriminator consists of another filter IF/B, a second limiter II, and a phase comparator which performs analogue multiplication. The filter IF/B only selects the fundamental (sinusoidal) component of the output f_i, from limiter I and feeds this into limiter II. This second IF circuit is arranged so that its output lags the input by 90^o at resonance, by more than 90^o at higher frequencies (than f_o) and less than 90^o for lower frequencies. The limiter II generates a rectangular waveform (as in limiter I) and the phase comparator performs an analogue multiplication. The output is then a rectangular wave, the product of two square waves. At resonance, this square wave will have a frequency $2f_o$ with a mark/space ratio which varies with the phase difference of the inputs. So if $f_i = f_o$, (the resonance condition) then after integration and DC amplification, the signal is fed into the vco and no change is necessary. If $f_i > f_o$, the phase introduced by IF/B, ϕ will be greater than 90^o. The resultant waveform will still fundamentally have a frequency of $2f_o$ but the mark/space ratio will be less than unity. This will then result in a small negative voltage which after integration and amplification will cause the f_{vco} to reduce a corresponding amount to bring it back to f_o. When $f_i < f_o$, a similar mechanism operates again but in the reverse manner. Consequently, the frequency from the voltage controlled oscillator f_{vco} tracks the Doppler signal f_D with a nearly constant f_o. (Figure D-4). The tracker output is obtained from the voltage which drives the vco. This voltage is linearly related to the Doppler frequency and hence to the fluid velocity (Equation (d-5)).

The frequency tracker normally requires a near-continuous input signal, but if this is not available, a dropout mechanism is employed to

hold the last known signal until a new signal arrives. The ratio of

$$\frac{\text{time during which no signal is processed}}{\text{total time}}$$

is referred to as the 'dropout rate'. There are three origins to this dropout mechanism (Durst, Melling and Whitelaw, 1976). The first is due to small concentration of particles, the second to an inability on the part of the tracker, to catch up with rapidly changing frequencies, and the third to signal amplitudes which are too small for the tracker. The first cause may be regarded as a random effect and can be made unimportant. The second introduces a systematic error which can be important especially for low turbulence intensity. The ability of the tracking system to follow rapid frequency changes depends on a number of instrument factors including the time constants of the components which constitute the tracking loop, the filter bandwidth and the location of the Doppler frequency on a particular instrument range. The influence of these factors also varies from range to range. The use of light-frequency shifting methods allows the location of the Doppler frequency at any preferred position and range, and hence can assist to optimise the use of the tracker.

D-4 Changes of Media

For the measurement of fluid flowing in a confined region such as pipe and channel flow, Equation (d-5a) has to be modified to include the effects of refraction due to the light passing through media of different refractive indices. Consider the example below of water flowing between two transparent walls. The surrounding medium is air.

Figures D-5a,b shows the effect on two laser beams when directed through a transparent wall and into another fluid, water in this case. The refractive indices of air, wall, water are denoted n_a, n_1, n_w, and $n_a < n_w < n_1$ is assumed.

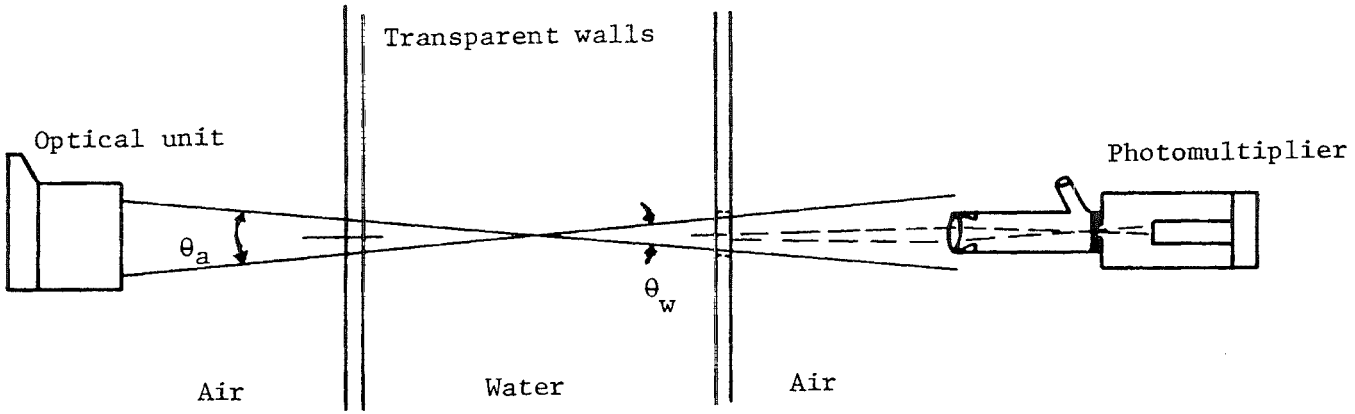

Figure D-5a : LDA Traversing Three Different Media

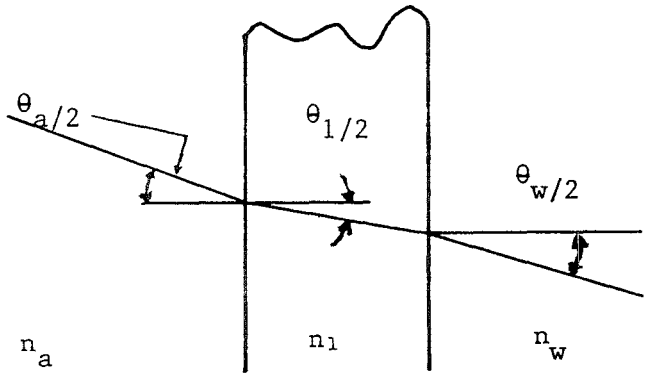

Figure D-5b : The Effect of Different Media on the Direction of the Laser Beam

From the law of optics, it is known that when a light beam travels from one medium to another medium which is optically more dense, the beam is refracted toward the normal of the surface element as illustrated in Figures D-5a,b. The relation between the two media and the angles of refraction is:

$$n_a \sin\frac{\theta_a}{2} = n_1 \sin\frac{\theta_1}{2} \quad . \quad \text{(Snell's law)} \qquad \text{(d-7)}$$

In the reverse situation of light travelling from a medium into an optically less dense medium, the light is bent away from the normal of the surface element and Equation (d-7) is still valid. In the case of the three media :

$$n_a \sin\frac{\theta_a}{2} = n_1 \sin\frac{\theta_1}{2} = n_w \sin\frac{\theta_w}{2} \qquad \text{(d-7a)}$$

The total effect of these refractions on the situation shown in Figure D-5a is shown in Figure D-6.

Instead of the point of focus and measurement being at P if the measurement is conducted in air, the point P moves to P' a distance of Δs. The increment Δs can be evaluated as the sum of effects of refraction due to the light passing first through the transparent wall, and then through the water.

Another relation which is of relevance is that expressing the change in wavelength due to the light wave travelling through media of different refractive indices. The relation is:

$$n_1 \lambda_1 = n_2 \lambda_2 \qquad \text{(d-8)}$$

where n_1, n_2 are the refractive indices and λ_1, λ_2 are the light wavelengths in that medium. This becomes important when evaluating the velocity of fluid using Equation (d-5).

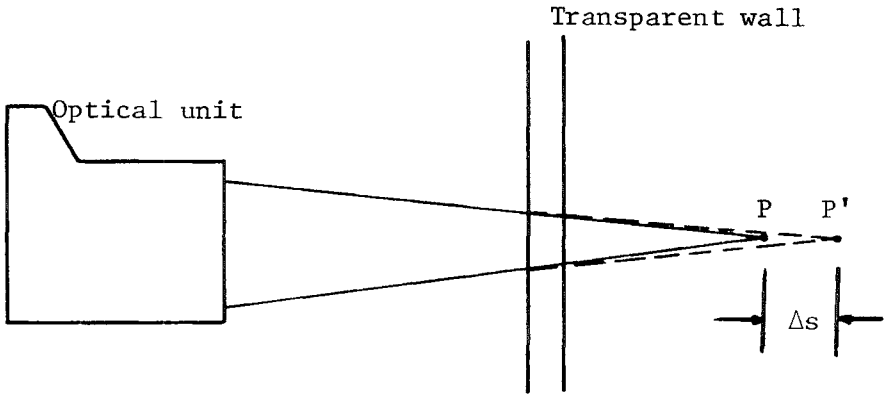

Figure D-6 : The Change in Position of Intersection Volume due to the Laser Beams Traversing Three Different Media

D-5 Electronic Processing Equipment

The equipment used to process the LDA signal is as illustrated in Figure 4.8. This included the purpose-built equipment of Disa, a Fast Fourier Transform (FFT) computing spectrum analysis, and a dual trace oscillosocope.

An explanatory sketch of the Disa equipment is given in Figure D-7. The high voltage source supplies power to the photomultiplier and the return signal is fed into the Frequency tracker pre-amplifier. From there it enters the tracker system and thence to the meter. The output signal is fed to the digital voltmeter which gives the mean component of velocity corresponding to the DC component of the signal. The same signal is fed to the signal conditioner which has facilities to supress DC signals, amplify and filter the AC signal as well as a summing and subtraction network. The input to and output from the frequency tracker are monitored on the dual trace oscilloscope. The output of the signal conditoner can then be fed to an RMS unit and the spectrum analyser. For this work, another RMS unit, built by Thermo Systems Incorp. (TSI) was used. This unit had a digital display as well as facility to measure DC.

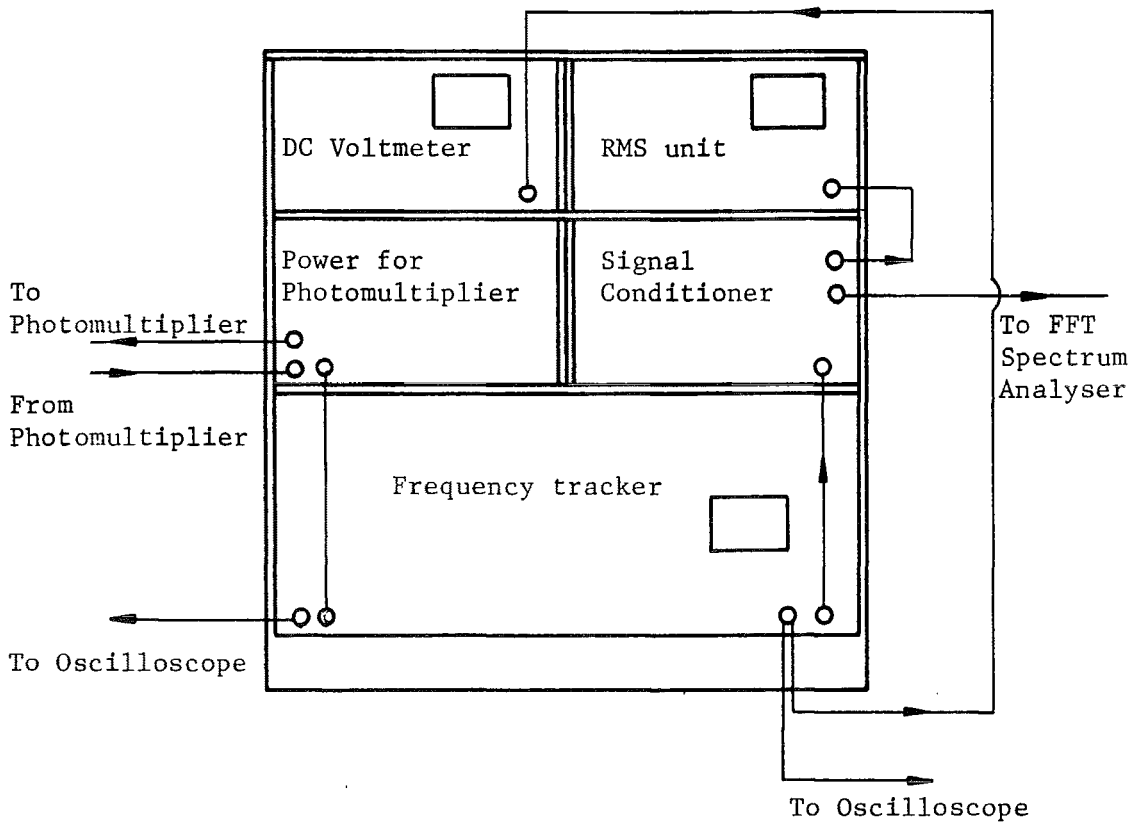

Figure D-7 : Block Diagram of Disa Electronic Equipment

APPENDIX E

THE ERRORS IN VELOCITY MEASUREMENT

Two types of errors can occur in the measurement of velocity components. The first type is that associated with the accuracy of the beam position and the second type is that associated with the velocity measurement.

The height of the measuring volume above the flat section can be estimated to within half of the beam diameter. This height was checked at 10 mm intervals during the experiment at the centre of the channel and at positions close to the sides of the channel. The most critical region was near the floor where there was a significant velocity gradient. Away from the floor, the mean and fluctuating components of velocity did not vary significantly as shown in Chapter 5. The accuracy of the height measurement was 0.33 mm which was half of the beam diameter. The region of greatest velocity shear is the lowest 10 to 20% of the boundary layer. This region was nominally 10 mm in depth, and an error of 0.33 mm represented 3.3% of the depth.

The error associated with the velocity measurement was a function of a number of factors. These factors included the calibration of the frequency tracker, the measurement of the intersection angle, and the variation of refractive index due to changes in the water temperature. The calibration of the frequency tracker is shown in Figure B-3 and it relates the output voltage to the Doppler frequency. By using the Bragg cells only the slope of the calibration curve is required.

The calibrations of Figure B-3 were carried out with a signal generator providing the source frequency tracker. This frequency was monitored by a frequency counter. The supply frequency was accurate to 5 Hz and over a range of 50 kHz this was an accuracy of 0.01%. The voltage

reading was accurate to 0.01 volt and for a minimum of 2 volts, represented less than a 1% error.

The velocity was evaluated from (see Appendix D) :

$$u = \frac{f \times \lambda}{2\sin(\frac{\theta}{2})} \times \frac{n_a}{n_w}$$

where f is the Doppler frequency, λ is the laser wavelength, $\frac{\theta}{2}$ is half the intersection angle, and n_a, n_w the refractive indices of air and water respectively.

The estimate of the intersection angle θ is dependent on the measurement of the lengths of the isosceles triangle which included θ (Figure 4.6b). The angle $\frac{\theta}{2} = \tan^{-1}(\frac{d_1}{\ell_1})$. The lengths d_1 and ℓ_1 can be estimated to an accuracy of half the laser beam diameter. These inaccuracies represent about 2% of d_1 and less tha 0.2% of ℓ_1.

The passing of the laser beams through water involved a change in the wavelength due to the change in refractive index. The refractive indices of air and water are :

$$n_a \ (760 \text{ mm Hg}, \ 20^oC) \ = \ 1.000277$$

and

$$n_w \ (0^oC) \ = \ 1.334$$

respectively (Disa, 1). The change in refractive index of water due to temperature changes has been given (Disa, 1) as $\Delta n_w = 0.0001/^oC$. For water temperatures of 14^oC to 18^oC, this represented $\Delta n_w = 0.0014$ to 0.0018. The errors introduced to n_w by assuming $n_w = 1.334$ were less than 0.5%. The accuracy of λ has been given (Disa, 1) as 0.4%.

The total of the accumulated errors in the measurement and evaluation of the velocity was the sum of the above errors and this amounted to less than 5%.

APPENDIX F

INVISCID STABILITY ANALYSIS OF A DENSITY INTERFACE SUBJECT TO A MEAN VELOCITY SHEAR

F-1 Introduction

Two layers of fluid of densities ρ_0 and ρ_1 move with mean velocities $\bar{U}_0$ and $\bar{U}_1$ (see Figure F-1). The aim is to evaluate the wavelength of the first instability and the corresponding phase velocity at the interface of the two layers of fluid.

F-2 The Kelvin-Helmholtz Instability

Let the two layers of fluid be infinitely deep and wide with the upper layer being freshwater with a free surface above and the lower layer being saltwater. The equations of motion and the boundary conditions have been presented by Krauss (1973) and will not be reprinted here. These equations reduce to the following fourth-order characteristic equation (see Krauss 1973) :

$$(\bar{U}_0 - c)^4 + \frac{\rho_1}{\rho_0}(\bar{U}_0 - c)^2 (\bar{U}_1 - c)^2 \coth \kappa h_0 \coth \kappa(H - h_0)$$

$$- \frac{g\rho_1}{\kappa\rho_0}\left[(\bar{U}_1 - c)^2 \coth \kappa(H - h_0) + (\bar{U}_0 - c)^2 \coth \kappa h_0\right]$$

$$+ \frac{g^2}{\kappa^2}\left[\frac{\rho_1 - \rho_0}{\rho_0}\right] = 0 \quad . \qquad \text{(f-1)}$$

The subscripts 0 and 1 refer to the upper and lower layers respectively. A sketch of the flow situation is shown in Figure F-1. The free surface is located at z=0 and the interface is located at $z = h_0$. The depth of

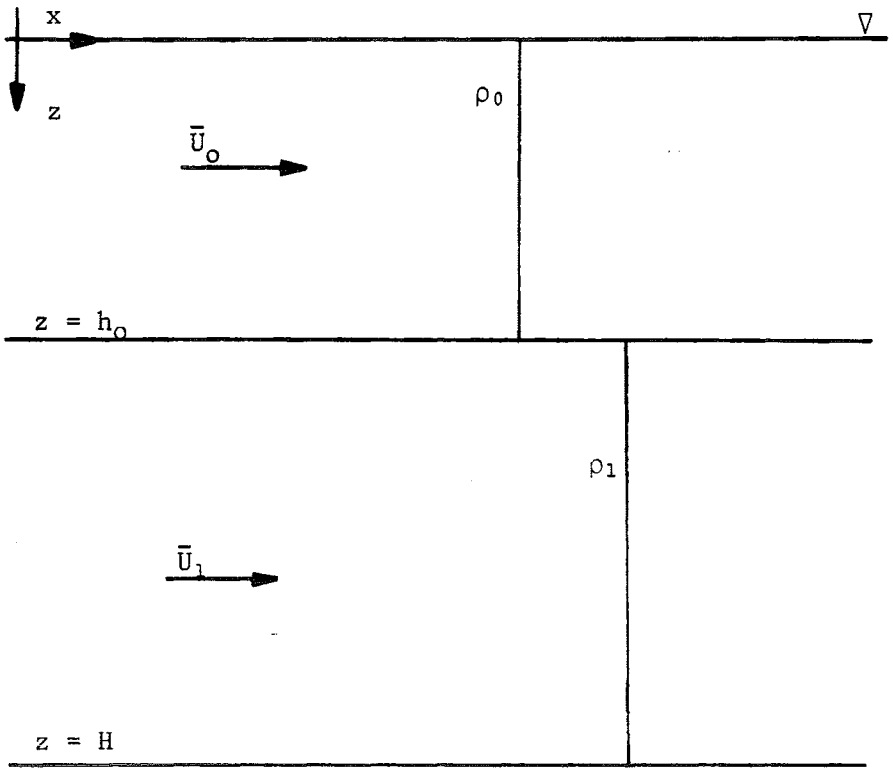

Figure F-1 : Sketch of Two Layers of Fluid of Densities ρ_0 and ρ_1 and Mean Velocities $\bar{U}_o$ and $\bar{U}_1$

the lower layer is h_1 so that $H = h_0 + h_1$ is the total depth. The wavenumber is $\kappa = \frac{2\pi}{\lambda}$ where λ is the wavelength, c is the phase velocity, and g is gravitational acceleration. The two layers of different densities are not given time for molecular diffusion to occur such that the mean density profile is a step function.

Equaton (f-1) is applicable to the situation where the velocity profiles are not necessarily determined by the density profile, unlike the tube experiments of Thorpe (1973) in which the velocity and density profiles were intimately related.

Equation (f-1) can be simplified if the terms involving the hyperbolic cotangent functions can be assumed to be nearly equal to 1, that is coth $\kappa(H-h_0) \sim 1$ and coth $\kappa h_0 \sim 1$ for the observed range of κh_0 and $\kappa(H-h_0)$. The validity of this assumption is discussed in Section F-6. In particular, if $\frac{h_0}{\lambda} > \frac{1}{2}$, then $\kappa h_0 > \pi$ and coth $\pi = 1.0037$. Similarly, with $\kappa(H-h_0) = 2\pi\ (H-h_0)/\lambda$, provided that $(H-h_0)/\lambda > \frac{1}{2}$, then $\kappa(H-h_0) > \pi$ and coth $\kappa(H-h_0)$ 1.00374. The behaviour of the hyperbolic cotangent is shown in Figure F-2. At very large positive x, coth x approaches the value of unity from above, hence the assumption that coth $x \sim 1$ for $x = \pi$ involves an error of less than 0.4%.

For two infinitely deep layers of water of different densities or if the terms coth κh_0 and coth $\kappa(H-h_0)$ are equal to unity, then Equation (f-1) reduces to :

$$(\bar{U}_0-c)^4 + \frac{\rho_1}{\rho_0}(\bar{U}_0-c)^2(\bar{U}_1-c)^2 - \frac{g}{\kappa}\frac{\rho_1}{\rho_0}\left[(\bar{U}_1-c)^2 + (\bar{U}_0-c)^2\right] + \frac{g^2}{\kappa^2}\left(\frac{\rho_1-\rho_0}{\rho_0}\right) = 0 \qquad \text{(f-2)}$$

or

$$\left[(\bar{U}_0-c)^2 - \frac{g}{\kappa}\right]\left[\rho_0(\bar{U}_0-c)^2 + \rho_1(\bar{U}_1-c)^2 - \frac{g}{\kappa}(\rho_1-\rho_0)\right] = 0 \qquad \text{(f-3)}$$

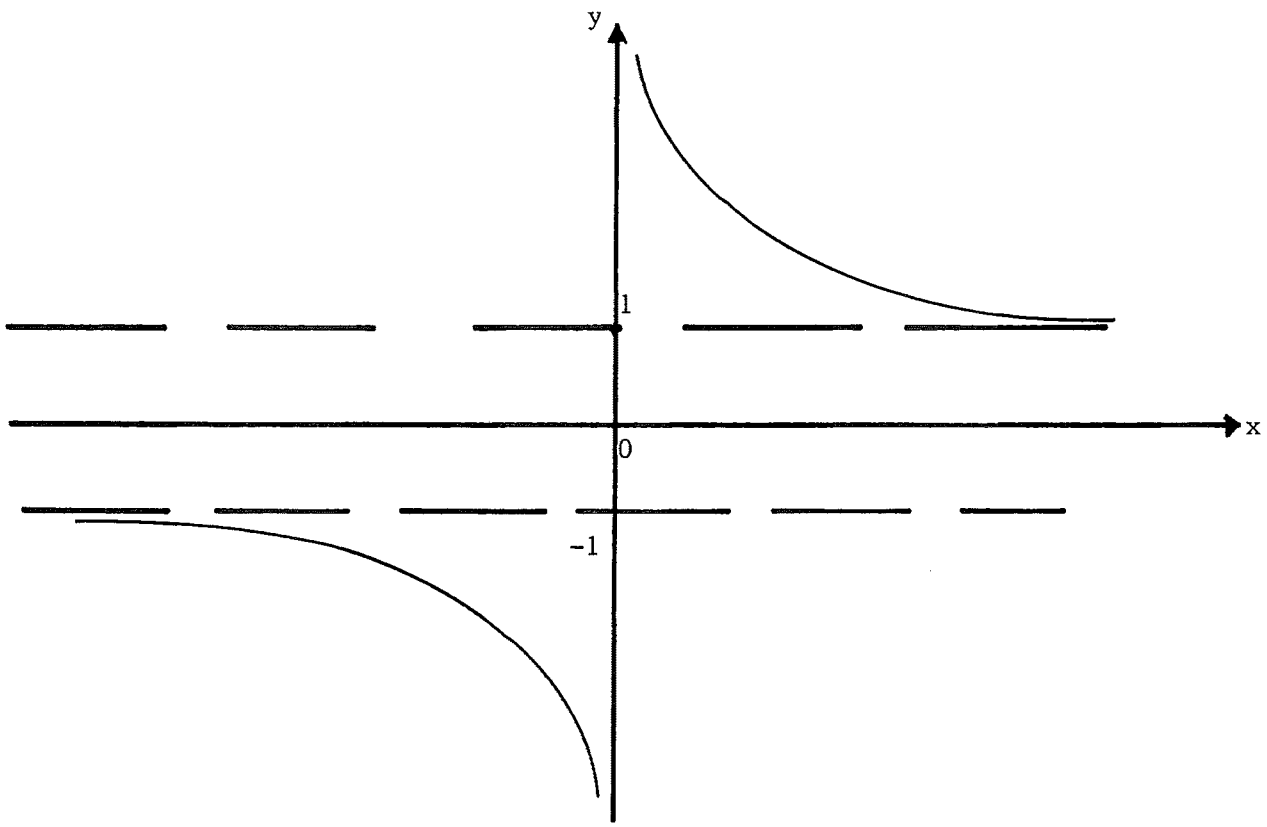

Figure F-2 : The Curve of y = coth x

where

$$(\overline{U}_o - c)^2 = \frac{g}{\kappa} \qquad \text{(f-4)}$$

is the solution for surface waves. The wave at the interface travels at a phase velocity obtained from :

$$\rho_o(\overline{U}_o - c)^2 + \rho_1(\overline{U}_1 - c)^2 - \frac{g}{\kappa}(\rho_1 - \rho_o) = 0 \qquad \text{(f-5)}$$

The solutions to Equation (f-5) are :

$$c = \frac{\rho_o\overline{U}_o + \rho_1\overline{U}_1}{\rho_o + \rho_1} \pm \sqrt{\frac{g}{\kappa}\frac{\rho_1-\rho_o}{\rho_1+\rho_o} - \frac{\rho_1\rho_o}{(\rho_1+\rho_o)^2}(\overline{U}_1 - \overline{U}_o)^2} \qquad \text{(f-6, f-7)}$$

Equations (f-6, f-7) represent the phase velocities of the interfacial waves. This result has been given by Lamb (1932), Turner (1973), Krauss (1973) and others. The first term of Equations (f-6, f-7) is a weighted mean velocity of both layers and the waves move relative to this velocity with a phase velocity which is related to the velocity shear across the interface. The stability of the interface is dependent on the terms under the radical of Equations (f-6, f-7). If

$$\frac{1}{\kappa} = \frac{\lambda}{2\pi} < \frac{(\overline{U}_o - \overline{U}_1)^2\,\rho_o\rho_1}{g\,(\rho_1^2 - \rho_o^2)} \qquad \text{(f-8)}$$

the square root is imaginary so that the disturbances are growing exponentially and stationary relative to the weighted mean velocity. This is the Kelvin-Helmholtz (K-H) instability and it occurs at a sufficiently large wavenumber for a given velocity difference. At very large wavenumbers, capillarity which is neglected under the inviscid assumption becomes important and limits the instability.

If the lower layer is stationary, $\bar{U}_1 = 0$, the most unstable or critical wavelength of the Kelvin-Helmholtz type is obtained by equating the radical of Equations (f-6, f-7) to zero, that is

$$\lambda_c = \frac{2\pi \bar{U}_o^2}{g} \left[\frac{\rho_o \rho_1}{\rho_1^2 - \rho_o^2} \right]$$

or

$$\lambda_c = \frac{2\pi \bar{U}_o^2}{g} \frac{1}{\frac{\Delta\rho}{\rho_1} \left[1 + \frac{\rho_1}{\rho_o} \right]} \qquad \text{(f-9)}$$

The phase velocity is

$$c = \frac{\bar{U}_o}{1 + \frac{\rho_1}{\rho_o}} \qquad \text{(f-10)}$$

If $\rho_1 \sim \rho_o$,

$$\lambda_c = \frac{\pi \bar{U}_o^2}{g \frac{\Delta\rho}{\rho_1}} \qquad \text{(f-11)}$$

and

$$c = \frac{\bar{U}_o}{2} \qquad \text{(f-12)}$$

F-3 A Hypothesis where $c = \bar{U}_o$

As an alternative to the hypotehsis that the observed waves arise as a result of Kelvin-Helmholtz shear instability, consider an analogy with the generation of surface waves by the wind (Phillips 1977), in which the dominant phase speed of the waves matches that of the wind (which in this case, is the speed of the upper layer). Then for $c = \bar{U}_o$ and $\bar{U}_1 = 0$ (lower layer stationary) Equations (f-6, f-7) reduce to :

$$(\rho_1 \bar{U}_o)^2 = \left[\frac{g}{\kappa} \frac{\rho_1 - \rho_o}{\rho_1 + \rho_o} - \frac{\rho_1 \rho_o}{(\rho_1 + \rho_o)^2} \bar{U}_o^2 \right] (\rho_1 + \rho_o)^2$$

or

$$\rho_1(\rho_0 + \rho_1)\,\overline{U}_0^2 = \frac{g}{\kappa}\,(\rho_1 + \rho_0)\,(\rho_1 - \rho_0) \qquad \text{(f-13)}$$

The most unstable wavenumber is :

$$\kappa = \frac{g}{\overline{U}_0^2}\,\frac{\Delta\rho}{\rho_1} \qquad \text{(f-14)}$$

and the corresponding wavelength is :

$$\lambda_c = \frac{2\pi\,\overline{U}_0^2}{g\,\frac{\Delta\rho}{\rho_1}} \qquad \text{(f-15)}$$

The phase velocity is $c = \overline{U}_0$ (f-16)

The values of λ_c and c given by Equations (f-15) and (f-16) are twice the values of the Kelvin-Helmholtz instability.

F-4 Comparison of the Inviscid Theory with Experiments

Observations of the density interface have shown that the waves at the interface did not grow exponentially but were maintained at near constant amplitude by the turbulence and velocity shear of the upper layer (see Figures 6.2a, 6.2b, 6.2c).

The wave crests were sufficiently well-defined to enable estimates of wavelength to be made from photographs and video-tape recordings. These observations of λ_c the critical wavelength, have been plotted against Ri_δ in Figure F-3. The critical wavelengths of the K-H instability, that is, Equation (f-9) and of Equation (f-15) have been included for comparison. The data in Figure F-3 shows that the observed

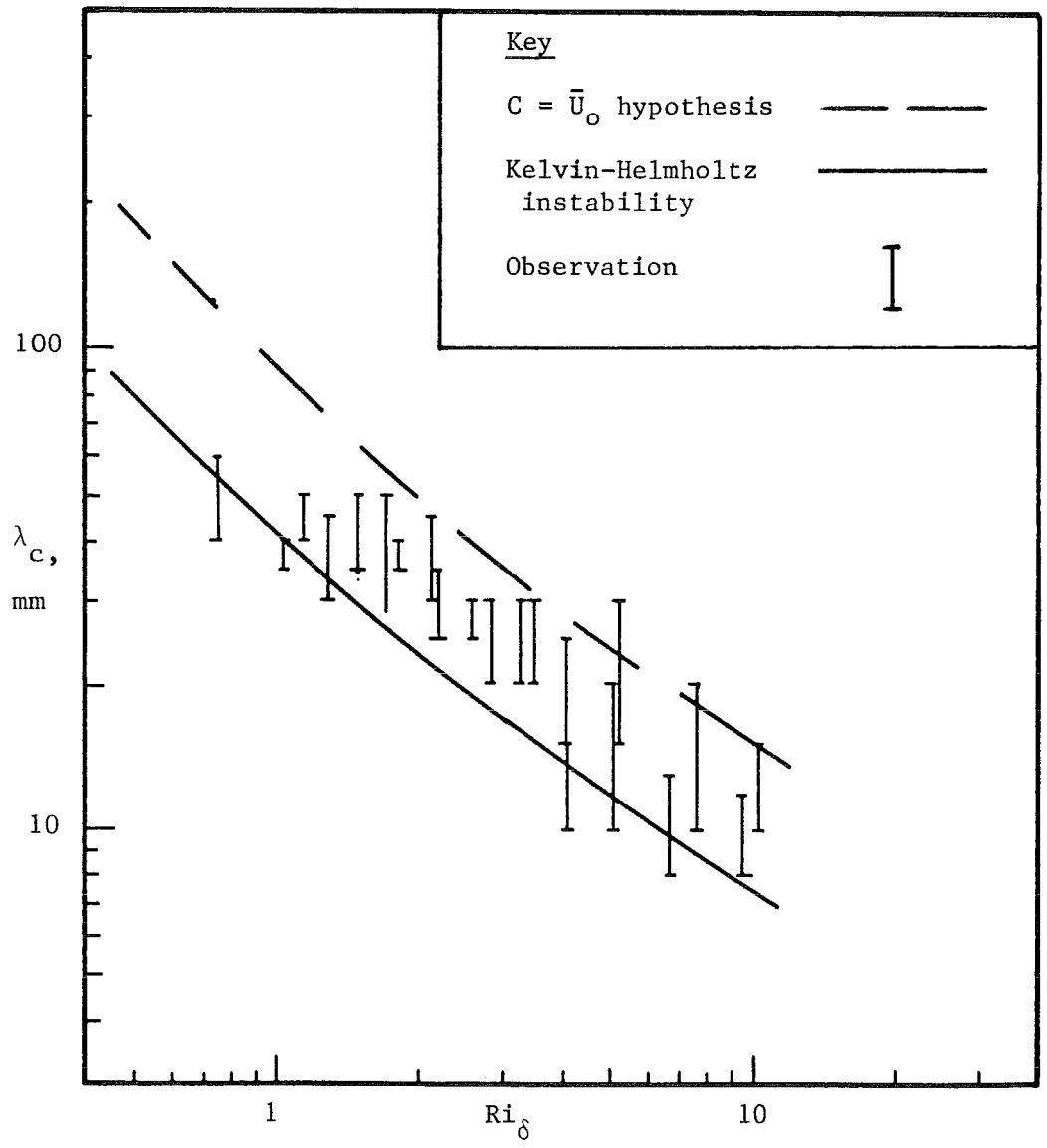

Figure F-3 : Observed Interfacial Wavelengths

wavelengths fall mainly between the curves given by Equations (f-10) and (f-15). For $Ri_\delta \simeq 1.0$, the observed wavelength is very similar to the K-H criterion while at very high values of Ri_δ the observed wavelengths appear to approach that for which $c = \bar{U}_o$. However, as shown in Figure F-3, some observations at $Ri_\delta \sim 5$ have indicated that small wavelengths of the order of the K-H instability have been recorded. The Kelvin-Helmholtz criterion and the criterion of phase velocity being equal to the mean velocity of the upper layer may thus be considered to be the lower and upper bounds respectively for the interfacial wave behaviour.

Some estimates of the phase velocity of the interfacial waves are shown in Figure F-4 for $\bar{U}_o = 0.0732$ m/s and $\bar{U}_o = 0.0813$ m/s and in Figure F-5 for $\bar{U}_o = 0.0909$ m/s. The phase velocity from the K-H criterion (Equation f-10) is also included as well as the velocity of the upper layer (Equation f-16). The data for the experiments are located between curves represnted by these two equations. In Figure F-4, the curves identified with (1) and (2) refer to $\bar{U}_o = 0.0732$ m/s and $\bar{U}_o = 0.0813$ m/s respectively.

Due to the unusual flow regime, some estimates of phase velocity were higher than $\bar{U}_o$. This situation occurred near the side of the channel whereas in the middle region of the channel the phase velocity was less. The waves were timed over a maximum distance of 290 mm and in some cases, particularly at large Ri_δ, only a distance of 160 mm was used. The shorter distance was used because the wave profile was not easily discernible near the upstream region of the cavity where the wave heights were of order 1-2 mm. The travel time of the waves over the 290 mm was about 4 seconds and 2 seconds over the 160 mm distance. As such, this estimate of travel time was made a number of times so that an average time was obtained. If an error of 0.5 seconds occurred, this imposed an error of 25% in the phase velocity.

Most of the estimates of phase velocity are located between the curves given by Equations (f-10) and (f-16). The presentation of data in

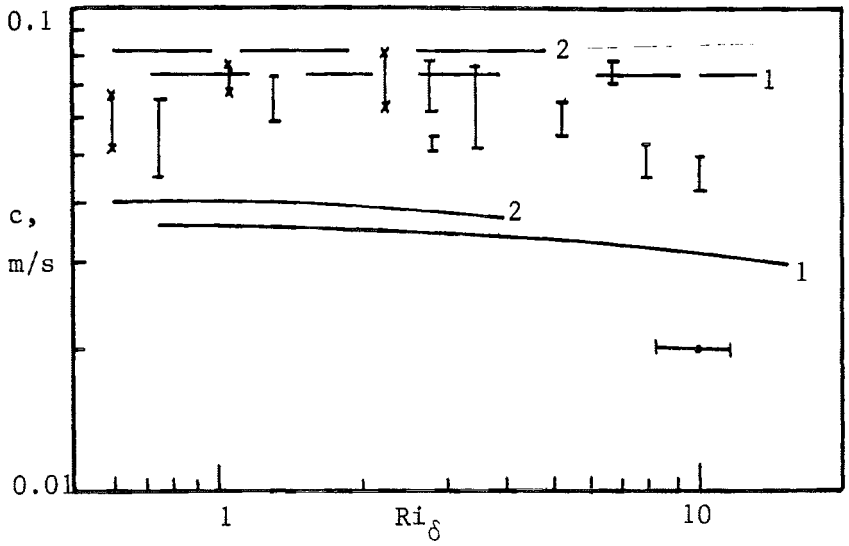

Figure F-4 : Observed Values of Phase Velocity of Interfacial Waves, $\bar{U}_o$ = 0.0732 m/s. $\bar{U}_o$ = 0.0813 m/s

Key		
$\bar{U}_o$, m/s	0.0732	0.0813
c = $\bar{U}_o$ hypothesis	— — 1	— — 2
Kelvin-Helmholtz instability	——— 1	——— 2
Observation	I	⧗

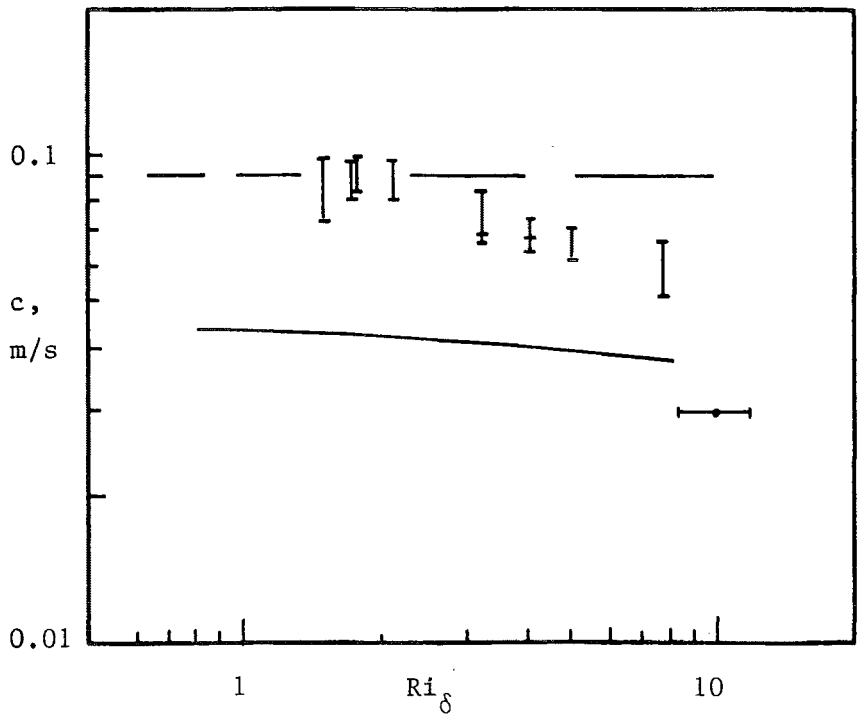

Figure F-5 : Observed Values of Phase Velocity of Interfacial Waves, $\bar{U}_o$ = 0.0909 m/s

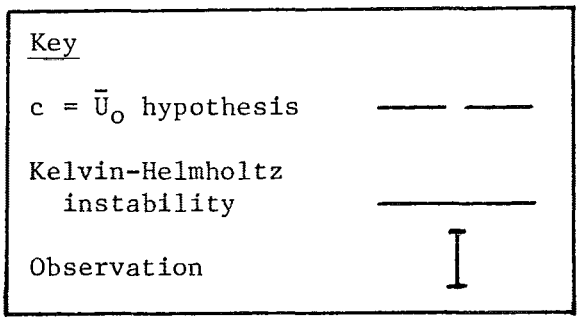

Figures F-3, F-4, and F-5 support the suggestion that the two inviscid analyses of the Kelvin-Helmholtz instability and the hypothesis that $c = \overline{U}_o$ can provide lower and upper bounds for the interfacial wave behaviour.

F-5 Further Remarks on High Richardson Number Behaviour

The results presented in Section F-3 show that the Kelvin-Helmholtz instability is a good model of the initial wave behaviour at small Richardson numbers. However, at larger Richardson numbers, the Kelvin-Helmholtz instability does not suitably describe the behaviour. A comparison of the observations for $Ri_\delta \sim 2$ with the study by Browand and Winant (1973, Figure 4) suggets that the observed interfacial waves may be of the type called Holmboe (1962) waves. These waves (named by Browand and Winant 1973) do not roll up as do the Kelbvin-Helmholtz billows (Thorpe 1973), but retain some wave shape with sharp crests and troughs. These Holmboe waves are shown in Figure F-6.

There has not been much work done on these Holmboe waves or on the breaking mechanism when fluid is shed or ejected from the crests. However, some preliminary work carried out by Yoshida (1977) and Thorpe (1978) as well as the earlier work by Holmboe (1962) and Browand and Winant (1973) provide some ideas.

F-6 The Effect of the Cavity Depth on the Interfacial Behaviour

In Section F-2 it was assumed that $\coth \kappa h_o \sim 1$ and $\coth \kappa(H-h_o) \sim 1$. A check on the ratios $\frac{h_o}{\lambda_c}$ and $(H-h_o)/\lambda_c$ is necessary to justify these assumptions. The largest observed wavelength was of order 60 mm and the depth of the cavity was nominally 32.5 mm. The upper layer depths h_o were 135, 105, and 75 mm for each of the three flow regimes.

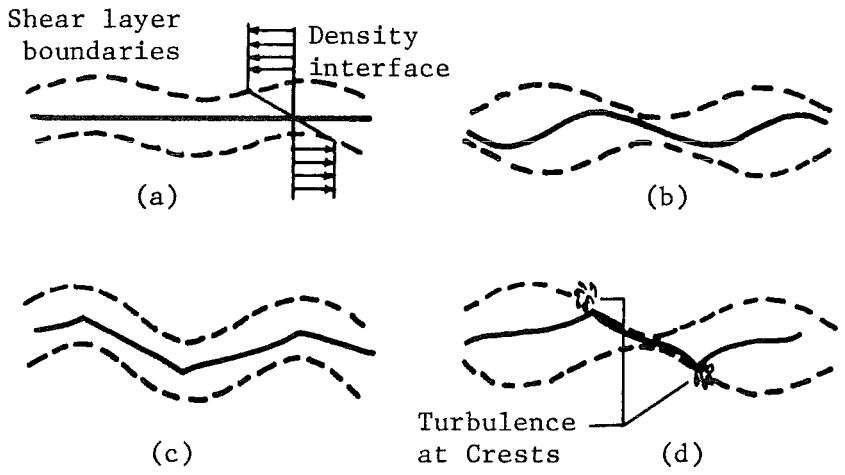

Figure F-6 : Sketch of Holmboe Waves (after Browand and Winant 1973)

The ratios for the largest λ_c are

$$(H-h_o)/\lambda_c \sim \tfrac{1}{2}$$

and

$$h_o/\lambda_c \gtrsim 1.25$$

so that the errors incurred in the above assumptions were of order 1%. The bottom of the cavity had a very small influence on the behaviour of the interface and the waves were behaving as deep water waves.

APPENDIX G

THE DERIVATION OF THE SLOPE OF THE INTERFACE

G-1 Introduction

Observations of the density interface subjected to a mean velocity shear have shown that the interface tilts at a small angle ϕ to the horizontal. In these experiments the interface was disrupted by waves, wisps of saline solution were thrown upwards and local regions of recirculating flow were present at the upstream and downstream ends of the cavity. The aim of this appendix is to compare the observed slope of the interface with a calculated slope of some of the experiments.

G-2 The Flow Structure Within the Cavity

The flow structure in the cavity was not measured but observations and reviews of photographs and video-tape recordings showed that the cavity flow was laminar in experiments in which the ratio of interfacial wavelength to cavity depth was less than one and the Richardson number greater than 2. In experiments for which $Ri_\delta < 2$, the wavelength was the same or greater than the cavity depth, that is $\lambda_c/h_1 \gtrsim 1$. Figure 6.2a showed the interfacial wave pattern of an experiment for which $Ri_\delta = 1.05$ and the ratio $\lambda_c/h_1 \sim 2$. The relatively large wave amplitude would have affected the flow structure of the cavity. In Figures 6.2b and 6.2c, the waves were shorter in length and much smaller in amplitude. Review of video-tape recordings did not suggest that the cavity flow was turbulent.

The replacement saline solution through the floor at both the upstream and downstream ends also affected the cavity flow although these effects were considered to be localised.

G-3 The Interfacial Slope Under Ideal Conditions

The slope of the interface can be estimated if a number of assumptions are made. These assumptions are :

(i) The upper layer flow does not change due to the change in surface roughness from perspex to saline solution. The flow characteristics upstream of and over the cavity are considered to be the same.

(ii) The neglect of all of the following effects which involve momentum transfer :

(a) The localised regions of recirculating flow at the upstream and downstream ends of the cavity.

(b) The generation of the interfacial waves.

(c) The sidewall stresses of the cavity and secondary motions within the cavity.

(d) The entrainment of the saline solution by the upper layer.

A sketch of the flow situation is shown in Figure G-1 with the upper layer being contained in an open channel of rectangular cross-section. This upper layer flows over a cavity which lies in the floor of the channel. The channel floor is horizontal and the upper layer is driven by a hydrostatic pressure gradient. Shear stresses on the channel floor τ_o and on the walls τ_w oppose the upper layer flow. The channel is wide and shallow so that $\tau_o \times A_o$ is assumed to be much greater than $\tau_w \times A_w$ where A_o and A_w are the wetted areas of the floor and

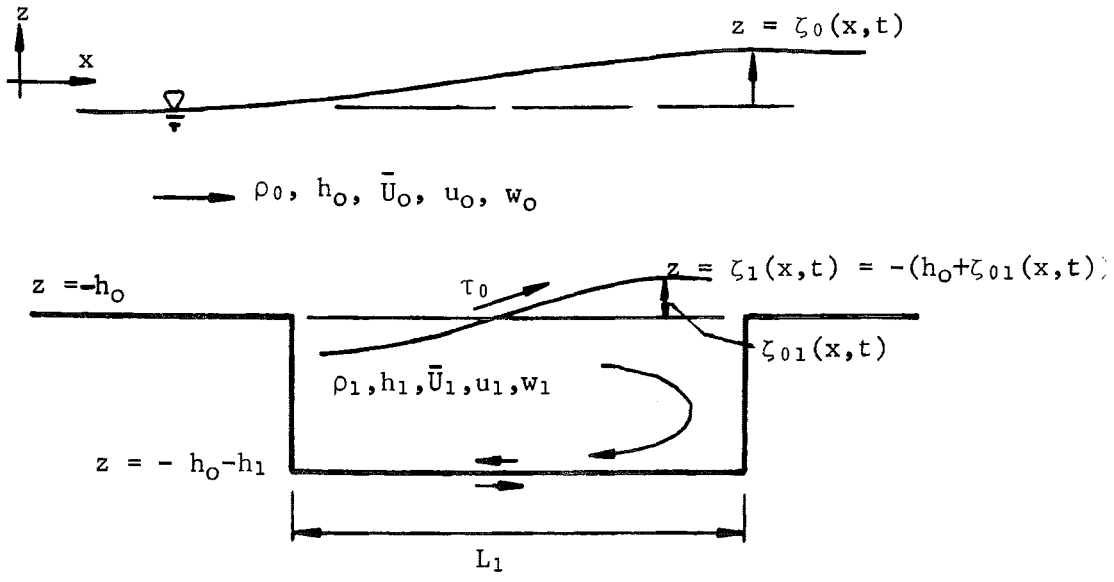

Figure G-1 : Motion of Water Layer of Density ρ_0 over Cavity of Saltwater of Density ρ_1

sides respectively. Thus it is also assumed that τ_w can be neglected.

The motion in the water or upper layer is turbulent while the motion in the cavity or lower layer is laminar. The mean level of the free surface is z = 0 and ζ_o is a perturbation about the mean. The interface is located at z = - h_o and ζ_{o_1} is the perturbation of the interface about z = - h_o. The perturbation can also be written as :

$$z = \zeta_1(x,t) = -(h_o - \zeta_{o_1}) \quad .$$

The hydrostatic assumption would be valid over most of the channel width except very close to the sides where there is an inflow. Near the centre of the channel, in the upper layer, the hydrostatic assumption implies that the vertical velocity component is zero, and the streamlines are nearly parallel (Henderson 1966). In the lower layer, the streamlines are nearly parallel in regions away from the endwalls of the cavity.

For the upper layer, the z-momentum equation reduces to :

$$\frac{\partial}{\partial z} p_o = - \rho_o g \quad . \qquad (g\text{-}1)$$

Using η as a dummy variable, integrate in the z-direction from η = z to $\eta = \zeta_o$ to obtain :

$$\int_z^{\zeta_o} \frac{\partial}{\partial z} p_o \, d\eta = - \int_z^{\zeta_o} \rho_o g \, d\eta$$

$$p_o\Big|_{\eta = \zeta_o} - p_o\Big|_{\eta = z} = \rho_o g(z - \zeta_o)$$

Now $p_o\Big|_{\eta = \zeta_o}$ is also the atmospheric pressure p_a, hence the above equation

can be written as :

$$p_o\Big|_{\eta = z} - p_a = \rho_o g(\zeta_o - z) \quad . \tag{g-2}$$

Write $p_o\Big|_{\eta = z} = p_o(z)$ and differentiate Equation (g-2) w.r.t. x to obtain :

$$\frac{\partial}{\partial x} p_o(z) = \frac{\partial}{\partial x} p_a + \rho_o g \frac{\partial}{\partial x} \zeta_o \tag{g-3}$$

For the lower layer, the momentum equation in the z direction is :

$$\frac{\partial}{\partial z} p_1 = - \rho_1 g \tag{g-4}$$

Integrating in the z direction from z to ζ_1

$$\int_z^{\zeta_1} \frac{\partial}{\partial z} p_1 \partial\eta = \int_z^{\zeta_1} -\rho_1 g d\eta$$

or

$$p_1\Big|_{\eta = \zeta_1} - p_1\Big|_{\eta = z} = - \rho_1 g(\zeta_1 - z)$$

or

$$p_1(z) = \rho_1 g(-h_o + \zeta_{o1} - z) + p_1(\zeta_1) \tag{g-5}$$

where

$$p_1(z) = p_1\Big|_{\eta = z} \quad , \quad p_1(\zeta_1) = p_1\Big|_{\eta = \zeta_1}$$

and

$$\zeta_1 = - h_o + \zeta_{o1} \quad .$$

The term $p_1(\zeta_1)$ is equal to the pressure in the upper layer for $z = \zeta_1$ and

Equation (g-2) can be substituted into (g-5) to give :

$$p_1(z) = \rho_1 g(-h_o+\zeta_{o1}-z) + p_o(\zeta_1)$$

or

$$\begin{aligned} p_1 &= \rho_1 g(-h_o+\zeta_{o1}-z) + \rho_o g(\zeta_o-\zeta_1) + p_a \\ &= \rho_1 g(-h_o+\zeta_{o1}-z) + \rho_o g(\zeta_o+h_o-\zeta_{o1}) + p_a \\ &= -\rho_1 gz - g(\rho_1-\rho_o)(h_o-\zeta_{o1}) + \rho_o g\zeta_o + p_a \\ &= -\rho_1 gz + g\Delta\rho\zeta_1 + \rho_o g\zeta_o + p_a \quad . \end{aligned} \tag{g-6}$$

where

$$\Delta\rho = \rho_1 - \rho_o \quad .$$

Differentiate Equations (g-6) with respect to x to obtain :

$$\frac{\partial}{\partial x} p_1 = g\Delta\rho \frac{\partial \zeta_1}{\partial x} + \rho_o g \frac{\partial \zeta_o}{\partial x} + \frac{\partial}{\partial x} p_a$$

$$= g\Delta\rho \frac{\partial \zeta_{o1}}{\partial x} + \rho_o g \frac{\partial \zeta_o}{\partial x} + \frac{\partial}{\partial x} p_a \quad .$$

The atmospheric pressure gradient in the x-direction is negligible as the air above the water is not in motion, hence :

$$\frac{\partial}{\partial x} p_1 = g\Delta\rho \frac{\partial \zeta_{o1}}{\partial x} + \rho_o g \frac{\partial \zeta_o}{\partial x} \tag{g-7}$$

Consider a small element of fluid of dimensions dx by dz by 1 and the flow is two dimensional (Figure G-2a).

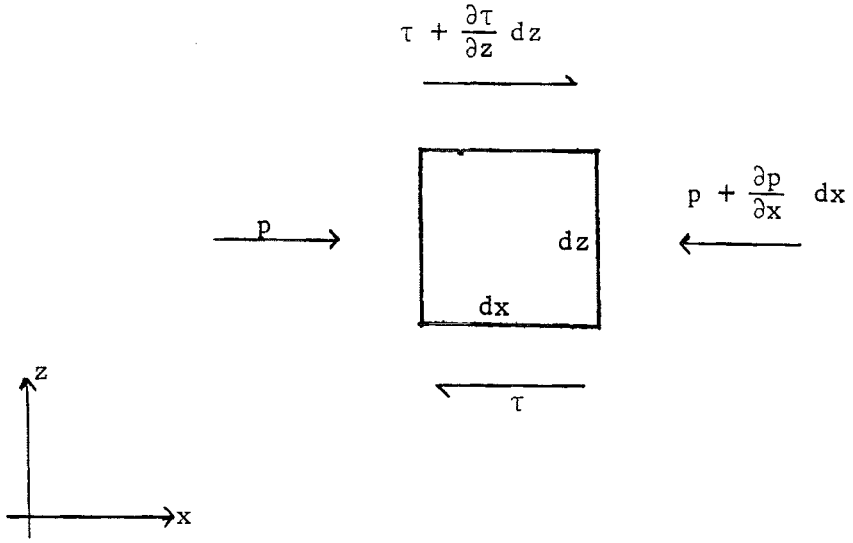

Figure G-2a : Forces in x-direction on a Two-dimensional Fluid Element

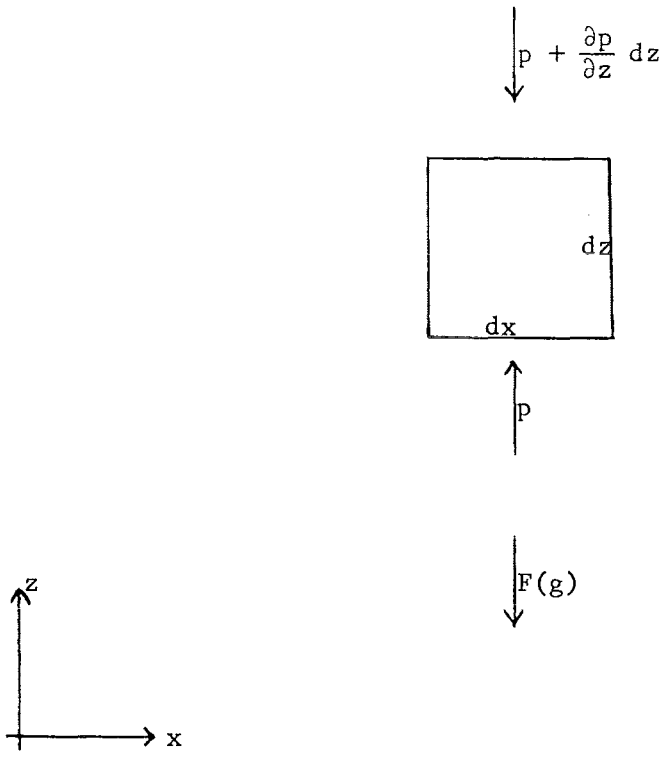

Figure G-2b : Forces in z-direction on a Two-dimensional Fluid Element

Summing the forces in the x-direction, gives :

$$\rho \frac{\partial u}{\partial t} \, dxdz = (\tau + \frac{\partial \tau}{\partial z} dz)dx - \tau dx$$

$$- (p + \frac{\partial p}{\partial x} dx)dz + pdz$$

or

$$\rho \frac{\partial u}{\partial t} = \frac{\partial \tau}{\partial z} - \frac{\partial p}{\partial x} \qquad \text{(g-8)}$$

A similar analysis in the z-direction (Figure G-2b), gives:

$$\rho \frac{\partial w}{\partial t} = pdx - (p+\frac{\partial p}{\partial z} dz)dx - F(g)dxdz$$

$$= \frac{\partial p}{\partial z} dzdx - F(g)dxdz \quad . \qquad \text{(g-9)}$$

where F(g) is the contribution due to g. In steady state, F(g) is balanced by $\partial p/\partial z$. The momentum equation for the upper layer is, after combining Equations (g-3) and (g-8) :

$$\left(\rho_o \frac{\partial u}{\partial t}\right)_o = \frac{\partial \tau}{\partial z} - \rho_o g \frac{\partial}{\partial x} \zeta_o \qquad \text{(g-10)}$$

The momentum equation for the lower layer is, from Equations (g-7) and (g-8) :

$$\left(\rho_1 \frac{\partial u}{\partial t}\right)_1 = \frac{\partial \tau}{\partial z} - g\Delta\rho \frac{\partial}{\partial x} \zeta_{o1} - \rho_o g \frac{\partial}{\partial x} \zeta_o \qquad \text{(g-11)}$$

Integrate Equation (g-10) from $-h_o$ to 0 :

$$\int_{-h_o}^{o} \rho_o \frac{\partial u}{\partial t}\, dz = \int_{-h_o}^{o} \frac{\partial \tau}{\partial z}\, dz - \rho_o g \int_{-h_o}^{o} \frac{\partial}{\partial x} \zeta_o\, dz \qquad \text{(g-10a)}$$

or

$$\rho_o \int_{-h_o}^{o} \frac{\partial u}{\partial t}\, dz = \int_{-h_o}^{o} \frac{\partial \tau}{\partial z}\, dz - \rho_o g \frac{\partial \zeta_o}{\partial x} \int_{-h_o}^{o} dz$$

The boundary conditions for Equation (g-10a) are :

$$\tau(0) = 0 \quad , \quad \tau(-h_o) = \tau_o \quad .$$

Consistent with the two-dimensional flow assumption, write :

$$\int_{-h_o}^{o} \frac{\partial u}{\partial t}\, dz = \frac{\partial}{\partial t} \bar{U}_o\, h_o$$

where $\bar{U}_o$ is the bulk mean velocity of the layer.

Equation (g-10a) can be written as :

$$\rho_o \frac{\partial}{\partial t} \bar{U}_o h_o = - \tau_o - \rho_o g h_o \frac{\partial}{\partial x} \zeta_o \quad . \qquad \text{(g-12)}$$

Integrate Equation (g-11) from $-h_o-h_1$ to $-h_o$

$$\int_{-h_o-h_1}^{-h_o} \rho_1 \frac{\partial u}{\partial t}\, dz = \int_{-h_o-h_1}^{-h_o} \frac{\partial \tau}{\partial z}\, dz - \int_{-h_o-h_1}^{-h_o} g\Delta\rho\, \frac{\partial}{\partial x}\, \zeta_{o1}\, dz - \int_{-h_o-h_1}^{-h_o} \rho_o g\, \frac{\partial}{\partial x}\, \zeta_o dz \qquad \text{(g-11a)}$$

$$-\rho_1 \int_{-h_o-h_1}^{-h_o} \frac{\partial u}{\partial t}\, dz = \int_{-h_o-h_1}^{-h_o} \frac{\partial \tau}{\partial z}\, dz - g\Delta\rho\, \frac{\partial \zeta_{o1}}{\partial x} \int_{-h_o h_1}^{-h_o} dz - \rho_o g\, \frac{\partial \zeta_o}{\partial x} \int_{-h_o-h_1}^{-h_o} dz$$

The boundary conditions for Equation (g-11a) are :

$$\tau(-h_o) = \tau_o \quad , \quad \tau(-h_o - h_1) = \tau_1 \quad .$$

For two-dimensional flow, write :

$$\int_{-h_o-h_1}^{-h_o} \frac{\partial u}{\partial t}\, dz = \frac{\partial}{\partial t}\, \overline{U}_1\, h_1$$

where $\overline{U}_1$ is the bulk mean velocity of the layer.

Then Equation (g-11a) can be written as :

$$\rho_1 \frac{\partial}{\partial t}\, \overline{U}_1 h_1 = \tau_o - \tau_1 - g\Delta\rho h_1 \frac{\partial}{\partial x}\, \zeta_{o1} - \rho_o g h_1 \frac{\partial}{\partial x}\, \zeta_o \qquad \text{(g-13)}$$

write Equations (g-12) and (g-13), as :

$$\frac{\partial}{\partial t}\, \overline{U}_o = -\frac{\tau_o}{\rho_o h_o} - g\, \frac{\partial}{\partial x}\, \zeta_o \qquad \text{(g-14)}$$

$$\frac{\partial}{\partial t}\, \overline{U}_1 = \frac{\tau_o - \tau_1}{\rho_1 h_1} - g\, \frac{\Delta\rho}{\rho_1}\, \frac{\partial}{\partial x}\, \zeta_{o1} - g\, \frac{\rho_o}{\rho_1}\, \frac{\partial}{\partial x}\, \zeta_o \qquad \text{(g-15)}$$

For steady state in the upper and lower layers, Equations (g-14) and (g-15) become :

$$\frac{\partial}{\partial x}\zeta_o = -\frac{\tau_o}{g\rho_o h_o} \qquad \text{(g-16)}$$

and

$$\frac{\partial}{\partial x}\zeta_{o1} = -\frac{\rho_o}{\Delta\rho}\frac{\partial}{\partial x}\zeta_o + \frac{\tau_o - \tau_1}{g\Delta\rho h_1} \qquad \text{(g-17)}$$

The free surface slope is shown in Equation (g-16) to be supported by the shear stress on the floor of the channel. Combine Equations (g-16) and (g-17) to obtain:

$$\frac{\partial}{\partial x}\zeta_{o1} = \frac{\tau_o}{g\Delta\rho h_o} + \frac{\tau_o - \tau_1}{g\Delta\rho h_1}$$

$$= \frac{1}{g\Delta\rho}\left(\frac{\tau_o}{h_o} + \frac{\tau_o - \tau_1}{h_1}\right) \qquad \text{(g-18)}$$

Equation (g-18) gives the interfacial slope in terms of the shear stresses at the interface and at the bottom of the cavity plus the depths of the two layers and the density difference.

The shear stress at the bottom of the cavity is $\tau_1 = -\frac{\tau_o}{2}$ (Baines and Knapp 1965) if the flow in the cavity is laminar and is driven by a shear stress at the interface. The fluid near the interface is forced downstream, down the downstream end, against the mean flow, along the bottom and up the windward end of the cavity (Baines and Knapp 1965). The resulting Couette-Poiseuille flow is valid where the streamlines are parallel and does not include the secondary effects of shear stress at the cavity wall, waves at the interface, mass transfer due to entrainment,

and the influx of replacement saline solution.

G-4 The Interfacial Slope in Experimental Conditions

The slope of the interface in an experiment is affected by a number of factors which were assumed to be negligible in Section G-3. Equation (g-18) has to be modified to include the effects of these factors. The modified form of Equation (g-18) is :

$$\frac{\partial}{\partial x}\,\zeta_{o1} = \frac{1}{g\Delta\rho}\left[\frac{\tau_o}{h_o} + \frac{\tau_o - \tau_1}{h_1}\right] + \frac{1}{g\Delta h_1}\left[\tau_s + \tau_e + \tau_i\right] \qquad \text{(g-19)}$$

where

τ_s = sidewall stresses and secondary motions,

τ_e = stress required for entrainment of cavity fluid,

τ_i = stress required to generate interfacial waves.

The difficulty in evaluating Equation (g-19) arises from attempting to estimate the contribution of these extra terms. As no measurements of the particular quantities were made, the estimates are based on order of magnitude arguments.

The term τ_s accounts for contributions from the cavity sidewall stresses, and any secondary motions and dissipation mechanisms not directly accounted by the other terms. The distribution of shear stress with depth shows a sign change in the Couette-Poiseuille flow pattern such that $\frac{\tau(z)}{\tau_o}$ is equal to 1 at the interface, and $\frac{\tau(z)}{\tau_o} = -\frac{1}{2}$ at the bottom of the cavity (Baines and Knapp 1965). The cavity sidewall shear stress should not exceed τ_o and may be the order of the stress on the cavity floor. This sidewall shear stress can be estimated to be in the range $\frac{\tau_o}{10}$ to τ_o. The secondary motions are usually of the order of one-tenth of the mean velocity. These motions then scale as $\frac{u_*}{10}$ and the contribution

to τ_s is $\frac{\rho o u_*^2}{100}$. Any other dissipative effects should also scale as $\frac{\rho o u_*^2}{100}$ as the effects would be of the same order as the secondary motions. These last two effects are small compared to the shear stress term and can be neglected so τ_s scales in the range $\frac{\tau_o}{10}$ to τ_o.

The stress required to entrain the cavity fluid τ_e can be scaled with $E_*^2 = \left[\frac{u_e(F)}{u_*}\right]^2$. The variation of E_* with Richardson number is given by :

$$E_* = 0.016\ Ri_\delta^{-\frac{3}{2}} \pm 25\% \qquad (6.13)$$

The laminar flow in the cavity is consistent with Ri > 2 then $10^{-4} < E_* < 10^{-2}$. As a typical value, let $E_* = 5x10^{-3}$.

Then :

$$E_*^2 = 2.5 \times 10^{-5}$$

or

$$\frac{u_e(F)^2}{g'h_1} = 2.5x10^{-5}\ \frac{u_*^2}{g'h_1} \qquad (g\text{-}20)$$

Equation (g-20) shows that the stress required to cause entrainment of cavity fluid is of order $10^{-5}\ \tau_o$ and can be neglected. Hence the contribution to the interfacial slope can also be neglected.

The estimate of τ_i is unknown even though there has been some work done on estimating a similar stress component for waves on the ocean surface. Csanady (1982) has suggested that for the waves on the ocean surface, this stress component scaled as $\frac{\overline{u'^2}}{gL_b}$ where L_b is a length scale for the breaker zone and $\overline{u'^2}$ scaled as the Reynolds stress. As there is

no known estimate for interfacial waves, it was decided not to include a value of τ_i.

After neglecting τ_e and τ_i, Equation (g-19) becomes :

$$\frac{\partial}{\partial x}\ \zeta_{o1} = \frac{1}{g\Delta\rho}\ \left[\frac{\tau_o}{h_o} + \frac{\tau_o - \tau_1}{h_1}\right] + \frac{\tau_s}{g\Delta\rho h_1} \qquad \text{(g-21)}$$

Choose τ_s to be $\frac{\tau_o}{10}$ as a conservative estimate, then Equation (g-21) becomes :

$$\frac{\partial}{\partial x}\ \zeta_{o1} = \frac{1}{g\Delta\rho}\ \left[\frac{\tau_o}{h_o} + \frac{1.5\ \tau_o}{h_1} + \frac{\tau_o}{10h_1}\right]$$

or

$$\frac{\partial}{\partial x}\ \zeta_{o1} = \frac{\tau_o}{g\Delta\rho h_1}\ \left[1.6 + \frac{h_1}{h_o}\right]$$

In these experiments, $\frac{h_1}{h_o}$ varied between 0.24 and 0.43. A small number of experiments were photographed showing the slope of the interface at the side of the cavity which was 295 mm from the centreline. These are shown in Figures G-3a,b,c. The slope of the interface at the 260 mm station has been evaluated using Equation (g-21) and compared with the measured slopes from the photographs of the three experiments. This data is shown in Table G-1.

Table G-1 : Comparison of Calculated and Measured Interfacial Slopes

Ri_δ	$\frac{\partial\zeta_{o1}}{\partial x}$ (calculated)$_{260}$	$\frac{\partial\zeta_{o1}}{\partial x}$ (measured)$_{295}$	$\frac{\partial\zeta_{o1}/\partial x\ \text{(calculated)}_{260}}{\partial\zeta_{o1}/\partial x\ \text{(measured)}_{295}}$
2.85	5.7×10^{-3}	24.1×10^{-3}	0.24
4.04	5.0×10^{-3}	20.7×10^{-3}	0.24
7.95	2.3×10^{-3}	13.8×10^{-3}	0.17

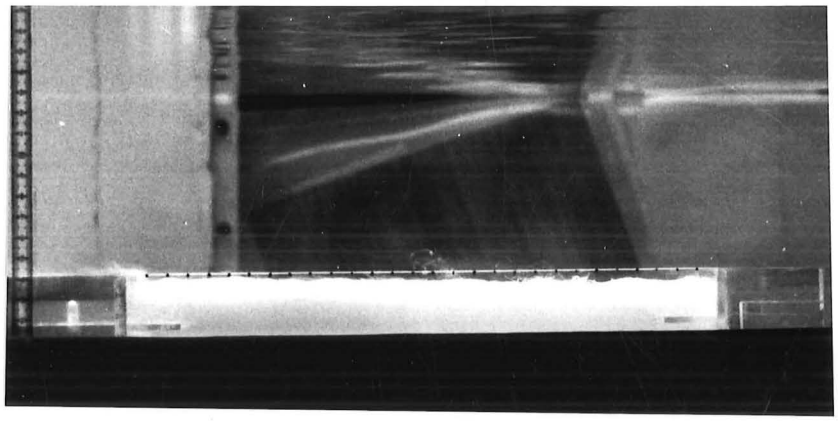

Figure G-3a : Slope of Interface at Side of Cavity :
Ri_δ = 2.85, $\Delta\rho/\rho_0$ = 0.1014, $CaCl_2$, U_o = 0.0732 m/s

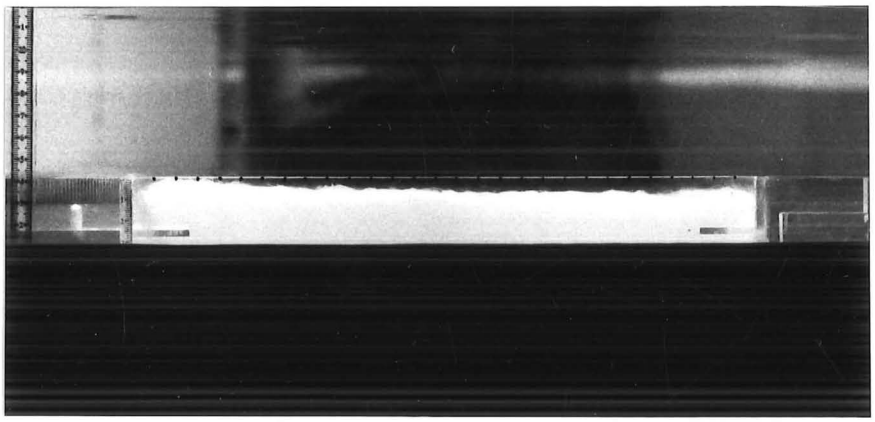

Figure G-3b : Slope of Interface at Side of Cavity :
Ri_δ = 4.04, $\Delta\rho/\rho_0$ = 0.2137, $CaCl_2$, U_o = 0.0909 m/s

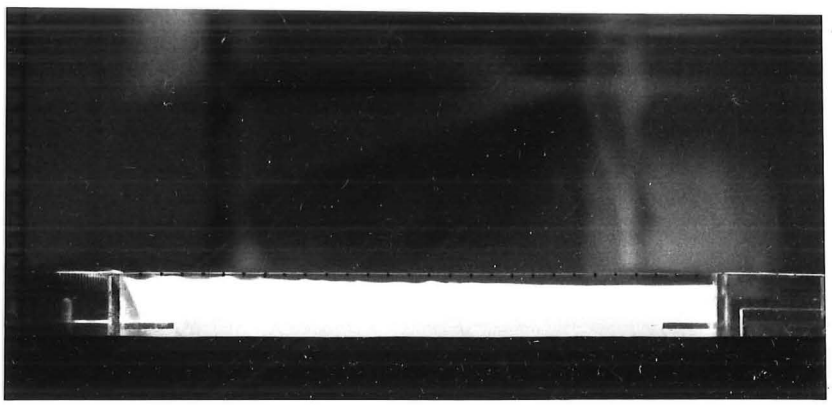

Figure G-3c : Slope of Interface at Side of Cavity :
Ri_δ = 7.95, $\Delta\rho/\rho_0$ = 0.2516, $CaCl_2$, U_o = 0.0732 m/s

G-5 Comparison of Measured and Calculated Slopes

The measured slope at the side of the cavity was 4 to 5 times the calculated slope at the 260 mm station. As the interfacial slope is proportional to the applied shear stress, this suggests that the effective shear stress at the side of the cavity may be 4 to 5 times the shear stress at the 260 mm station. This has been attributed to the interaction of the 'side leakage' with the mean flow which resulted in a high effective shear stress at the side of the cavity (Chapter 5). Lack of measurements at the side has prevented a suitable comparison being made. It is not accurately known what errors are involved in the value of shear stress at the side, although errors in τ_0 may be 30-40% (Chapter 5). A second source of error is in the measurement of interfacial slope. Variations of ± 1mm in heights of 4-8 mm may give errors of up to 25%. The third error source is the assumed invariance of u_* between the perspex boundary and the interface of freshwater and dense saline solution. The magnitude of this third error cannot be estimated as no measurements were made. It would have been difficult to obtain reliable measurements with the Laser Doppler Anemometer within a medium which had a fluctuating refractive index. These three sources of error are the main contributors which affected the comparison of calculated and measured slopes.

APPENDIX H

REGIONS OF RECIRCULATING FLOW

A consequence of the tilt of the interface and the requirement that the interface at the downstream end of the cavity be kept at the top of the cavity, was the region of recirculating flow at the upstream end of the cavity. This was similar to flow over a backward-facing step as the interface level at the upstream end may be of order 10 mm below the top of the cavity. This height varied slightly with Richardson number although from Appendix G, this difference should decrease with an increase in Richardson number.

The flow over a backward-facing step is shown in Figure H-1a and in detail in Figure H-1b. The presence of filaments or wisps of saline solution moving against the direction of upper layer mean flow confirmed the presence of recirculating flows. This was later checked with an injection of dye just upstream of the cavity.

The region of recirculating flow at the downstream end was periodic because this only occurred when part of the interfacial wave trough contacted the wall. When the wave crest was at the wall, the upper layer flow was guided over the cavity edge and no recirculation occurred (Figure H-2a). However, when part of the wave trough was at the wall, the upper layer flow forced the wave trough below the original level (Figure H-2b). Review of video-tape recordings have shown that this behaviour is due to a small region of recirculating flow reinforcing the periodic drop in the level of the interface.

The recirculating region at the upstream end of the cavity was about 2-5 cm in length whereas the corresponding region at the downstream end of the cavity was about 1-2 cm in length. A detailed study of recirculating flows was outside the scope of this work.

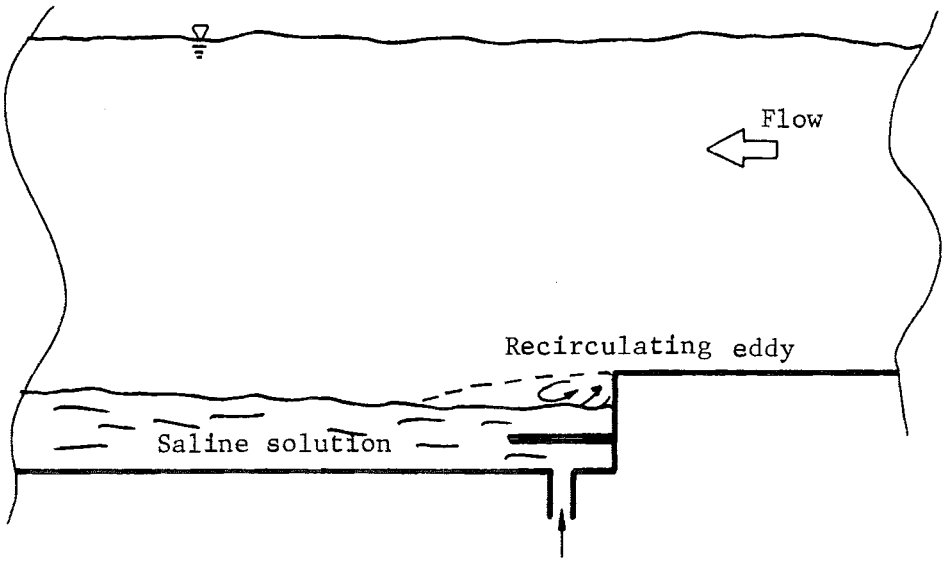

Figure H-1a : The Recirculating Flow Structure at the Upstream End of the Cavity

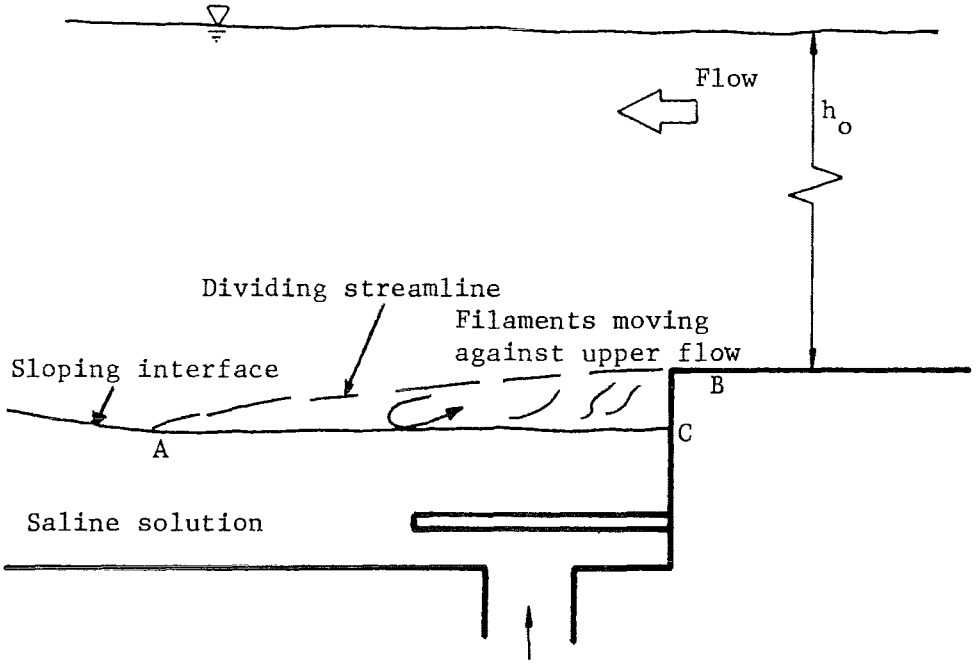

Figure H-1b : Enlarged View of Upstream End of Cavity

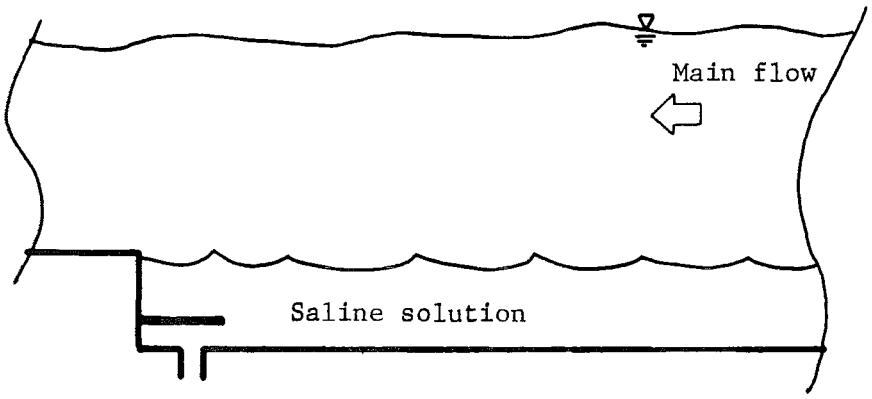

(a) Figure H-2a : Flow over Downstream End of Cavity when Wave Crest is at Edge

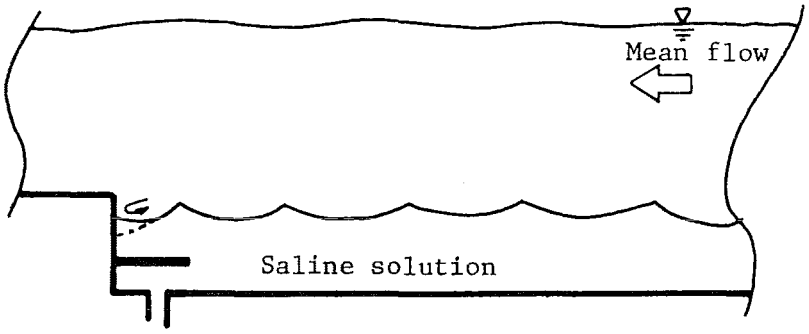

(b) Figure H-2b : Flow over Downstream End of Cavity when Part of Wave Trough is at Edge

APPENDIX I

EVALUATION OF THE ENTRAINMENT VELOCITY $u_e(F)$

I-1 The Flux Entrainment Velocity

The required entrainment velocity $u_e(F)$ was an average over the interfacial area and was assumed to be constant. Consequently, the distributions of mean velocity and density were not required and integral forms were used. The experimental flow situation is shown in Figure I-1. The terms Q_o, Q_u, Q_l, Q_e and Q_T represented the upstream volume flowrate, the volume flowrate over the model, the volume flowrate below the model, the volume entrainment rate, and the total volume flowrate downstream of the model. The flow system was fully recirculating so that Q_T eventually became Q_o at a later time. During the experiment the density ρ_o of the upper layer increased so that the difference of the densities of the upper and lower layers $\Delta\rho = \rho_1 - \rho_o$ decreased. This $\Delta\rho$ became smaller as the experiment progressed. As will be shown later, the change in the ratio $\frac{\Delta\rho}{\rho_o}$ due to the increase in density of the upper layer was of the order of 0.1% and the resulting change to the Richardson was of the same order.

The volume flowrates were defined as :

$$Q_o = Q_u + Q_i = \iint \overline{U}_o \, dydz \quad . \tag{i-1}$$

$$Q_e = \iint w \, dxdy \tag{i-2}$$

where w was the upward velocity of saline solution at the interface.

$$Q_T = Q_o + Q_e \tag{i-3a}$$

$$= \iint \overline{U}_o \, dydz + \iint u_e(F) \, dxdy \tag{i-3b}$$

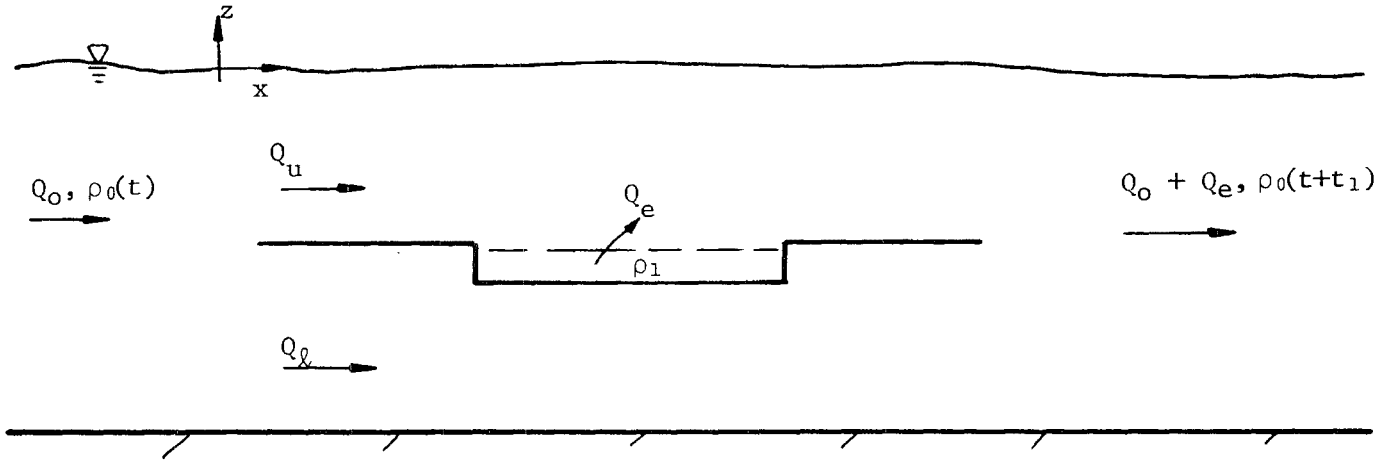

Figure I-1 : Flow Situation in Open Channel

The densities $\rho_o(t)$, $\rho_o(t+t_1)$ represented the upper layer density at some time t and at a time $t + t_1$ after entrainment had begun respectively. The time t_1 was that taken for the saline solution and water to be thoroughly mixed. The density ρ_1 of the saline solution was assumed to be constant during the experiment. This will be shown later in the discussion of errors. After the initial start-up and adjustment, the water-saline solution interface was kept at a constant level throughout the experiment with a steady influx of solution to replace the entrained fluid.

The conservation of mass required that :

$$Q_o\rho_o(t) + Q_e\rho_1 = (Q_o + Q_e)\rho_o(t + t_1) \qquad \text{(i-4)}$$

or $$Q_e\rho_1 = Q_o(\rho_o(t+t_1) - \rho_o(t)) + Q_e\rho_o(t+t_1)$$

then $$Q_e = Q_o \frac{(\rho_o(t+t_1) - \rho_o(t))}{\rho_1 - \rho_o(t+t_1)} \qquad \text{(i-5)}$$

From Equation (i-2)

$$Q_e = \iint w \, dxdy \quad ,$$

now assume that

$$Q_e = \bar{w} \; xA_1$$

where $\bar{w}$ was the spatial average flux entrainment velocity of saline solution and A_1 was the area of the cavity opening. These assumptions were consistent with the integral representation of the mean

velocity. Then :

$$\overline{w} \quad xA_1 = Q_o \frac{(\rho_o(t+t_1) - \rho_o(t))}{\rho_1 - \rho_o(t+t_1)}$$

The initial density of the freshwater was $\rho_o(t=0) = \rho_o(0)$. From experiments $\rho_1-\rho_o(t+t_1) \sim \rho_1-\rho_o(t) \sim \rho_1-\rho_o(0)$ for $t, t_1 > 0$, and $\rho_o(t+t_1) - \rho_o(0) \sim 10^{-3}\rho_o(0)$ then $\rho_1 - \rho_o(t+t_1) >> \rho_o(t+t_1) - \rho_o(0)$.
Write $\rho_1-\rho_o(0) = \Delta\rho$ so that the space averaged flux entrainment velocity can be expressed as :

$$\overline{w} \quad = \quad \frac{Q_o}{A_1} \times \frac{\rho_o(t+t_1) - \rho_o(t)}{\Delta\rho} \quad . \qquad \text{(i-6)}$$

When the experiment was at steady state Q_o and Q_e were constant, hence $\overline{w}$ was constant over a time, say t_2. The flux entrainment velocity :

$$u_e(F) = \frac{1}{t_2} \int_t^{t+t_2} \overline{w} \, dt \qquad \text{(i-7)}$$

was also constant. Write, with the overbar signifying average, Equation (i-6) as :

$$u_e(F) = \overline{\left[\frac{Q_o}{A_1} \times \frac{\rho_o(t+t_1) - \rho_o(t)}{\Delta\rho}\right]}$$

$$= \frac{1}{A_1} \times \overline{\frac{Q_o}{\Delta\rho} [\rho_o(t+t_1) - \rho_o(t)]} \quad .$$

Choose t_1 to be equal to T where T was the time required to recycle the total volume V_o of water in the system. Then :

$$Q_o \quad = \quad \frac{V_o}{T}$$

and

$$u_e(F) = \frac{1}{A_1} \times \overline{\frac{V_o}{T\Delta\rho}\left[\rho_o(t+T) - \rho_o(t)\right]}$$

or

$$u_e(F) = \frac{V_o}{A_1} \times \frac{1}{\Delta\rho}\overline{\left[\frac{\rho_o(t-T) - \rho_o(t)}{T}\right]} \quad . \qquad \text{(i-8)}$$

As the experiment was at steady state, the term in brackets in Equation (i-8) was the rate of change of density :

$$\overline{\left[\frac{\rho'(T)}{T}\right]}$$

where

$$\rho'(T) = \rho_o(t+T) - \rho_o(t).$$

If the changes in the values of V_o and $\Delta\rho$ were small, then :

$$\left[\frac{\rho'(T)}{T}\right]$$

should be nearly constant. This also meant that if a different time interval $t' > T$ was chosen, and conditions were still steady, Equation (i-8) still gave the same value of $u_e(F)$, that is :

$$\overline{\left[\frac{\rho'(t')}{t'}\right]} = \overline{\left[\frac{\rho'(T)}{T}\right]} \quad .$$

This assumed that $(V_o/\Delta\rho)$ was constant in each case.

The flux entrainment velocity was evaluated from Equation (i-8) and in all the experiments the time interval was chosen to be $t_1 \sim 500$ seconds. The pump flowrate was about 10 litres/sec and the approximate value of $T \sim 2900$ litres/10 litres per second or $T \sim 290$ seconds for the largest volume of water used in the experiments.

I-2 Error Analysis

The assumption that $\frac{V_o}{\Delta\rho}$ was nearly constant during experiments can be checked. The largest errors occurred in the smallest value of V_o and smallest $\Delta\rho$. At small Richardson numbers, about 40 litres of saline solution were used. This corresponded to $\rho_1 = 1.0486\ \rho_o$. Experimental details showed that $\rho'(t_1)$ was of order $0.001\ \rho_o(0)$. The error in assuming that V_o was constant amounted to 1.6% and the assumption that $\Delta\rho$ was constant resulted in less than a 0.2% error. The value of $\frac{V_o}{\Delta\rho}$ at the end of the above experiment was :

$$V_o(1 + \frac{40}{2500})/\Delta\rho(1-.021) \sim 1.04(\frac{V_o}{\Delta\rho}) \quad .$$

Hence there was an error of about 4% in the evaluation of $u_e(F)$ from Equation (i-8) if the initial value of $(\frac{V_o}{\Delta\rho})$ was assumed.

The addition of a volume V_1 of saline solution also resulted in the slight reduction of the mean velocity through the working section. The addition of 40 litres caused the water level in the working section to rise about 7 mm. The maximum reduction in the mean velocity through the working section was about 3% but in the other experiments this velocity reduction was about 1%.

The Richardson number was evaluated with initial values of the parameters. A 3% reduction in U_o only produced a difference of less than 1% in δ_t as δ_t scaled as $U_o^{-1/5}$. The Richardson number at the end of the

experiment was :

$$Ri_\delta \text{ (end)} = g \frac{\Delta\rho(1-.021) \quad \delta_t(1-0.01)}{\rho_o(1+.001) \quad \overline{U}_o{}^2(1-.03)^2}$$

$$= g \frac{\Delta\rho}{\rho_o} \frac{\delta_t}{\overline{U}_o{}^2} \left[\frac{0.979 \times 0.99}{1.001 \times .97^2}\right]$$

$$= 1.029 \left[g \frac{\Delta\rho}{\rho_o} \frac{\delta_t}{\overline{U}_o{}^2}\right]$$

or within 3% of the initial value. The sum of each of the errors associated with each term of Ri_δ except δ_t amounted to about 8%. The reason for the difference of error estimates was attributed to the way the experiment was run. The entrainment of saline solution built up the salt concentration in the recirculating water system. This increased $\rho_o(t)$ and decreased $\Delta\rho$ while also increasing the volume in the water system. This raised the water level in the working section which in turn reduced $\overline{U}_o$. However, this particular experimental setup resulted only in small changes in $\Delta\rho$, ρ_o, $\overline{U}_o$, and δ_t.

The flow over the cavity was not measured so no comparison could be made between estimated δ_t and measured δ_t. However, as a first estimate, choose the error to be about 10% so that the error in Ri_δ is about 13%.

The density of the saline solution was checked during experiments by removing a small amount from near the bottom of the cavity and measuring the conductivity. The measurements showed less than a 1% difference between the cavity solution and the original measurement when the solution was made up.

The conductivity meter and probes (Glover 1970) output a voltage which was directly proportional to the conductivity of the water. This output voltage was recorded on a continuous chart and by evaluating the

rate of change in voltage, the conductivity rate change was also obtained. A calibration of conductivity versus density was obtained from standard saline solutions which were prepared prior to experimentation. The error in the calibration of the probes from a curve such as Figure B-4 was about 3%. The value of Q_o was determined from another calibration curve which could have a small error of about 5%.

The determination of the mean level of the interface was made difficult because of the fluctuations of the wave train. The criterion which was applied to the experiment was that the influx of saline solution was set at a rate Q_e, so that solution was not being forced over the edge of the cavity at the downstream end. This was difficult to quantify and as Figure 6.9 showed, the identical experiments had differences in $\frac{u_e(F)}{u_*}$ of order 25% although there were a small number in which these differences were of order 40%. As the experiments were not carried out with a deliberate drop in the interfacial height, the relation between Q_e and the height is unknown. The density of the saline solutions can be determined to an accuracy of 1% by the conductivity (Radiometer) meter and with the assistance of standard tables from a handbook of chemistry and physics (Weast 1975). The sum of the errors which had accumulated in evaluating $u_e(F)$ was about 25% and this included the error due to the fluctuating level of the interface.

The difference $\rho_o(t+\Delta t) - \rho_o(t)$ was usually less than 500 mg NaCℓ/litre solution. This amounted to :

$$\frac{\rho_o(t+\Delta t) - \rho_o(t)}{\rho_o(t)} \sim 5 \times 10^{-3}$$

The differences were similar in the experiments involving CaCℓ and the assumption that $\rho_o(t+\Delta t) \sim \rho_o(t)$ resulted in an error of less than 1%.

APPENDIX J

MEASUREMENTS OF THE NONDIMENSIONAL ENTRAINMENT VELOCITY AND RELEVANT RICHARDSON NUMBER

The measurements of the entrainment $u_e(F)$ are contained in this Appendix with the values of the length and velocity scales of the Richardson number.

$\overline{U}_o$, m/s = the bulk mean velocity in the upper layer

$= \frac{Q_o}{A_o}$, where Q_o and A_o are volume flowrate and mean cross-sectional area of in the channel working section.

u_*, m/s = friction velocity at the 150 mm position south of the channel centreline and is considered as representative of the channel flow.

δ_t, m = depth of the new turbulent boundary layer which has formed over the cavity due to a change of roughness,

$$= 0.37\ L_1 \left[\frac{\upsilon_1}{U_o L_1}\right]^{1/5} \quad \text{(Schlichting 1979)}$$

where L_1 is the cavity length, and υ_1 is the kinematic viscosity of the denser fluid.

$\Delta\rho$ = $\rho_1 - \rho_o$, density difference between the lower and upper layers of fluid.

$u_e(F)$ = the flux entrainment velocity.

Ri_δ = $g \frac{\Delta\rho}{\rho_o} \frac{\delta_t}{\overline{U}_o^2}$, the form of the Richardson number used to present the results of this work.

The results of the sodium chloride experiments are listed separately from the calcium chloride experiments.

Table J-1 : Sodium Chloride Experiments

$\bar{U}_o$, m/s	u_*, m/s	$\Delta\rho/\rho_o$	δ_t, m	Ri_δ	$u_e(F)/\bar{U}_o$	$u_e(F)/u_*$
0.0732	0.0087	0.0182	14.70×10^{-3}	0.49	33.79×10^{-4}	28.43×10^{-3}
0.0732	0.0087	0.0182	14.70×10^{-3}	0.49	35.92×10^{-4}	30.23×10^{-3}
0.0732	0.0087	0.0282	14.75×10^{-3}	0.76	19.36×10^{-4}	16.30×10^{-3}
0.0732	0.0087	0.0282	14.75×10^{-3}	0.76	20.91×10^{-4}	17.59×10^{-3}
0.0909	0.0105	0.0486	14.20×10^{-3}	0.82	20.42×10^{-4}	17.74×10^{-3}
0.0909	0.0105	0.0486	14.20×10^{-3}	0.82	23.67×10^{-4}	20.50×10^{-3}
0.0813	0.0099	0.0486	14.53×10^{-3}	1.05	14.88×10^{-4}	12.22×10^{-3}
0.0813	0.0099	0.0486	14.53×10^{-3}	1.05	17.20×10^{-4}	14.11×10^{-3}
0.0813	0.0099	0.0486	15.53×10^{-3}	1.05	15.21×10^{-4}	12.49×10^{-3}
0.0909	0.0105	0.0677	14.30×10^{-3}	1.15	15.14×10^{-4}	13.10×10^{-3}
0.0732	0.0087	0.0486	14.83×10^{-3}	1.32	12.12×10^{-4}	10.2×10^{-3}
0.0732	0.0087	0.0486	14.83×10^{-3}	1.32	15.38×10^{-4}	12.94×10^{-3}
0.0813	0.0099	0.0677	14.62×10^{-3}	1.47	8.43×10^{-4}	6.92×10^{-3}
0.0813	0.0099	0.0677	14.62×10^{-3}	1.47	8.71×10^{-4}	7.16×10^{-3}
0.0909	0.0105	0.0894	14.44×10^{-3}	1.53	9.04×10^{-4}	7.83×10^{-3}
0.0909	0.0105	0.0894	14.44×10^{-3}	1.53	12.24×10^{-4}	10.60×10^{-3}
0.0909	0.0105	0.1008	14.52×10^{-3}	1.74	9.46×10^{-4}	8.21×10^{-3}
0.0909	0.0105	0.1008	14.52×10^{-3}	1.74	8.51×10^{-4}	7.36×10^{-3}
0.0732	0.0087	0.0677	14.93×10^{-3}	1.85	4.47×10^{-4}	3.70×10^{-3}
0.0732	0.0087	0.0677	14.93×10^{-3}	1.85	5.87×10^{-4}	4.94×10^{-3}
0.0909	0.0105	0.124	14.69×10^{-3}	2.16	5.66×10^{-4}	4.93×10^{-3}
0.0909	0.0105	0.124	14.69×10^{-3}	2.16	5.02×10^{-4}	4.34×10^{-3}
0.0813	0.0099	0.1008	14.85×10^{-3}	2.22	4.38×10^{-4}	3.59×10^{-3}
0.0732	0.0087	0.0894	15.10×10^{-3}	2.47	5.83×10^{-4}	4.9×10^{-3}
0.0909	0.0105	0.1478	14.89×10^{-3}	2.61	3.61×10^{-4}	3.12×10^{-3}
0.0909	0.0105	0.1478	14.89×10^{-3}	2.61	4.33×10^{-4}	3.75×10^{-3}

$\bar{U}_o$, m/s	u_*, m/s	$\Delta\rho/\rho_o$	δ_t, m	Ri_δ	$u_e(F)/\bar{U}_o$	$u_e(F)/u_*$
0.0813	0.0099	0 124	15.02×10^{-3}	2.76	3.57×10^{-4}	2.94×10^{-3}
0.0813	0.0099	0.124	15.02×10^{-3}	2.76	2.64×10^{-4}	2.19×10^{-3}
0.0732	0.0087	0.1008	15.16×10^{-3}	2.80	4.53×10^{-4}	3.81×10^{-3}
0.0909	0.0105	0.1804	15.30×10^{-3}	3.28	4.77×10^{-4}	4.13×10^{-3}
0.0909	0.0105	0.1804	15.30×10^{-3}	3.28	2.70×10^{-4}	2.30×10^{-3}
0.0732	0.0105	0.124	15.34×10^{-3}	3.48	2.03×10^{-4}	1.71×10^{-3}
0.0813	0.0099	0.1804	15.62×10^{-3}	4.18	2.39×10^{-4}	1.96×10^{-3}
0.0813	0.0099	0 1804	15.62×10^{-3}	4.18	2.06×10^{-4}	1.69×10^{-3}
0.0732	0.0087	0.1478	15.55×10^{-3}	4.21	2.33×10^{-4}	1.96×10^{-3}
0.0732	0.0087	0.1478	15.55×10^{-3}	4.21	2.64×10^{-4}	2.23×10^{-3}
0.0732	0.0087	0.1478	15.55×10^{-3}	4.21	3.11×10^{-4}	2.62×10^{-3}
0.0732	0.0087	0.1804	15.95×10^{-3}	5.27	1.68×10^{-4}	1.42×10^{-3}

Table J-2 : Calcium Chloride Experiments

$\bar{U}_o$, m/s	u_*, m/s	$\Delta\rho/\rho_o$	δ_t, m	Ri_δ	$u_e(F)/\bar{U}_o$	u_e/u_*
0.0909	0.0105	0.1014	14.71×10^{-3}	1.77	7.33×10^{-4}	6.34×10^{-3}
0.0732	0.0087	0.1014	15.37×10^{-3}	2.85	2.77×10^{-4}	2.33×10^{-3}
0.0909	0.0105	0.1775	15.46×10^{-3}	3.26	2.26×10^{-4}	1.95×10^{-3}
0.0909	0.0105	0.2137	15.93×10^{-3}	4.04	1.55×10^{-4}	1.34×10^{-3}
0.0909	0.0105	0.26	16.66×10^{-3}	5.14	1.14×10^{-4}	0.99×10^{-3}
0.0732	0.0087	0.1775	16.15×10^{-3}	5.25	1.87×10^{-4}	1.57×10^{-3}
0.0909	0.0105	0.3036	17.56×10^{-3}	6.33	1.12×10^{-4}	0.97×10^{-3}
0.0732	0.0087	0.218	16.69×10^{-3}	6.66	0.89×10^{-4}	0.75×10^{-3}
0.0909	0.0105	0.3488	18.76×10^{-3}	7.77	0.88×10^{-4}	0.45×10^{-3}
0.0732	0.0087	0.2516	17.26×10^{-3}	7.95	0.82×10^{-4}	0.69×10^{-3}
0.0909	0.0105	0.3957	20.34×10^{-3}	9.56	0.55×10^{-4}	0.47×10^{-3}
0.0732	0.0087	0.3036	18.34×10^{-3}	10.19	0.54×10^{-4}	0.45×10^{-3}
0.0732	0.0087	0.3488	19.6×10^{-3}	12.52	0.36×10^{-4}	0.3×10^{-3}
0.0732	0.0087	0.3957	21.24×10^{-3}	15.39	0.29×10^{-4}	0.25×10^{-3}

APPENDIX K

ENTRAINMENT EXPERIMENTS WITH SHORTER CAVITIES

K-1 Introduction

A number of exploratory experiments were conducted in two shorter cavities of the same width as the full size cavity. In total, six experiments were conducted in a 90 mm long cavity and a further six experiments were conducted in a 30 mm long cavity. In each set of experiments, three experiments were carried out with $\overline{U}_o$ = 0.0732 m/s and the remaining three were carried out with $\overline{U}_o$ = 0.0909 m/s.

K-2 Observations of Experiments in the 90 mm Cavity

Observations of the six experiments in the 90 mm cavity showed a similar behaviour to that observed in the full-size cavity at low Ri_δ. Figure K-1a shows an experiment with $\frac{\Delta\rho}{\rho_o}$ = 0.0282 and $\overline{U}_o$ = 0.0732 m/s. The waves at the interface appear very similar to the waves shown in Figure 6.1. Filaments of the saline solution can be seen leaving the wave crests and carried downstream. For higher $\frac{\Delta\rho}{\rho_o}$ and lower values of $\overline{U}_o$, the interfacial waves were less sharp but saline solution filaments were being ejected upwards into the upper layer and carried downstream.

K-3 Observations of Experiments in the 30 mm Cavity

The experiments in the 30 mm cavity showed that only one wave cycle was present at the interface. Figure K-1b shows an experiment with $\frac{\Delta\rho}{\rho_o}$ = 0.124 and $\overline{U}_o$ = 0.0732 m/s. Filaments of saline solution were being ejected upwards mainly at the cavity walls. A sketch of the observed

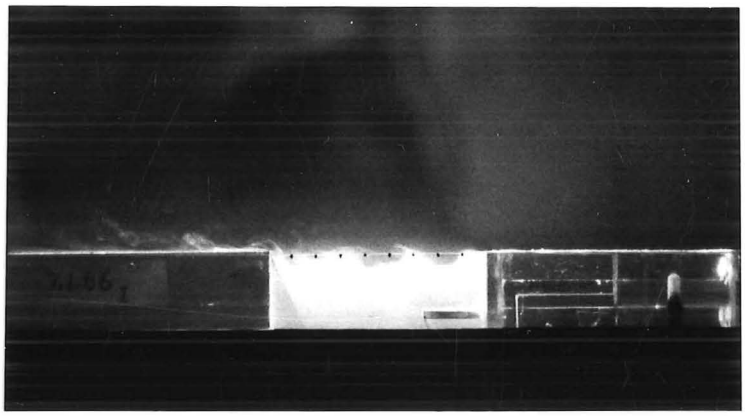

Figure K-1a : View of Interfacial Wave Region at Side of Cavity - 90 mm Cavity : Ri_a = 0.62, $\Delta\rho/\rho_0$ = 0.0282, $\bar{U}_o$ = 0.0732 m/s

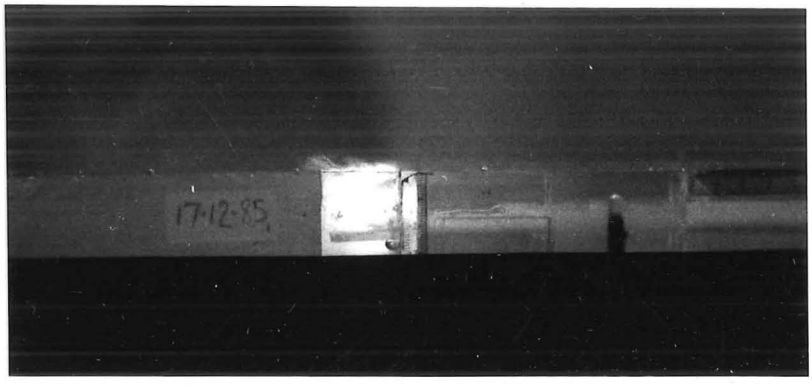

Figure K-1b : View of Interfacial Wave Region at Side of Cavity - 30 mm Cavity : Ri_a = 1.14, $\Delta\rho/\rho_0$ = 0.124, $\bar{U}_o$ = 0.0732 m/s

wave is shown in Figure K-2a, b. Figure K-2a shows the interfacial wave crest near the upstream end and a region of recirculating flow at the downstream end. A half cycle later, shown in Figure K-2b, the crest has reached the downstream wall. At large values of $\frac{\Delta\rho}{\rho_o}$ and $\bar{U}_o$ = 0.0732 m/s, the interfacial wave appeared similar to a standing wave with a frequency of about 1 Hz while at smaller $\frac{\Delta\rho}{\rho_o}$ and $\bar{U}_o$ = 0.0909 m/s, the interfacial wave crest was travelling downstream. The vertical scale of the motion was 5-10 mm.

K-4 Measurements of Entrainment from the 90 mm and 30 mm Cavity

In these experiments the wave height in almost all the experiments was greater than δ_t, hence the relevant lengthscale for the Richardson number was 2a. The velocity scale was the bulk mean velocity $\bar{U}_o$. The measurements of $\frac{u_e(F)}{\bar{U}_*}$ versus Ri_a where $Ri_a = \frac{g\ 2a}{\bar{U}_o^2}$ are shown in Figure K-3. The same data is also presented in the form $\frac{u_e(F)}{\bar{U}_o}$ versus Ri_a in Figure K-4. The distribution of data points in both figures are very similar. The data points from the 90 mm cavity are located in Figure K-3 close to the curve given by Equation (6.13) and in Figure K-4 close to the curve given by Equation (6.14).

The data points from the 30 mm cavity with $\bar{U}_o$ = 0.0909 m/s are located close to the data from the 90 mm cavity in both Figures K-3 and K-4. However, the data from experiments with $\bar{U}_o$ = 0.0732 m/s are located below the other data points. These differences are too large to be included in the bounds of experimental error. The data from the 30 mm cavity can also be represented by a $E_* \propto Ri_\delta^{-1}$ relation. The large differences in data presentation suggests that some other mechanism other than the wave-breaking mechanism is dominant. As these experiments were

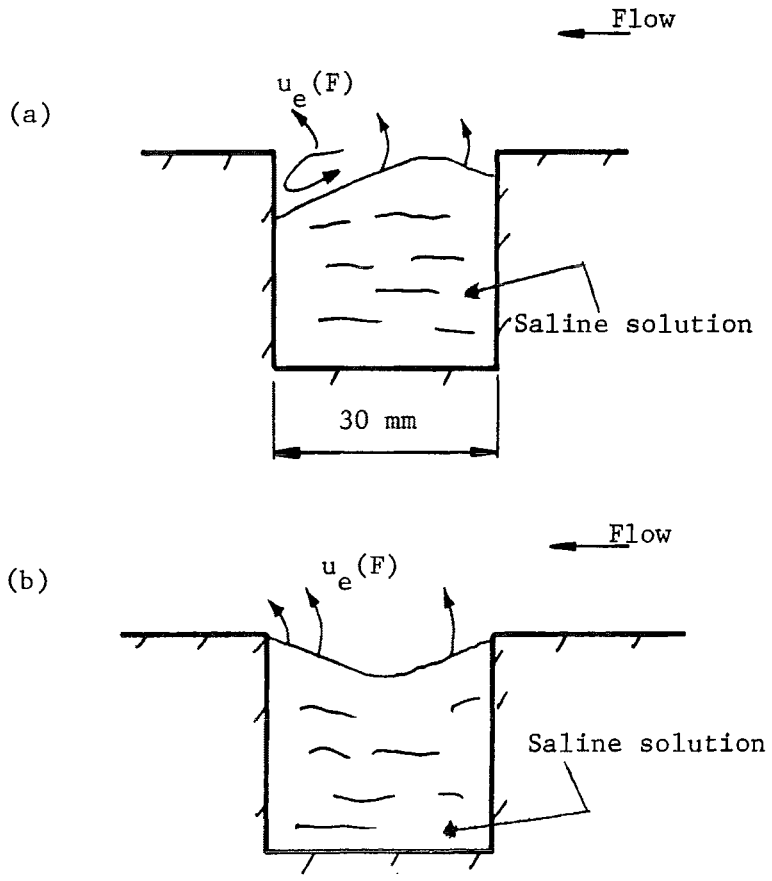

Figure K-2a,b : Standing Wave Pattern Observed in Some Experiments in the 30 mm Cavity

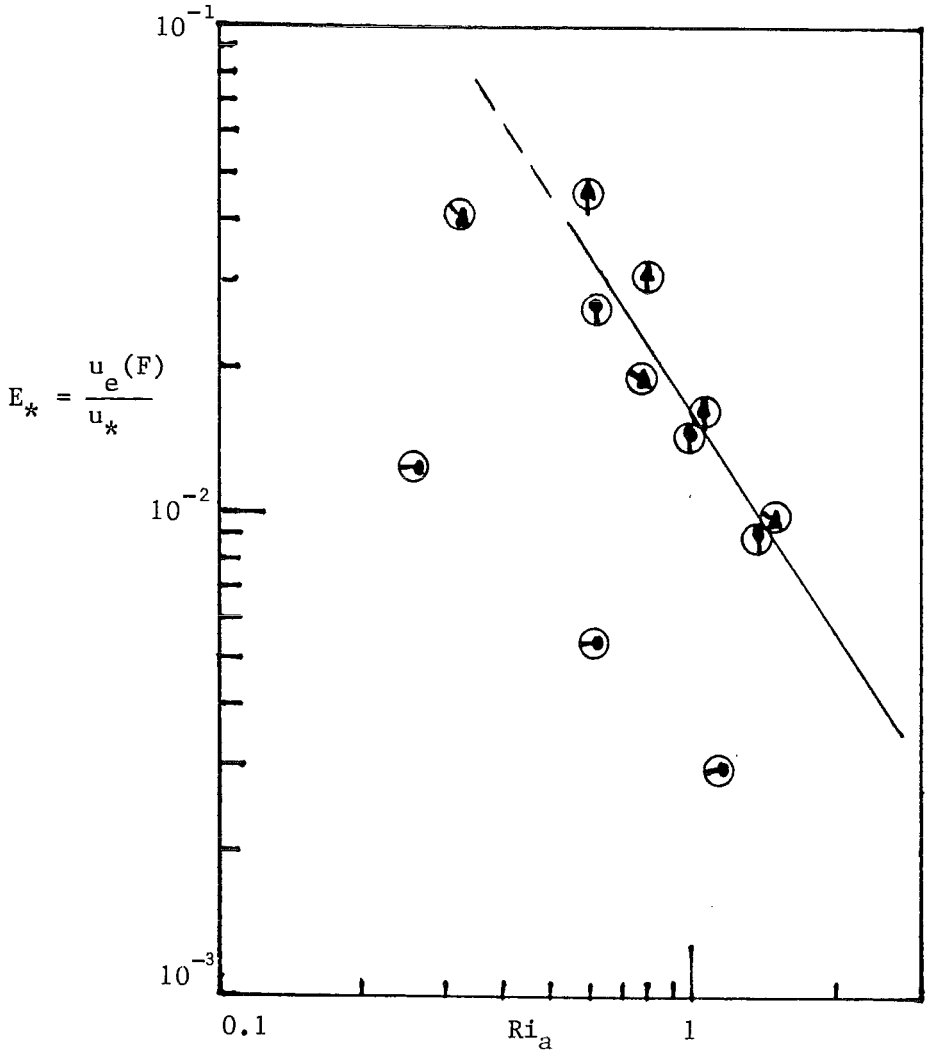

Figure K-3 : Entrainment Data - 90 mm and 30 mm cavities : E_* vs. Ri_a

Key		
$\bar{U}_o$,m/s	30 mm cavity	90 mm cavity
0.0732	⊖	⊕
0.0909	◔	◕

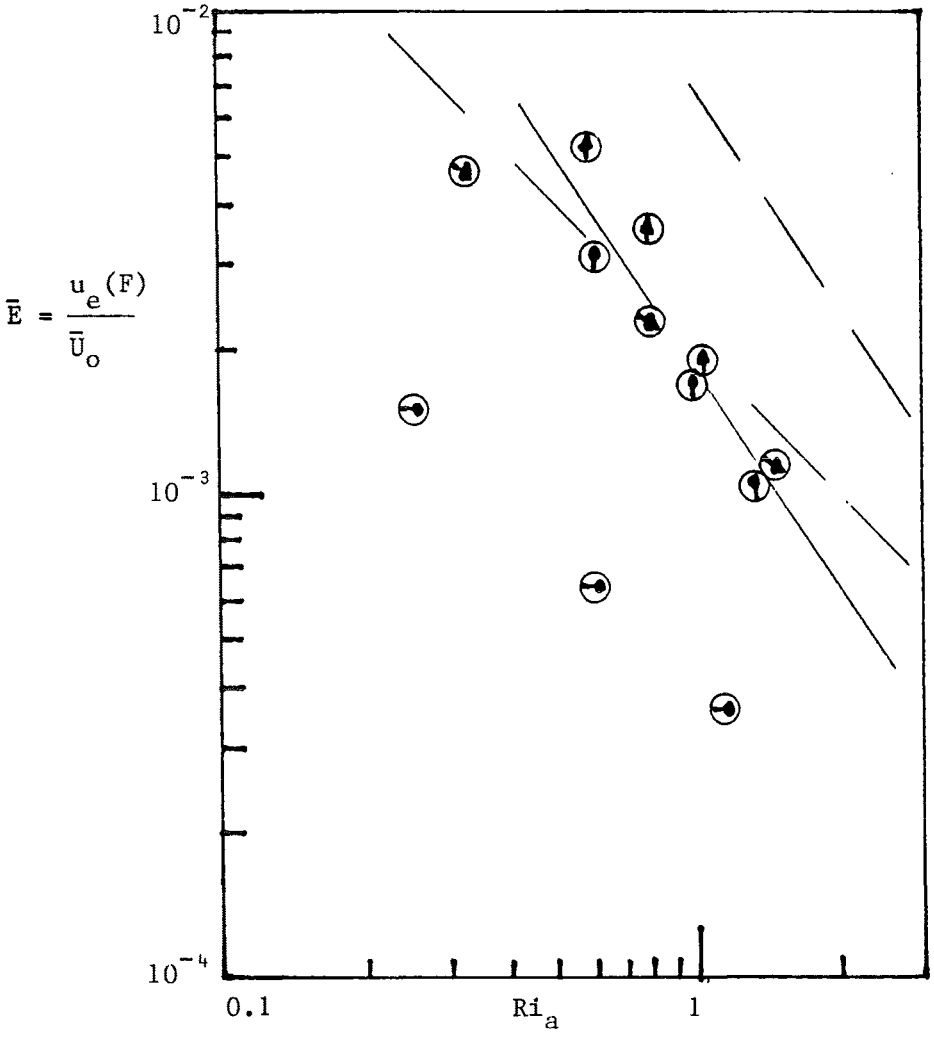

Figure K-4 : Entrainment Data - 90 mm and 30 mm Cavities : $\bar{E}$ vs. Ri_a

Key		
$\bar{U}_o$,m/s	30 mm cavity	90 mm cavity
0.0732	⊖	⊖
0.0909	⊖	⊖

intended to be exploratory, no further discussion will be raised. Table K-1 lists the data from these experiments.

Table K-1 : Entrainment Data from 90 mm and 30 mm Cavities

$\bar{U}_o$, m/s	$\frac{\Delta\rho}{\rho_o}$	ν_i, m^2/s	δ_t, mm	2a, mm	$\frac{u_e(F)}{u_*}$	Ri_δ	Ri_a
90 mm cavity							
0.0909	0.0282	1.042×10^{-6}	5.54	~15	4.77×10^{-2}	0.185	0.60
0.0909	0.0677	1.108×10^{-6}	5.61	~10	3.15×10^{-2}	0.45	0.80
0.0909	0.124	1.267×10^{-6}	5.76	~ 7	1.65×10^{-2}	0.85	1.03
0.0732	0.0282	1.042×10^{-6}	5.78	~12	2.71×10^{-2}	0.3	0.62
0.0732	0.0677	1.108×10^{-6}	5.86	~ 8	1.47×10^{-2}	0.73	0.99
0.0732	0.124	1.267×10^{-6}	6.02	~ 5	0.90×10^{-2}	1.37	1.14
30 mm cavity							
0.0909	0.0282	1.042×10^{-6}	2.3	~10	4.07×10^{-2}	0.08	0.33
0.0909	0.0677	1.108×10^{-6}	2.33	~10	1.94×10^{-2}	0.19	0.80
0.0909	0.124	1.267×10^{-6}	2.39	~10	0.97×10^{-2}	0.35	1.47
0.0732	0.0282	1.042×10^{-6}	2.4	~ 5	1.26×10^{-2}	0.124	0.26
0.0732	0.0677	1.108×10^{-6}	2.43	~ 5	0.55×10^{-2}	0.30	0.62
0.0732	0.124	1.267×10^{-6}	2.5	~ 5	0.3×10^{-2}	0.57	1.14